Crack Growth Behaviour of Pipeline Steels under Variable Pressure Fluctuations in a High pH Environment

by

Hamid Niazi

A thesis submitted in partial fulfillment of the requirements for the degree of

Doctor of Philosophy

in
Materials Engineering

Department of Chemical and Materials Engineering
University of Alberta

Abstract

High pH Stress Corrosion Cracking (HpHSCC) in the pipeline steel has been a threat for buried pipeline integrity since the first occurrence in the 1960s. Much research has been devoted to understanding the causes of this phenomenon and remedies for mitigation of HpHSCC failures. In addition to developing the methods and strategies to mitigate such failures, the knowledge of HpHSCC cracks growth behaviour has been at the forefront of pipeline industries' attention. This knowledge helps pipeline operators to estimate the reliable lifespan of the cracked pipe. Parkins proposed the bathtub model to show the time-dependent behaviour of HpHSCC crack growth. Accordingly, a pipe susceptible to HpHSCC may go through the five sequential stages *viz.* incubation stage, crack nucleation and early stage of crack development (stage 1a), crack development to provide the mechanical driving force for sustainable crack growth (stage 1b), mechanically derived crack propagation (stage 2), and rapid crack growth to failure (stage3). There are two significant imperfections associated with the current model. First, stage 1b, the lifetime determining stage in HpHSCC crack growth, has been less studied. Parkins assumed random crack initiation and crack coalescence causes stochastic crack propagation. Second, Parkins employed either monotonic loading or constant amplitude loading conditions in the early experiments. However, pipelines experience variable amplitude loading conditions during their operations. The load interaction effects remain to be studied.

This research attempts to study the HpHSCC crack growth Behaviour under both constant amplitude and variable amplitude loading conditions at stage 1b and stage 2 to address the bathtub model's problems, as mentioned earlier. In this study, compact tension specimens made from X65 pipeline steel were used, and the environmental conditions were 0.5 M Na_2CO_3 and 1 M $NaHCO_3$ at 40 °C and applied cathodic protection of -590 $mV_{SCE.}$

For stage 1b, it is shown that the crack growth rate is highly sensitive to loading characteristics, so that the highest crack growth rate was obtained under constant amplitude cyclic loading with the stress ratio (*R*-ratio=minimum stress/maximum stress) of 0.2 and frequency of 10^{-2} Hz. On the other hand, high *R*-ratio cycles showed the lowest crack propagation rate. Variable amplitude loading waveforms composed of a number of high *R*-ratio cycles flowed by an underload cycle (low *R*-ratio cycle) showed an intermediate crack propagation rate. It was observed large load fluctuations (*i.e.* low *R*-ratio cycles) form a cyclic plastic zone at the preexisting crack tip. The cyclic plastic zone is a breeding ground for secondary cracks initiation close to the existing crack tip. If these cracks merge to the main crack, the crack length on the free surface increases, followed by increasing the mechanical driving force for crack propagation in depth. Crack initiation and crack coalescence is the primary mechanism for crack propagation during stage 1b. Increasing the number of minor cycles between two underload cycles enhances the crack growth rate by increasing the chance for crack coalescence and more available time for low-temperature creep strain to be exhausted.

The dominant mechanism for HpHSCC crack growth in Stage 2 is anodic dissolution or repeated rupture and passive film formation at the crack tip. The loading condition at this stage is potent enough to provide sustainable crack growth. There is a power-law relationship between stage 2 HpHSCC crack growth and strain rate. The strain rate is a function of several parameters, including mean stress intensity factor, amplitude as well as the frequency of load fluctuation. Similar to crack propagation in stage 1b, low *R*-ratio cycles, particularly high-frequency ones, assist secondary cracks initiation on the free surface.

The implication of this study's results for the pipeline operators is to control the pressure fluctuations and minimize underload cycles, particularly high-frequency ones. Such cycles

increase the chance for secondary crack initiation on the pipe's free surface, followed by crack coalescence. Additionally, such cycles generate higher strain rates and increase the crack propagation rate at stage 2. Ergo, avoiding underload cycles increases the pipe's reliable lifetime.

Preface

This thesis is an original work by Hamid Niazi. Chapter 2 of this thesis has been accepted for publication as H. Niazi, R. Eadie, W. Chen. H. Zhang, "*High pH Stress Corrosion Cracking Initiation and Crack Evolution in Buried Steel Pipelines: A Review*," Engineering Failure Analysis. Chapter 4 of this thesis has been submitted as H. Niazi, G. Nelson, L, Lamborn, R. Eadie, W. Chen, H. Zhang, "*Crack Growth Sensitivity to the Magnitude and Frequency of Load Fluctuation in Stage 1b of High pH Stress Corrosion Cracking*." Chapter 5 of this thesis is accepted for publication as H. Niazi, Sh. Wang, L. Lamborn, R. Eadie, W. Chen, H. Zhang, "*Effects of Load Interactions on the Onset of Stage Two of High pH Stress Corrosion Cracking,*" Journal of Pipeline Science and Engineering. I was responsible for data collection and analysis, as well as the manuscript composition. Chapter 6 of this study has been published as H. Niazi, K. Chevil, E. Gamboa, L. Lamborn, W. Chen, H. Zhang, "*Effects of Loading Spectra on High pH Crack Growth Behaviour of X65 Pipeline Steel*, " Corrosion 76 (6), p. 601-615.

I was responsible for data collection and analysis, as well as the manuscript composition. Prof. Hao Zhang and Prof. Weixing Chen have been the supervisory authors.

Dedicated to My Beloved Family

Acknowledgement

Since September 2016, I have been given the privilege of studying at the University of Alberta. I would like to thank my supervisors, **Prof. Hao Zhang** and **Prof. Weixing Chen**, who opened a new era in my life by providing me with the opportunity to study at UoA. Hereby, I want to express my heartful and utmost gratitude towards the vision, patience, guidance, unconditional support, and wealth of knowledge they provided through my studies.

I would like to thank **Prof. Dongyang Li** as well for all his supports during this study. I would also like to express my deep appreciation to **Prof. Reg Eadie** for his kind guidance and instructive comments on my research.

Additional thanks to the technical staff of the Department of Chemical and Materials Engineering for all their assistance (in alphabetical order by the first name): Amy Chow, Dave Parlin, Herb Green, James McKinnon, Kevin Heidebrecht, Lily Laser, Marion Pritchard, Mia Law, Nathan Gerein, and Walter Boddez.

A big thanks to my colleagues (in alphabetical order by the first name): Devin Engel, Greg Nelson, Joshua Knechtel, Jerome Ang, Jiaxi Zhao, Keqian Hu, Lu Sun, Olatinka Tenhinse, Rui Ning Li, Shidong Wang, and Zhezu Xu. I would also like to thank Ms. Elaheh Alizadeh Rabiei for her kind advice for improving the illustrations in this study.

My gratitude also goes to all my friends for the support they offered me while pursuing this research. I would like particularly thank Mohammad Khalkhali, Amir Moeini, Yashar Behnamian, Taghi Amiri, and Reza Khalkhali.

I would like to acknowledge the financial support from Natural Science and Engineering Research Council (NSERC), TC Energy, Enbridge and Pipeline Research Council International (PRCI).

Last but not least, I would like to express my immense gratitude to my parents for all their boundless love, the sacrifices they made, and their unconditional supports. I would like to thank my siblings for their kind support and for being role models in my life.

Hamid Niazi

Table of Contents

List of tables

List of Figures

Chapter 1 Introduction

1. 1 Introduction

Pipelines are an integral part of the global energy infrastructure. They are the most reliable and cost-effective way of transporting large oil and gas volumes over long distances. For instance, more than 3 million miles of oil and gas pipelines exist in the United States and Canada today [1], [2]. It is of the utmost importance to ensure that pipelines operate under the safest condition to protect humans, the environment, assets, and the economy. Hence, pipeline manufacturing [3], design, operation[4], and inspection[5], [6] are under detailed consideration. However, pipelines might encounter failures caused by manufacturing defects[7], incorrect operations[7], natural disasters[1], [8], corrosion [9], [10], and cracking mechanism[11]–[14]. Identifying the causes for failures and the remedies to mitigate or control the failures are of paramount importance.

Among different reasons for failure in pipelines, Stress Corrosion Cracking (SCC) is reported as a frequent damage mode and is a significant challenge associated with underground pipeline integrity [12], [15], [16]. SCC in steel pipelines manifests itself through the formation of crack colonies on the pipe's external surface. In most cases, the cracks are shallow and longitudinally orientated. The propagation of these cracks in thickness direction leads to leakage or sudden failure of the pipe [16]–[25]. Two distinguished categories of SCC in terms of metallographic features have been recognized in buried pipelines *viz.* Intergranular Stress Corrosion Cracking (IGSCC) and Transgranular Stress Corrosion Cracking (TGSCC). The first failures caused by IGSCC and TGSCC were documented in 1965 [26] and 1985 [13][27], respectively. Either type of SCC happens under different environmental conditions that cause distinguished crack growth mechanisms. Table 1.1 compares the required environmental conditions for either kind of SCC in

steel pipelines. IGSCC happens in high pH aqueous environment composed of a high concentration of carbonate bicarbonate ions at a specific pipe's potential range. Therefore, this type of SCC is the so-called High pH Stress Corrosion Cracking (HpHSCC). The crack growth mechanism for HpHSCC is anodic dissolution at the grain boundaries, which results in intergranular crack propagation. On the other hand, TGSCC occurs in a dilute carbonate-bicarbonate solution with a pH of 6.5, and it is so-called Near-Neutral pH SCC (NNpHSCC)through the mechanism of hydrogen-enhanced corrosion fatigue.

Table 1.1. Comparison between high pH SCC and Near Neutral pH SCC [27], [28].

High pH SCC	Near Neutral pH SCC
High pH – classical SCC pH≈9.	Low pH or near-neutral pH–non-classical SCC pH≈6.5.
Concentrated carbonate/bicarbonate solution.	Dilute groundwater containing dissolved CO_2.
Sharp intergranular crack.	Transgranular and quasi-cleavage crack morphology.
Little lateral corrosion.	Appreciable lateral corrosion.
Narrow potential range no more than 100 mV.	Occurs in a wide potential range.
Coal tar, asphalt tape coating.	High resistivity tape coatings.
Temperature-dependent.	Not affected by temperature in the range of 5 to 45˚C.

In North America, statistics show that eleven pipeline operators experience a total number of 546 failures associated with SCC (HpHSCC or NNpHSCC) between 1965 to 2010. Those failures were either in-service or caused by the hydrostatic test. Almost two-thirds of the failures (361 out of 546) were associated with HpHSCC including, 59 in-service failures and 298 hydrostatic failures. In four cases, the fracture surfaces were a mixed-mode of HpHSCC and NNpHSCC. Figure 1.1 shows the frequency of failures caused by HpHSCC between 1965 to 2010 in North America [29]. The annual rate of in-service failures caused by HpHSCC is about 1.5 for the US transmission

pipeline over the last few decades. In-service HpHSCC failures follow a decreasing trend because of integrity management policies adopted by different companies. However, HpHSCC failures during hydrostatic tests keep happening in North America.

Additionally, the occurrence of the HpHSCC in Russia [31], where it was believed NNpHSCC threatens pipelines, raises the concern that HpHSCC failures increases as the pipeline ages increases. It is worth mentioning that most of the HpHSCC failures happen after 20-30 years of service [17]. Therefore, the HpHSCC threat is not over, and there is still a need to improve our knowledge about the phenomenon, inspection methods.

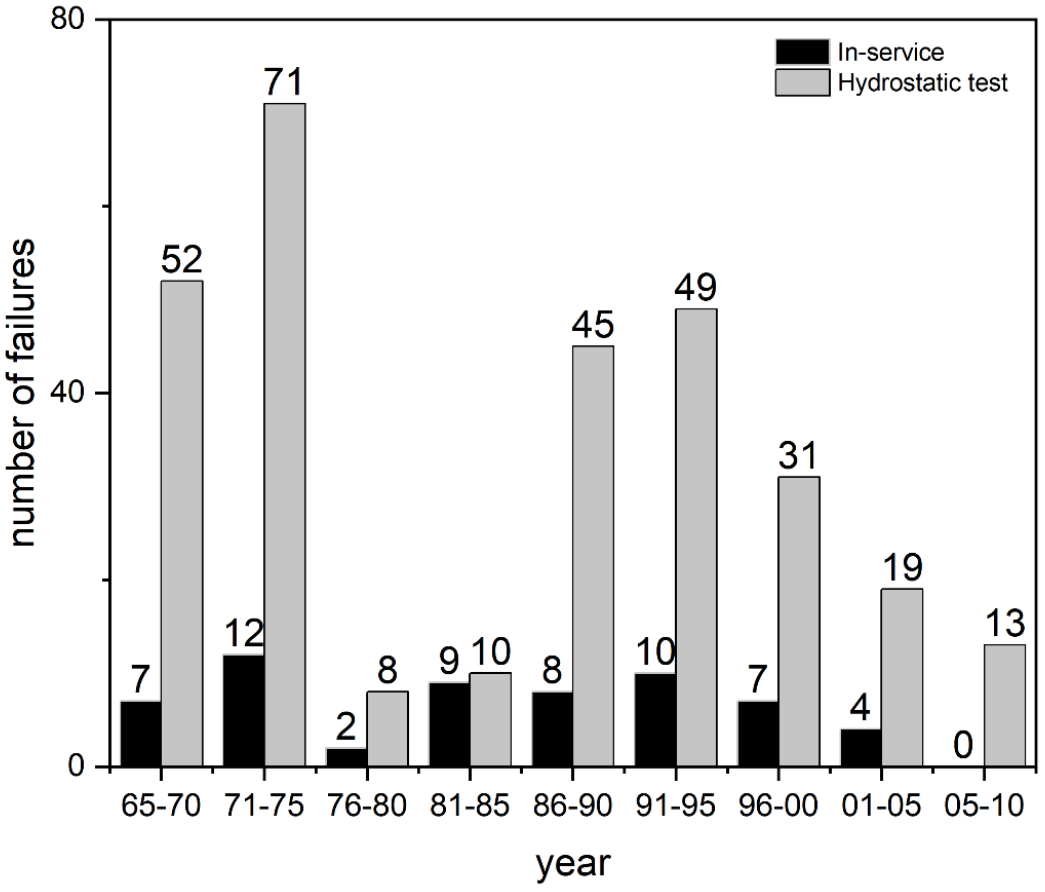

Figure 1.1. Frequency of the occurrence of HpHSCC between 1965 and 2010 [29].

According to the above introduction, attempts to prevent HpHSCC are unsuccessful, and HpHSCC happens inevitably. Hence, it is of paramount importance to predict the reliable lifetime of the cracked pipelines. As will be discussed in more detail in chapter two, the early stage of HpHSCC determines the lifetime of pipes susceptible to HpHSCC. Crack geometry evolution during this stage provides the mechanical driving force (known as threshold value) for sustainable crack propagation. There is a knowledge gap relating to the crack growth behaviour when the threshold is not achieved. The laser focus of this study is the impacts of mechanical loading conditions on HpHSCC crack evolution during the early stage of HpHSCC. This is a novel contribution of the study, and the results can improve the current understanding of the early stages of HpHSCC. Furthermore, HpHSCC crack growth under variable amplitude loading waveform has been studied during stage 1b and stage 2. This study's results are expected to improve the current modelling of HpHSCC and provide a more accurate estimate of the cracked pipes' lifespan.

1. 2 Thesis Outline

According to the above introduction, it is essential to understand the crack growth behaviour regarding the environmental factors, metallurgical conditions, and tensile stresses applied to the HpHSCC cracked pipes. Reviewing the available literature showed that there are two significant knowledge gaps in the current understanding of HpHSCC. First, the current understanding is based on the conducted tests under monotonic load or constant amplitude cyclic loading conditions. However, pipelines undergo variable amplitude loading conditions similar to other engineering components. Second, crack propagation during the early stages is assumed random and independent of loading conditions. Hence, this study is designed to study the HpHSCC crack growth behaviour under constant and variable amplitude loading conditions. This report consists of eight chapters, as its structure is briefly described in the following paragraphs.

Chapter 2, entitled "*High pH Stress Corrosion Cracking Initiation and Crack Evolution in Buried Steel Pipelines: A Review*," provides a comprehensive literature review on HpHSCC phenomena through studying the time-dependent crack growth model for HpHSCC. This model is the so-called "bath-tub" model and involves five sequential stages before failure because of HpHSCC. This chapter elaborates on the synergistic effects of metallurgical parameters, environmental conditions, and mechanical loading conditions at any given stage. Accordingly, the gaps in knowledge about HpHSCC are highlighted. This chapter is followed by Chapter 3, where the used samples, employed apparatus, and adopted experimental methods to carry out this research are detailed.

Chapter 4, entitled *"Crack Growth Sensitivity to the Magnitude and Frequency of Load Fluctuation in Stage one oh High pH Stress Corrosion Cracking,"* reports the HpHSCC crack growth behaviour early stage of crack advancement under constant amplitude loading conditions. This chapter argues that the loading characteristics influence the HpHSCC crack growth at early stages and play a part in crack evolution. It is showed the large and rapid load fluctuation assists crack growth through the crack coalescence mechanism.

Chapter 5, entitled "*Effects of Load Interactions on the Onset of Stage Two of High pH Stress Corrosion Cracking*," focuses on the load interactions at the early stage of HpHSCC crack evolution. This chapter generalizes the main idea from chapter 4 and investigates the early stage of HpHSCC crack propagation behaviour under variable amplitude loading waveform.

Chapter 6, entitled "*Effects of Loading Spectra on High pH Crack Growth Behaviour of X65 Pipeline Steel,*" reports the effect of variable amplitude loading conditions on stage 2 of HpHSCC crack growth. The crack growth mechanisms stage 2 are elaborated and correlated to variable amplitude loading waveforms.

Chapter 7 presents a summary of the finding and propose some idea for future work. Finally, the references used in this thesis are reported in alphabetical order.

References

[1] P. Venturino, J. N. Booman, M. O. Gonzalez, and J. L. Otegui, "Pipeline failures due to lightning," Engineering Failure Analysis 64, 2016, p. 1–12.

[2] "Pipeline Across Canada," 2016. [Online]. Available: https://www.nrcan.gc.ca/energy/infrastructure/18856.

[3] F. Hasan, J. Iqbal, and F. Ahmed, "Stress corrosion failure of high-pressure gas pipeline," Engineering Failure analysis 14 (5), 2007, p. 801–809.

[4] T. C. Pharris and R. L. Kolpa, "Overview of the design, construction, and operation of interstate liquid petroleum pipelines.," United States, 2008.

[5] M. Xie and Z. Tian, "A review on pipeline integrity management utilizing in-line inspection data," Engineering Failure Analysis 92, 2018, p. 222–239.

[6] H. R. Vanaei, A. Eslami, and A. Egbewande, "A review on pipeline corrosion, in-line inspection (ILI), and corrosion growth rate models," International Journal of Pressure Vessel and Piping 149, 2017, pp. 43–54.

[7] L. Dai, D. Wang, T. Wang, Q. Feng, and X. Yang, "Analysis and Comparison of Long-Distance Pipeline Failures," Journal of Petroleum Engineering 217, 2017, p. 3174636.

[8] N. K. Psyrras and A. G. Sextos, "Safety of buried steel natural gas pipelines under earthquake-induced ground shaking: A review," Soil Dynamics and Earthquake Engineering 106, 2018, pp. 254–277.

[9] H. Castaneda and O. Rosas, "External Corrosion of Pipelines in Soil," Oil and Gas Pipelines. 2015, p. 265–274.

[10] J. A. Beavers and N. G. Thompson, “External Corrosion of Oil and Natural Gas Pipelines,” ASM Handb., vol. 13C, 2006, pp. 1015–1026,

[11] J. L. Alamilla, E. Sosa, C. A. Sánchez-Magaña, R. Andrade-Valencia, and A. Contreras, “Failure analysis and mechanical performance of an oil pipeline,” Materials and Design 50, 2013, p. 766–773.

[12] H. R Hajibagheri, A. Heidari, and R. Amini, “An experimental investigation of the nature of longitudinal cracks in oil and gas transmission pipelines,” Journal of Alloys Compounds, vol. 741, 2018, p. 1121–1129,.

[13] W. Chen, “An Overview of Near-Neutral pH Stress Corrosion Cracking in Pipelines and Mitigation Strategies for Its Initiation and Growth,” Corrosion 72 (6), 2016, p. 962–977.

[14] W. Chen, “Modeling and Prediction of Stress Corrosion Cracking of Pipeline Steels” in: A. M. -El-Sherik (Eds), Trends in Oil and Gas Corrosion Research and Technologies, Woodhead Publishing, Boston, 2016, p. 707–748.

[15] M. A. Mohtadi-Bonab, M. Eskandari, H. Ghaednia, and S. Das, “Effect of Microstructural Parameters on Fatigue Crack Propagation in an API X65 Pipeline Steel,” Journal of Materials Engineering Performance 25 (11), 2016, pp. 4933–4940.

[16] National Energy Board, “Stress corrosion cracking on Canadian oil and gas pipelines,” Natl. Energy Board, Calgary, Alberta, 1996.

[17] S. A. Shipilov and I. Le May, “Structural integrity of ageing buried pipelines having cathodic protection,” Engineering Failure Analysis 13 (7), 2006, pp. 1159–1176.

[18] B. Saleem, F. Ahmed, M. A. Rafiq, M. Ajmal, and L. Ali, “Stress corrosion failure of an X52 grade gas pipeline,” Engineering Failure Analysis 46, 2014, pp. 157–165.

[19] J. A. Beavers and R. G. Worthingham, “The Influence of Soil Chemistry on SCC of Underground Pipelines,” 2002, no. 36207. pp. 1671–1678.

[20] R. N. Parkins and P. M. Singh, “Stress Corrosion Crack Coalescence,” Corrosion 46 (6), 1990, pp. 485–499.

[21] E. Gamboa, “Inclined stress corrosion cracks in steel pipelines,” Corrosion. Engineering Science and Technology 50 (3), 2015, p. 191–195.

[22] O. Lavigne, E. Gamboa, W. Costin, M. Law, V. Luzin, and V. Linton, “Microstructural and mechanical factors influencing high pH stress corrosion cracking susceptibility of low carbon line pipe steel,” Engineering Failure Analysis 45, 2014, p. 283–291.

[23] A. W. Peabody and R. L. Bianchetti, Control of Pipeline Corrosion Second Edition. 2000.

[24] I. Thompson and J. R. Saithala, “Review of pipeline coating systems from an operator’s perspective,” Corrosion Engineering Science and Technology 51 (2), 2016, p. 118–135.

[25] R. Norsworthy, “Coatings Used In Conjunction With Cathodic Protection Shielding Vs Non-Shielding Pipeline Coatings.” NACE International.

[26] Federal Power Commission, “Final staff report on investigation of Tennessee Gas Transmission Company Pipeline No. 100-1 failure near Natchitoches,” Washington, DC, 1965.

[27] J. a. Beavers and B. a. Harle, “Mechanisms of High-pH and Near-Neutral-pH SCC of Underground Pipelines,” Journal of Offshore Mechanics and Arctic Engineering, 123 (3), 2001, p. 147.

[28] M. J. Wilmott, T. R. Jack, G. Van Boven, and R. Sutherby, “Pipeline Stress Corrosion Cracking: Crack Growth Sensitivity Studies Under Simulated Field Conditions,” in Corrosion 96. NACE International, 1996.

[29] A. D. Batte, R. R. Fessler, J. E. Marr, and S. C. Rapp, “Managing the Threat of SCC in Gas Transmission Pipelines.” 2012, p. 379–388.

[30] M. H. R. R. Fessler, A. D. Batte, Integrity management of stress corrosion cracking in gas pipeline. New York: ASME Stnadards Technology, LLC, 2008.

[31] I. V Ryakhovskikh, R. I. Bogdanov, and V. E. Ignatenko, “Intergranular stress corrosion cracking of steel gas pipelines in weak alkaline soil electrolytes,” Engineering Failure Analysis 94, 2018, p. 87–95.

[32] J. Beavers and T. A. Bubenik, “Stress Corrosion Cracking,” in: A. M. -El-Sherik (Eds), Trends in Oil and Gas Corrosion Research and Technologies, Woodhead Publishing, Boston, 2016, p. 295–314.

Chapter 2 High pH Stress Corrosion Cracking Initiation and Crack Evolution in Buried Steel Pipelines: A Review[1]

2. 1 Introduction

The aim of the current chapter is to provide an overview of intergranular stress corrosion cracking of pipeline steels. The first documented failure caused by HpHSCC in a high-pressure gas transmission pipeline dates back to the mid-1960s in Natchitoches, Louisiana, USA [1]. That failure resulted in gas release, a subsequent explosion, fire, and 17 fatalities [2]. Since then, similar failures, albeit usually less deadly, have been reported around the world [3–15]. Most of the HpHSCC incidents have occurred in coated pipelines protected by cathodic current and within the first 30 km downstream from a compressor or pump station in gas or oil pipelines, respectively [16,17]. In this location, the pipeline typically experiences the highest temperatures and the most severe loading conditions [16,18].

The typical failure can be described as follows. A disbonded coating accompanied by exposure to an aqueous solution of high concentrations of carbonate-bicarbonate ions and precipitated salts are typically found in the vicinity of the HpHSCC cracks[16,17,19–22]. The cathodic protection is found to have been partially lost beneath the coating, and the electrochemical potentials at the cracking regions are between -540 to -690 mV_{SCE}, with the exact range dependent on temperature. HpHSCC failures manifest themselves through another common characteristic, the presence of

[1] A version of this chapter has been accepted for publication. H. Niazi, R. Eadie, W. Chen, H. Zhang, "High pH stress corrosion cracking initiation and crack evolution in buried steel pipelines: a review, Engineering Failure Analysis

longitudinally oriented intergranular crack colonies, an example of which is shown in Figure 2.1. Both the area adjacent to the cracks and the cracks' walls are covered by a black film, which is mostly composed of magnetite and sometimes contains small quantities of iron carbonate. This black film is passivating and protects the steel against general corrosion, and consequently, no evidence of general corrosion is usually observed on the external surfaces of the pipes. Furthermore, the protective film keeps the cracks' sides in close juxtaposition unless the stresses in the region are sufficient to open the cracks [11,13,23,24].

Figure 2.1. HpHSCC colonies on the external surface of the gas pipe detected by Magnetic Particle Inspection (MPI) [25].

HpHSCC in pipeline steel is a time-dependent deterioration phenomenon that occurs as the synergistic effects of material, environment, and tensile stress combine to cause the phenomenon. Figure 2.2 shows a model of the time-dependent behaviour of HpHSCC in pipeline steel. This model is known as the bathtub model, and it was originally proposed by Parkins [26]. In order to be consistent with fracture mechanics' conventions, a slightly revised numbering system is used,

compared to that initially proposed by Parkins. As is evident, there are five sequential stages in HpHSCC, which are briefly discussed below.

- Incubation stage: this stage involves formation of a partially occluded environment (high concentration aqueous solution of carbonate and bicarbonate) beneath the coating, partial loss of cathodic protection, and pitting corrosion.
- Stage 1a: this stage involves crack initiation through selective dissolution at the grain boundaries that experience local stresses greater than the threshold value for crack initiation. The threshold value depends on surface condition (such as surface defects, surface roughness, mill scale, surface residual stress, *etc.*) and the magnitude of and fluctuations in the applied load. The early stage of crack propagation is short in duration, yet it is characterized by the highest crack growth rate. The crack growth rate decreases gradually, and the cracks grow sporadically and may cease to grow.
- Stage 1b: small crack nucleation continues at multiple sites and grows similarly to stage 1a. However, adjacent cracks are found to coalesce to form larger cracks. Accordingly, the crack growth rate at this stage is stochastic, and cracks may experience alternate periods of dormancy and activity. The cracks' initiation sites and the interaction between stress fields of nearby cracks influence the crack growth during this stage.
- Stage 2: this stage is characterized by sustainable crack growth through an anodic dissolution mechanism in the presence of adequate stresses. The crack growth rate at this stage follows a power law with the crack tip strain rate and can be correlated to fracture mechanics' parameters like stress intensity factor (K). The upper boundary for crack propagation can be calculated by Faraday's second law since crack growth is by anodic dissolution.

- Stage 3: the crack growth behaviour at this stage is very rapid and may be unstable. The HpHSCC cracked pipeline must be replaced or repaired prior to the onset of this stage. Otherwise, the rapid crack propagation at this stage may cause leakage or fracture of the pipe, and this will pose a risk to humans, the environment, infrastructure, and the economy.

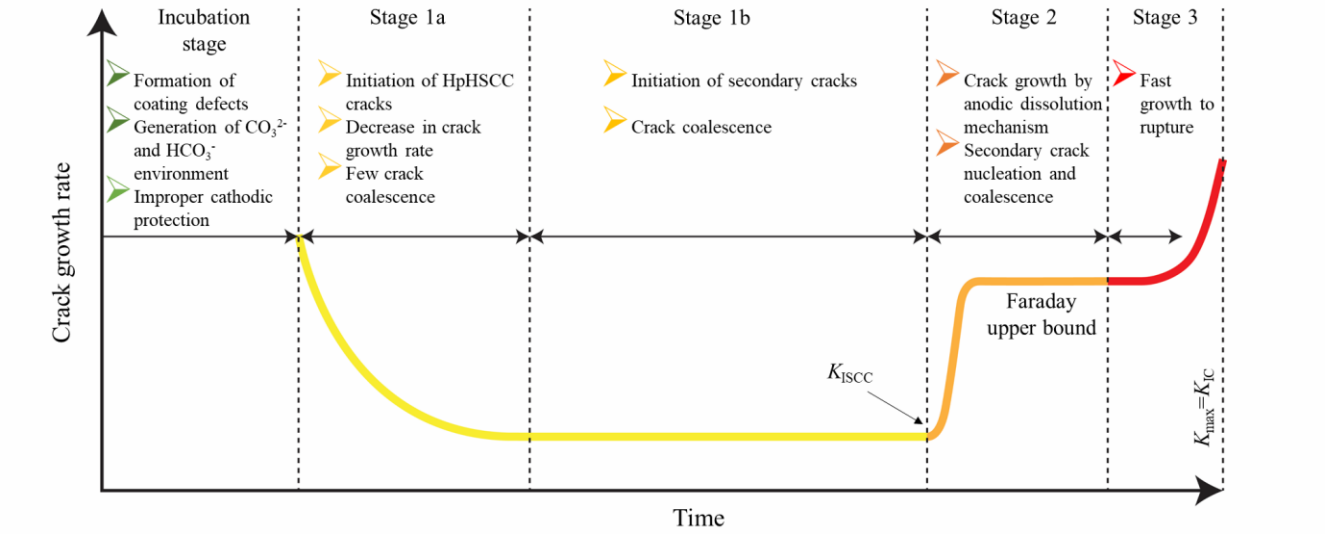

Figure 2.2. Schematic illustration of time-dependent HpHSCC crack initiation and growth under field conditions [27].

To date, considerable research efforts have been made to understand the environmental, metallurgical, and mechanical parameters that contribute to the HpHSCC phenomena. There have been a number of papers that have reviewed the metallurgical parameters, environmental circumstances, and mechanical loading conditions that comprise the HpHSCC phenomenon [28–33]. The early papers were mainly by Parkins and co-workers, and the latter papers mainly by Beavers and co-workers. The available reviews provide great insight into the phenomenon; however, these reviews pay less attention to the interactions between contributing parameters at each stage. Since the overall goal of HpHSCC modelling is to accurately predict the reliable

lifespan of the vulnerable pipes, it is important to understand the relationships between the events that the pipeline may undergo at each stage. The current paper adopts an approach to review HpHSCC in pipeline steels through elaborating different aspects and interactions between contributing parameters in HpHSCC at each stage with more emphasis on mechanical loading conditions and the load patterns experienced by the linepipe based on research at the University of Alberta. As well, this paper highlights the remaining gaps in knowledge about HpHSCC and proposes future research areas to improve HpHSCC modelling.

2. 2 Incubation Stage

A series of three interrelated events are essential to this stage:

1. Generation of a potent environment for HpHSCC, specifically high concentration carbonate bicarbonate environment accompanied by partial loss of cathodic protection under the disbonded coating. It is the condition of the cathodic protection and the higher local temperatures that make possible the development of this high concentration environment.

2. Changing internal pressure during the operation of the pipeline lead to the following modifications in the pipeline steel. Mechanical properties (cyclic hardening or softening) ii. Surface structure (changes in mill scale and defect structures such as persistent slip bands) iii. Residual stresses.

3. Changes in the steel's surface configuration and composition mainly because of electrochemical processes caused by the environment (corrosion).

2. 2. 1 Formation of the HpHSCC Environment

The potent environment for HpHSCC results from the formation of an occluded environment beneath the pipe's breached coating, composed of high concentrations of carbonate-bicarbonate ions (the standard solution for HpHSCC laboratory experiments is an aqueous solution of 0.5 M

Na_2CO_3 and 1 M $NaHCO_3$) followed by partial loss of cathodic protection at the coating defects caused by the shielding of the coating. The formation of such an environment depends on several factors, including coating properties [34,35], temperature [35], soil chemistry [1,36], groundwater pH [36,37], electrochemical reactions [20], penetration rates of oxygen and carbon dioxide into the disbonded area [1], and the presence of the required cations and anions beneath the coating [1]. Hence, the generation of the HpHSCC environment in the field is time-consuming, and the timing varies for different locations, coatings and ambient temperatures [1,38]. A simple mechanism for the generation of this environment is discussed below and shown schematically in Figure 2.3 (a) to (e).

Generation of the HpHSCC environment begins with the formation of coating defects such as disbonded areas and holidays (open mouth disbonded area in the coating). These coating defects are shown schematically in Figure 2.3 (a). It is worth mentioning that the coating deterioration is more probable at higher temperatures, *i.e.,* the chance for coating defect formation is higher within the first 30 km downstream from the compressor or pump station [17], since this is typically the highest temperature region. Once the groundwater with a pH typically near 7 comes into contact with the steel by penetrating the coating defect, the hydroxyl content increases because of the following cathodic reactions. (reaction 1 and 2 and Figure 2.3 (b) [39,40].

$$2H_2O + 2e^- \rightarrow H_2 + 2OH^- \quad (1)$$

$$O_2 + 2H_2O + 4e^- \rightarrow 4OH^- \quad (2)$$

The increase in OH^- concentration attracts carbon dioxide, which is dissolved in the groundwater. The carbon dioxide in the groundwater is generated from either geological reactions or decaying organic materials [1,20,41–44]. When all the free trapped CO_2 in the water beneath the coating is consumed by OH^- through reactions 3 and 4, a solution of carbonate-bicarbonate forms and an

equilibrium between CO_2-related species will be achieved according to equilibrium Equation 2.1 and illustrated in Figure 2.3 (c).

$$CO_2 + OH^- \rightarrow HCO_3^- \quad (3)$$

$$HCO_3^- + OH^- \rightarrow CO_3^{2-} + H_2O \quad (4)$$

$$HCO_3^- \rightarrow CO_3^{2-} + H_2O \quad (5)$$

$$\log\left(\frac{CO_3^{2-}}{HCO_3^-}\right) = -10.34 + pH \quad \text{Eq'n. 2.1}$$

High concentrations of anions, in particular bicarbonate, are needed for HpHSCC crack initiation and growth [1,45]. It has been shown that a high concentration of carbonate ions decreases the corrosion resistance of steel pipelines [46]. Two mechanisms lead to the increase in carbonate and bicarbonate concentrations. First, the cathodic current from the CP system, as well as the accumulated negative charges beneath the coating (from formation of carbonate and bicarbonate ions), attracts cations to the disbonded area to keep the balance of electrical charges. At the same time, other anions such as Cl^- and SO_4^{2-} are repelled from the disbonded volume (Figure 2.3 (d)). Divalent cations such as Ca^{2+} and Mg^{2+} are not soluble in the basic solution and precipitate as carbonate minerals at the outer surface of the coatings [1,22,36,42]. On the other hand, univalent cations such as K^+ and Na^+ dissolve in the trapped water beneath the coating [1,22,36,42]. Statistical analysis was conducted in Western Canada (Alberta) in order to determine the role of cations and soil chemistry in both HpHSCC sites and non-HpHSCC sites. The results showed that not only the electrolyte beneath the coating but also the surrounding soil contain higher concentrations of sodium and potassium ions at HpHSCC sites compared to non-HpHSCC sites [36]. The presence of such cations plays a vital role in the formation of the potent environment for HpHSCC. In the absence of such cations beneath the coating, the basic solution with a pH of 9

could form; however, it is not sufficiently concentrated in carbonate and bicarbonate for HpHSCC. In addition, evaporation of the solution caused by either the high temperature of the pipe section or an increase in soil temperature during the dry season may contribute to increasing the carbonate-bicarbonate concentration [1]. Deposition of sodium carbonate and sodium bicarbonate salts beneath the coating and minerals containing calcium or magnesium at the outer surface of the coatings result from the evaporation of the solution [16,20–22] (Figure 2.3 (e)).

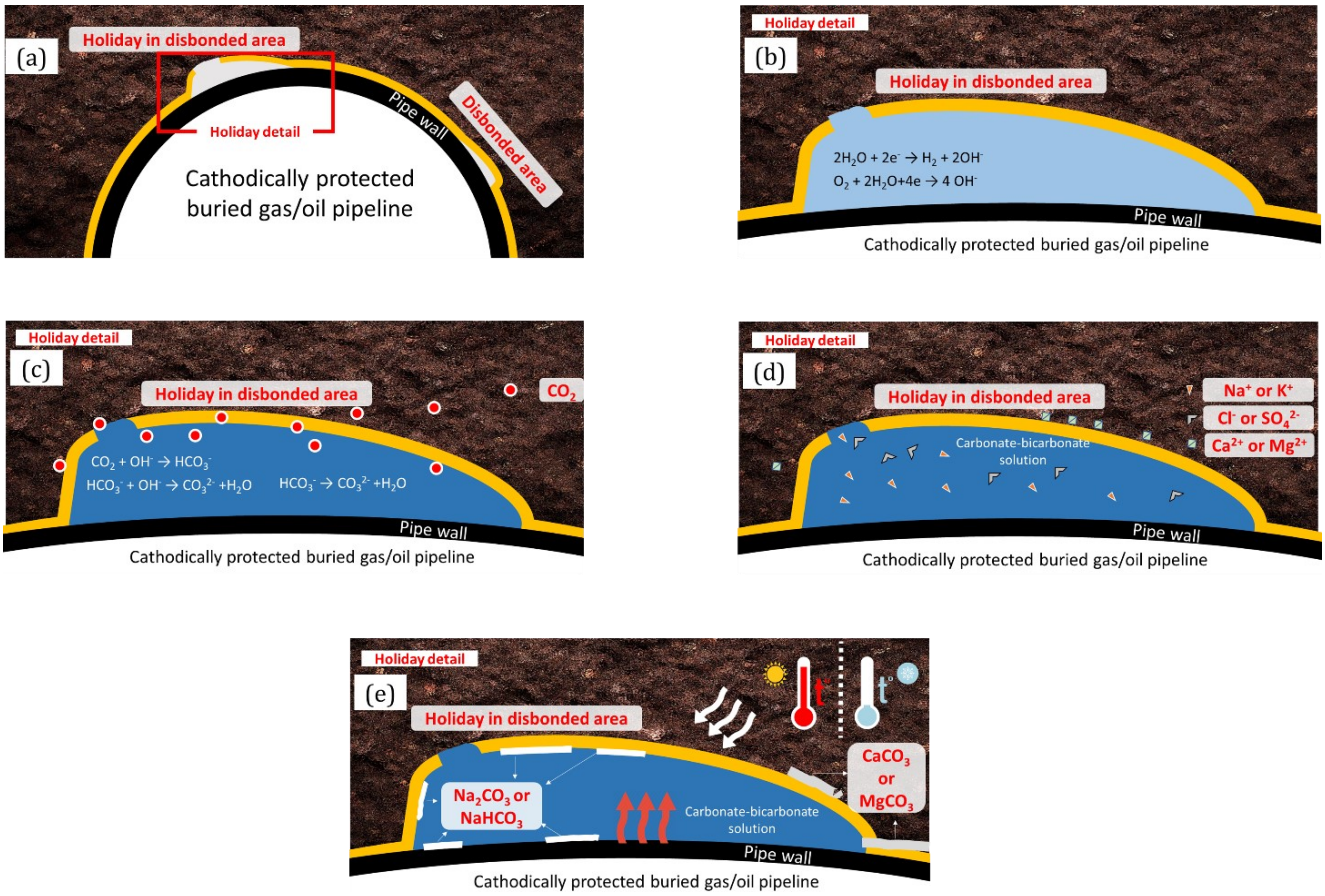

Figure 2.3. Schematic illustration of (a) a defect in the coating, (b) penetration of groundwater beneath the coating and generation of hydroxyl ions, (c) formation of carbonate and bicarbonate ions, (d) migration of anions and cations from and to the disbonded area, respectively, (e) deposition of carbonate mineral beneath the coating and on the outer surface of the coating.

The resulting high concentration carbonate-bicarbonate solution with a pH of 9-10 will not cause HpHSCC unless the electrochemical potential of the pipe falls within the required range (-540 to -690 mV_{SCE}). The potential window for cracking varies with temperature so that an increase in temperature widens the susceptible potential range for HpHSCC and shifts the susceptibility towards more negative values [23,29]. The most negative potential of the pipe-to-soil for a non-CP-protected coated underground pipe is about -740 mV_{SCE}, which is clearly beyond the cracking range. The application of cathodic protection shifts the potential to more negative values than -740 mV_{SCE}. However, the potential of the pipe section might fall within the cracking range locally for several reasons. It is well established that there is a potential gradient along the pipeline under the disbonded coating [29,47,48]. The potential gradient varies with the geometry of the coating defect, the pipe's surface conditions, the applied potential to the mouth of the coating defect, and the distance from the holiday. Figure 2.4 shows how the level of polarization varies with time for different distances from the holiday in disbonded area with the thickness of 0.13 mm when the potential at the holiday mouth was set at -850 (SCE). The surface of the steel was oxidized and exposed to 1 N Na_2CO_3 – 1 N $NaHCO_3$. According to Figure 2.4, the level of polarization decreases as the distance from the holiday increases. Although the polarization level is improving gradually, the potential of the pipes falls within the cracking potential window for a certain time period. As the distance from the crevice mouth increases, the period when the pipe's potential is within the cracking range is longer. Overprotection, *i.e.,* more negative potential at the mouth of crevice, is not effective in avoiding the localized potential drop into the cracking range because of the formation of hydrogen gas bubbles. Such hydrogen bubbles cause potential drops as well as difficulty in controlling the potential under the disbonded coating [18,49]. Furthermore, the hydrogen might diffuse into the pipe and make it more brittle [50]. Diffusion of the atomic

hydrogen into the steel transforms the mechanism for crack propagation from intergranular to transgranular [51]. Additionally, several reasons including shielding effects of the disbonded coating [49], deposition of salts beneath the disbonded area, seasonal changes, *i.e.,* loss of CP during the dry season [18], deposition of corrosion products [6], and AC current interference [52,53] could move the potential into the cracking range.

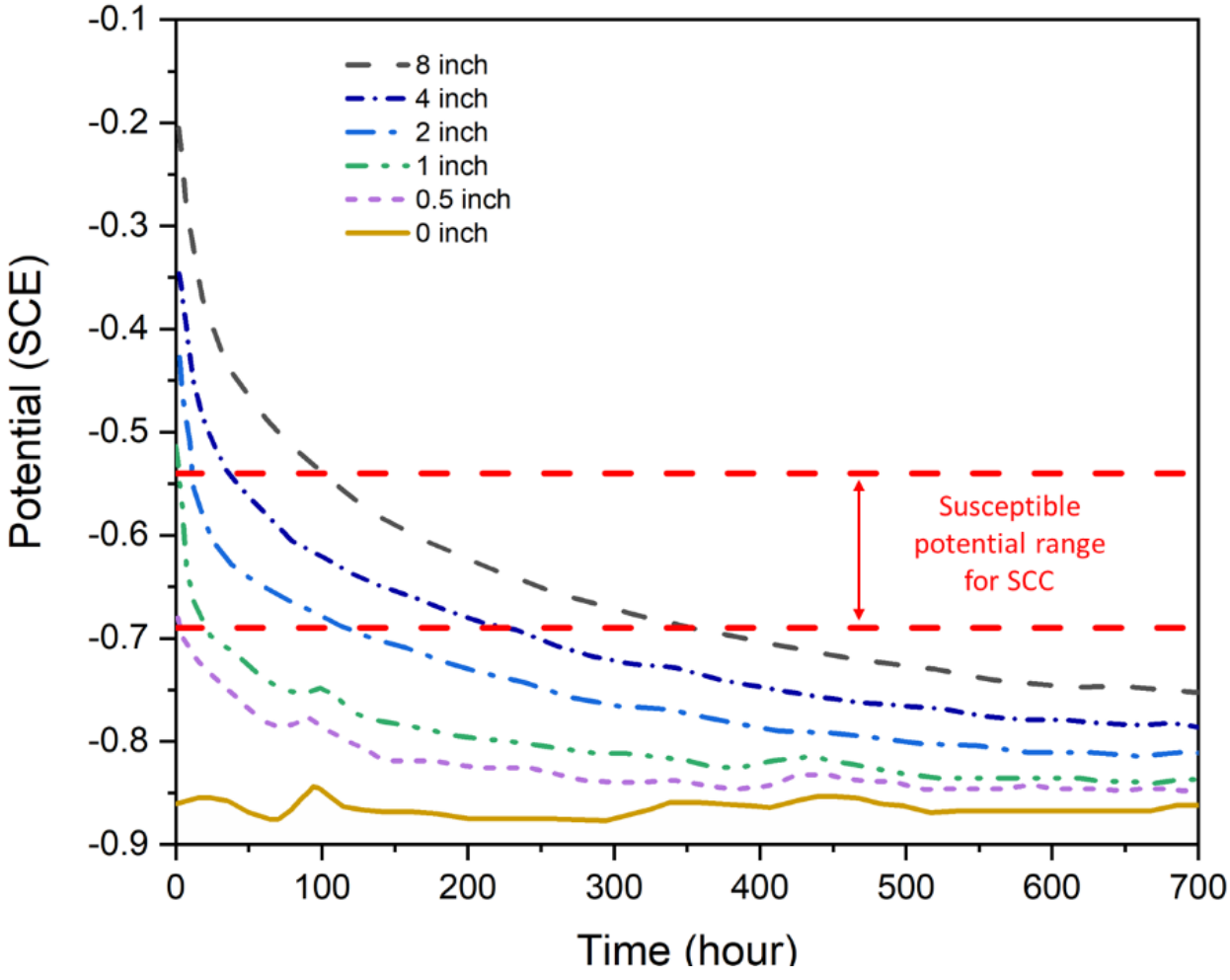

Figure 2.4. Variation of the potential with time for various distances from the holiday when the potential of the holiday was set at -850 mV_{SCE}. The steel surface was oxidized, the electrolyte was 1N Na_2CO_3-1N $NaHCO_3$ solution, and the crevice thickness was 0.13 mm [49].

2. 2. 2 Changes in Pipes' Properties and Internal Stresses

The largest stress in pipeline steel is usually the hoop stress and is caused by the internal pressure of the fluid in the pipeline [30,54]. Fluctuation in the internal pressure of the pipe causes pipelines to operate under variable amplitude cyclic loading or fatigue loading [2][55]. The relative pressure level and large loading events vary along the pipeline. Accordingly, there are three types of loadings, depending on the location of the pipe sections. Within the first 30 km downstream from the compressor or pump station (where most of the HpHSCC failures occur), the loading condition is the type I loading, which is also known as "underload pressure fluctuation." Real examples of this loading condition in gas and oil pipelines from Canadian SCADA (Supervisory Control And Data Acquisition) data are shown in Figure 2.5 (a) and (b), respectively. As is evident from Figure 2.5, this type of loading condition involves two types of load cycles with regards to their stress ratio, *R*-ratio (minimum stress/maximum stress). These cycles are categorized as sporadic low *R*-ratio cycles, known as underload cycles, and more frequent high *R*-ratio cycles called minor cycles. Further characteristics of Type-I pressure fluctuation are summarized in Table 2.1. Information about other types of pressure fluctuation along the pipeline steels can be found elsewhere [56–58].

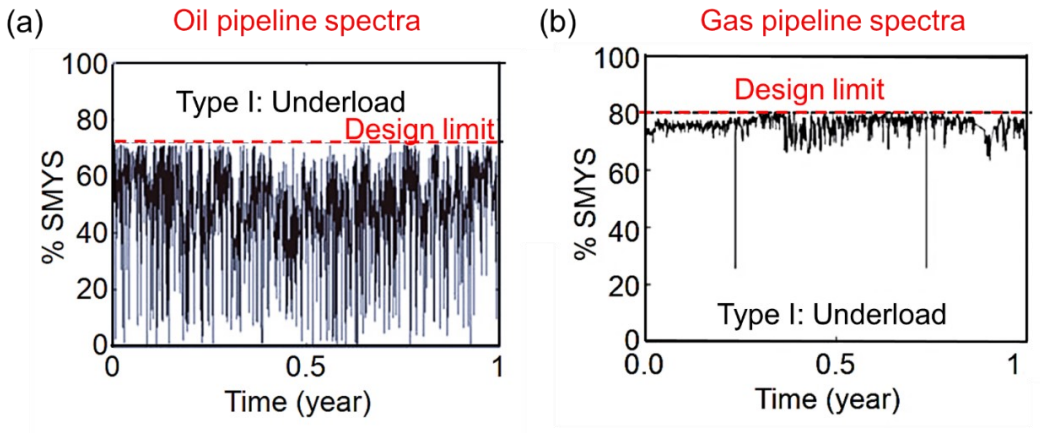

Figure 2.5. Type I (underload pressure fluctuation) of pressure fluctuations happening within the first 30 km downstream from (a) pump in oil pipelines (b) compressor in gas pipeline [58].

Given the variable cyclic loading condition that pipelines experience during their operation, steel pipelines undergo significant metallurgical events. These occur both during and after the formation of the HpHSCC environment. In this section, the focus will be on the events happening in the incubation stage, such as cyclic work hardening/work softening [57], changes in the distribution of residual stresses [59], microplastic deformation etc. [60].

Table 2.1. Characteristics of Type I pressure fluctuation in gas and oil pipelines [58]

Item	Oil pipelines	Gas pipelines
Typical number of underload cycles/year	537	8
Range of unloading frequency (Hz)	6.9×10^{-6} - 1×10^{-1}	1.3×10^{-6} - 9.1×10^{-5}
Range of loading frequency (Hz)	5.1×10^{-6} - 1×10^{-2}	1.3×10^{-6} - 5.2×10^{-6}
Number of minor cycles between underload cycles	0-26	0-37

The cyclical nature of hoop stress has deleterious effects for HpHSCC. Drawing comparisons between cyclic stress-strain responses and monotonic stress-strain curves for a range of pipeline steels showed that the cyclic stress-strain curves fall below the monotonic curves. Examples are shown in Figure 2.6 [60]. Note that in this figure, the mean stress is drawn for the cyclic loading to exaggerate the effect of cyclic loading. A range of steels in that study showed similar behaviour. Remarkable changes in work hardening rate occurred at a strain of about 10^{-3} for stress-strain curves under cyclic loading conditions. Parkins found that there is a direct relationship between the stresses associated with the changes in work hardening rate and the threshold stress for HpHSCC crack initiation, as will be discussed in section 2. 3. 1[60].

Pre-cyclic loading up to the maximum stress below the yield point creates persistent slip bands at the steel's surface as well as localized plastic deformation at stress-raisers. These locations can then act as anodes during subsequent exposure to a corrosive environment and have a higher tendency for anodic dissolution. Hence, micro-cracks can form on the external surface as soon as a corrosive environment is established [59,61].

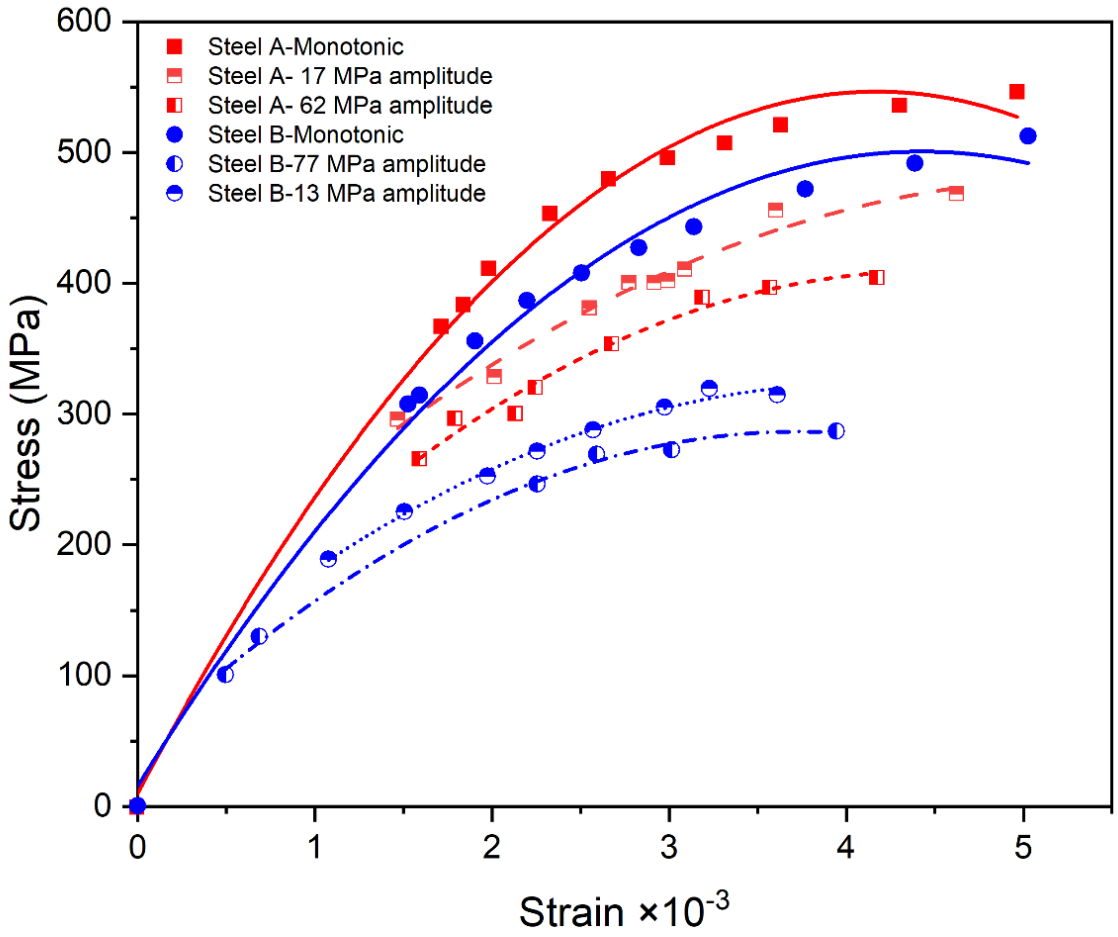

Figure 2.6. Monotonic and cyclic stress-strain data of two steels [60]. (For cyclic condition, tests were started at the minimum stress with regards to the stress amplitude, and plastic strains approaching 10^{-6}/cycle were measured.)

The other structural changes that sometimes occur during this stage are changes in the distribution of residual stress in the pipeline steels. The steel pipelines are usually fabricated through various stages of cold plastic forming of steel plates or steel coils. These metal-forming processes generate residual stress in the steels [59]. Furthermore, there are different treatments such as shot peening, welding etc., that also leave residual stress in steel pipelines either near the free surface or across the thickness. The residual stresses can be either compressive or tensile, and their magnitudes vary at different spots [10,62,63]. However, the net force in the thickness direction must be equal to

zero, so tensile forces at the surface are balanced by compressive forces in the interior. It is well known that the presence of residual compressive stress on the pipe's surface increases the resistance to SCC [56]. Research has shown that the cyclic loading can change the residual stress on the surface of the pipes [59]. Obviously, if the tensile residual stress increases on the surface, the resistance against crack initiation and growth decreases.

2. 2. 3 Changes in Surface Condition

At this early stage, the surface of the linepipe can change in several aspects. First, localized fracture of the mill scale might occur because of the plastic deformation generated by variable amplitude loading waveforms [64]. Secondly, localized corrosion could happen near coating defects, where the groundwater or corrosive media comes into contact with a pipe's outer surface, particularly at metallurgical discontinuities like MnS inclusions or at locations where the mill scale is broken. In the latter case, a galvanic cell forms with the cathodic mill scale and accelerates the corrosion of the steel. Corrosion of the MnS particles at the surface leads to pit formation. These electrochemical processes might occur before the establishment of a HpHSCC environment [65,66]. The localized corrosion is in accordance with the field observations that report crack initiation from the root of the pits or at fractures in the mill scale [8,11–13,67]. Localized corrosion might also occur before the generation of the HpHSCC environment. As was mentioned earlier, cyclic loading before the existence of a corrosive environment can accelerate subsequent corrosion and microcrack formation at metallurgical discontinuities when later exposed to corrosive environments [59,61].

Another important change in the surface condition at this stage is grain boundary etching and formation of a passive film composed of iron oxide and iron carbonate on the free surface of the pipe, where the steel is in direct contact with the HpHSCC environment [11,12,68–71]. An

example of intergranular etching under HpHSCC environmental conditions is shown in Figure 2.7, which illustrates intergranular corrosion on an unstressed steel exposed to a carbonate-bicarbonate environment at the electrochemical potential of -650 mV_{SCE} and 75 ˚C for 30 s [33]. The intergranular corrosion will cease after longer exposure to the cracking environment since passive film gradually forms the grain boundaries [72].

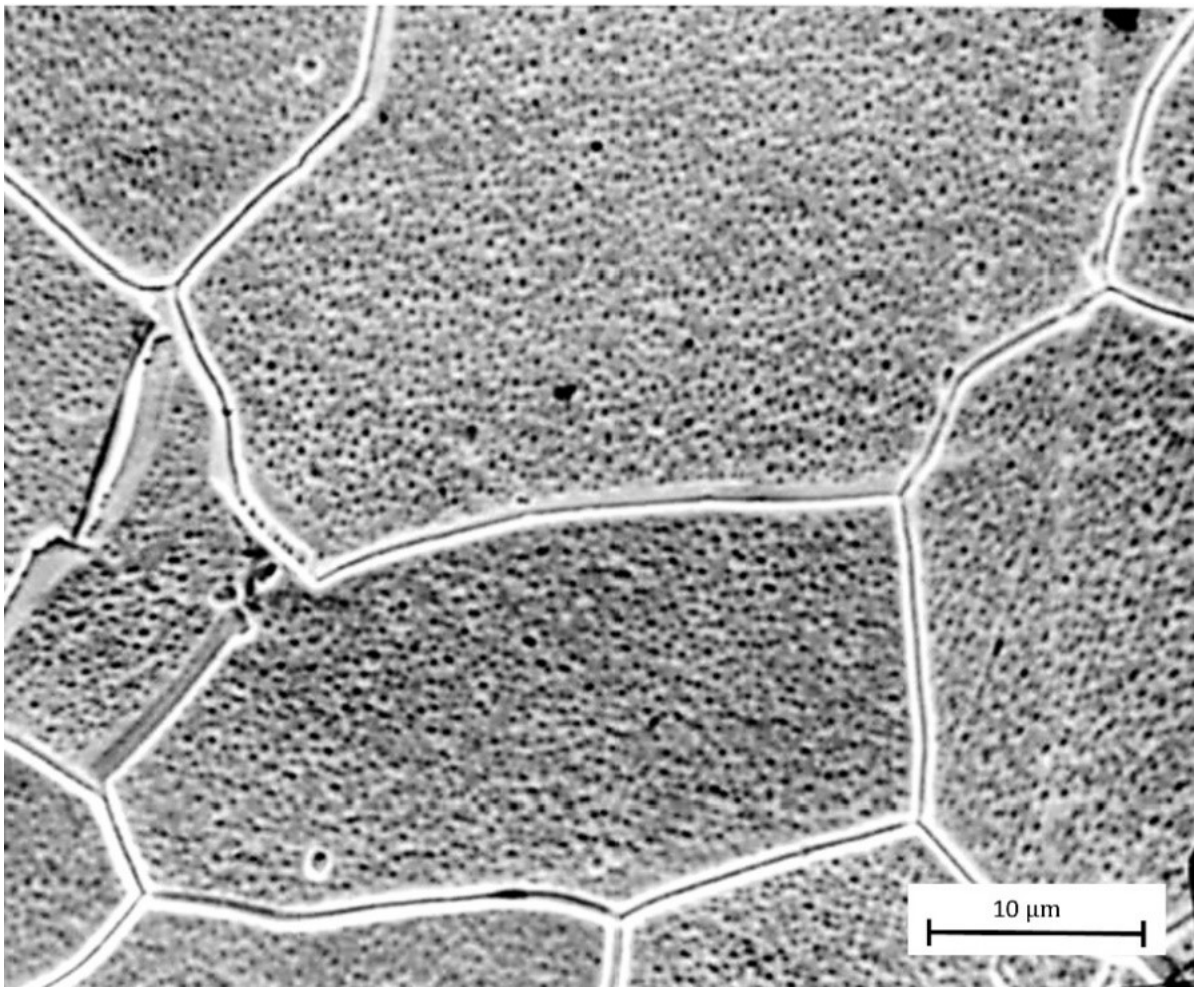

Figure 2.7. Intergranular corrosion on an unstressed steel exposed to the carbonate-bicarbonate environment at the potential of -650 mV_{SCE} and 75 ˚C for 30 s [33].

At the end of the incubation stage, it is expected that an occluded environment for HpHSCC has been created beneath the coating and a passive film covers the intergranularly etched surface of

the pipes. In addition to this, stress risers such as pits and micro-cracks might have formed on the external surface of the pipe.

2. 3 Stage 1a: Crack Initiation and Early Stage Crack Growth

As discussed and shown in Figure 2.7, intergranular corrosion ceases as soon as passive film forms on the penetrating tip of intergranular corrosion. The mechanism for both crack initiation and growth relies on fracture of the brittle passive film along the grain boundaries which results from localized plastic deformation generated by load application and/or other sources of stress. For crack initiation, further progress in intergranular corrosion (along the outer surface and also in the depth direction) occurs by intergranular cracking. Crack initiation and growth occur as the synergistic interaction of material, environment, and mechanical loading conditions. The material-environment combination determines the corrosion rate, passivation/re-passivation kinetics, and properties of the passive film. Any environmental or metallurgical parameters that are in favour of the stability of the passive film (either increase in resistance against fracture or acceleration of film formation) delays crack initiation and growth. Secondly, the interaction between the material and the applied loads determines the frequency of fracture of the passive film; and hence crack initiation and growth rate. Stage 1a includes crack initiation and early-stage crack growth, which are independently discussed below.

2. 3. 1 Crack Initiation

There is a threshold condition for HpHSCC crack initiation that, when exceeded, provides the condition for transformation of intergranular corrosion to intergranular cracking. The threshold for crack propagation is always reported as either a stress or as stress as a fraction of the yield stress. According to Figure 2.5, pipelines that are operated below the maximum allowable stress (that is below 80% of SMYS [57]) can experience HpHSCC. Under field conditions, HpHSCC failures at

an operating hoop stress as low as 24% of SMYS have been reported [12,14]. Obviously, increases in hoop stress increase the probability of HpHSCC failure [73]. This means the threshold value of operating stress for HpHSCC crack initiation is not a constant value and depends on several factors such as loading conditions, residual stress, presence of stress raisers, surface conditions *etc.* Therefore, the determination of an accurate value for threshold stress for any individual steel is difficult.

However, experimental data under controlled conditions in the laboratory has revealed some trends in the variation of the threshold value. First and foremost, it has been shown that the threshold stress is highly dependent on load fluctuations [74,75]. Figure 2.8 shows the variation of threshold value versus the stress ratio, R, of the varying stress for a range of pipeline steels, where R = minimum stress / maximum stress in the cycle. In this figure, the mean stresses applied to different sections of tapered specimens were used as the threshold value. In addition, the yield strengths of the steels are shown in Figure 2.8. The threshold stress under static loading condition (R-ratio= 1) is about equal to the yield strength of the steels, and the threshold stress decreases as the R-ratio decreases [60]. Parkins proposed that there was a decrease of 81 MPa in threshold value for each 0.1 decrease in the R-ratio value of the cycle. Parkins found that the threshold stresses under cyclic loading conditions approximated the stresses at which the work hardening rate of the steel changed under the cyclic loading condition (See Figure 2.6). These results suggest that microplastic deformation under cyclic loading, provides the mechanical driving force for crack initiation by providing a film-free condition at some grain boundaries where the passive films are fractured.

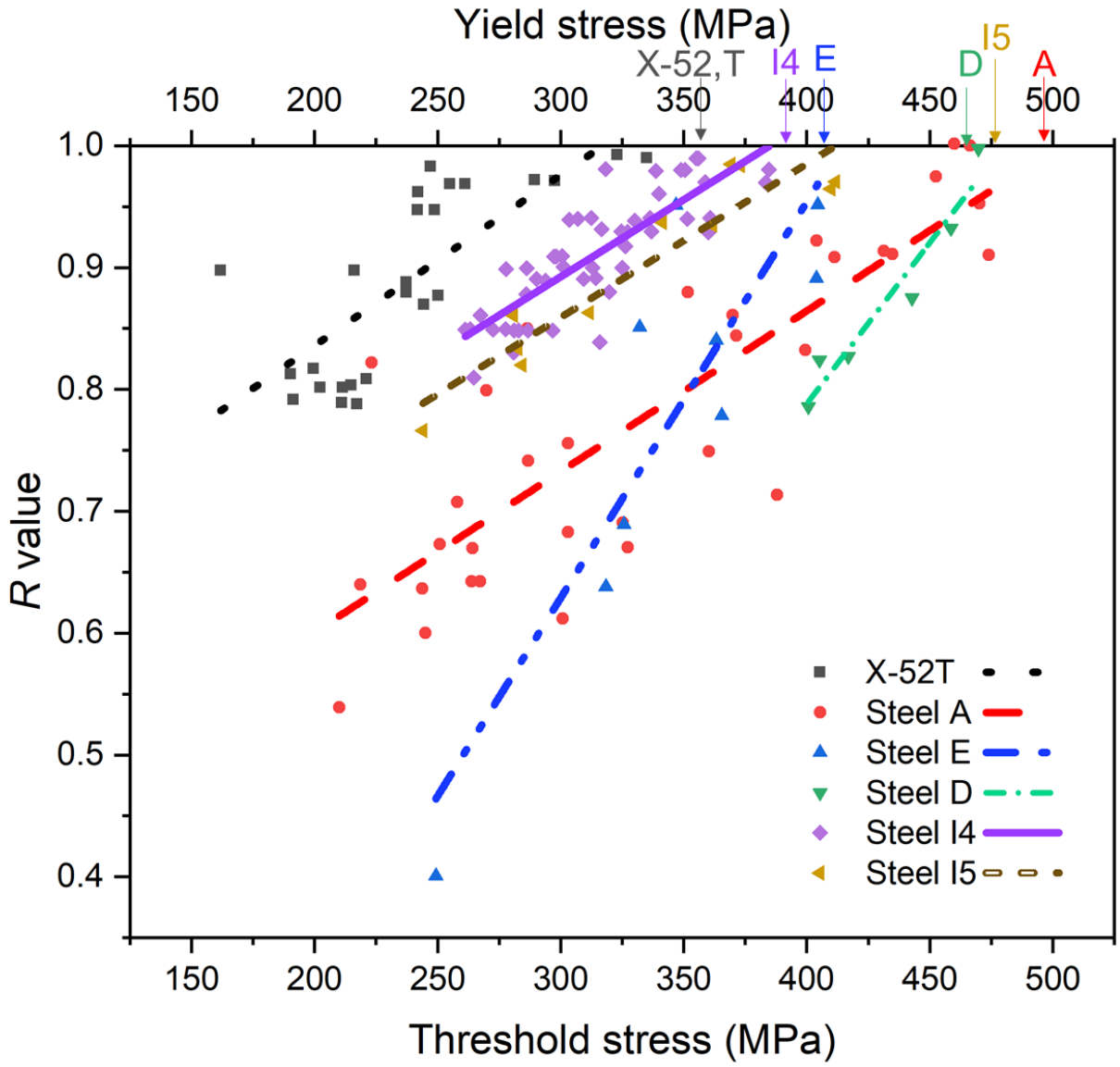

Figure 2.8. Effect of *R*-ratio on threshold stress for HpHSCC of different steels exposed to the carbonate-bicarbonate environment at 75 ˚C and -650 mV_{SCE}. Data points were calculated from the mean stress applied to specimens (data extracted from reference [60]).

The other factor that increases the probability of cracking is an increasing residual tensile stress. In the case of near-neutral pH SCC (NNpHSCC), it has been shown that the mean residual tensile stress adjacent to the SCC colonies was almost twice as high as that in the non-SCC regions [76]. In the same manner, the presence of residual stress within 1.5 mm from the outer surface of the

pipeline was observed in failures caused by HpHSCC [4,7]. First, tensile residual stress will add to the applied stress in order to reach the threshold value for crack initiation [57]. Beavers found that the average range of residual stress was between 112 to 320 MPa in regions that experienced SCC. Even the lower bound of this residual stress range contributes significantly to providing the threshold stress for HpHSCC cracks (compare with the threshold stresses from Figure 2.8). Secondly, it has been proven that tensile residual stress is favourable to pitting corrosion [77]. Crack initiation from the pits' tips in different grades of pipeline steels is shown in Figure 2.9 [11,66], and the presence of pits near the HpHSCC regions has been reported in some cases [3,8,11,12,14,66,78]. These pits were probably formed prior to the establishment of the HpHSCC environment [66]. Non-metallic inclusions like MnS act as preferred places for pitting corrosion [67]. A statistical analysis of the samples from pipes with many years of underground exposure and corrosion shows is a direct correlation between the number of cracks and the number of pits [79]. Pits are a breeding ground for crack initiation for three reasons. First, the chemical composition and chemical potential can change in the pits that cause crack initiation [67]. Secondly, the protective film that forms on the pits' surfaces may not be as protective as on the pipe surface [79]. Thirdly, pits on the external surface of the pipe would act as stress risers [79–81]. The stress concentration factor around the pits increases with both the pit's depth and the pit's tip curvature [66,79].

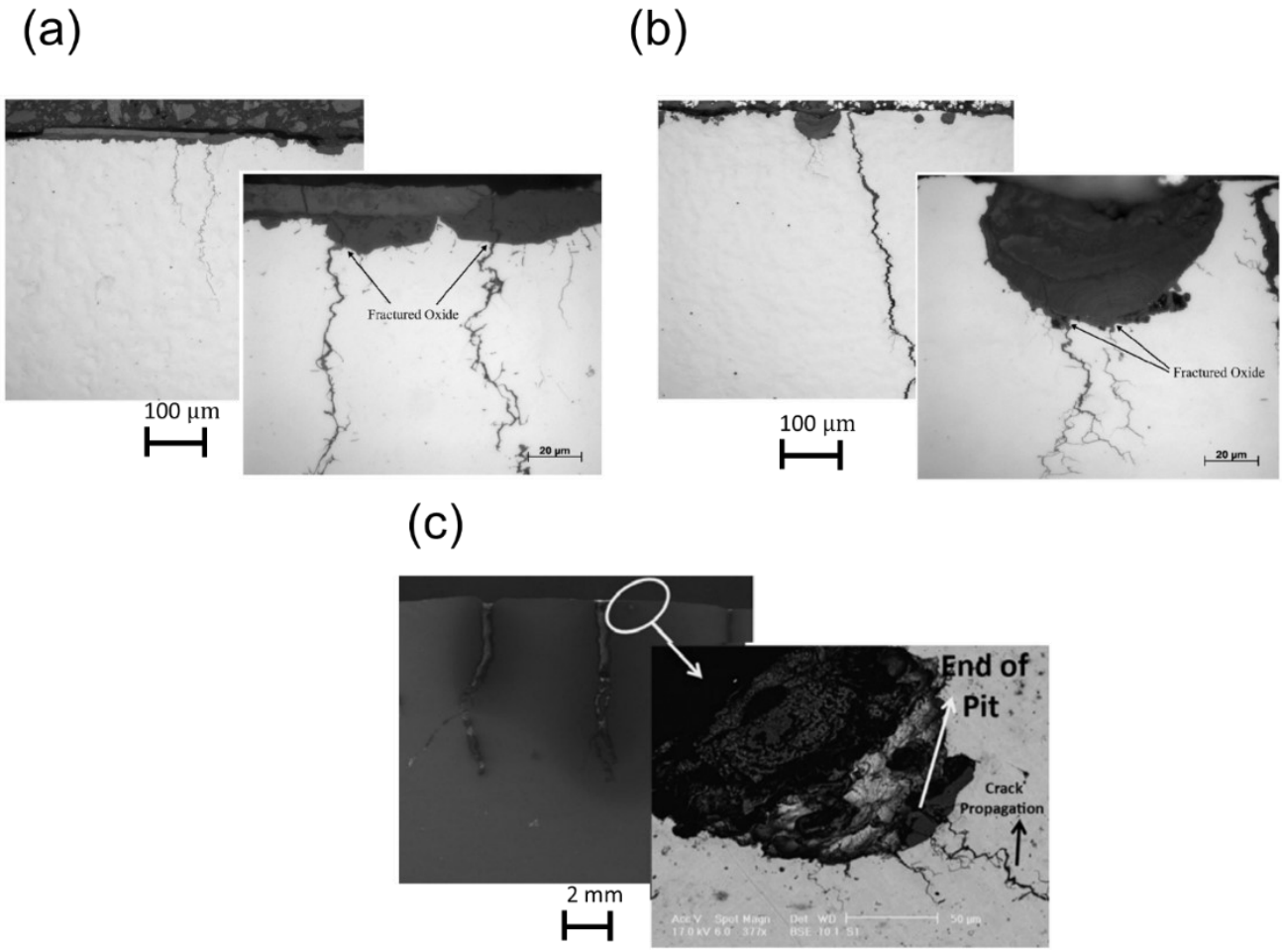

Figure 2.9. Initiation and growth of intergranular cracks at the tip of a pit in different grades of steels (a)X-42 [66] (b) X-65[66] (c) X-60 [11].

In addition to pits, surface conditions play a crucial role in the crack initiation stage. Figure 2.10 compares threshold stress for HpHSCC crack initiation for three different steels under mill-scaled and polished conditions. It is clear that HpHSCC cracks initiate at lower threshold stresses on the mill-scaled surfaces compared to polished surfaces, machined surfaces, and grit-blasted surfaces [64,78,82]. As has been noted, mill-scaled surfaces keep the potential of the pipe within the cracking window for a longer time at coating holidays [49,78]. Furthermore, fracture of the mill scale may cause localized corrosion and pit formation on the external surface of the pipe [78].

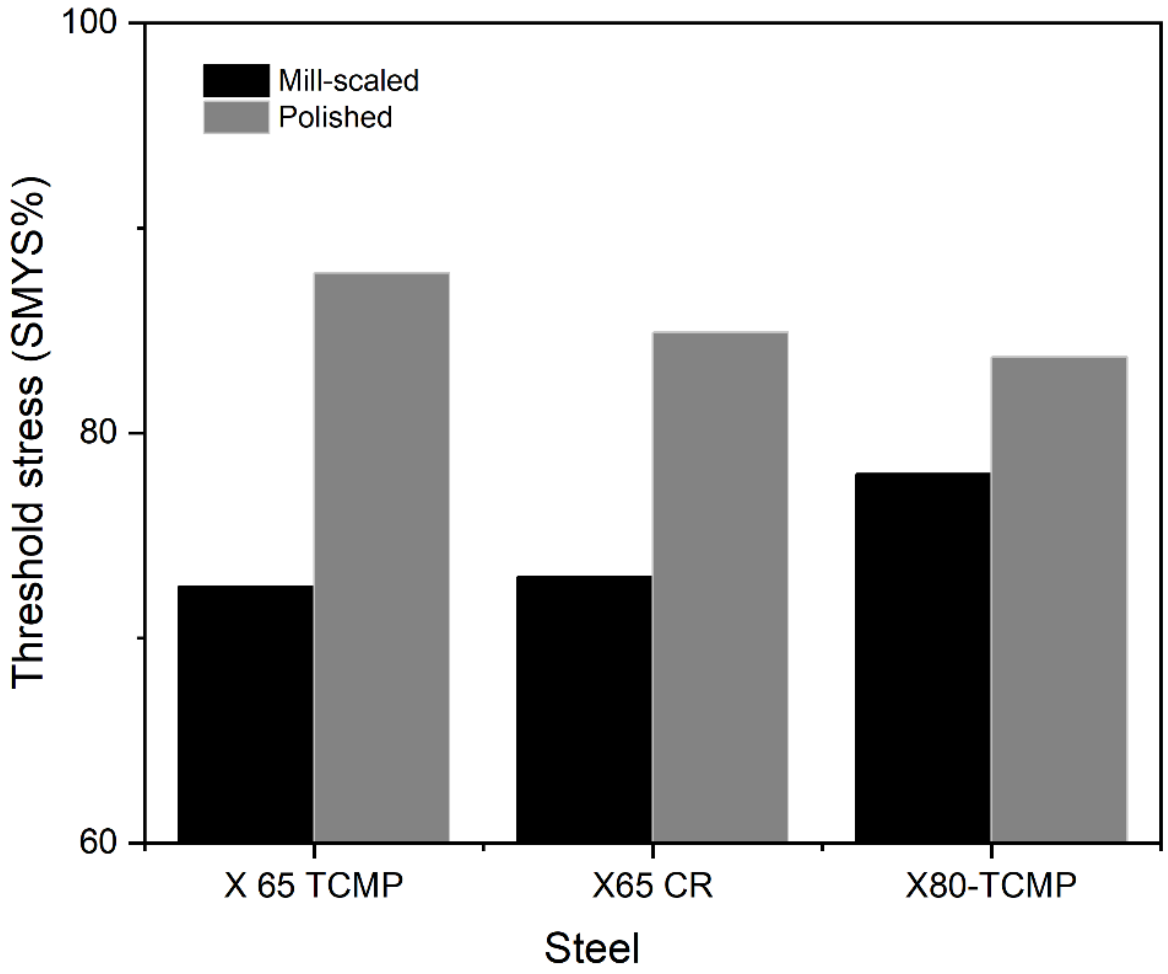

Figure 2.10. Comparison between the threshold stress for stage 1 of HpHSCC for different steels with mill scaled and polished surfaces. The loading condition was R=0.5 and frequency of 10^{-3} Hz [64].

Asahi *et al.* [64] removed the mill scale by either pickling or grit blasting. They observed that removing the mill scale by pickling had no pronounced effect on the threshold stress for crack initiation. On the other hand, steel resistance against HpHSCC crack initiation was improved by applying grit blasting to remove the mill scale. This is likely because grit blasting imparts compressive stresses in the layer below the mill scale; consequently, it influences the stresses available for crack initiation. Figure 2.11 (a) shows the area near the mill-scaled surface in X65

pipeline steel. A decarburized layer below the mill scale accompanied with a large grain size compared to sublayers is seen in this figure. Figure 2.11 (b) shows the changes in grain structure as well as an increase in hardness of the layer after grit blasting. Figure 2.11 (c) shows the microhardness profile of the grit-blasted and mill-scaled surface of X65 pipeline steel. Accordingly, grit blasting increases the resistance against HpHSCC crack initiation through changes in grain structure, generation of compressive stress and increase in hardness. Carbon is a strengthening element in microalloyed steel. Hence, the decarburized layer has lower yield strength, and it plastically deforms at lower applied stresses [83,84]. Additionally, refining the grain size is another way to increase the yield strength according to the Hall-Petch equation [85,86]. As the area near the mill scale has a larger grain size, these grains are deformed more easily, and this contributes to crack initiation. On the other hand, grit blasting changes the grain structure and forms more elongated grains with compressive residual stress [64].

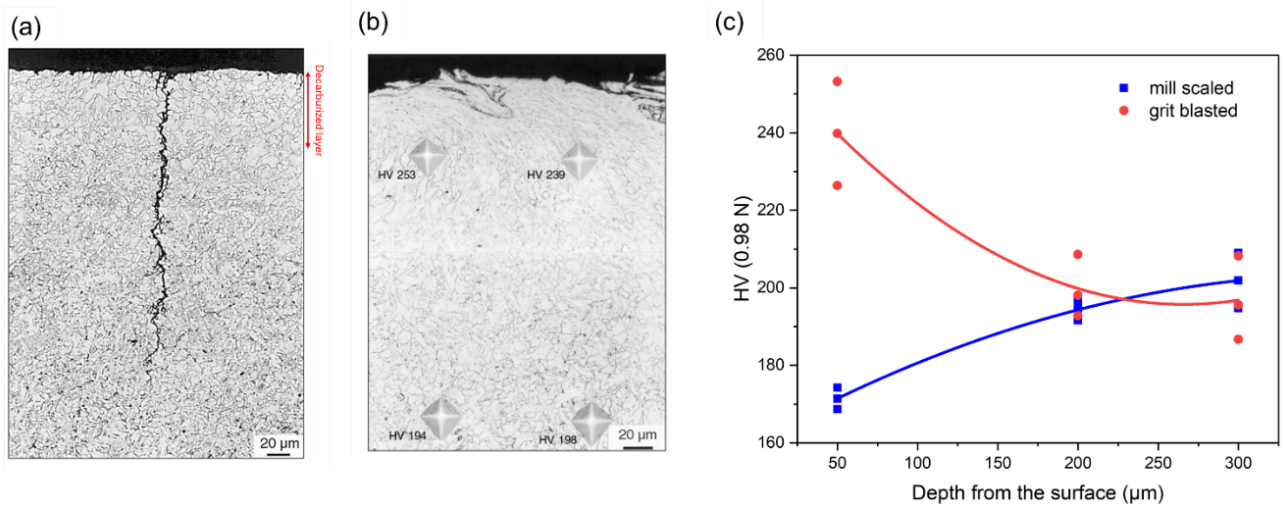

Figure 2.11. (a) Cross-section of the steel near the mill-scaled surface where cracks are initiated, (b) the area near the grit-blasted surface, (c) hardness profile for mill-scaled and grit-blasted surfaces of X65 quenched and tempered steel [64].

Grit blasting or similar surface treatments also change the surface roughness. It has been shown that excessive grit blasting has a negative impact on the HpHSCC resistance of pipeline steels. In 2007, Kentish [81] showed that the relative time to failure (ratio of time to failure in HpHSCC environment to that in oil) decreases if the surface roughness exceeds 11 µm, as shown in Figure 2.12. Surface roughness provides stress risers and can act similarly to pits. The surface roughness level of 2, 4 and 6 µm causes stress concentration of 1.4, 1.9, 2.4 in 4130 steel, respectively [87]. Therefore, there is an optimum amount of grit blasting and shot peening where the benefits of the compressive stress and increase in hardness are achieved, and the negative impacts of the increased roughness are avoided.

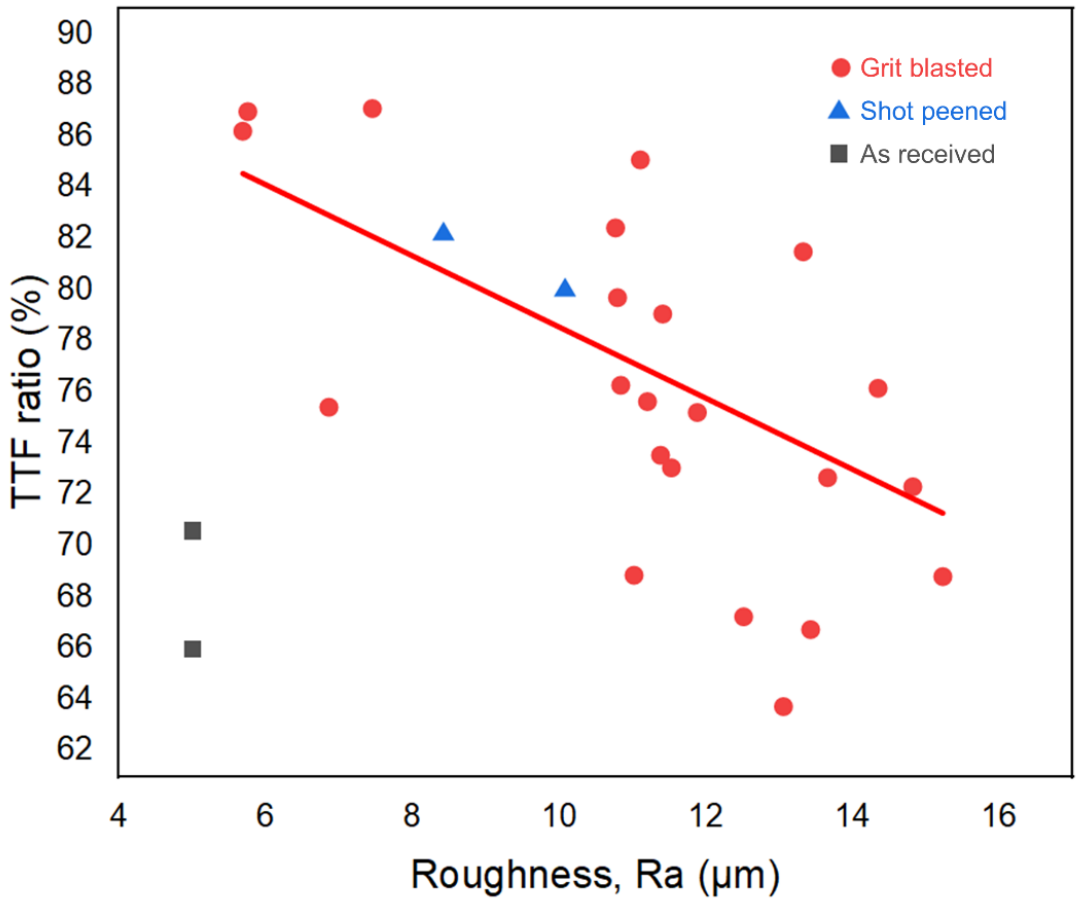

Figure 2.12. Effect of surface roughness on time to failure of X70 pipeline steel [81].

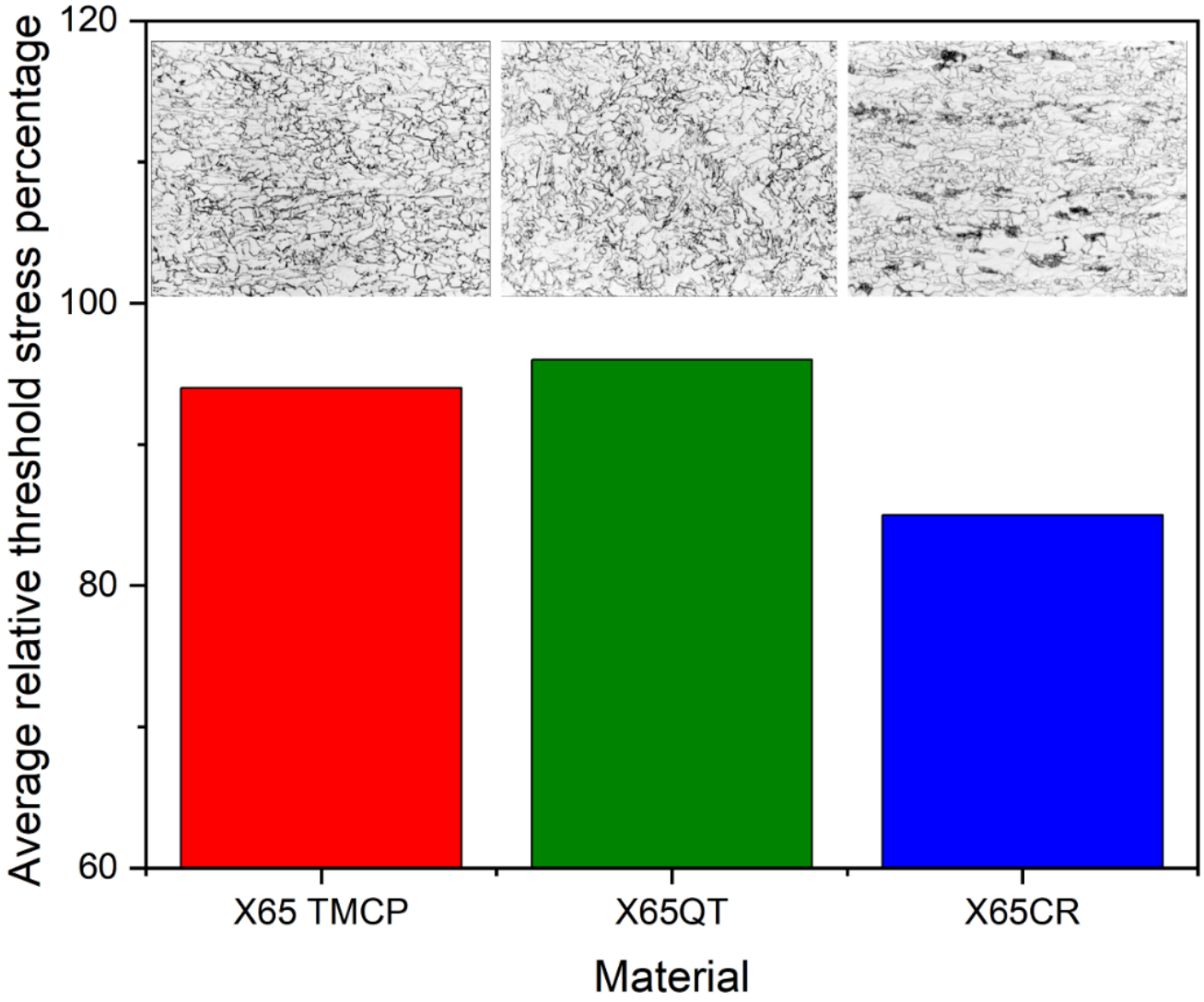

Figure 2.13. Average threshold stress percentage of three different X65 pipeline steels and their corresponding microstructures [64].

As discussed earlier, large grain size decreases the threshold value for HpHSCC because the yield point decreases as the grain size increases, and microplastic deformation is not uniformly distributed, *i.e.,* it is concentrated at the smaller number of grain boundaries. For the same reasons, more uniform microstructures like bainitic structures are more resistant against HpHSCC crack initiation compared to ferrite-pearlite structures [8,64]. Figure 2.13 shows the microstructure as well as the average relative threshold stress (threshold stress divided by yield stress) of three

different X65 pipeline steels. The microstructures for X65 TMCP (thermo-mechanically controlled processed), X65 QT (quenched and tempered), and X65 CR (carbon reduced) steels are bainitic ferrite, bainite, and ferrite-pearlite, respectively. The X65 TMCO and X65 QT are more resistant against HpHSCC crack initiation [64]. Similarly, Cerny and Linhart [8] reported more susceptibility of the non-homogeneous zones like heat-affected zones for crack initiation than the base metal and weld metal in X60 pipeline steel [8]. Min *et al.* studied the susceptibility of X65 and X80 pipeline steels to stress corrosion cracking under HpHSCC environmental conditions. It was shown that high strength X80 pipeline steel, composed of fine acicular ferrite grain and granular bainite, is resistant against intergranular cracking, unlike X65 composed of ferrite and pearlite. However, X80 steel is susceptible to transgranular cracking because of the interference of hydrogen embrittlement [88,89].

From the above discussion, HpHSCC cracks may initiate at different sites, and the threshold value is variable and depends on several factors. Once initiated, cracks will propagate by the anodic dissolution mechanism at grain boundaries, discussed in the next section.

2. 3. 2 Early Stage of HpHSCC Crack Growth

The newly initiated cracks are semi-elliptical, where the crack length on the free surface (2c) is more than twice the crack depth (a). Figure 2.14 illustrates an example of a nucleated crack in X65 pipeline steel. From the fracture-mechanics point of view, stress is intensified in the vicinity of the metallurgical discontinuities like the intergranular crack shown in Figure 2.14. The crack driving force near the crack tip can be predicted by the stress intensity factor. The stress intensity factor represents the available mechanical driving force for propagation of an existing crack caused by the applied stress to the pipe (mainly by hoop stress), and it depends on both crack geometry, specifically the square root of the crack length and the stress level. For the crack shown in Figure

2.14, the stress intensity factor on the free surface ($K_{surface}$) and stress intensity factor in depth tip (K_{depth}) corresponding to applying the 60% SMYS loading are calculated and shown. Considering the small dimensions of the intergranular fissure at this stage, in particular the crack depth, both K_{depth} and $K_{surface}$ are relatively small. As will be discussed in Section 2. 5, the minimum K for sustainable crack growth, which is known as K_{ISCC}, and is much higher than the K values at this stage (it is about 21 MPa.m$^{0.5}$ under static loading conditions). Hence, stress intensification caused by small intergranular cracks does not cause continuous fracture of the passive film on the grain boundary.

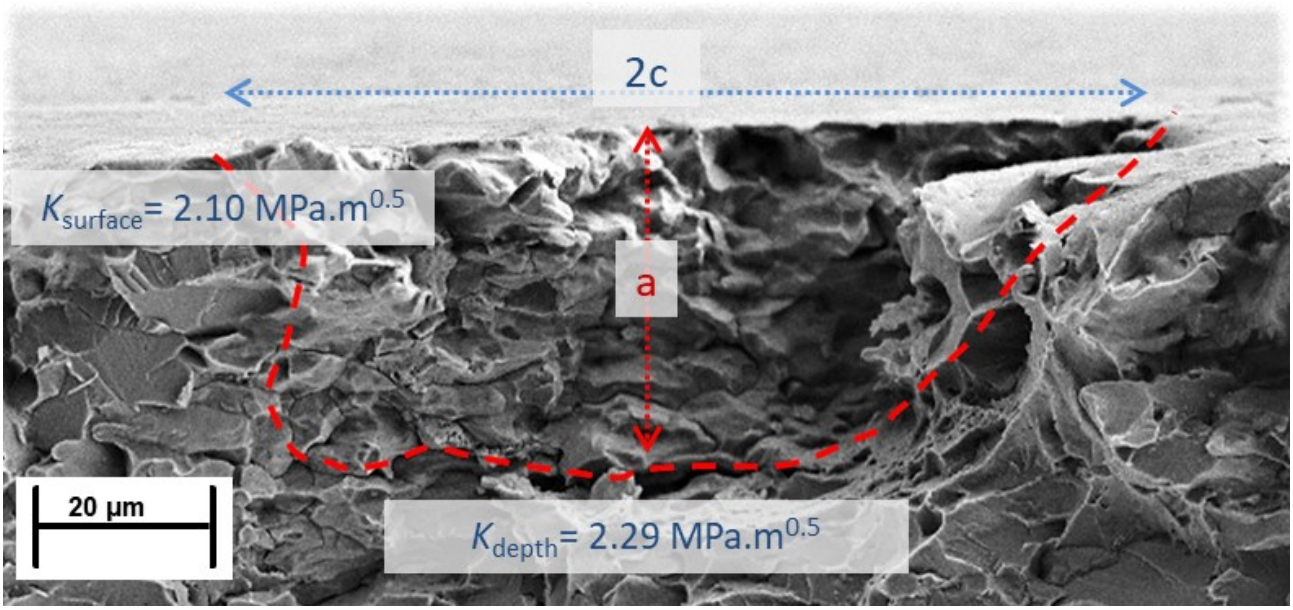

Figure 2.14. Newly initiated crack on the free surface of X65 pipeline steels with a thickness of 9 mm and calculated stress intensity factors under 60% SMYS loading condition [90].

Figure 2.15 shows the variation of maximum crack depth and the crack growth rate versus the number of cycles (*i.e.* increase in time) for cracks initiated on the surface of the pipe [91]. The maximum crack depth increases and reaches a limiting size after 20 or so cycles. At the same time, the crack propagation rate decreases gradually. As the crack geometry changes in this stage, K_{depth}

slightly increases (Further discussion about the changes in stress intensity factor with crack geometry can be found in Section 4). However, it will remain far below the K_{ISCC} since the depth-direction crack growth is limited at this stage. As the newly nucleated crack is propagating, the pipe's body may place obstacles in the way of the intergranular crack and limit the crack size. Once an intergranular crack forms and propagates, it generates local plastic deformation. The generated strain fractures the passive film, and this promotes early-stage crack growth. As the crack propagates, the area near the penetrating crack tip is work-hardened because of the plastic deformation in this region, in particular at the depth tip [57,60]. The argument is made that the surrounding work-hardened grains increase the resistance to further plastic deformation. Although this is true, it also applies to every crack in a work hardening material. Additionally, residual stress often follows a decreasing trend below the outer surface of the pipe [59]. Therefore, the depth crack tip, once it penetrates the tensile layer, will relax this tensile force, and the crack will only be subjected to the stresses from internal pressurization. Thus, the stress acting on the crack is lower once the crack relaxes the tensile residual stress. It is not clear that this is sufficient to explain the growth rate curve seen in Figure 2.15. One additional factor to consider is the contribution of low-temperature creep during cyclic loading.

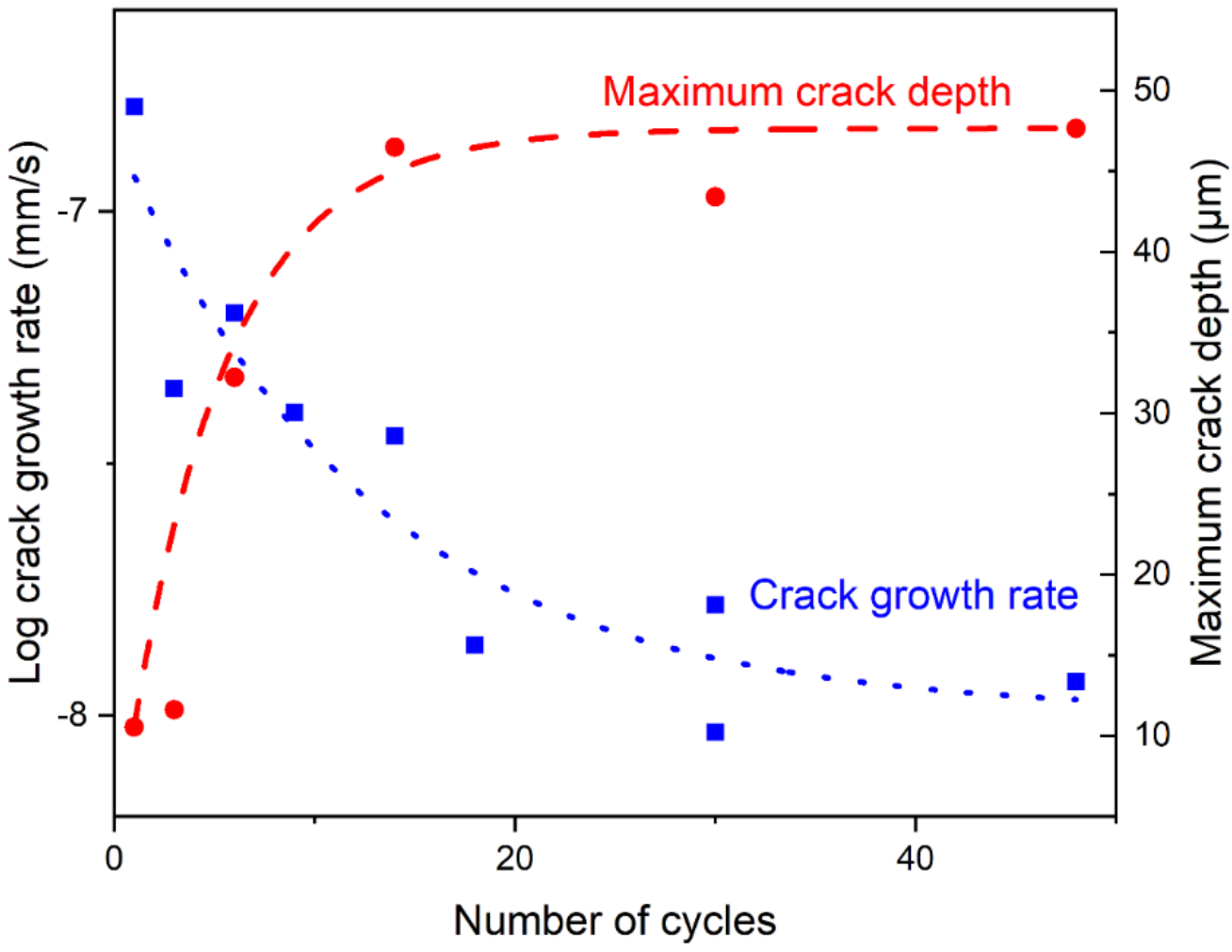

Figure 2.15. Variation of the crack growth rate and maximum crack depth versus the number of cycles at stage 1a [91].

The initial crack growth rate at the onset of this stage is characterized with the highest crack growth rate in the bathtub model. The highest crack growth rate stems from the existence of low-temperature creep. For pipelines that are operating under variable amplitude loading conditions, low-temperature creep sustains the strain at the crack tip and causes crack propagation [92]. Low-temperature creep is a function of several factors, including the magnitude of the applied stress, metallurgical conditions, amplitude of the loading cycle, and loading strain rate [93]. If the local stress exceeds the yield strength ahead of the growing crack, the steel experiences a phenomenon

known as low-temperature creep under cyclic loading conditions [26,59,94]. This phenomenon occurs in metals that develop strain hardening, like pipeline steels, as shown in Figure 2.6. Under monotonic loading conditions, where the load is increasing at a constant rate, plastic strain increases the internal stress, which causes lower mobility of the glissile dislocations. Hence, further motion of dislocations (*i.e.*, more strain) requires an increase in applied stress. However, this behaviour might change when the load is wholly or partially removed under a cyclic-loading condition. This condition is shown in Figure 2.16. Here, the amount of strain decreases during the unloading event from point A to point B. On the reloading event, the strain may increase until the strain rate decreases by work hardening again. Therefore, the amount of strain exceeds point C and reaches point D, where the strain rate is reduced because of work hardening. The additional strain between point C and D is low temperature creep that occurred during the cyclic loading. The reason for this behaviour is changes in the dislocation network and their movement. Up to point A, there are two types of dislocations *viz.* glissile dislocations, *i.e.*, mobile dislocation whose motion causes plastic deformation, and sessile dislocations that are unable to glide and hence sometimes act as obstacles for mobile dislocation movement. Here, the strain rate just before the unloading event is slowing implying that a large amount of the shear stress acting on mobile dislocation is impeded because of internal stresses from sessile dislocations and other obstacles. At the onset of unloading, the mechanical driving force to move dislocations forward decreases and the repellent stresses from the sessile dislocations force the glissile dislocations to move backward. This backward movement of dislocations might be accompanied by either cross slip of dislocations or rearrangement of obstacle dislocations by internal stresses. These phenomena, which resemble recovery during annealing of a work hardened structure, continue up to point B, where the reloading begins. During the reloading, the mobile dislocations glide again and regenerate the

strain; however, because of the aforementioned changes in the microstructure the work hardening is postponed until the strain rate decreases again at point D. This effect is cumulative with each of the repeated load cycles, *i.e.*, the total strain increases after each cycle [94]. However, the creep strain increment gradually decreases which is followed by a decrease in generated strain to form the film-free condition. The reduction in low temperature creep rate along with the barriers caused by work-hardening and/or the effects of sublayers' residual stress facilitate film formation on the penetrating tip. Therefore, the crack becomes dormant and ceases to grow further, as shown in Figure 2.15. Thus, it is the loss of low temperature creep that leads to dormancy. This effect is clearly important since if we could control this creep, we could control dormancy, and this would offer a means of reducing and delaying the damaging effects of HpHSCC.

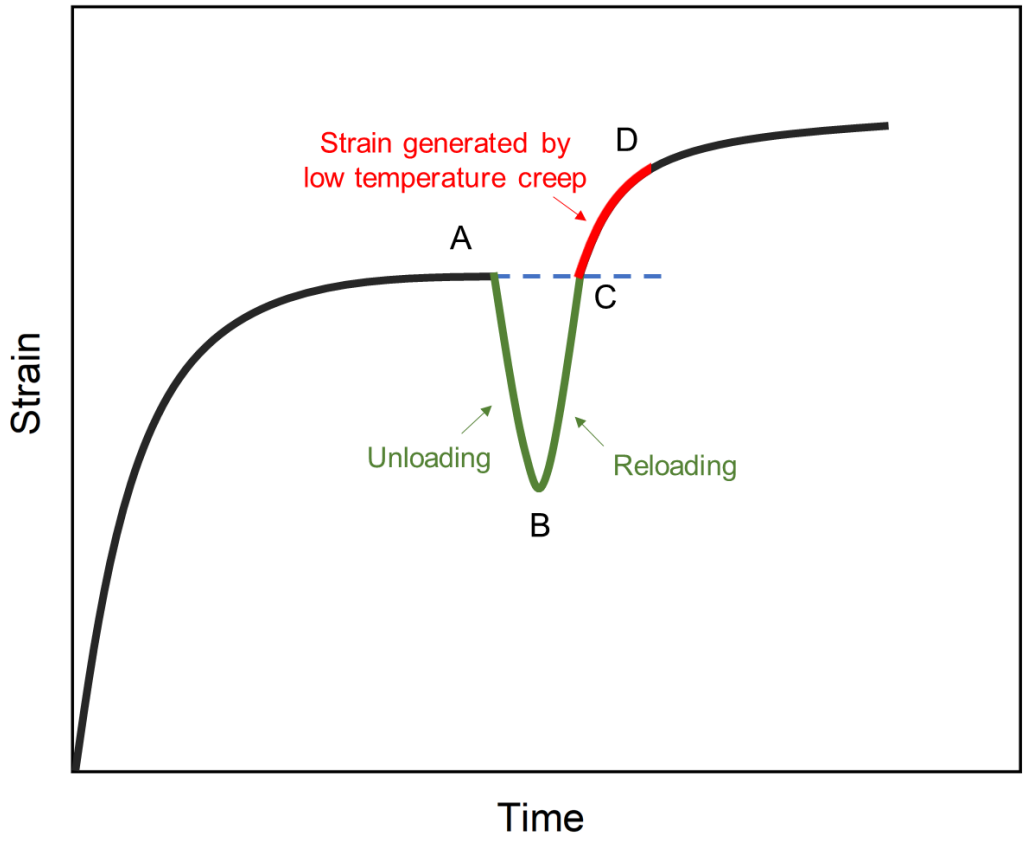

Figure 2.16. Schematic illustration of low-temperature creep caused by cyclic loading.

At the end of this stage, it is expected that shallow cracks with a depth of about 50 μm have been formed at multiple sites. These cracks have ceased to grow and no longer have sufficient mechanical driving force to provide a film-free condition ahead of the crack tip.

2. 4 Stage 1b: Preparation of the Conditions for Mechanically Derived Crack Growth

This stage, which encompasses a large portion of the pipeline's lifespan, is characterized by the continuous initiation of small intergranular cracks followed by eventual coalescence of these cracks as they grow and approach one another. During this stage, the events described in stage 1a continue at multiple sites. Figure 2.17 shows examples of the variation in the number of cracks per millimetre along the gauge length of the tapered specimens under cyclic conditions at two different stress levels and frequencies [60]. According to Figure 2.17, the crack nucleation at this stage shows some sensitivity to the loading condition. First, the number of cracks increases as the number of loading cycle increases, regardless of the stress level and frequency. Secondly, the crack nucleation rate is higher at higher stresses; however, the increases slow down, and the number of cracks reaches a plateau after long times of exposure [95]. This condition is illustrated in Figure 2.17, as the number of cracks for all situations are converging after a long period of time (around 100 days). Additionally, the crack nucleation rate is higher at a higher frequency for stresses equal to or greater than the threshold stress [60].

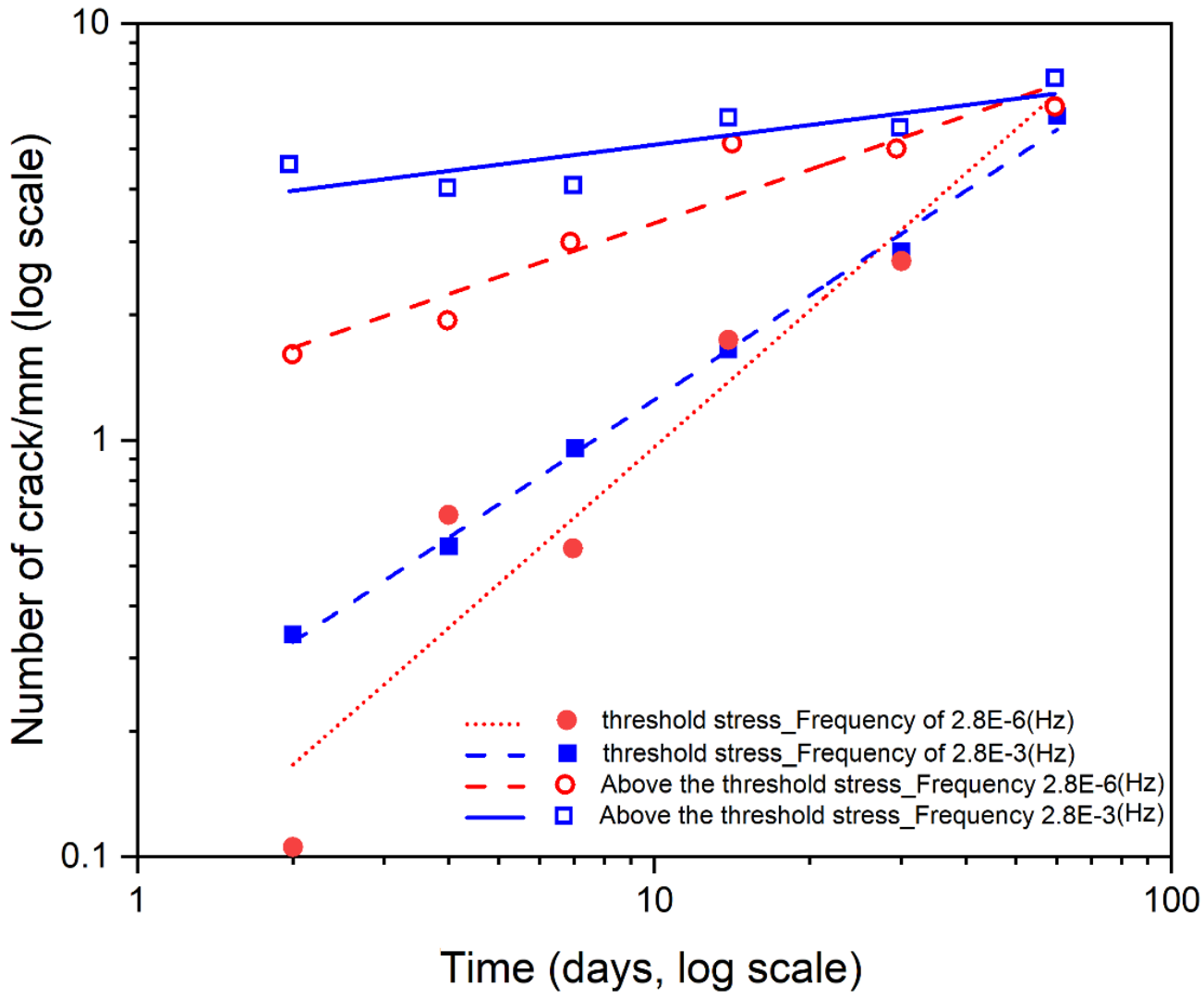

Figure 2.17. Variation of the number of cracks per millimetre of the tapered specimen gage length with the test time at two different stress levels under cyclic loading conditions at two frequencies [60].

Moreover, it has been shown that the number of cracks for a certain period of time increases for mill-scaled surfaces as compared to the polished surfaces used in some laboratory experiments [95]. Although the ultimate number of cracks is equal to the number of grain boundaries, this condition is not actually applicable because of the shielding effects of cracks as the cracks become more numerous and hence closer together. Then, some of the smaller cracks cease to grow because

of the stress shielding effects of the larger adjacent cracks [60]. The cracks will grow to varying degrees, yet the fate of almost all of the cracks will be dormancy, as described in the previous section. However, relatively nearby cracks might merge and form larger cracks on the free surface of the pipe. This mechanism is highly dependent on the spatial distribution of the cracks. Although crack nucleation at this stage is random to some extent, there is some evidence that shows there are some preferred regions for crack initiation, as shown in Figure 2.18 (a to c). In Figure 2.18 (a), a high density of cracks is nucleated at the bottom of the pit, which increases the chance for crack coalescence. In Figure 2.18 (b), it is evident that micro-cracks are formed between the nearest tips of two relatively large cracks (along the line AB) that assist crack coalescence. Figure 2.18 (c) illustrates nucleation of cracks near the pre-existing cracks' tips. It is worth mentioning that Figure 2.18 (b) and (c) are actually in stage 1b, as they are relatively long cracks appropriate for later stages. However, it is possible to consider the same behaviour, yet at a smaller scale, for this earlier stage. Based on the crack coalescence mechanism, cracks may show frequent growth and dormancy periods. Hence, crack growth at this stage is stochastic and highly dependent on new crack initiation and crack coalescence [31,57,60,95–98].

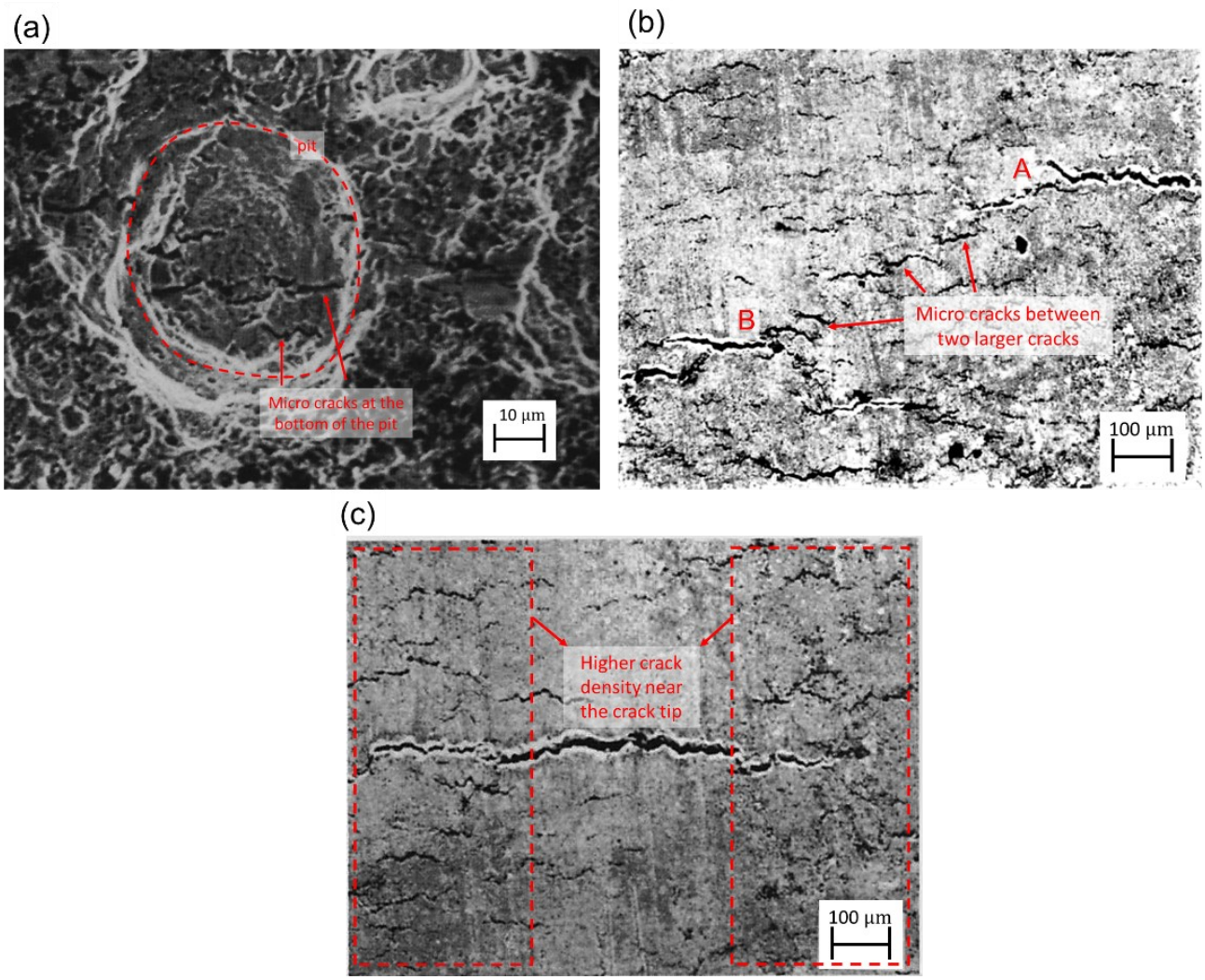

Figure 2.18. Nucleation of cracks (a) at the bottom of a pit (b) along the line between the nearest tips of two relatively large crack (c) crack initiation near the large crack's tips [95].

Both field and experimental observations show that the probability of crack coalescence increases with the condition that the distance normal to the crack length (y) decreases and/or the average length of two adjacent cracks ($2C$) increases. Figure 2.19 shows merged and non-merged cracks from an examination of in-service pipelines. The spatial distribution of the cracks is schematically shown at the right bottom of Figure 2.19, and $2C$ is the average of $2C_1$ and $2C_2$. Accordingly, Parkins expressed the condition for crack coalescence by Equation 2.2:

y≤0.14 (2C) Eq'n. 2.2

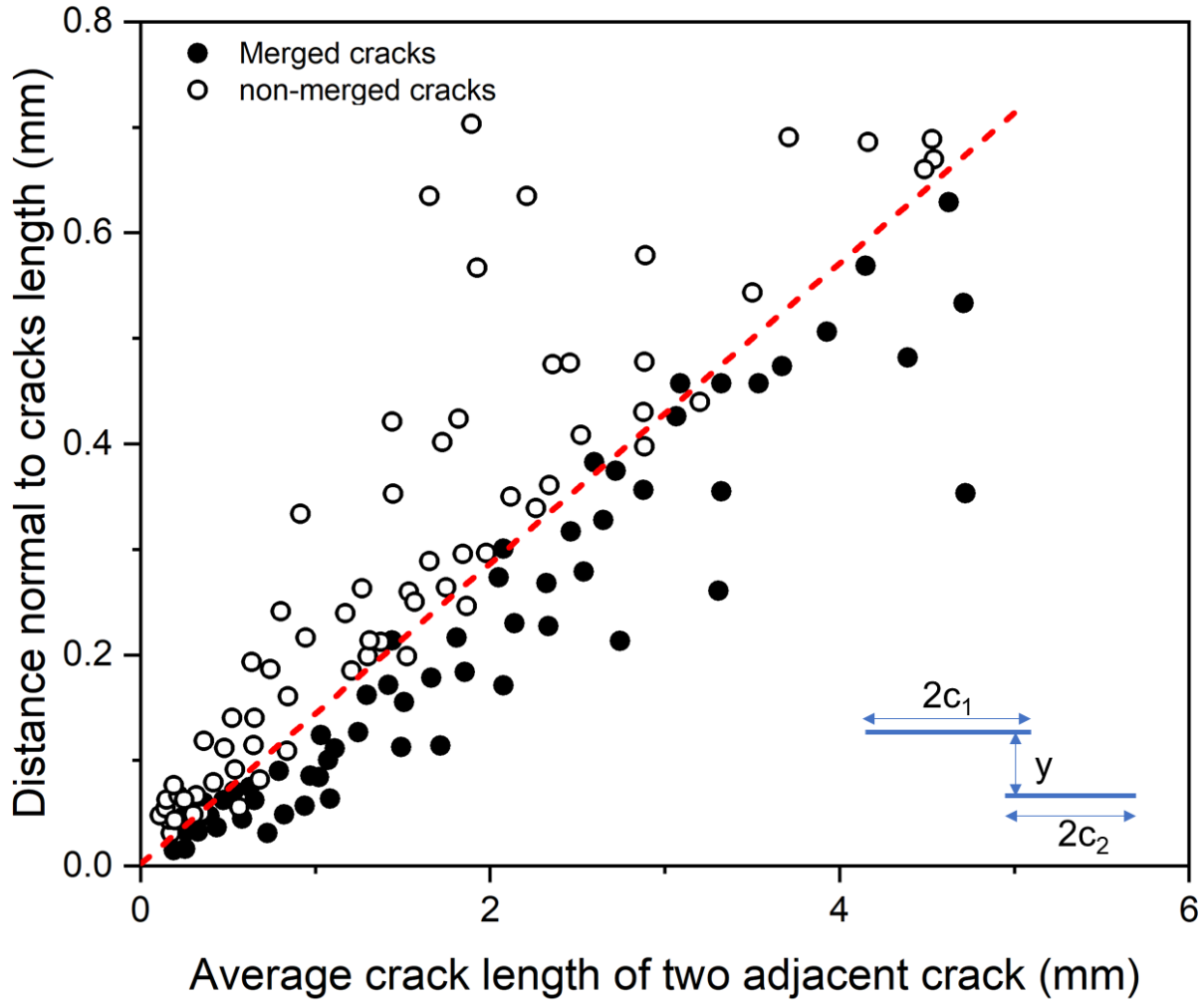

Figure 2.19. Crack coalescence data from a laboratory test of three steels exposed to the carbonate-bicarbonate solution at the temperature of 75 ˚C [60].

Although the crack propagation at this stage is of paramount importance and determines the pipeline's lifetime, the available literature related to the crack growth at this stage is limited. The above discussions (multiple crack initiations and crack coalescence) are based on laboratory experiments under constant amplitude loading waveforms. As mentioned earlier, most HpHSCC failures happen within 30 km downstream from the compressor, where pipelines experience Type I pressure fluctuation (see Figure 2.5). Therefore, the load interaction effects of cyclic loading

must be considered. Similar to other engineering components, the load interaction might accelerate or retard crack growth [99,100]. In general, underload cycles (cycles possessing some relatively lower *R*-ratio cycles) accelerate crack growth [57,101]. In the case of pipeline steel, it has been shown that the underload cycles play a crucial role in near-neutral pH stress corrosion cracking [102,103]. Some work has been done recently to extend this to HpHSCC. Figure 2.20 shows HpHSCC crack growth rate in mm/s under different loading waveforms. HpHSCC crack growth varies significantly by loading scenario so that low *R*-ratio constant amplitude cycles demonstrate one order of magnitude higher crack growth compared to other waveforms. However, converting the crack growth rates to mm per loading block shows that all loading waveforms containing low *R*-ratio cycles cause similar crack growth rates. A loading block is a load cycle in constant amplitude tests and composes of 50 high *R*-Ratio cycles or a period of static load followed by an underload cycle. These results show that underload cycles have a detrimental effect on HpHSCC crack growth behaviour at this stage. It is proposed based on the experimental observation that underload cycles facilitate initiation of the secondary cracks near the crack, which assists the crack growth through a crack coalescence mechanism [90].

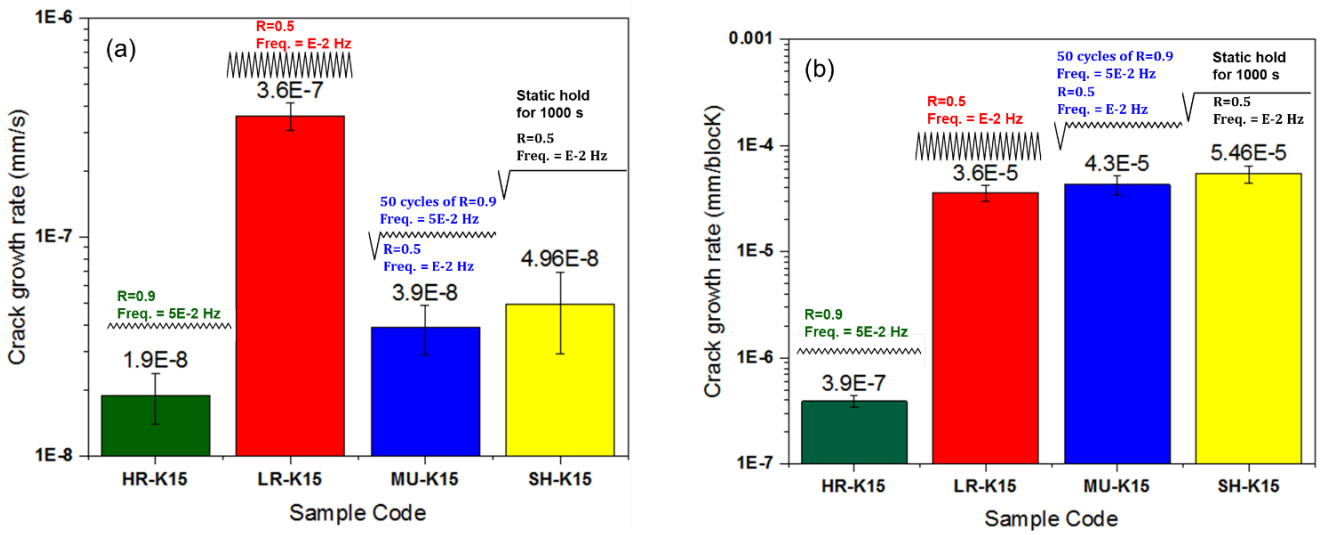

Figure 2.20. The effect of loading waveform on HpHSCC crack growth behaviour under different loading conditions in terms of (a) *da/dt* (b) in terms of *da*/dblock [90].

This stage (new crack initiation and crack coalescence) continues until the mechanical driving force at the crack tip, in particular, the depth tip, reaches the critical mechanical threshold for HpHSCC crack growth. The mechanical threshold for stage 2 of HpHSCC will be discussed in detail in section 2. 5. 1. The events that occur during this stage assist in achieving the prerequisites for stage 2 of crack growth by increasing the mechanical driving force and/or reducing the critical threshold value.

First and foremost, the changes in the geometry of the cracks, which are because of either crack coalescence or less often individual crack growth, fortifies the mechanical driving force at the depth tip of semi-elliptical cracks. This condition is shown in Figure 2.21, where the stress intensity factor on the surface tip ($K_{surface}$) and depth tip (K_{tip}) are calculated for different cracks geometries on the external surface of a 9-mm thick X65 pipeline steel loaded to 75% of SMYS. The larger cracks in this figure were formed through the merging of smaller cracks. Evidently, crack

coalescence on the free surface is accompanied by increases in K_{depth}, *i.e.,* an increase in the mechanical driving force for crack propagation.

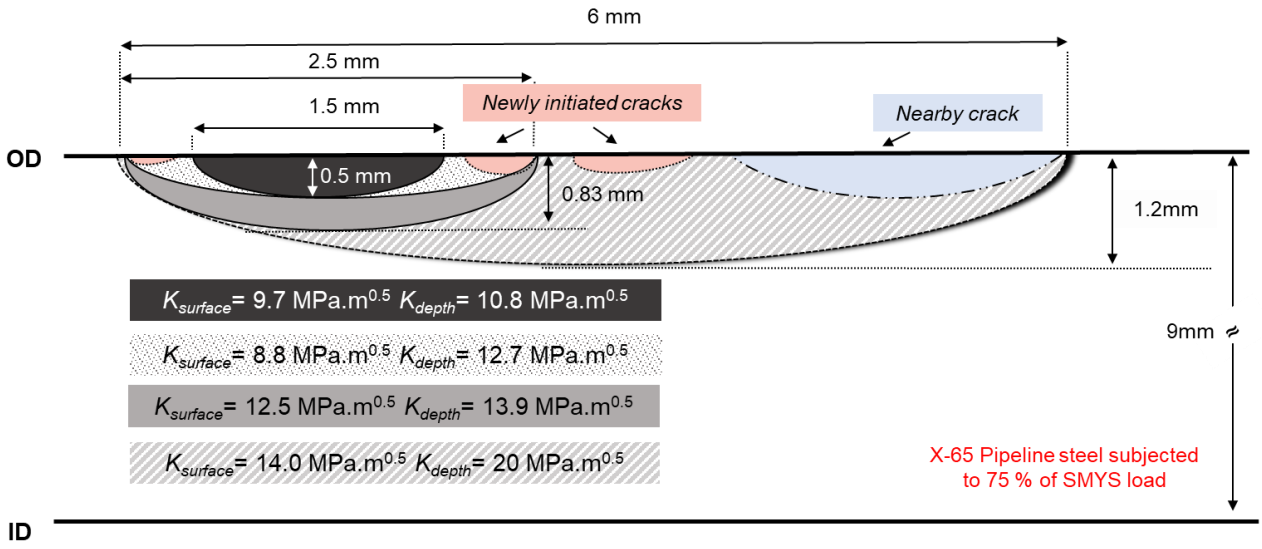

Figure 2.21. Schematic illustration of the small crack coalescence and crack geometrical changes that increase K_{depth} to the threshold value. The cracks are colour-coded to the K calculations.

Secondly, the load interactions, in particular the acceleration effect of underload cycles, speed up the crack geometry evolution; and consequently, it causes the early onset of stage 2. Thirdly, the mechanical driving force can reach the threshold value in the presence of special abnormalities in the pipe surface (such as dents or other mechanical damage) and/or adding other sources of stresses such as macroscopic pipeline bending stresses from soil movement as an example [57]. Fourthly, the environmental conditions (such as temperature, cathodic potential, and chemical composition of the solution) may change and decrease the threshold value for stage 2 and accelerate the onset of stage 2 [57].

2. 5 Stage 2: Mechanically Derived HpHSCC Crack Growth

Crack propagation at this stage is fast compared to stage 1, and a cracked pipeline confirmed to be at stage 2 must be monitored and repaired before the onset of stage 3. In the next section, the

threshold conditions for mechanical crack growth by HpHSCC and the crack growth mechanisms for this stage are discussed.

2. 5. 1 Threshold for Stage 2 of HpHSCC Crack Growth

By the end of stage 1, an intergranular flaw is formed with the critical dimensions for the applied load conditions. The synergistic effects of environmental conditions, pipe properties, flaw geometry, and mechanical loading conditions determine a threshold value for HpHSCC. The physical meaning of threshold is that sustainable crack growth is achieved, in particular in the pipe's thickness direction. Beyond the threshold, the crack growth rate increases significantly in comparison with previous stages. For a given material-environment system, the threshold condition is related to the combination of flaw geometry and loading condition [104,105]. There are several threshold definitions for HpHSCC as outlined below:

- K_{ISCC}: This is known as the critical stress intensity factor for SCC and represents the minimum stress intensity factor (K_I) at the crack tip that can cause continuing crack growth under static loading conditions. As shown in Figure 2.22 (a), K_{ISCC} has been determined as 21 MPa.m$^{0.5}$ for a pipeline steel exposed to the HpHSCC environment at 75 ˚C [106,107].
- **ΔK_{th}:** Parkins observed that the minimum stress intensity factor at which the crack growth behaviour changes varies under low-frequency cyclic-loading conditions. Figure 2.22 (b) shows the growth rate versus a range of ΔK values for pipeline steel exposed to an HpHSCC environment at different mean stress intensity factors (K_m) ranges below K_{ISCC}. There is a critical ΔK (ΔK_{th}) at which crack growth behaviour changes. Accordingly, stage 2 of HpHSCC can start at a stress intensity factor below K_{ISCC} in the presence of cyclic loading [106].

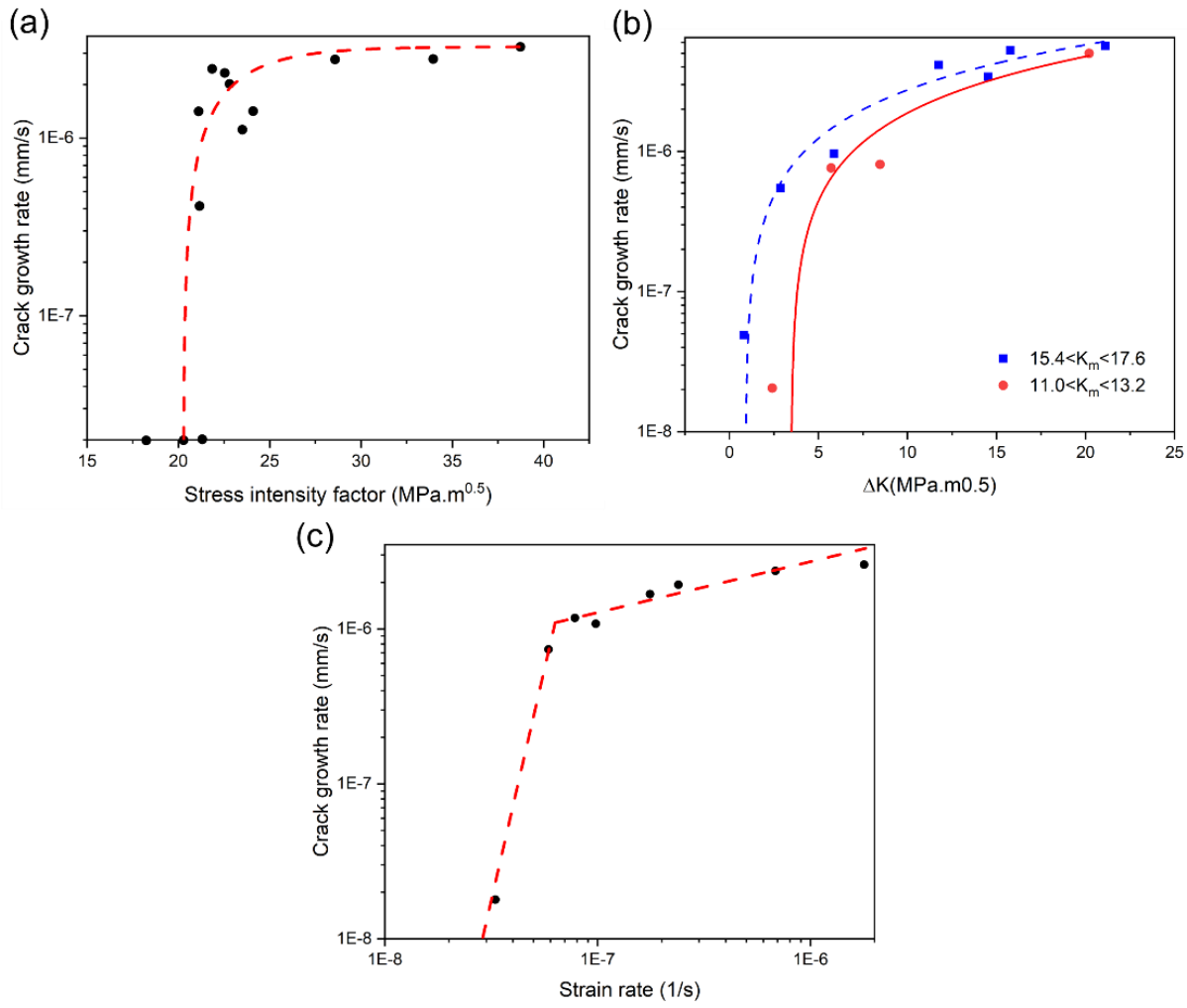

Figure 2.22. (a) threshold condition under static load (K_{ISCC}) [106], (b) ΔK_{th} condition under cyclic loading at different K_m and frequency of 0.19 Hz [106] (c) strain-rate threshold based on the applied strain rate to the bulk of pre-cracked specimens [74].

- **Critical Strain rate:** The minimum crack tip strain rate that provides a sustained film-free condition at the crack tip. Figure 2.22 (c) illustrates crack growth rate versus applied strain rate to the pre-cracked specimen [74]. As is evident, the crack growth rate increases significantly when the applied crack tip strain rate increases to about 10^{-7} (1/s). However, the crack tip strain rate (CTSR) can be different from the strain rate of the bulk pipe. It is worth mentioning that there is no existing direct correlation between the loading

parameters and the critical crack tip strain rate. Since the cracks are propagating through the grain boundaries, the ideal condition is to use critical strain rate threshold at the grain boundaries [57,63]. Such a critical crack tip strain rate or threshold grain boundary strain rate for HpHSCC has not been defined yet, although improved models for strain rate have been derived and will be discussed here.

2. 5. 2 Crack Propagation in Stage 2

Three different mechanisms can be contributing at the same time to cause crack advance at this stage. These mechanisms are elaborated below:

- **Anodic Dissolution Mechanism**

The primary crack growth mechanism at stage 2 is film rupture followed by anodic dissolution. At this stage, the mechanical driving force is strong enough to rupture the passive film at the crack tip and provides the condition that bare metal is exposed to the corrosive environment. The galvanic cell composed of cathode (passivated crack wall) and anode (bare metal at the crack tip) forms, and the crack propagates through localized anodic dissolution at the crack tip [23,27,108–110]. Anodic dissolution continues unless re-passivation occurs at the crack tip. Two possible conditions can be considered for this crack growth mechanism. First, continuous exposure of the crack tip to the corrosive environment, which is an extreme condition. Figure 2.23 (a) shows this condition where film formation at the crack tip is prohibited because of the severe loading conditions, and the crack tip is continuously exposed to a HpHSCC environment. Under this condition, the maximum crack growth rate (the upper boundary for HpHSCC) is calculated from Faraday's second law, as expressed in Equation 2.3 [31,74,110].

$$\text{Maximum crack growth rate} = i_a \frac{M}{zF\rho} \qquad \text{Eq'n. 2.3}$$

where M, Z, and ρ are atomic weight, valence and density of iron, respectively. The i_a represents anodic current density obtained by a fast scan rate potentiodynamic polarization test [26,27,57,109]. The fast scan rate potentiodynamic polarization test simulates the condition that film formation is being avoided [69,108,110,111].

The second condition is repeated formation and rupture of the passive film at the crack tip, as is shown in Figure 2.23 (b). Under this condition, crack tip dissolution is limited to the time interval between film rupture and subsequent re-passivation events. Therefore, competition between film formation and film rupturing mechanisms determines the crack growth rate. Strain rate is a multifaceted parameter that judges the competition between film formation and film rupture. Equation 2.4 is derived from Equation 2.3 to correlate the crack growth rate to strain rate. Based on Equation 2.4, the crack growth rate ($\dot{a}$) and crack tip strain rate ($\dot{\varepsilon}_{tip}$) follow a power-law relationship [27,108,109,112,113]. This power-law relation is evident in Figure 2.22 (c) at higher strain rates than the threshold value, although the crack tip strain rate can be different from the x-axis in this figure.

$$\dot{a} \approx \frac{1}{1-n}\frac{M}{zF\rho}\left(\frac{t_\circ}{\varepsilon_F}\right)^n i_a^* \dot{\varepsilon}_{tip}^{\,n} \qquad \text{Eq'n. 2.4}$$

In this equation, $t_\circ$, ε_F, i_a^*, and n are a critical time for anodic current density decaying from its peak value, fracture ductility of the passive film, peak current density immediately after the film rupture event, and exponent of transient current decay, respectively. $\dot{\varepsilon_{tip}}$ represents the crack tip strain rate, which provides the mechanical driving force to rupture the passive film during stage 2. $\dot{\varepsilon_{tip}}$varies with the loading parameters and geometry of the crack [114].

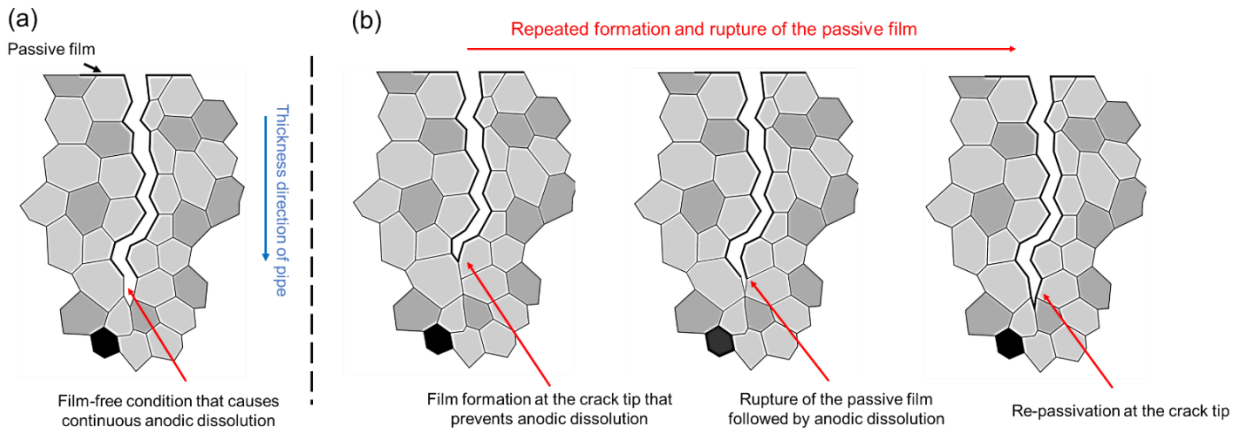

Figure 2.23. HpHSCC crack growth under the anodic dissolution mechanism (a) continuous exposure of the crack tip to a corrosive environment, (b) repeated formation and rupture of the passive film at the crack tip.

Considerable effort has been made to define a crack tip strain rate [31,108,114,115]. Most of the derived strain rate equations are applicable to either constant load or cyclic loading conditions. Therefore, they consider only the maximum load or load fluctuations. Additionally, the strain generated by crack advance is neglected in these expressions. In 2014, Lu derived Equation 2.5 that expresses the crack tip strain rate composed of two components *viz.* strain rate caused by crack tip movement ($\dot{\varepsilon}_a$) and strain rate generated by repeated crack tip open-closure ($\dot{\varepsilon}_K$). One of the merits of this equation is its applicability to both static loading and cyclic loading conditions.

$$\dot{\varepsilon}_{tip} = \dot{\varepsilon}_a + \dot{\varepsilon}_K = \frac{\dot{a}}{r_\circ}\frac{2N}{N-1}\frac{\beta\sigma_Y}{E}\left[\ln\left(\frac{K_m^2 - K_{ISCC}^2}{\pi r_\circ \sigma_Y^2}\right)\right]^{\frac{N+1}{N-1}} + \varepsilon_\circ f\left(\frac{1-R^*}{1+R^*}\right)^2\left(K_m^2 - K_{ISCC}^2\right) \quad \text{Eq'n. 2.5}$$

where $r_\circ$, N, β, σ_y, E, f, and ε_0 are specific length for crack tip strain rate calculation, strain-hardening coefficient, Rice's coefficient, yield strength, the elastic modulus of pipeline steel, frequency, and cyclic crack tip strain rate coefficient, respectively. R^* is an effective stress ratio and defined via Equation 2.6 [113].

$$R^* = \begin{cases} \dfrac{K_{\min}}{K_{\max}}; & K_{\min} \geq K_{ISCC} \\ \dfrac{K_{ISCC}}{K_{\max}}; & K_{\min} < K_{ISCC} < K_{\max} \end{cases}$$

Eq'n. 2.6

The strain rate proposed by Lu shows reasonable agreement with existing experimental data [27,108].

Once the crack tip is in a film-free condition, electrochemical parameters determine the dissolution rate. In other words, the strain rate determines how often the film-free condition forms and electrochemical parameters determine how fast dissolution occurs. Therefore, the electrochemical parameters in Equations 2.3 and 2. 4 must be considered. Figure 2.24 illustrates the dependency of intergranular crack growth rates to different environmental conditions. There is a potential range that leads to intergranular stress corrosion cracking. Under any given environmental condition (chemical composition and temperature), there is a specific potential that leads to the highest crack growth rate. Additionally, temperature not only widens the potential range for cracking, but also shifts it to more negative potentials. The changes in crack growth rates are directly related to the kinetics of anodic dissolution under the film-free condition [116].

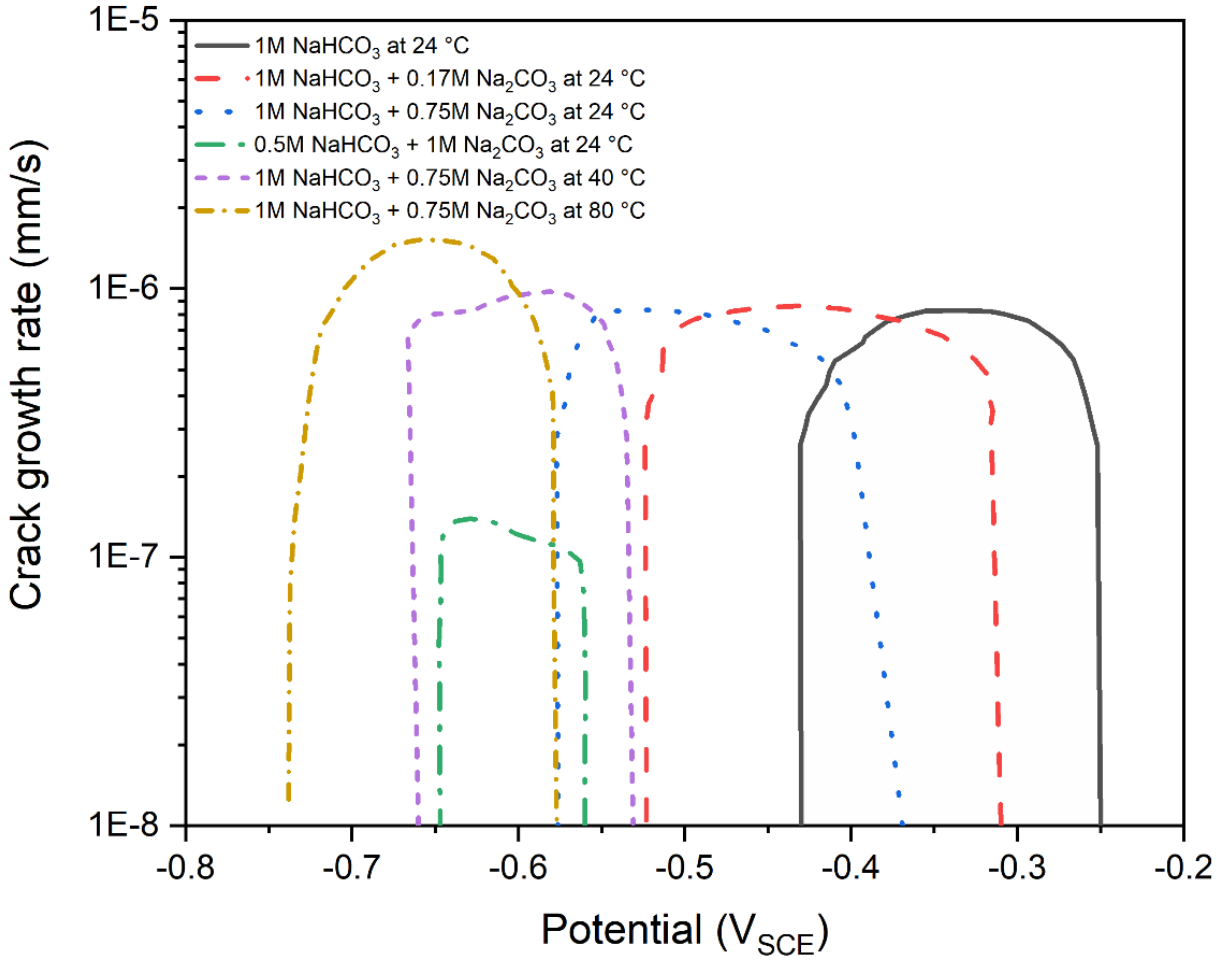

Figure 2.24. Variation of intergranular crack growth rates obtained from slow strain rate tests under different environmental conditions [116].

In addition to the environmental parameters, mechanical loading conditions as well as loading history influence the anodic current dissolution during the exposure of the pipeline steel to a HpHSCC environment. Figure 2.25 shows potentiodynamic polarization curves for stressed pipeline steel in high concentration carbonate-bicarbonate solutions. An increase in applied stress not only shifts the potentiodynamic curves to higher current density, but also narrows the passive potential range [34,47,117]. In the same manner, pre-strained pipeline steels show higher current density in a potentiodynamic polarization test in HpHSCC environment [118]. The changes in

electrochemical behaviour of pre-strained and/or stressed pipeline steels imply that the SCC-affected region, which experiences higher stress compared to bulk metal and localized plastic deformation, corrodes faster [34,47].

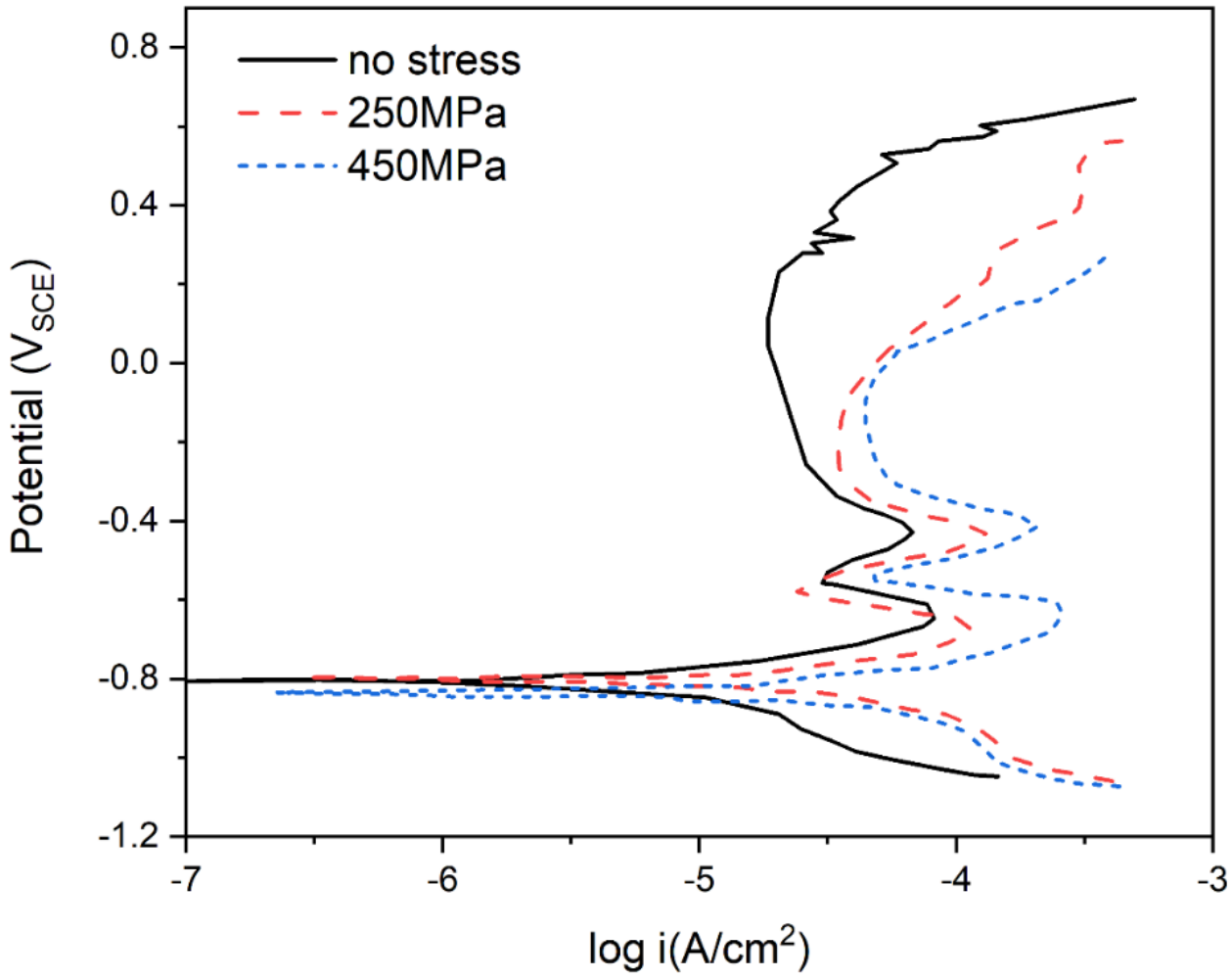

Figure 2.25. Potentiodynamic polarization curves of carbon steel in the carbonate-bicarbonate environment at different stress levels [117].

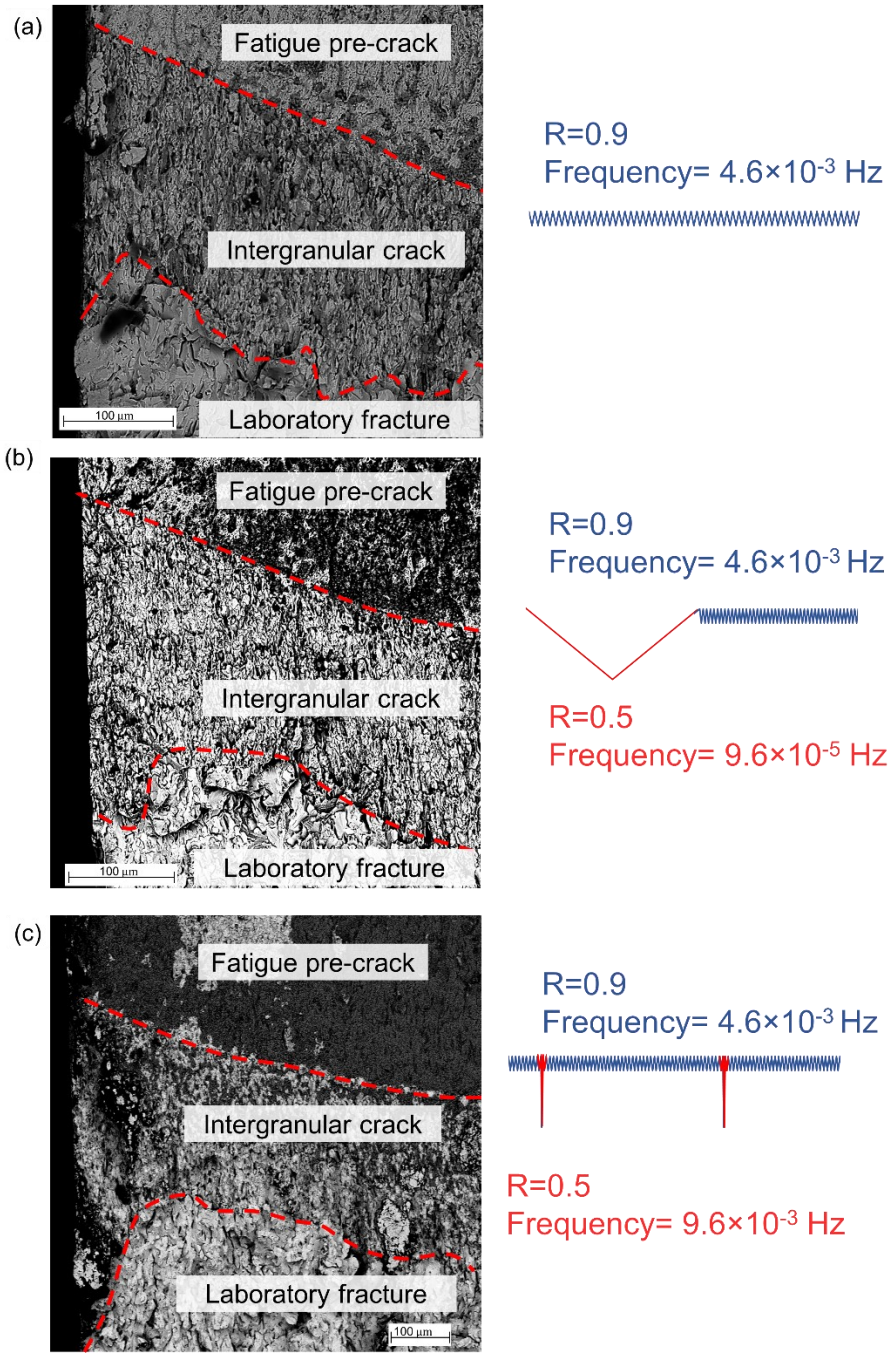

Figure 2.26. The fracture surface of CT specimens near the free surface under different loading condition containing an intergranular ribbon between transgranular fatigue pre-crack region and cleavage lab fracture (a) high *R*-ratio constant amplitude cycle, (b) variable amplitude containing low-frequency low *R*-ratio cycles, (C) variable amplitude containing high-frequency low *R*-ratio cycles [27].

- **Secondary Crack Nucleation and Crack Coalescence**

The secondary mechanism for crack propagation at this stage is nucleation of secondary cracks and coalescence with the main crack on the free surface of the pipes, similar to the crack behaviour in stage 1b. Figure 2.26 shows the area near the free surface of compact tension specimens exposed to an HpHSCC environment under three loading conditions [27]. This mechanism is sensitive to loading waveforms, and it is enhanced under variable amplitude loading conditions, in particular those containing high frequency low *R*-ratio cycles. These results imply that the low *R*-ratio cycles facilitate secondary crack nucleation ahead of the main crack tip. Therefore, the chance for crack coalescence increases on the free surface [27]. Similarly, to stage 1b, an increase in the surface length of the crack causes an increase in mechanical driving force at the depth tip. Additionally, the large crack coalescence on the free surface that can occur would cause a significant increase in the crack growth rate on the free surface tip as well as the depth tip [26,57].

- **Corrosion Fatigue Crack Propagation**

In addition to the above mechanisms, mechanical fatigue might contribute to crack propagation in stage 2. Considering the exposure of the pipe to the corrosive environment, the term "*corrosion fatigue*" might suit better for this mechanism. However, the contribution of this mechanism is always small because the load cycles are of such low frequency in pipeline steels, particularly in gas pipelines. The Paris' law shown in Equation 2.7 provides the crack growth caused by fatigue here. In this equation C, and n_F are the coefficient and exponent of the Paris equation, respectively. Lu derived Equation 2.7 from the Paris' law to express the contribution of fatigue in terms of crack growth per unit time. Accordingly, an increase in any of K_m, frequency, or amplitude of load fluctuation increases the contribution of corrosion fatigue at this stage. Therefore, this mechanism becomes more significant when K_m and ΔK increase as a result of crack advance during stage 2.

$$\text{Fatigue crack growth rate} = Cf\left(2\frac{1-R}{1+R}\right)^{n_F} K_m^{\,n_F} \qquad \text{Eq'n. 2.7}$$

2. 5. 3 Crack Propagation Path

From the above discussion, the main mechanism for HpHSCC crack growth is repeated formation and rupture of the passive film ahead of the crack tip, which causes cracks to propagate intergranularly. Cracks also can propagate through pearlite grains on the condition that the pearlite lamellae are parallel to the crack growth path [119]. It was initially hypothesized that segregation of different elements (in particular carbon, phosphorous, and sulphur) to the grain boundaries caused the more brittle passive film to form in this region. This hypothesis was made on the role of segregation in intergranular crack propagation in different material-environment systems [70,120,121]. However, this speculation was finally rejected as no solid evidence of significant segregation of alloying elements was ever found in different steels undergoing HpHSCC. In some cases, the alloying elements even increased the resistance of the steels towards HpHSCC crack formation [119,122–131]. In 2009, Afrin and Szpunar studied the grain boundary character and texture of the HpHSCC-cracked X65 pipeline steels in Canada. They found the preferential path of intergranular to be through high angle boundaries (HAB); whereas, low angle boundaries (LAB) and special coincident lattice site grain boundaries (CSL) ($\sum$11, $\sum$13b and probably $\sum$5) are statistically crack-resistant [9]. A similar study was conducted by Roccisano *et al.* on cracked X42 and X65 pipeline steels in 2020 that confirmed that most of the cracked grain boundaries were high angle grain boundaries both along and across the crack, as is shown in Figure 2.27. However, this study reported $\sum$3, $\sum$7, and $\sum$11 CSL are resistant to cracking [66]. It has been suggested that LAB and special CSL boundaries might arrest short cracks and cause dormancy [9,80]. It has been proposed that LAB and special CSL boundaries reduce the built-up strain energy in the boundaries

and are able to induce slip in adjacent grains. Therefore, plastic deformation becomes easier and the propensity for intergranular cracking decreases [132,133].

It has been shown that crystallographic texture affects intergranular stress corrosion cracking [4,9,66,134]. Roccisano *et al.* showed that cracking is more probable in the least dominant texture in both X46 and X65 steels [66]. Arafin and Szpunar found boundaries of {100}||rolling plane textured grains are more susceptible to HpHSCC [9]. Lavigne *et al.* corelated inclined intergranular crack propagation in the thickness direction with crystallographic texture, *i.e.,* the presence of shear texture that changed the local strain and deflected the crack [134].

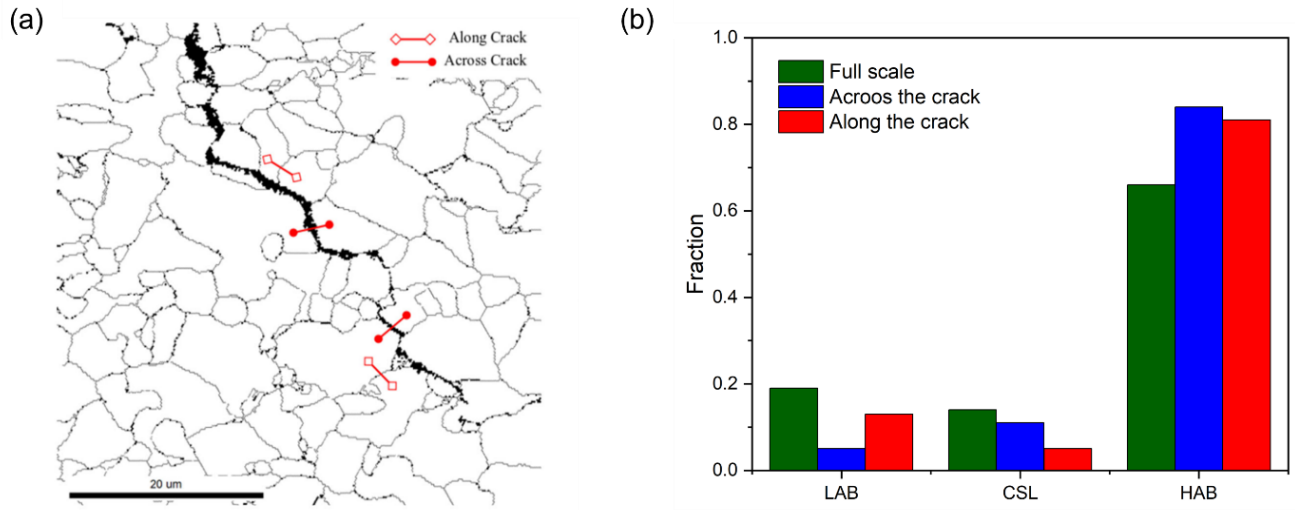

Figure 2.27. (a) Interactive misorientation along and across the crack in X65 pipeline steel, (b) analysis of the grain boundary characteristics along and across the cracks [66].

2. 6 stage 3: Rapid Crack Growth

Stage 3 of HpHSCC crack propagation is short and has no engineering significance except that it must be avoided. The cracked pipeline must be repaired or replaced before the onset of stage 3. At the end of stage 3, rapid crack propagation yields to either rupture or leakage for low and high fracture toughness, respectively [135].

2. 7 Review of HpHSCC from a Mechanistic Viewpoint

As soon as the environmental conditions for HpHSCC are established, shallow cracks nucleate at multiple spots and coalesce (stage 1) to form stage-2 critical cracks that cause sustainable crack growth during stage 2. As the crack propagates, the geometrical crack evolution increases the mechanical driving force at the depth tip of the crack, *i.e., K* in the case of static load and ΔK in the case of cyclic loading (see Figure 2.21). Figure 2.28 shows the crack growth velocity versus mechanical driving force under static loading (red dashed line) and cyclic loading (blue dotted line) conditions. Crack growth during stage 1 is stochastic, and cracks experience periods of dormancy and propagation. Therefore, the overall crack growth rate seems to be uncorrelated to K and ΔK as the crack growth rate decreases with an increase in the mechanical driving force. However, the instantaneous crack growth rate might increase when two nearby cracks coalesce increasing the stress intensity factors for both cracks. Regardless of the type of loading, stage 1 largely controls the lifetime of the pipeline, while sustainable crack propagation occurs above the threshold value for stage 2. Stage 1 is shorter under cyclic loading conditions for three reasons. First, cyclic loading assists the crack nucleation (see Figure 2.8 and Figure 2.17). Subsequently, more chance for crack coalescence is expected under cyclic loading condition. Additionally, the crack growth rates under variable amplitude conditions show that the low R-ratio cycles enhance the crack growth during stage 1. Secondly, threshold for stage 2 is a function of loading conditions. The threshold for stage 2 of HpHSCC could be defined as the condition when the maximum stress intensity factor exceeds K_{ISCC} (under constant loading condition) or the maximum ΔK exceeds ΔK_{th} (under cyclic loading condition). At the onset of stage 2, the crack propagation rate under static load (where $K > K_{\mathrm{ISCC}}$) is higher compared to that in the cyclic loading condition (where $\Delta K > \Delta K_{\mathrm{th}}$). With an increase in time, the crack propagation rate under cyclic loading conditions increases

probably because of more contribution of metal fatigue (increase in K_m and ΔK in the Paris Law equation). Crack propagation at this stage is directly related to strain rate at the crack tip and can be formulized by linear-elastic-fracture-mechanics (LEFM) parameters such as K and ΔK. Therefore, the crack growth rate increases as the mechanical driving force (either K or ΔK) increases. Equation 2.8 is a superposition model that can be used for HpHSCC crack growth behaviour.

$$\frac{da}{dt} = \left(\frac{da}{dt}\right)_{stage1} + \left(\frac{da}{dt}\right)_{stage2-SCC} + \frac{1}{f}\left(\frac{da}{dN}\right)_{stage2-CF} \qquad \text{Eq'n. 2.8}$$

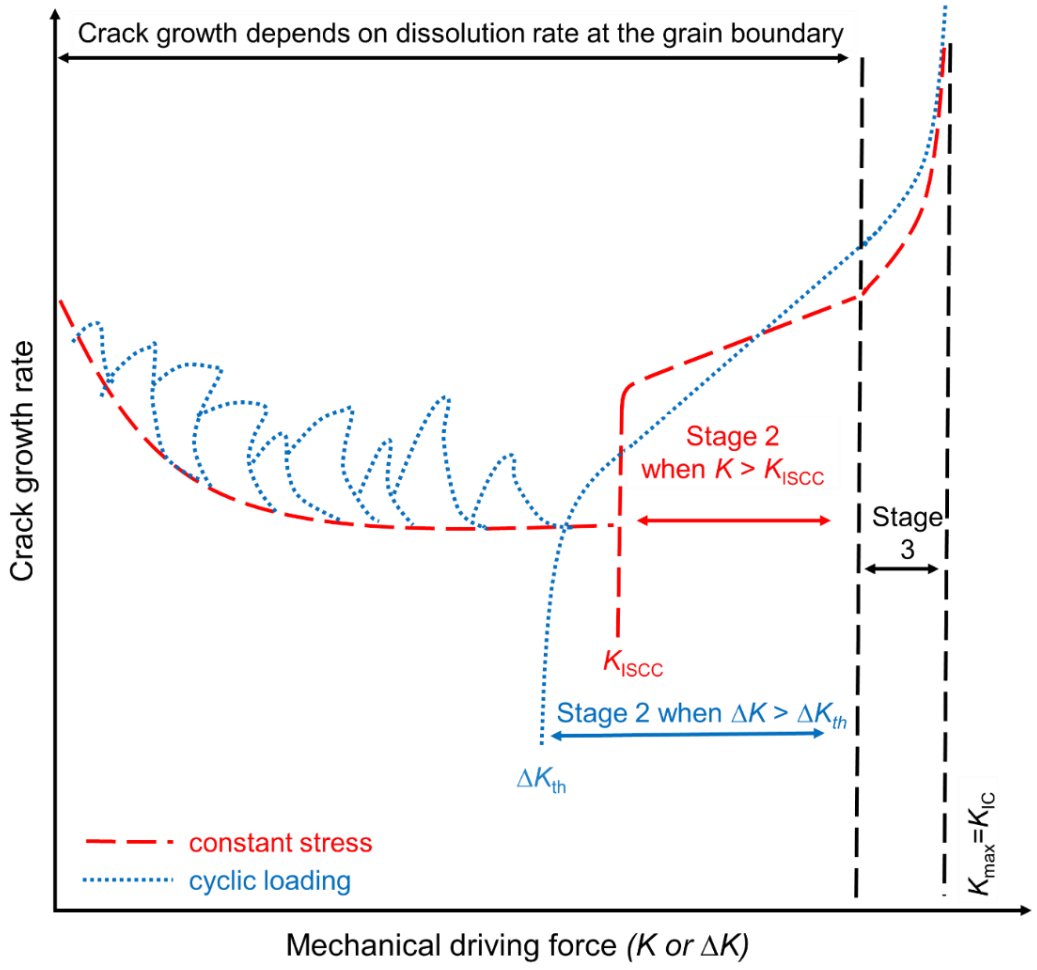

Figure 2.28. The HpHSCC crack growth rate versus mechanical driving force at the depth tip of crack (either K or ΔK) [57].

In this equation, $(da/dt)_{stage1}$ represents the crack growth mechanisms in stage 1, $(da/dt)_{stage\ 2\text{-}SCC}$ stands for crack growth caused by the anodic dissolution mechanism, $(da/dN)_{stage2\text{-}CF}$ is the contribution of corrosion fatigue at stage 2. Equations 2.3 and 2.7 express $(da/dt)_{\text{stage 2-SCC}}$ and $(da/dN)_{stage2\text{-}CF}$, respectively and are able to correlate stage 2 of crack growth rate to the fracture mechanics' parameters. However, the correlation between loading parameters and crack growth at stage 1 still remains unclear, as will be discussed in the following section.

2. 8 Gaps in Knowledge about HpHSCC

Although considerable research has been conducted related to HpHSCC in pipeline steels, there are some facets of the phenomenon that remain either unknown or imperfect.

- The mechanisms for crack initiation remain to be clarified. In particular, the threshold value for HpHSCC crack initiation is determined through either constant amplitude cyclic loading or static loading conditions. Under these conditions, the load-history-dependent phenomena in the steel have been neglected. Variable amplitude loading conditions might change the threshold for HpHSCC crack initiation. Additionally, experimental and/or numerical simulations are needed to understand the phenomena that cause a decreasing growth rate trend in the early stage crack growth rate profile. It would be advantageous to know exactly why cracks slow down and under what conditions their growth continues.
- The lifetime of pipelines susceptible to HpHSCC is limited by the onset of stage 2. *Ergo*, it is of paramount importance to understand the conditions that can cause a state of dormancy of crack propagation in order to delay stage 2 and increase the lifespan of the pipeline. To date, most of the attempts of modelling HpHSCC have paid more attention to stage 2. The correlation between crack growth mechanisms in stage 1 and mechanical loading conditions has remained unclear. In the bathtub model, it has been assumed that

crack nucleation is a random process that happens at multiple sites with different sensitivities to crack initiation with regards to hoop stress. Accordingly, the interaction between the stress fields of nearby cracks' tips causes crack coalescence. However, there are some preferred regions for secondary-crack initiation (see Figure 2.18), and the details of the interaction between the stress fields of the cracks remain unclear. The preliminary results (Figure 2.20) show that the interaction between underload cycles and minor cycles accelerate crack propagation at stage 1b and causes early onset of stage 2. Further experimental investigations are needed to correlate the stage 1b crack growth rate to the loading conditions. An interactive approach that considers time-dependent phenomena and load-history-related phenomena should be adopted for stage 1b to determine how to delay the onset of stage 2.

- Once the crack geometry evolution becomes clear for stage 1b, a more accurate definition of a threshold value for stage 2 will be available. This would certainly make a great contribution to the lifetime modelling of HpHSCC in buried pipelines.
- There is limited information about HpHSCC crack growth behaviour under variable amplitude loading conditions in stage 2. More experimental research is needed to improve the modelling of the HpHSCC for this stage. The number of available papers that link the crack growth path to grain boundary character in the case of steel pipelines are limited. Few available papers are case studies that report failure analysis and field observation rather than systematic studies in the context of anodic dissolution mechanism. Further investigations are needed to determine whether film formation or film rupture are affected at the HAB. The results of such investigations could play a crucial role in developing alloys more resistant to HpHSCC.

References

[1] F. Song, Predicting the Effect of Soil Seasonal Change on Stress Corrosion Cracking Susceptibility of Buried Pipelines at High Ph, NACE Int. - Conf. Expo. 35 (2015) 1–27.

[2] S.A. Shipilov, I. Le May, Structural integrity of ageing buried pipelines having cathodic protection, Eng. Fail. Anal. 13 (2006) 1159–1176. doi:https://doi.org/10.1016/j.engfailanal.2005.07.008.

[3] B. Saleem, F. Ahmed, M.A. Rafiq, M. Ajmal, L. Ali, Stress corrosion failure of an X52 grade gas pipeline, Eng. Fail. Anal. 46 (2014) 157–165. doi:10.1016/j.engfailanal.2014.08.011.

[4] O. Lavigne, E. Gamboa, W. Costin, M. Law, V. Luzin, V. Linton, Microstructural and mechanical factors influencing high pH stress corrosion cracking susceptibility of low carbon line pipe steel, Eng. Fail. Anal. 45 (2014) 283–291. doi:10.1016/j.engfailanal.2014.07.011.

[5] A.D. Batte, R.R. Fessler, J.E. Marr, S.C. Rapp, Managing the Threat of SCC in Gas Transmission Pipelines, (2012) 379–388. doi:10.1115/IPC2012-90231.

[6] I. V Ryakhovskikh, R.I. Bogdanov, V.E. Ignatenko, Intergranular stress corrosion cracking of steel gas pipelines in weak alkaline soil electrolytes, Eng. Fail. Anal. 94 (2018) 87–95. doi:https://doi.org/10.1016/j.engfailanal.2018.07.036.

[7] R. Sutherby, W. Chen, Deflected Stress Corrosion Cracks in the Pipeline Steel, (2004) 113–121.

[8] I. Černý, V. Linhart, An evaluation of the resistance of pipeline steels to initiation and early growth of stress corrosion cracks, Eng. Fract. Mech. 71 (2004) 913–921. doi:https://doi.org/10.1016/S0013-7944(03)00011-0.

[9] M.A. Arafin, J.A. Szpunar, A new understanding of intergranular stress corrosion cracking resistance of pipeline steel through grain boundary character and crystallographic texture studies, Corros. Sci. 51 (2009) 119–128. doi:https://doi.org/10.1016/j.corsci.2008.10.006.

[10] O. Lavigne, E. Gamboa, J. Griggs, V. Luzin, M. Law, A. Roccisano, High-pH inclined stress corrosion cracking in Australian and Canadian gas pipeline X65 steels, Mater. Sci. Technol. 32 (2016) 684–690. doi:10.1080/02670836.2015.1132030.

[11] E. Sadeghi Meresht, T. Shahrabi Farahani, J. Neshati, Failure analysis of stress corrosion cracking occurred in a gas transmission steel pipeline, Eng. Fail. Anal. 18 (2011) 963–970. doi:https://doi.org/10.1016/j.engfailanal.2010.11.014.

[12] S.S. Abedi, A. Abdolmaleki, N. Adibi, Failure analysis of SCC and SRB induced cracking of a transmission oil products pipeline, Eng. Fail. Anal. 14 (2007) 250–261. doi:https://doi.org/10.1016/j.engfailanal.2005.07.024.

[13] C. Manfredi, J.L. Otegui, Failures by SCC in buried pipelines, Eng. Fail. Anal. 9 (2002) 495–509. doi:https://doi.org/10.1016/S1350-6307(01)00032-2.

[14] P.J. Kentish, Influence of surface characteristics on the stress corrosion cracking resistance of steel gas pipelines, University of South Australia, 2007.

[15] I. Cerny, D. Mikulova, P. Novak, Conditions of Stress Corrosion Crack Growth and Retardation in X70 Steel in Carbonate Environments, Commun. - Sci. Lett. Univ. Zilina. 12 (2010). http://komunikacie.uniza.sk/index.php/communications/article/view/968.

[16] T.J. Barlo, Field Investigation of Stress Corrosion Cracking, in: 5th Symp. Line Pipe Res. Am. Gas Assoc. InC, Arlington, 1974: p. T1.

[17] B.Y. Fang, A. Atrens, J.Q. Wang, E.H. Han, Z.Y. Zhu, W. Ke, Review of stress corrosion cracking of pipeline steels in “low” and “high” pH solutions, J. Mater. Sci. 38 (2003) 127–132. doi:10.1023/A:1021126202539.

[18] F. King, Development of Guidelines for Identification of SCC Sites and Estimation of Re-inspection Intervals for SCC Direct Assessment, 2010.

[19] R. Norsworthy, Coatings Used In Conjunction With Cathodic Protection Shielding Vs Non-Shielding Pipeline Coatings, (n.d.).

[20] T.R. Jack, K. Krist, B. Erno, R.R. Fessler, Generation of Near Neutral pH and High pH SCC Environments on Buried Pipelines, (n.d.).

[21] F. King, T. Jack, M. Kolar, R. Worthingham, A Permeable Coating Model for Predicting the Environment at the Pipe Surface Under CP-Compatible Coatings, (2004) 175–181.

[22] M. Wilmott, B. Erno, T. Jack, R. Worthingham, The Role of Coatings in the Development of Corrosion and Stress Corrosion Cracking on Gas Transmission Pipelines, (1998) 399–408. doi:10.1115/IPC1998-2048.

[23] R.N. Parkins, Stress Corrosion Cracking of Pipelines - Its Control or Prevention, Corros. 96. (1996) 12. https://doi.org/.

[24] B.N. Leis, Initiation of SCC on Gas Transmission Pipelines in Related Cracking Environments, Corros. 96. (1996) 18. https://doi.org/.

[25] L.J. Zadow, Characterisation of the morphology of inclined SCC cracks in Australian gas pipelines., (2014).

[26] R.N. Parkins, 1990 Plenary Lecture: Strain Rate Effects in Stress Corrosion Cracking, Corrosion. 46 (1990) 178–189.

[27] H. Niazi, K. Chevil, E. Gamboa, L. Lamborn, W. Chen, H. Zhang, Effects of Loading Spectra on High pH Crack Growth Behaviour of X65 Pipeline Steel, CORROSION. (2020). doi:10.5006/3472.

[28] J. a. Beavers, B. a. Harle, Mechanisms of High-pH and Near-Neutral-pH SCC of Underground Pipelines, J. Offshore Mech. Arct. Eng. 123 (2001) 147. doi:10.1115/1.1376716.

[29] J.A. Beavers, Integrity management of natural gas and petroleum pipelines subject to stress corrosion cracking, Corrosion. 70 (2014) 3–18. doi:10.5006/0998.

[30] J. Beavers, T.A. Bubenik, 12 - Stress corrosion cracking, in: A.M.B.T.-T. in O. and G.C.R. and T. El-Sherik (Ed.), Woodhead Publ. Ser. Energy, Woodhead Publishing, Boston, 2017: pp. 295–314. doi:https://doi.org/10.1016/B978-0-08-101105-8.00012-7.

[31] R.N. Parkins, Current Topics in Corrosion: Factors Influencing Stress Corrosion Crack Growth Kinetics, CORROSION. 43 (1987) 130–139. doi:10.5006/1.3583125.

[32] R.N. Parkins, The Controlling Parameters In Stress Corrosion Cracking, in 5th Symp. Line Pipe Res., Arlington, 1974: pp. U1–U40.

[33] R.N. Parkins, A Review of Stress Corrosion Cracking of High-Pressure Gas Pipelines, Corros. 2000. (2000) 23. https://doi.org/.

[34] Y.F. Cheng, R. Norsworthy, Pipeline Coatings, (2016).

[35] J.A. Beavers, C.L. Durr, B.S. Delanty, High-pH SCC: Temperature and Potential Dependence for Cracking in Field Environments, (1998) 423–437.

[36] J.A. Beavers, R.G. Worthingham, The Influence of Soil Chemistry on SCC of Underground Pipelines, (2002) 1671–1678.

[37] R.N. Parkins, C.S. O'dell, R.R. Fessler, Factors affecting the potential of galvanostatically polarised pipeline steel in relation to SCC in CO_3^{2-}—$HCO3^-$ solutions, Corros. Sci. 24 (1984) 343–374. doi:http://dx.doi.org/10.1016/0010-938X(84)90018-0.

[38] Z. Abbasi, H. Niazi, M. Abdolrazzaghi, W. Chen, M. Daneshmand, Monitoring pH Level Using High-Resolution Microwave Sensor for Mitigation of Stress Corrosion in Steel Pipelines, IEEE Sens. J. (2020) 1. doi:10.1109/JSEN.2020.2978086.

[39] G.I. Ogundele, W.E. White, Some Observations on Corrosion of Carbon Steel in Aqueous Environments Containing Carbon Dioxide, CORROSION. 42 (1986) 71–78. doi:10.5006/1.3584888.

[40] G.I. Ogundele, W.E. White, Observations on the Influences of Dissolved Hydrocarbon Gases and Variable Water Chemistries on Corrosion of an API-L80 Steel, CORROSION. 43 (1987) 665–673. doi:10.5006/1.3583847.

[41] J.A. Beavers, N.G. Thompson, External Corrosion of Oil and Natural Gas Pipelines, ASM Handb. 13C (2006) 1015–1026. doi:10.1361/asmhba0004213.

[42] L. Yan, R. Worthingham, F. King, J. Been, Factors Affecting the Generation of High-pH Environments Required for Stress Corrosion Cracking (SCC), (2012) 511–524.

[43] H. Hikita, S. Asai, T. Takatsuka, Absorption of carbon dioxide into aqueous sodium hydroxide and sodium carbonate-bicarbonate solutions, Chem. Eng. J. 11 (1976) 131–141. doi:https://doi.org/10.1016/S0300-9467(76)80035-4.

[44] J.A. Beavers, B.A. Harle, Ipc1996-18 60, (1996).

[45] E.A. Charles, R.N. Parkins, Generation of Stress Corrosion Cracking Environments at Pipeline Surfaces, (1995).

[46] F. Xie, D. Wang, C. Yu, Y. Zong, M. Wu, Effect of HCO^{3-} Concentration on the Corrosion Behaviour of X80 Pipeline Steel in Simulated Soil Solution, 12 (2017) 9565–9574. doi:10.20964/2017.10.42.

[47] A.Q. Fu, Y.F. Cheng, Electrochemical polarization behaviour of X70 steel in thin carbonate/bicarbonate solution layers trapped under a disbonded coating and its implication on pipeline SCC, Corros. Sci. 52 (2010) 2511–2518. doi:http://dx.doi.org/10.1016/j.corsci.2010.03.019.

[48] R. Brousseau, S. Qian, Distribution of Steady-State Cathodic Currents Underneath a Disbonded Coating, CORROSION. 50 (1994) 907–911. doi:10.5006/1.3293481.

[49] R.R. Fessler, A.J. Markworth, R.N. Parkins, Cathodic Protection Levels under Disbonded Coatings, CORROSION. 39 (1983) 20–25. doi:10.5006/1.3580809.

[50] Effects Of Anodic Protection On SCC Behaviour Of X80 Pipeline Steel In High-pH Carbonate-Bicarbonate Solution, Arch. Metall. Mater.. 60 (2015) 1009. doi:10.1515/amm-2015-0251.

[51] S. Longfei, L. Zhiyong, L. Xiaogang, D. Cuiwei, Stress Corrosion Cracking of Simulated Weld Heat-Affected Zone on X100 Pipeline Steel in Carbonate/Bicarbonate Solution, J. Mater. Eng. Perform. 29 (2020) 2574–2585. doi:10.1007/s11665-020-04750-9.

[52] M. Zhu, C. Du, X. Li, Z. Liu, S. Wang, J. Li, D. Zhang, Effect of AC current density on stress corrosion cracking behaviour of X80 pipeline steel in high pH carbonate/bicarbonate solution, Electrochim. Acta. 117 (2014) 351–359. doi:https://doi.org/10.1016/j.electacta.2013.11.149.

[53] M. Zhu, G. Ou, H. Jin, C. Du, X. Li, Z. Liu, Influence of AC waveforms on stress corrosion cracking behaviour of pipeline steel in high pH solution, Corros. Eng. Sci. Technol. 51 (2016) 18–24. doi:10.1179/1743278215Y.0000000028.

[54] N.E. Board, Stress corrosion cracking on Canadian oil and gas pipelines, Natl. Energy Board, Calgary, Alberta. (1996).

[55] J. Been, F. King, L. Fenyvesi, R. Sutherby, A Modelling Approach to High pH Environmentally Assisted Cracking, (2004) 83–100. doi:10.1115/IPC2004-0361.

[56] W. Chen, An Overview of Near-Neutral pH Stress Corrosion Cracking in Pipelines and Mitigation Strategies for Its Initiation and Growth, CORROSION. 72 (2016) 962–977. doi:10.5006/1967.

[57] W. Chen, 30 - Modelling and prediction of stress corrosion cracking of pipeline steels A2 - El-Sherik, A.M. BT - Trends in Oil and Gas Corrosion Research and Technologies, in: Woodhead Publ. Ser. Energy, Woodhead Publishing, Boston, 2017: pp. 707–748. doi:https://doi.org/10.1016/B978-0-08-101105-8.00030-9.

[58] Z. Jiaxi, C. Karina, Y. Mengshan, B. Jenny, K. Sean, V.B. Greg, K. Richard, C. Weixing, Statistical Analysis on Underload-Type Pipeline Spectra, J. Pipeline Syst. Eng. Pract. 7 (2016) 4016007. doi:10.1061/(ASCE)PS.1949-1204.0000241.

[59] W. Chen, S.-H. Wang, R. Chu, F. King, T.R. Jack, R.R. Fessler, Effect of precyclic loading on stress-corrosion-cracking initiation in an X-65 pipeline steel exposed to near-neutral pH soil environment, Metall. Mater. Trans. A. 34 (2003) 2601–2608. doi:10.1007/s11661-003-0019-y.

[60] R.N. Parkins, E. Belhimer, W.K. Blanchard, Stress Corrosion Cracking Characteristics of a Range of Pipeline Steels in Carbonate-Bicarbonate Solution, CORROSION. 49 (1993) 951–966. doi:10.5006/1.3316023.

[61] S.-H. Wang, W. Chen, F. King, T.R. Jack, R.R. Fessler, Precyclic-Loading-Induced Stress Corrosion Cracking of Pipeline Steels in a Near-Neutral-pH Soil Environment, CORROSION. 58 (2002) 526–534. doi:10.5006/1.3277644.

[62] E. Gamboa, M. Giuliani, O. Lavigne, X-ray microtomography observation of subsurface stress corrosion crack interactions in a pipeline low carbon steel, Scr. Mater. 81 (2014) 1–3. doi:http://dx.doi.org/10.1016/j.scriptamat.2014.01.038.

[63] G. J., G. E., L. O., A review of modelling high pH stress corrosion cracking of high pressure gas pipelines, Mater. Corros. 67 (2015) 251–263. doi:10.1002/maco.201508454.

[64] H. Asahi, T. Kushida, M. Kimura, H. Fukai, S. Okano, Role of Microstructures on Stress Corrosion Cracking of Pipeline Steels in Carbonate-Bicarbonate Solution, CORROSION. 55 (1999) 644–652. doi:10.5006/1.3284018.

[65] J. Kuniya, H. Anzai, I. Masaoka, Effect of MnS Inclusions on Stress Corrosion Cracking in Low-Alloy Steels, CORROSION. 48 (1992) 419–425. doi:10.5006/1.3315955.

[66] A. Roccisano, S. Nafisi, R. Ghomashchi, Stress Corrosion Cracking Observed in Ex-service Gas Pipelines: A Comprehensive Study, Metall. Mater. Trans. A. 51 (2020) 167–188. doi:10.1007/s11661-019-05496-3.

[67] R.N. Parkins, Localized corrosion and crack initiation, Mater. Sci. Eng. A. 103 (1988) 143–156. doi:https://doi.org/10.1016/0025-5416(88)90562-9.

[68] F. Hasan, J. Iqbal, F. Ahmed, Stress corrosion failure of high-pressure gas pipeline, Eng. Fail. Anal. 14 (2007) 801–809. doi:https://doi.org/10.1016/j.engfailanal.2006.11.002.

[69] R.N. Parkins, S. Zhou, The stress corrosion cracking of C-Mn steel in CO2-HCO3 −CO32 − solutions. II: Electrochemical and other data, Corros. Sci. 39 (1997) 175–191. doi:http://dx.doi.org/10.1016/S0010-938X(97)89248-7.

[70] J. Might, D.J. Duquette, Stress Corrosion Cracking of High-Purity Carbon Steel in Carbonate Solutions, CORROSION. 52 (1996) 428–434. doi:10.5006/1.3292130.

[71] T. Tanupabrungsun, D. Young, B. Brown, S. Nešic, Construction And Verification of Pourbaix Diagrams For CO2 Corrosion of Mild Steel Valid Up to 250°C, Corros. 2012. (2012).

[72] R.N. Parkins, Mechanistic Aspects of Intergranular Stress Corrosion Cracking of Ferritic Steels, CORROSION. 52 (1996) 363–374. doi:10.5006/1.3292124.

[73] M.H. R. R. Fessler, A. D. Batte, INTEGRITY MANAGEMENT OF STRESS CORROSION CRACKING IN GAS PIPELINE, ASME Stnadards Technology, LLC, New York, 2008.

[74] R.N. Parkins, The application of stress corrosion crack growth kinetics to predicting lifetimes of structures, Corros. Sci. 29 (1989) 1019–1038. doi:https://doi.org/10.1016/0010-938X(89)90091-7.

[75] R. Fessler, T.D. Using, Threshold-Stress Determination Using Tapered Specimens and Cyclic Stresses, (1984) 368–382.

[76] J.A. Beavers, J.T. Johnson, R.L. Sutherby, Materials Factors Influencing the Initiation of Near-Neutral pH SCC on Underground Pipelines, (2000). doi:10.1115/IPC2000-221.

[77] G. Van Boven, W. Chen, R. Rogge, The role of residual stress in neutral pH stress corrosion cracking of pipeline steels. Part I: Pitting and cracking occurrence, Acta Mater. 55 (2007) 29–42. doi:https://doi.org/10.1016/j.actamat.2006.08.037.

[78] T.K. Beavers, R.N. Christman, J.A. Parkins, Some effects of surface condition on the stress corrosion cracking of line pipe steel, in: Corros. 87, San Francisco, 1987.

[79] T.K. Christman, Relationships Between Pitting, Stress, and Stress Corrosion Cracking of Line Pipe Steels, CORROSION. 46 (1990) 450–453. doi:10.5006/1.3585131.

[80] R. Pourazizi, M.A. Mohtadi-Bonab, J.A. Szpunar, Investigation of different failure modes in oil and natural gas pipeline steels, Eng. Fail. Anal. 109 (2020) 104400. doi:https://doi.org/10.1016/j.engfailanal.2020.104400.

[81] P. Kentish, Stress corrosion cracking of gas pipelines – Effect of surface roughness, orientations and flattening, Corros. Sci. 49 (2007) 2521–2533. doi:https://doi.org/10.1016/j.corsci.2006.12.014.

[82] Z.F. Wang, A. Atrens, Initiation of stress corrosion cracking for pipeline steels in a carbonate-bicarbonate solution, Metall. Mater. Trans. A. 27 (1996) 2686–2691. doi:10.1007/BF02652362.

[83] T.N. Baker, Microalloyed steels, Ironmak. Steelmak. 43 (2016) 264–307. doi:10.1179/1743281215Y.0000000063.

[84] C.J. Villalobos, A. Del-Pozo, B. Campillo, J. Mayen, S. Serna, Microalloyed Steels through History until 2018: Review of Chemical Composition, Processing and Hydrogen Service, Met. . 8 (2018). doi:10.3390/met8050351.

[85] M.-Y. Seok, I.-C. Choi, J. Moon, S. Kim, U. Ramamurty, J. Jang, Estimation of the Hall–Petch strengthening coefficient of steels through nanoindentation, Scr. Mater. 87 (2014) 49–52. doi:https://doi.org/10.1016/j.scriptamat.2014.05.004.

[86] V. Carretero Olalla, V. Bliznuk, N. Sanchez, P. Thibaux, L.A.I. Kestens, R.H. Petrov, Analysis of the strengthening mechanisms in pipeline steels as a function of the hot rolling parameters, Mater. Sci. Eng. A. 604 (2014) 46–56. doi:https://doi.org/10.1016/j.msea.2014.02.066.

[87] D. Arola, C.L. Williams, Estimating the fatigue stress concentration factor of machined surfaces, Int. J. Fatigue. 24 (2002) 923–930. doi:https://doi.org/10.1016/S0142-1123(02)00012-9.

[88] L.I.U.Z. ZHU Min DU Cuiwei, LI Xiaogang, LI Jiankuan, LI Qiong, JIA Jinghuan, Stress corrosion cracking behaviour and mechanism of x65 and x80 pipeline steels in high ph solution, Acta Met. Sin. 49 (n.d.) 1590–1596. https://www.ams.org.cn.

[89] M. Zhu, C. Du, X. Li, Z. Liu, S. Wang, T. Zhao, J. Jia, Effect of Strength and Microstructure on Stress Corrosion Cracking Behaviour and Mechanism of X80 Pipeline Steel in

High pH Carbonate/Bicarbonate Solution, J. Mater. Eng. Perform. 23 (2014) 1358–1365. doi:10.1007/s11665-014-0880-4.

[90] H. Niazi, H. Zhang, L. Lamborn, W. Chen, THE IMPACT OF PRESSURE FLUCTUATIONS ON THE EARLY ONSET OF STAGE II GROWTH OF HIGH PH STRESS CORROSION CRACK, in: Proc. 14th Int. Pipeline Conf. IPC2020, ASME, 2020.

[91] T.R. Baker, R.N. Parkins, G.G. Rochfort, Investigations Relating to Stress Corrosion Cracking on the Pipeline Authority's Moomba-to-Sydney Pipeline, in: Proc. 7th Symp. Line Pipe Res. Cat., 1986: pp. 21–27.

[92] B.N. Leis, SOME ASPECTS OF STRESS-CORROSION-CRACKING ANALYSIS FOR GAS TRANSMISSION PIPELINES, in: R.W. Revie, V.S. Sastri, M. Elboujdaini, E. Ghali, D.L. Piron, P.R. Roberge, P.B.T.-M.P.M. Mayer (Eds.), Proc. Metall. Soc. Can. Inst. Min. Metall., Pergamon, Oxford, 1991: pp. 107–121. doi:https://doi.org/10.1016/B978-0-08-041441-6.50014-X.

[93] W. Chen, H. Zhu, S.-H. Wang, Low Temperature Creep Behaviour of Pipeline Steels, Can. Metall. Q. 48 (2009) 271–283. doi:10.1179/cmq.2009.48.3.271.

[94] J.T. Evans, R.N. Parkins, Creep induced by load cycling in a C-Mn steel, Acta Metall. 24 (1976) 511–515. doi:http://dx.doi.org/10.1016/0001-6160(76)90094-8.

[95] R.N. Parkins, P.M. Singh, Stress Corrosion Crack Coalescence, CORROSION. 46 (1990) 485–499. doi:10.5006/1.3585136.

[96] W. Y.-Z., A.J. D., A. R., P.R. N., CRACK INTERACTION, COALESCENCE AND MIXED MODE FRACTURE MECHANICS, Fatigue Fract. Eng. Mater. Struct. 19 (1996) 51–63. doi:10.1111/j.1460-2695.1996.tb00931.x.

[97] M. Elboujdaini, R.W. Revie, Metallurgical factors in stress corrosion cracking (SCC) and hydrogen-induced cracking (HIC), J. Solid State Electrochem. 13 (2009) 1091–1099. doi:10.1007/s10008-009-0799-0.

[98] S. Wang, H. Niazi, L. Lamborn, W. Chen, Strain-shock-induced early stage high pH stress corrosion crack initiation and growth of pipeline steels, Corros. Sci. (2020).

[99] M. Skorupa, Load interaction effects during fatigue crack growth under variable amplitude loading—a literature review. Part I: empirical trends, Fatigue Fract. Eng. Mater. Struct. 21 (1998) 987–1006.

[100] M. Skorupa, Load interaction effects during fatigue crack growth under variable amplitude loading—a literature review. Part II: qualitative interpretation, Fatigue Fract. Eng. Mater. Struct. 22 (1999) 905–926.

[101] J. Zhao, W. Chen, S. Keane, J. Been, G. Van Boven, Development and validation of load-interaction based models for crack growth prediction, in: Int. Pipeline Conf., American Society of Mechanical Engineers, 2014: p. V002T06A077.

[102] M. Yu, X. Xing, H. Zhang, J. Zhao, R. Eadie, W. Chen, J. Been, G. Van Boven, R. Kania, Corrosion fatigue crack growth Behaviour of pipeline steel under underload-type variable amplitude loading schemes, Acta Mater. 96 (2015) 159–169. doi:http://dx.doi.org/10.1016/j.actamat.2015.05.049.

[103] M. Yu, W. Chen, R. Kania, G. Van Boven, J. Been, Crack propagation of pipeline steel exposed to a near-neutral pH environment under variable pressure fluctuations, Int. J. Fatigue. 82 (2016) 658–666. doi:http://dx.doi.org/10.1016/j.ijfatigue.2015.09.024.

[104] W. Chen, J. Zhao, K. Chevil, E. Gamboa, B. Alvarado, Threshold Geometrical Dimensions of Stage II Cracks Versus Required Resolution of Crack-Detection Techniques, (2018). doi:10.1115/IPC2018-78751.

[105] R.N. Parkins, Development of strain-rate testing and its implications, in: Stress Corros. Cracking—the Slow Strain-Rate Tech., ASTM International, 1979.

[106] R.N. Parkins, B.S. Greenwell, The interface between corrosion fatigue and stress-corrosion cracking, Met. Sci. 11 (1977) 405–413. doi:10.1179/msc.1977.11.8-9.405.

[107] B.N. Leis, R.N. Parkins, Mechanics and material aspects in predicting serviceability limited by stress-corrosion cracking, Fatigue Fract. Eng. Mater. Struct. 21 (1998) 583–601.

[108] A.K. Pilkey, S.B. Lambert, A. Plumtree, Stress Corrosion Cracking of X-60 Line Pipe Steel in a Carbonate-Bicarbonate Solution, 51 (1995) 91–96.

[109] H. Niazi, H. Zhang, K. Korol, W. Chen, High pH Crack Growth Sensitivity to Underload-Type of Pressure Fluctuations, (2018) V001T03A064. http://dx.doi.org/10.1115/IPC2018-78394.

[110] R.N. Parkins, Predictive approaches to stress corrosion cracking failure, Corros. Sci. 20 (1980) 147–166. doi:http://dx.doi.org/10.1016/0010-938X(80)90128-6.

[111] N.J.H. Holroyd, R.N. Parkins, The predictability of stress corrosion cracking susceptibility of steels in acetate solutions from potentiodynamic polarization curves, Corros. Sci. 20 (1980) 707–721. doi:http://dx.doi.org/10.1016/0010-938X(80)90052-9.

[112] F. Song, B. Lu, M. Gao, M. Elboujdaini, Development of a Commercial Model to Predict Stress Corrosion Cracking Growth Rates in Operating Pipelines, 2011.

[113] B.T. Lu, Further study on crack growth model of buried pipelines exposed to concentrated carbonate–bicarbonate solution, Eng. Fract. Mech. 131 (2014) 296–314. doi:http://dx.doi.org/10.1016/j.engfracmech.2014.08.006.

[114] J. Toribio, Local strain rate at crack tip: implications in stress corrosion cracking, Br. Corros. J. 32 (1997) 41–48. doi:10.1179/000705997798115165.

[115] L.M. Young, P.L. Andresen, T.M. Angeliu, Crack Tip Strain Rate: Estimates Based on Continuum Theory and Experimental Measurement, Corros. 2001. (2001) 15. https://doi.org/.

[116] R.N. Parkins, S. Zhou, The stress corrosion cracking of C$z.sbnd;Mn steel in CO2-HCO3 −-CO32 − solutions. I: Stress corrosion data, Corros. Sci. 39 (1997) 159–173. doi:http://dx.doi.org/10.1016/S0010-938X(96)00116-3.

[117] Y.F. Cheng, Stress Corrosion Cracking of Pipelines, John Wiley & Sons, Incorporated, New York, UNITED STATES, 2013. http://ebookcentral.proquest.com/lib/ualberta/detail.action?docID=1117022.

[118] J. Griggs, O. Lavigne, E. Gamboa, Influence of Strain on Current Densities and Stress Corrosion Cracking Growth Rates in X65 Pipeline Steel, CORROSION. 73 (2016) 192–198. doi:10.5006/2186.

[119] J. Li, M. Elboujdaini, B. Fang, R.W. Revie, M.W. Phaneuf, Microscopy Study of Intergranular Stress Corrosion Cracking of X-52 Line Pipe Steel, CORROSION. 62 (2006) 316–322. doi:10.5006/1.3280664.

[120] E.I. Meletis, R.F. Hochman, A review of the crystallography of stress corrosion cracking, Corros. Sci. 26 (1986) 63–90. doi:http://dx.doi.org/10.1016/0010-938X(86)90124-1.

[121] R.N. Parkins, P.W. Slattery, B.S. Poulson, The effects of alloying additions to ferritic steels upon stress corrosion cracking resistance, Corrosion. 37 (1981) 650–664.

[122] C.P. Hunt, The effect of impurities on the intergranular stress corrosion cracking of a C/Mn steel, Corros. Sci. 28 (1988) 901–922. doi:http://dx.doi.org/10.1016/0010-938X(88)90038-8.

[123] M. Elboujdaini, J. Li, M. Gao, G.P. Gu, Stress Corrosion Cracking - Microstructural and Material Property Preference for Crack Initiation of Linepipe Steel, Corros. 2004. (2004) 16. https://doi.org/.

[124] A. Atrens, J.Q. Wang, D.R.G. Mitchell, Grain Boundary Characterization of X42 Pipeline Steel in Relation to IGSCC, Corros. 2001. (2001) 9. https://doi.org/.

[125] J.Q. Wang, A. Atrens, D.R. Cousens, P.M. Kelly, C. Nockolds, S. Bulcock, Measurement of grain boundary composition for X52 pipeline steel, Acta Mater. 46 (1998) 5677–5687. doi:http://dx.doi.org/10.1016/S1359-6454(98)00246-8.

[126] J.Q. Wang, A. Atrens, D.R. Cousens, C. Nockolds, S. Bulcock, Boundary characterisation of X65 pipeline steel using analytical electron microscopy, J. Mater. Sci. 34 (1999) 1711–1719. doi:10.1023/A:1004530420338.

[127] J. Wang, A. Atrens, Microstructure and grain boundary microanalysis of X70 pipeline steel, J. Mater. Sci. 38 (2003) 323–330. doi:10.1023/A:1021169700779.

[128] A. Atrens, J.Q. Wang, K. Stiller, H.O. Andren, Atom probe field ion microscope measurements of carbon segregation at an α:α grain boundary and service failures by intergranular stress corrosion cracking, Corros. Sci. 48 (2006) 79–92. doi:https://doi.org/10.1016/j.corsci.2004.11.014.

[129] M.J. Danielson, R.H. Jones, K. Krist, Effect of Microstructure and Microchemistry on the SCC Behaviour of Pipeline Steels in a High pH Environment, (n.d.).

[130] M.J. Danielson, R.H. Jones, P.J. Dusek, Effect of Microstructure and Microchemistry on the SCC Behaviour of Archival and Modern Pipeline Steels in a High pH Environment, Corros. 2001. (2001) 22. https://doi.org/.

[131] J.Q. Wang, A. Atrens, D.R. Cousens, N. Kinaev, Microstructure of X52 and X65 pipeline steels, J. Mater. Sci. 34 (1999) 1721–1728. doi:10.1023/A:1004538604409.

[132] D.C. Crawford, G.S. Was, The Role of grain boundary misorientation in intergranular cracking of Ni-16Cr-9Fe in 360 °C argon and high-Purity water, Metall. Trans. A. 23 (1992) 1195–1206. doi:10.1007/BF02665051.

[133] X. Tong, H. Zhang, D. Li, Effects of misorientation and inclination on mechanical response of< 1 1 0> tilt grain boundaries in α-Fe to external stresses, Model. Simul. Mater. Sci. Eng. 22 (2014) 65016.

[134] O. Lavigne, E. Gamboa, V. Luzin, M. Law, M. Giuliani, W. Costin, The effect of the crystallographic texture on intergranular stress corrosion crack paths, Mater. Sci. Eng. A. 618 (2014) 305–309. doi:https://doi.org/10.1016/j.msea.2014.09.038.

[135] T. Shoji, V.S. Raja, Stress Corrosion Cracking : Theory and Practice, Woodhead Publishing, Oxford, 2011.

Chapter 3 Materials and method

3. 1 HpHSCC Mechanical Testing

3. 1. 1 Compact Tension Specimen Preparation

The current investigation was conducted on X65 pipeline steel with an outer diameter of 1067 mm and thickness of 12 mm. The chemical composition of this is reported in Table 3.1. Compact tension (CT) specimens with linear dimensions shown in Figure 3.1 are machined from the pipe. The orientation of the notch was parallel to the longitudinal direction of the pipe. Therefore, the path of crack propagation was parallel to the observed longitudinal cracks in the field. The CT specimens were mechanically polished by abrasive paper up to 600 grit, followed by ultrasonic cleaning in acetone for 15 minutes. After that, fatigue pre-cracking was conducted in the air, according to ASTM E647-08 [1]. As a result, a sharp crack was initiated from the root notch. The length of the pre-crack was controlled to be 2.5 ±0.2 mm on each side.

Table 3.1. Elemental composition of the X65 pipeline steel

Element	C	Mn	P	Si	Ni	Cr	Mo	Cu	V	Ni	Ti	Al	Fe
Wt %	0.06	1.43	0.01	0.31	0.06	0.06	0.02	0.21	0.03	0.07	0.01	0.02	Balance

The reason for using pre-cracked specimens in this study is the ease of controlling stress intensity factor (K)[2]. Stress intensity factor can be calculated through Equation 3.1:

$$K = \frac{P}{B\sqrt{W}} f\left(\frac{a}{W}\right) \qquad \text{Eq'n. 3.1}$$

where P is the applied load to CT specimen, B is the specimen thickness, a and W are shown in Figure 3.1. In this equation, $f(a/W)$ is a dimensionless factor known as a geometrical factor and can be calculated for CT specimen through Equation 3.2.

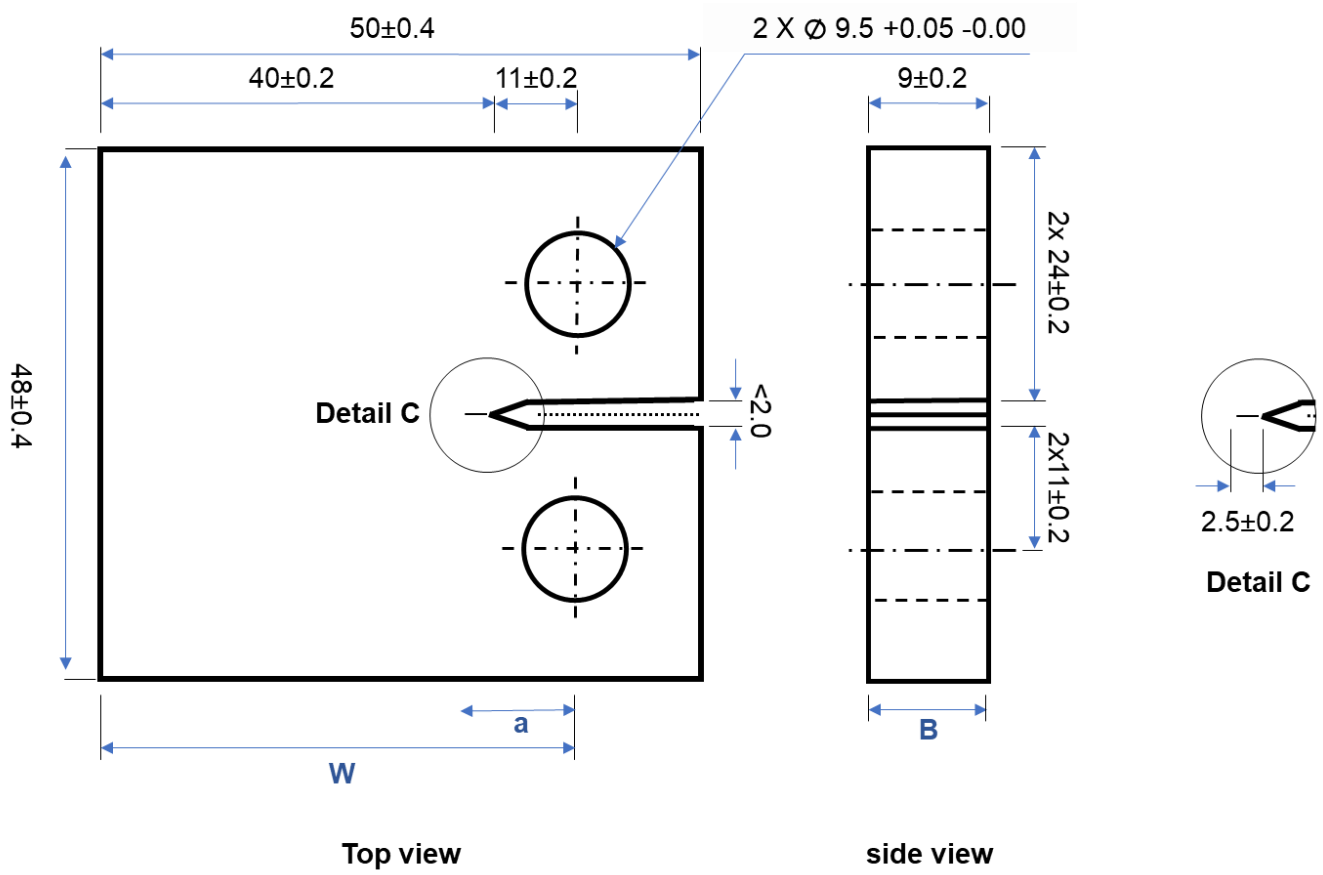

Figure 3.1. The dimensions of the CT specimens used in the current study.

$$f\left(\frac{a}{W}\right)=\frac{a+\frac{a}{W}}{\left(1-\frac{a}{W}\right)^{\frac{3}{2}}}\left[0.886+4.64\left(\frac{a}{W}\right)-13.32\left(\frac{a}{W}\right)^{2}+14.72\left(\frac{a}{W}\right)^{3}-5.60\left(\frac{a}{W}\right)^{4}\right]$$

Eq'n. 3.2

3. 1. 2 The Test Set-up for SCC Tests

For each test, two separated corrosion fatigue test cells were prepared. The configuration of the corrosion fatigue cells is shown in Figure 3.2. In each cell, a CT pre-cracked specimen was used as a cathode. A stainless-steel ribbon that surrounded the CT specimen was employed as an auxiliary electrode. The potentials were measure versus a Saturated Calomel Electrode (SCE). The

electrolyte of the corrosion fatigue cell was an aerated aqueous solution containing 0.5 M $NaHCO_3$ and 1 M Na_2CO_3 (also known as 1 N Na_2CO_3 and 1 N $NaHCO_3$). This solution at the temperature of 75 °C is known as a standard electrolyte for HpHSCC testing. However, the National Energy Board reported the temperature of soil, pipe, and natural gas is about 40 °C on leaving the compressor station in North America [3]. Therefore, the solution's temperature is tailored to 40 °C (rather than 75 °C) in this study to fit the context of the Canadian Pipeline Industry.

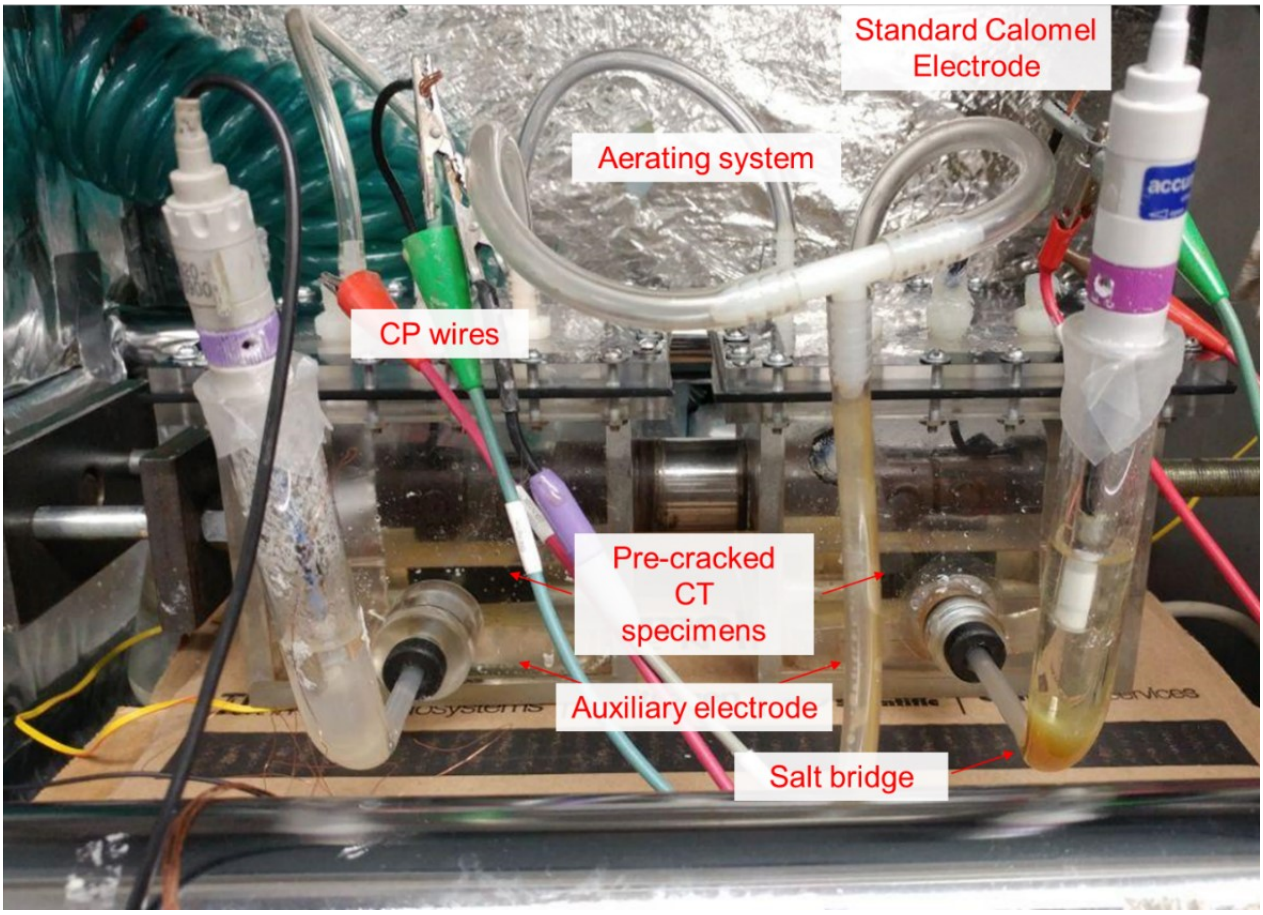

Figure 3.2. Corrosion fatigue cells were used in the studies [4].

According to the literature, the potential cracking range for HpHSCC is highly dependent on temperature. Figure 3.3 shows the variation of the cracking window with temperature for the 1N-1N solution[5]. According to this figure, the potential of the Pre-cracked CT specimens in the

corrosion Fatigue cells was selected -590 mV_{SCE}. This potential was applied to the specimens by employing a potentiostat. After setting up the corrosion fatigue cells, it was 24 h interval before starting the test to reach equilibrium in terms of temperature and potentials.

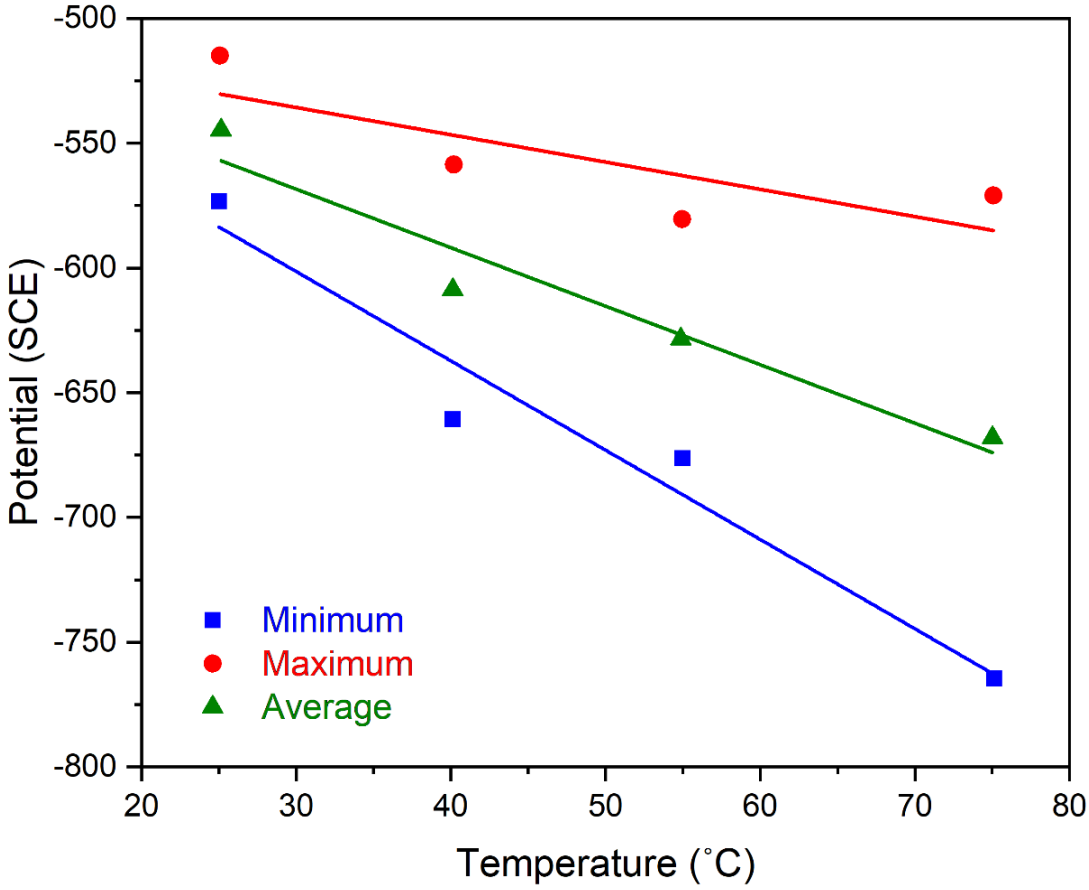

Figure 3.3. Variation of cracking potential range with temperature in the standard solution for HpHSCC [5].

The pre-cracked CT specimens in the corrosion fatigue cells were loaded by using a horizontal pneumatic loading frame shown in Figure 3.4. The loading machine was in an isolation chamber. The temperature was controlled to be 40 ± 0.2 ° C by using a heating system. The heating system includes a thermometer, a heater, and a fan.

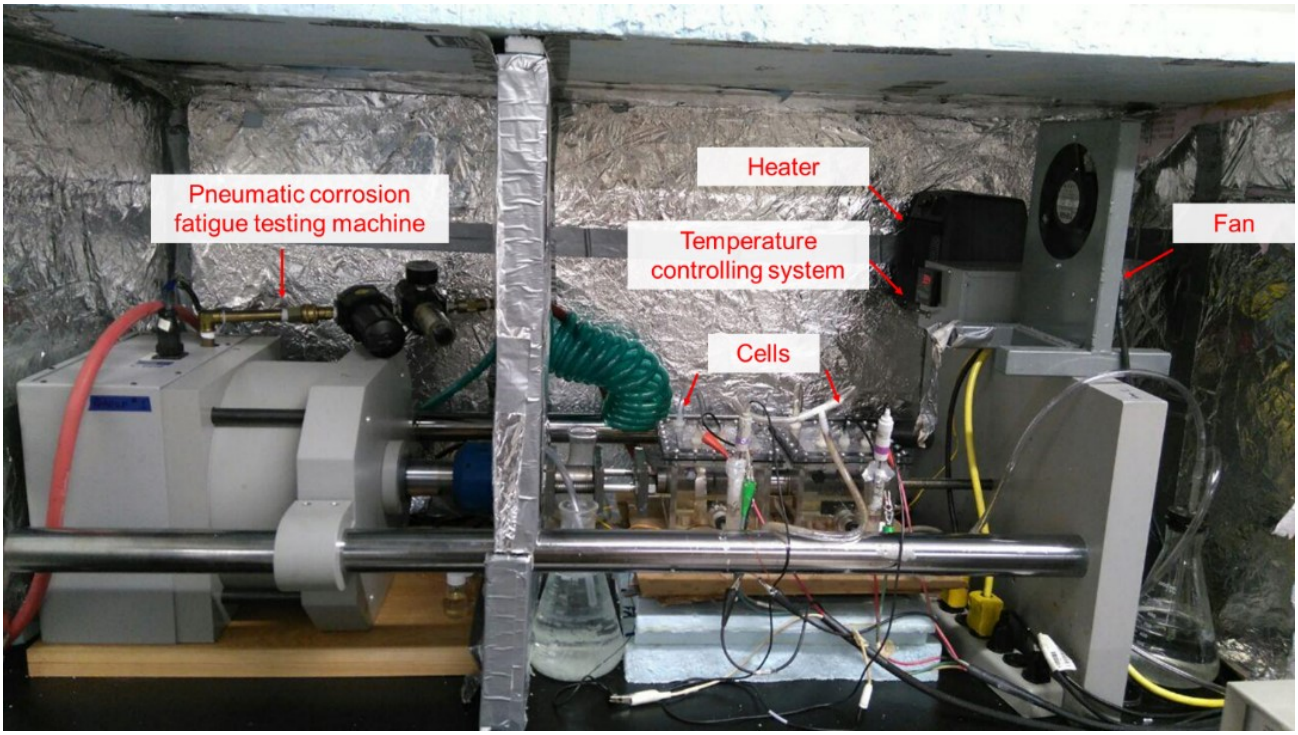

Figure 3.4. The used pneumatic corrosion fatigue testing machine in this study.

3. 1. 3 SCC Tests' Parameters

Different loading waveforms were applied to the pre-cracked CT specimen during the exposure to the HpHSCC test environment. Figure 3.5 shows an overview of the conducted tests in this study. Three maximum stress intensity factors were used in this study. According to the obtained results, the pre-cracked CT specimens experience stage 1b and stage 2 of HpHSCC crack growth when the K_{max} was 15 and 36 MPa.m$^{0.5}$, respectively. Hence, these two stress intensity factors were selected for further investigations.

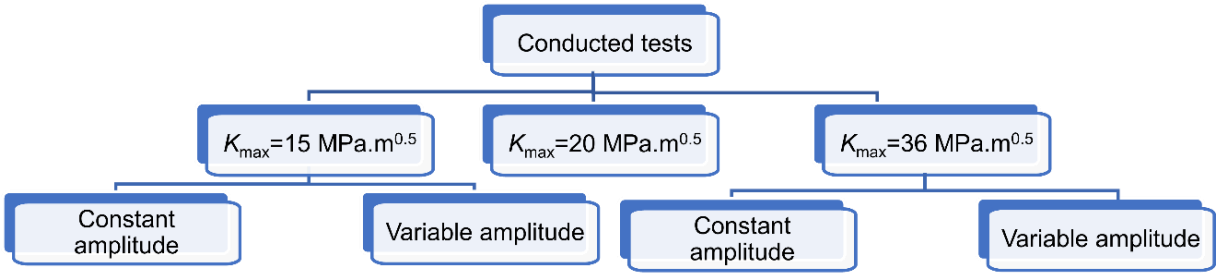

Figure 3.5. A flowchart showing an overview of the conducted tests in this study.

Constant amplitude and variable amplitude loading waveforms were designed and applied to pre-cracked CT specimens to study stage 1b and stage 2 of HpHSCC crack growth. Figure 3.6 (a) and (b) show the schematic of constant amplitude loading waveform and variable amplitude loading waveforms, respectively. The studied parameters are shown in these figures as well. Further information related to the test conditions is elaborated in each chapter.

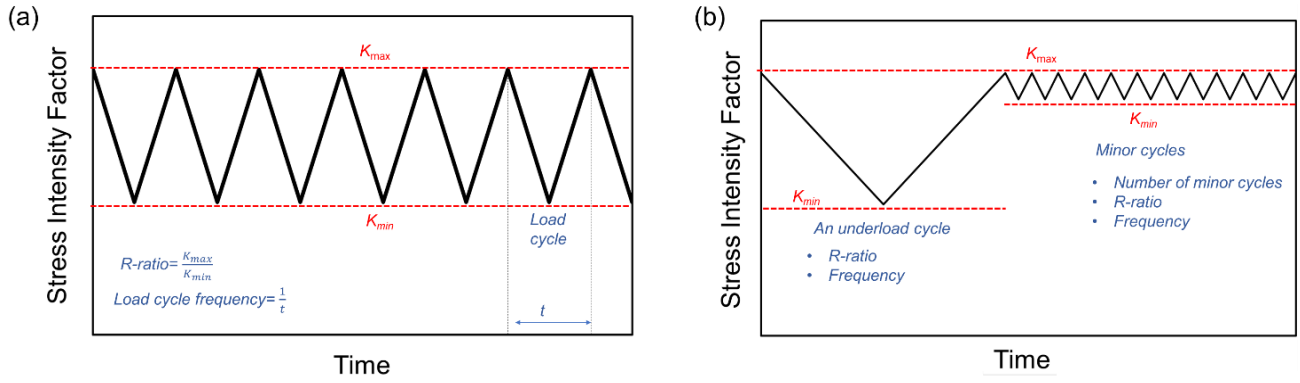

Figure 3.6. Schematic illustration of load scheme (a) constant amplitude (b) variable amplitude conditions.

3. 1. 4 Analysis of the Crack Growth

Using Scanning Electron Microscopy (SEM) equipped with energy dispersive spectroscopy (EDS) analyzer, the crack length was measured, and the fracture surface was studied. Before studying the

crack morphology on the exposed surfaces, the surfaces were polished by an oil-based diamond particle suspension and etched with Nital 5% to find the crack's clear path and the crack tip. Furthermore, the middle plane's crack path in the CT specimen's thickness was studied by cutting the specimens in the thickness direction. After curing the specimens, the middle sections were polished by abrasive paper up to 600 grit, followed by polishing with an oil-based diamond suspension. Afterward, the polished surfaces were etched using Nital 5%. After that, the CT specimens were fractured opened in liquid nitrogen. The fracture surfaces were deoxidized by an aqueous solution composed of 8 N HCL and 3.5 g/L hexamethylenetetramine. The fracture surfaces were studied by employing a scanning electron microscope. All the crack growth measurements in this study were conducted on the fracture surfaces.

3. 2 Electrochemical Measurements

As stated earlier, the current study's environmental conditions are tailored to fit the Canadian Pipeline Industry context. Hence, it is paramount to show the adjusted environmental conditions cause intergranular cracking. The standard protocol to study the environmental conditions that cause HpHSCC is conducting Potentiodynamic polarization tests at two sweep rates (fast and slow scan rate tests) in the test solution. If the potentials applied to steel falls within the active-to passive region, the environmental conditions are known potent environment for HpHSCC. In this study, potentiodynamic polarization tests were conducted on rectangular steel coupons cut from the X65 pipeline steels. The linear dimensions of coupons were 10 mm ×10 mm×9mm. The specimens were mounted in epoxy except for one surface with an area of 1 cm^2. That surface was mechanically polished by abrasive paper up to No. 600, followed by cleaning in ethanol. A three-electrode cell system, as a schematic is shown in Figure 3.7, was used. In this cell, the working electrode was the X65 coupon, and the counter electrode was a Pt plate. All the potentials were

measured versus the standard calomel electrode. A Gamry Reference 600 workstation was used to measure electrochemical measurements. The scan range was -1000 mV_{SCE} to 1000 mV_{SCE}. The fast and slow sweeping rates were 0.33 mV/s and 50 mV/s, respectively.

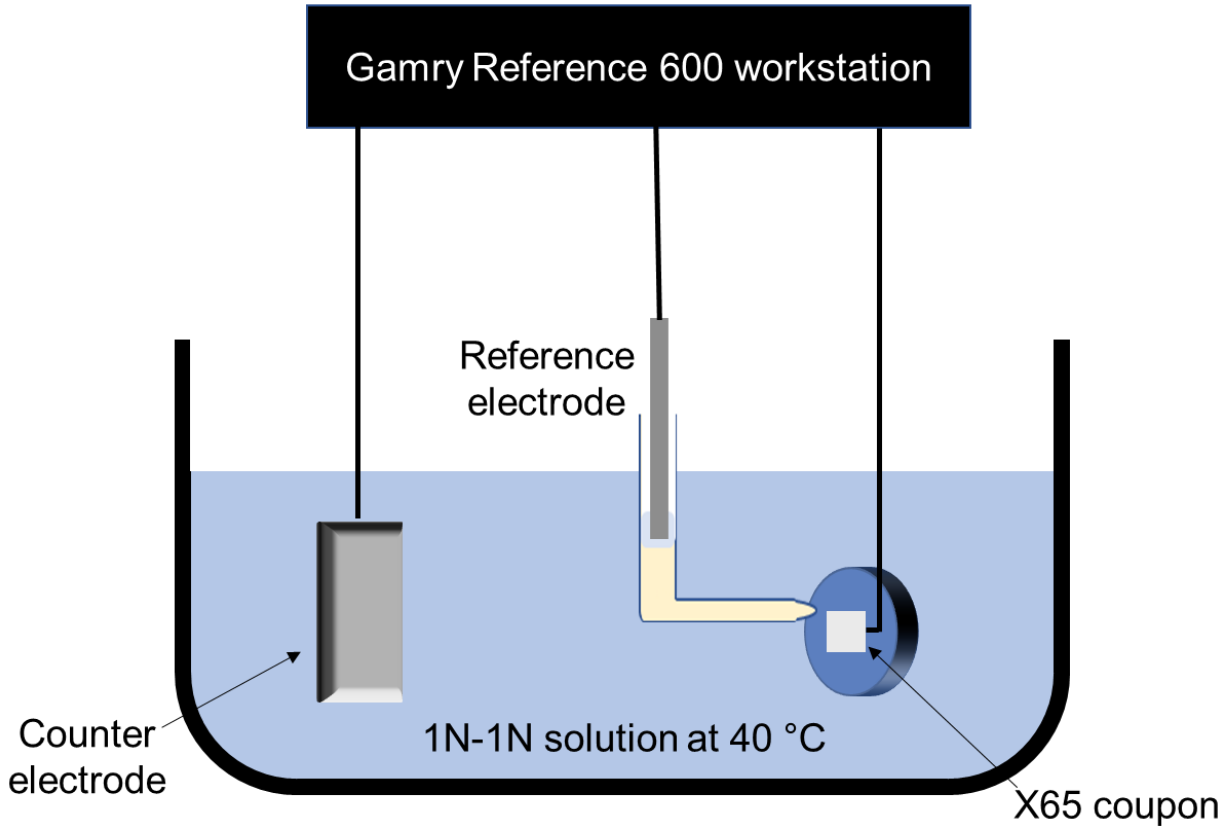

Figure 3.7. Schematic illustration of the electrochemical cell used in this study.

References:

[1] ASTM, “Standard Test Method for Measurement of Fatigue Crack Growth Rates E647-15e1,” ASTM B. Stand., pp. 1–49, 2016.

[2] B. F. Brown and C. D. Beachem, “A study of the stress factor in corrosion cracking by use of the pre-cracked cantilever beam specimen,” Corros. Sci., vol. 5, no. 11, pp. 745–750, 1965.

[3] N. E. Board, “Stress corrosion cracking on Canadian oil and gas pipelines,” Natl. Energy Board, Calgary, Alberta, 1996.

[4] H. Niazi, H. Zhang, K. Korol, and W. Chen, “High pH Crack Growth Sensitivity to Underload-Type of Pressure Fluctuations,” no. 51869. p. V001T03A064, 2018.

[5] J. A. Beavers, C. L. Durr, and B. S. Delanty, “High-pH SCC: Temperature and Potential Dependence for Cracking in Field Environments,” no. 40221. pp. 423–437, 1998.

Chapter 4 Crack Growth Sensitivity to the Magnitude and Frequency of Load Fluctuation in Stage 1b of High pH Stress Corrosion Cracking [1]

4. 1 Introduction

Any failure of a buried oil and gas transmission pipeline may pose a risk to human safety, the environment, the economy, and assets of the company and the country [1–3], because of the highly pressurized and flammable oil and gas inside the pipeline. Hence, the integrity management of the buried pipelines is of paramount importance, and several methods and measurements have been developed to promote the safe operation of the pipelines. For instance, pipes are protected against corrosion with the simultaneous application of cathodic protection and coatings to isolate the pipe from the local corrosive environment [4–8]. However, failure in the coating might result in the formation of occluded environments at the coating defect that are breeding grounds for Environmentally Assisted Cracking (EAC).

One of the common EAC mechanisms in pipeline steel is High pH Stress Corrosion Cracking (HpHSCC) [9,10]. The first occurrence of HpHSCC dates back to 1965 in Louisiana, USA [11,12]. Although many efforts have been made to understand the causes for HpHSCC and remedies to mitigate it, the average rate of in-service failure caused by HpHSCC is about 1.5 failures per year for US transmission pipelines over the last few decades [13,14]. HpHSCC failures keep happening during hydrostatic tests in North American pipelines [15]. The average age of pipelines that

[1] A version of this chapter is submitted for review as H. Niazi, G. Nelson, L, Lamborn, R. Eadie, W. Chen, H. Zhang, "Crack growth sensitivity to the magnitude and frequency of load fluctuation in stage 1b of high pH stress corrosion cracking"

underwent HpHSCC failures is 20-30 years [16]. This poses the question that the possibility for HpHSCC increases as the age of the pipeline increases. A piece of evidence for this implication is the incidence of HpHSCC in Russia, where it was believed that only Near Neutral pH Stress Corrosion Cracking threaten the buried pipeline [17]. Therefore, it is of paramount importance to improve our understanding about the HpHSCC crack evolution and enhance the current modelling to protect pipelines against HpHSCC threats. The current modelling is based on the Bathtub model proposed by Parkins, as discussed briefly in the following paragraph.

Parkins proposed the bathtub model to show the time-dependent HpHSCC crack propagation behaviour [3,14,18] for this form of EAC. According to the bathtub model, pipeline experience five sequential stages leading to a failure caused by HpHSCC, as shown in Figure 4.1. The first stage, which is labelled as the "*incubation stage*" in Figure 4.1, is the time to establish the appropriate environmental conditions that cause HpHSCC before cracking begins. Two requirements can characterize the potent environment: the formation of a high concentration aqueous carbonate-bicarbonate solution and the partial loss of cathodic protection near the coating defects [3]. The second stage, which is denoted as "*Stage 1a*" in Figure 4.1, is characterized by the emergence of short and shallow intergranular cracks on the pipe's uncoated surface. These cracks initially propagate at a high rate; however, they become dormant once they reach the limiting size of about 50 μm in-depth [19]. Work-hardening in the neighbouring areas [20] is one possible reason for the dormancy of the cracks at this stage. As the crack propagates, the passive film forms on the cracks' walls. The passive film might block the path of the corrosive environment to the crack tip and prevent further dissolution. Additionally, the plane strain condition in the depth tip reduces the amount of plasticity and can be considered additional possible reasons for the dormancy of the cracks in Stage 1a. Using experiments on tapered specimens, Parkins proposed

threshold stress for crack initiation, *i.e.*, the intergranular cracks nucleate at multiple sites if the stress exceeds a threshold value [21,22]. After their initiation, the cracks propagate in a stochastic manner so that the cracks, once initiated, experience periods of growth and dormancy [3,23,24]. This stage is shown as "Stage 1b" in Figure 4.1. The crack growth at this stage is either by re-activation of the existing crack or coalescence of adjacent cracks. The crack evolution at this stage continues until relatively long and deep cracks form on the free surface [25]. From the fracture mechanics point of view, the stress intensity factor at the depth tip (K_{depth}) of the crack at the end of Stage 1b reaches the threshold stress intensity factor for HpHSCC (K_{ISCC}) [3,26,27]. Thereafter, Stage 2 starts when the mechanical driving force at the crack tip causes sustainable crack growth through the film rupture mechanism [12,28–32]. The crack growth rate increases significantly in comparison with the previous stage. Therefore, the intergranular crack advances in the pipe's thickness within a relatively short time frame compared to Stage 1b. The crack propagation at this stage reduces the residual strength of the pipe significantly. Crack propagation at this stage is followed by Stage 3, where rapid crack growth results in immediate rupture and fracture of the pipe.

According to the above description and Figure 4.1, Stage 1b is the lifetime-determining stage in pipes vulnerable to HpHSCC. A recently published review paper that studies the chronological crack evaluation during HpHSCC failures [20] showed that much research is devoted to the incubation stage [33–35], Stage 1a [18,22,24,36], and Stage 2 [28–30,32]. In contrast, less attention had been paid to Stage 1b of HpHSCC [20]. The development of the bathtub model rest on the assumption that crack initiation and crack coalescence are random. Therefore, it is assumed that crack propagates in a stochastic manner, *i.e.* independent of existing cracks and loading conditions. It is of interest to identify the preferential regions for crack initiation during Stage 1b

if they exist. Preferential crack initiation in the vicinity of the existing crack followed by crack coalescence shortens Stage 1b. Therefore, understanding the HpHSCC crack growth at this stage is essential to predict the remaining lifetime of pipes susceptible to HpHSCC. The novelty of the current study is to study the crack propagation in Stage 1b regarding the loading condition and preexisting cracks.

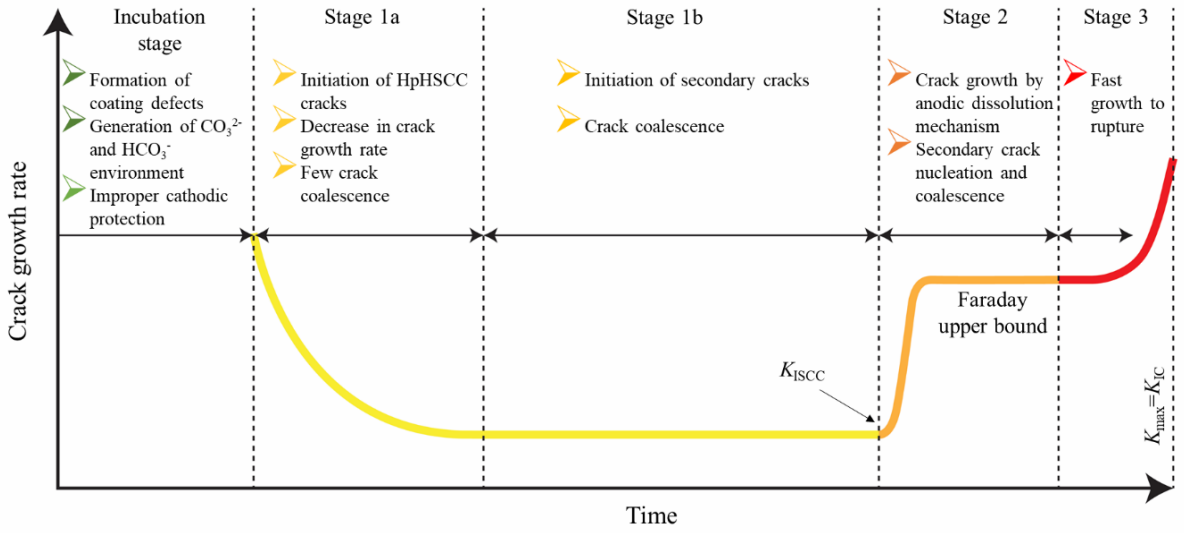

Figure 4.1. Schematic illustration of the bathtub model for HpHSCC [30].

This research is designed to investigate the role of loading conditions on crack propagation during Stage 1b. To simulate Stage 1b, a novel approach was used in which the side faces of the CT specimens were analyzed for crack initiation as a function of stress under plane stress conditions. Note that the stress intensity factor was kept less than K_{ISCC}. The crack morphologies on the side faces of the pre-cracked CT specimens are studied to identify the preferential crack initiation in the crack tip plastic zones. The crack growth rates under different loading conditions are measured based on the crack length on the fracture surfaces of the CT specimens. The correlation between crack growth behaviour and loading conditions is discussed.

4. 2 Experimental Procedure

4. 2. 1 Materials and Environment

Steel samples from a microalloyed line pipe steel with a wall thickness of 12 mm and an outer diameter of 1067 mm were used in this study. The chemical composition of the steel is reported in Table 4.1. Figure 4.2 shows the stress-strain curve of the used steel in this study. The ultimate tensile stress for this steel is 637 MPa. This particular steel shows discontinuous yielding, which is also known as the yield point phenomenon. The upper and lower yield points for this steel are 560 MPa and 555 MPa, respectively.

Table 4.1. Elemental composition of the microalloyed line pipe steel used in this study

Element	C	Mn	P	S	Si	Ni	Cr	Mo	Cu	V	Ni	Ti	Al	Fe
Wt %	0.06	1.43	0.01	0.005	0.3	0.06	0.06	0.02	0.21	0.03	0.07	0.01	0.02	Balance

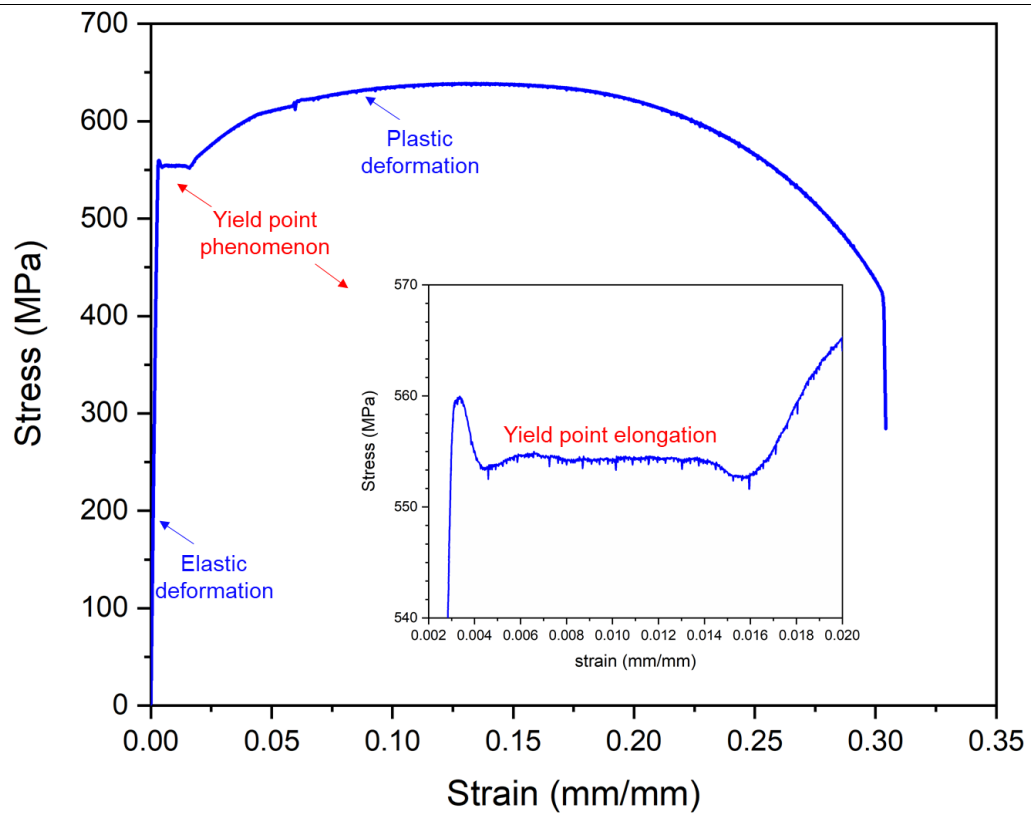

Figure 4.2. The stress-strain response of the microalloyed line pipe steel used in this study.

According to the Introduction, Stage 1b represent the condition that a crack is existing, and the stress intensity factor at the crack tip is smaller than K_{ISCC}. Hence, pre-cracked specimens were needed in the current study. Additionally, the maximum applied load to the pre-cracked specimens was chosen so that the maximum stress intensity factor remains less than K_{ISCC}. Compact tension (CT) specimens with the linear dimensions shown in Figure 4.3 were machined from the line pipe so that the notches were parallel to the longitudinal direction of the pipe. The specimen configuration allows the cracks to propagate perpendicular to the hoop direction, *i.e.,* in the same direction as the typical cracks in the field [37]. Sample preparation involved mechanically polishing by abrasive papers up to 600 grit, followed by ultrasonic cleaning in acetone for 15 minutes. Fatigue pre-cracking was conducted in air according to the ASTM E647-08 standard to produce a sharp crack tip at the notch of the machined specimens [38]. Crack initiation near the notch tip could be in any orientation, like the direction with maximum tensile stress or maximum shear stress. The crack propagation path is zigzag at higher magnification. However, the propagated pre-crack direction is perpendicular to the maximum tensile load on a global scale. The pre-crack length on each side of the specimens was measured at certain intervals in compliance with ASTM E647-08. The final length of the pre-crack on each side of the specimens was controlled to be 2.5±0.2 mm. A schematic illustration of the pre-cracked CT specimen and its dimensions is shown in Figure 4.3. Using the pre-cracked CT specimens gives the advantage of controlling the stress intensity factor at the crack tip. Hence, the crack can be controlled in Stage 1b, where the mechanical loading condition for Stage 2 has not been met. Equation 4. 1 expresses the stress intensity factor at the crack tip.

$$K = \frac{P}{B\sqrt{W}} f\left(\frac{a}{W}\right) \qquad \text{Eqn. 4. 1}$$

where P and B are the applied load to pre-cracked CT specimens during the test and specimen thickness, respectively. The parameters a and W are parameters depending on the dimensions of the pre-cracked CT specimens, as they ate shown in Figure 4.3. For the used CT specimens, a and W are e 13.6 mm and 40 mm, respectively. In Equation 4. 1, $f\,(a/W)$ represents a dimensionless factor related to the geometry of the pre-cracked CT specimen, and it is a function of a and W as shown in Equation 4. 2:

$$f\left(\frac{a}{W}\right)=\frac{a+\frac{a}{W}}{\left(1-\frac{a}{W}\right)^{\frac{3}{2}}}\left[0.886+4.64\left(\frac{a}{W}\right)-13.32\left(\frac{a}{W}\right)^{2}+14.72\left(\frac{a}{W}\right)^{3}-5.60\left(\frac{a}{W}\right)^{4}\right] \quad \text{Eqn. 4. 2}$$

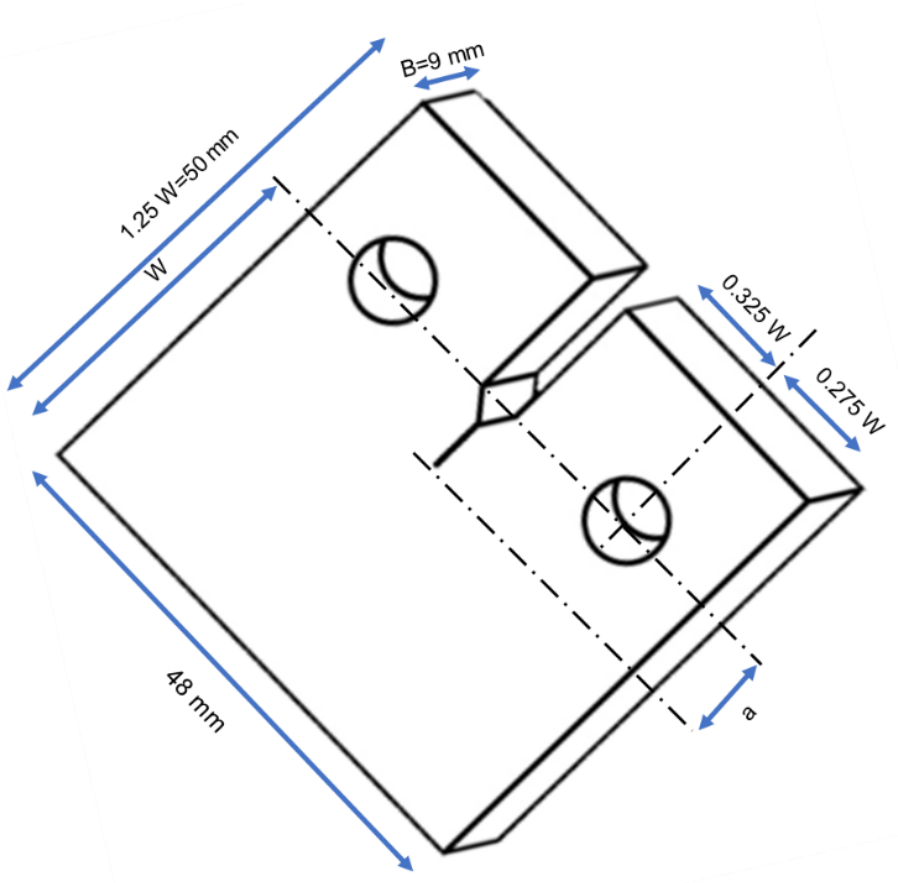

Figure 4.3. Schematic illustration of the pre-cracked CT specimen used in this study.

For each test, two separate cells were employed so that the two specimens replicated each other. Each cell involved a pre-cracked CT specimen, which acted as a working electrode. The potential of the CT specimens was maintained at -590 mV versus saturated the Standard Calomel Electrode (SCE) by employing a potentiostat. This potential of the CT specimens was initially selected within the potential range for HpHSCC reported in the literature [13]. Additionally, further potentiodynamic polarization tests conducted in this study proved that the used steel is susceptible to HpHSCC when the potential is between -575 to -625 mV_{SCE}, as will be discussed in the results and discussion section. The auxiliary electrode for the cell was a stainless-steel ribbon that surrounded the CT specimen. An aerated aqueous solution composed of 0.5 M Na_2CO_3 and 1 M $NaHCO_3$ at a temperature of 40 ±0.2 °C was used as an electrolyte for the cell. The electrolyte was identical to the standard electrolyte for HpHSCC (1 N Na_2CO_3 and 1 N $NaHCO_3$); however, the temperature was somewhat different (40 °C rather than 75 °C) to fit the context of the Canadian pipeline industry. Our previous work has demonstrated intergranular cracking under the test conditions using potentiodynamic polarization tests at two scan rates [30]. The corrosion fatigue tests started 24 hours after setting up the test cell to reach equilibrium in temperature and potential. It is worth mentioning that a black film covered the side faces the CT specimens after 24 hours of exposure to the test environment. The loading conditions for the tests will be described later in Section 4. 2. 3.

4. 2. 2 Potentiodynamic Polarization Test

The fast (33 mV/s) and slow (0.33 mV/s) scan rates potentiodynamic polarization tests were carried out in a solution of 0.5 M Na_2CO_3 and 1 M $NaHCO_3$ at 40 °C to evaluate the electrochemical response of the used steel under the environmental conditions in this study. Rectangular coupons with the linear dimensions of 10 mm × 10 mm × 9 mm were cut from the

line pipe steel. The coupons were mounted in the epoxy so that a face with the area of 1 cm^2 remained uncoated. Preparation of the coupons includes mechanical polishing by abrasive papers up to 600 grit and cleaning in ethanol. A Gamry Reference 600 Workstation using a three-electrode cell system was employed for electrochemical measurements. The three-electrode cell was composed of a prepared coupon as a working electrode, a platinum plate as a counter electrode, and a saturated calomel electrode as a reference electrode. The potential range for potentiodynamic polarization tests was between -1000 mV_{SCE} and 1000 mV_{SCE}.

4. 2. 3 Loading Parameters

A horizontal loading machine was used to apply different loading waveforms to the pin-hole loaded pre-cracked CT specimens. Our previous research [39] showed that the pre-cracked CT specimen is at Stage 1b of HpHSCC crack growth when K_{max} is equal to 15 $MPa.m^{0.5}$. Therefore, a K_{max} of 15 $MPa.m^{0.5}$ was selected for all the loading scenarios in this study. In total, nine constant amplitude loading waveforms were designed to study the effects of either amplitude or frequency of load fluctuation on Stage 1b of HpHSCC crack growth. The range of *R*-ratio (min. stress/max. stress) was 0.9 to 0.2, and the frequency range was 10^{-4} to 5×10^{-2} Hz. Table 4.2 summarizes the characteristics of the applied constant amplitude loading waveforms in this study.

4. 2. 4 Determination of Crack Growth Rate

After each test, a passive black film formed on the free surfaces of the CT specimens in contact with the HpHSCC test solution. It has been shown that this black film is composed of iron carbonate and iron oxide [29,40]. The exposed surfaces were polished slightly using an oil-based suspension of alumina to remove the black film. Afterward, the polished surfaces were etched with Nital (5%) to permit the study of the crack path and the grain structure using Scanning Electron Microscopy (SEM). Then, all the CT specimens were fractured at liquid nitrogen temperatures to

expose both fracture surfaces. An aqueous solution composed of 8 N HCl and 3.5 g/L hexamethylenetetramine was used to remove the passive films covering the crack fracture surfaces. The fracture surfaces were studied using SEM, and the lengths of primary and secondary intergranular cracks were measured on the fracture surfaces. The reported crack growth rates reflect the crack length on the edges of fracture surfaces, *i.e.,* crack propagation rates on the side face of the CT specimens.

Table 4.2. Details of constant amplitude loading waveforms

Sample ID	K_{max} (MPa.m$^{0.5}$)	R	ΔK (Mpa.m$^{0.5}$)	Frequency (Hz)	Number of cycles
R0.9_F5E-3	15	0.9	1.5	5×10^{-3}	11250
R0.9_F5E-2	15	0.9	1.5	5×10^{-2}	66000
R0.7_FE-2	15	0.7	4.5	10^{-2}	13200
R0.5_FE-4	15	0.5	7.5	10^{-4}	160
R0.5_FE-3	15	0.5	7.5	10^{-3}	1800
R0.5_FE-2	15	0.5	7.5	10^{-2}	13200
R0.2_FE-4	15	0.2	12	10^{-4}	160
R0.2_FE-3	15	0.2	12	10^{-3}	1800
R0.2_FE-2	15	0.2	12	10^{-2}	1200

4. 3 Results and discussions

4. 3. 1 Electrochemical Response of the Steel in the Test Solution

Figure 4.4 illustrates the fast and slow scan rate potentiodynamic polarization curves of the unstress steel in a solution of 0.5 M N_2CO_3 and 1 M $NaHCO_3$. The used steel showed active-passive behaviour under the test condition for both fast and slow scan rate tests. The slow scan rate test is employed to detect film formation and here stands for a progressive film formation. According to the slow scan rate potentiodynamic polarization curve, the corrosion potential and the primary passive potential are -855 mV_{SCE} and -650 mV_{SCE}, respectively. Conversely, the fast

scan rate will minimize film formation, which represents significant anodic activity because of film rupture events. Comparing fast and slow scan rate tests, there is a particular potential range where the electrochemical response of steel varies from significant anodic dissolution in film free condition to insignificant activity when the required time for film formation is provided. This potential range is labelled as the HpHSCC potential range in Figure 4.4, and it is known as the active-to-passive transition region. Two criteria were applied to determine the potential range in Figure 4.4. First, the fast scan rate current density must exceed 1 mA/cm^2. Secondly, the differences between the fast and slow scan rate must be greater than one order of magnitude [28,30,35,41,42]. According to Figure 4.4, the HpHSCC potential range is between -625 mV_{SCE} and -575 mV_{SCE}.

When the used steel is exposed to the test solution at the potential of -590 mV_{SCE}, intergranular corrosion occurs on the free surface of the steel, followed by the formation of a passive film on grains and penetrating tip of the intergranular corrosion. Therefore, unstressed steel experiences intergranular etching under the test condition. However, the passive film is brittle and prone to rupture upon applying adequate mechanical driving force. Suppose the mechanical driving force ruptures the passive film on the grain boundaries, intergranular corrosion proceeds and forms intergranular cracks[3,20,35,43,44]. Therefore, there is a threshold value that provides film free condition on the grain boundaries. The physical meaning of the threshold is the mechanical driving force that provides film free condition on the grain boundaries. In other words, the mechanical driving force fractures the passive film on the grain boundaries and suppresses re-passivation. Consequently, dissolution at the grain boundaries forms intergranular cracks. Similarly, intergranular cracks propagate through dissolution at the grain boundaries unless a passive film forms on the crack tip.

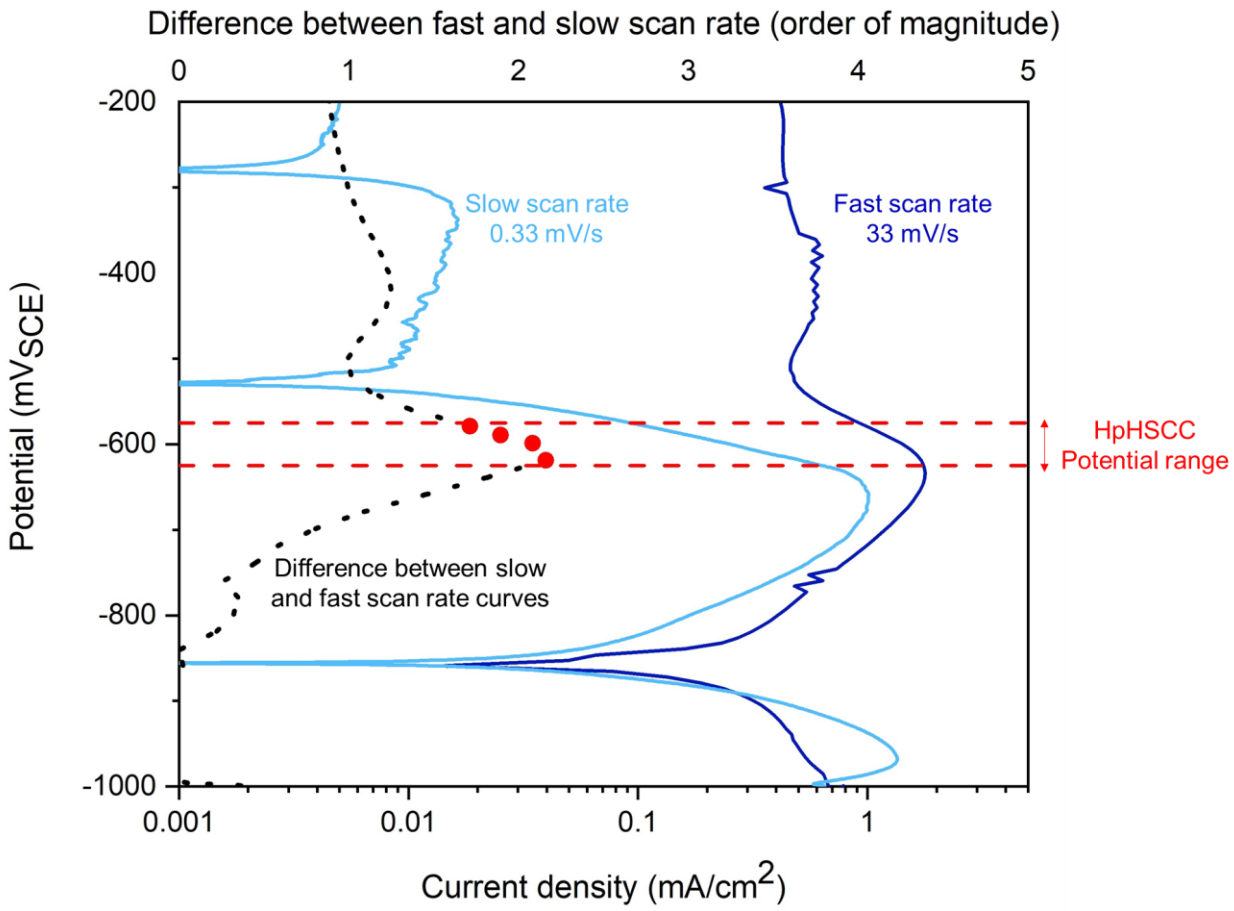

Figure 4.4. Fast (33 mV/s) and slow (0.33 mV/s) scan rates potentiodynamic polarization curves of the used steel in a solution of 0.5 M Na_2CO_3 and 1 M $NaHCO_3$ at a temperature of 40 °C along with a determination of Potential range for HpHSCC by comparing the fast and slow scan rate tests.

4. 3. 2 The Magnitude of Load Fluctuations

Constant amplitude loading schemes with different *R*-ratio and frequencies were applied to pre-crack CT specimens, where the K_{max} was kept at 15 MPa.m$^{0.5}$ for each waveform. The range of fluctuation in stress intensity factor was from 1.5 to 12 MPa.m$^{0.5}$, associated with *R*-ratios of 0.9 to 0.2. The maximum and minimum frequencies were 5×10^{-2} and 10^{-4} Hz, respectively.

Accordingly, the duration of one cycle was between 20 and 10000 seconds. All the test conditions result in crack advance on the sides of CT specimens, but no crack growth was observed in the middle section through the thickness of CT specimens. This condition can be considered as the crack propagation in Stage 1b [39].

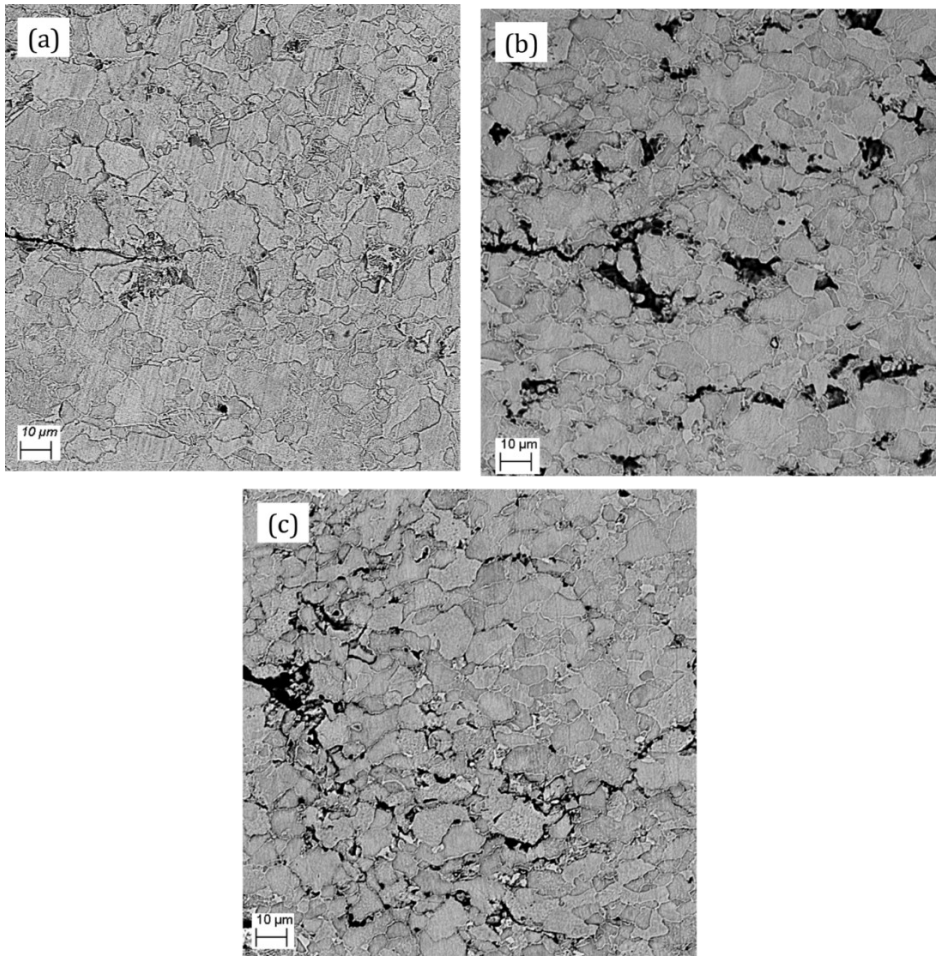

Figure 4.5. Crack tip morphologies at the area near the pre-crack tip tested under constant amplitude loading condition with different *R*-ratios (a) 0.9 at the frequency of 5×10^{-2} Hz, (b) 0.7 at the frequency of 10^{-2} Hz, (c) 0.5 at the frequency of 10^{-2} Hz.

Figure 4.5 depicts the area near the pre-crack tip on the side face of the CT specimens tested under three different *R*-ratios after polishing the black film and etching in Nital (5%). The frequency load cycles with *R*-ratio of 0.9 were 5×10^{-2} Hz, whereas the frequencies for *R*-ratio of 0.7 and 0.5 were

10^{-2} Hz. As can be seen, the crack morphology near the pre-crack tip is different for each *R*-ratio, although the K_{max} for all test conditions was the same. Figure 4.5 (a) shows no significant intergranular crack propagation for the R0.9_F5E-2 test condition. In contrast, R0.5_FE-2 test conditions resulted in a colony of intergranular cracks at the pre-crack tip, as shown in Figure 4.5 (c). Figure 4.5 (b) illustrates the obtained crack morphology under the R0.7_FE-2 test condition. Propagation of an intergranular crack from the pre-crack tip is evident, along with the evidence of secondary cracks initiation in the adjacent areas. These observations imply that propensity for intergranular cracking near an existing crack increases as the amplitude of load fluctuation increases.

4. 3. 3 Frequency of Load Fluctuation

Figure 4.6 displays the area near the pre-crack tip on the side face CT specimens tested under constant amplitude loading waveforms with the *R*-ratio of 0.5 at three different frequencies after polishing the black film and etching in Nital 5%. In this figure, two distinctive regions can be considered according to fracture mechanics principles, *viz.* crack tip plastic zone and elastic zone. The large dashed red curve shows the theoretical crack tip plastic zone, r_y, calculated by Equation 4. 3. In this equation, r_y is the radius of the plastic zone under plane stress condition, K_I is the mode I of stress intensity factor, σ_{ys} is yield strength, and θ is the angle between the crack plane and material element.

$$r_y(\theta) = \frac{1}{4\pi}\left(\frac{K_I}{\sigma_{ys}}\right)^2\left[1+\cos\theta+\frac{3}{2}\sin^2\theta\right] \qquad \text{Eq'n. 4.3}$$

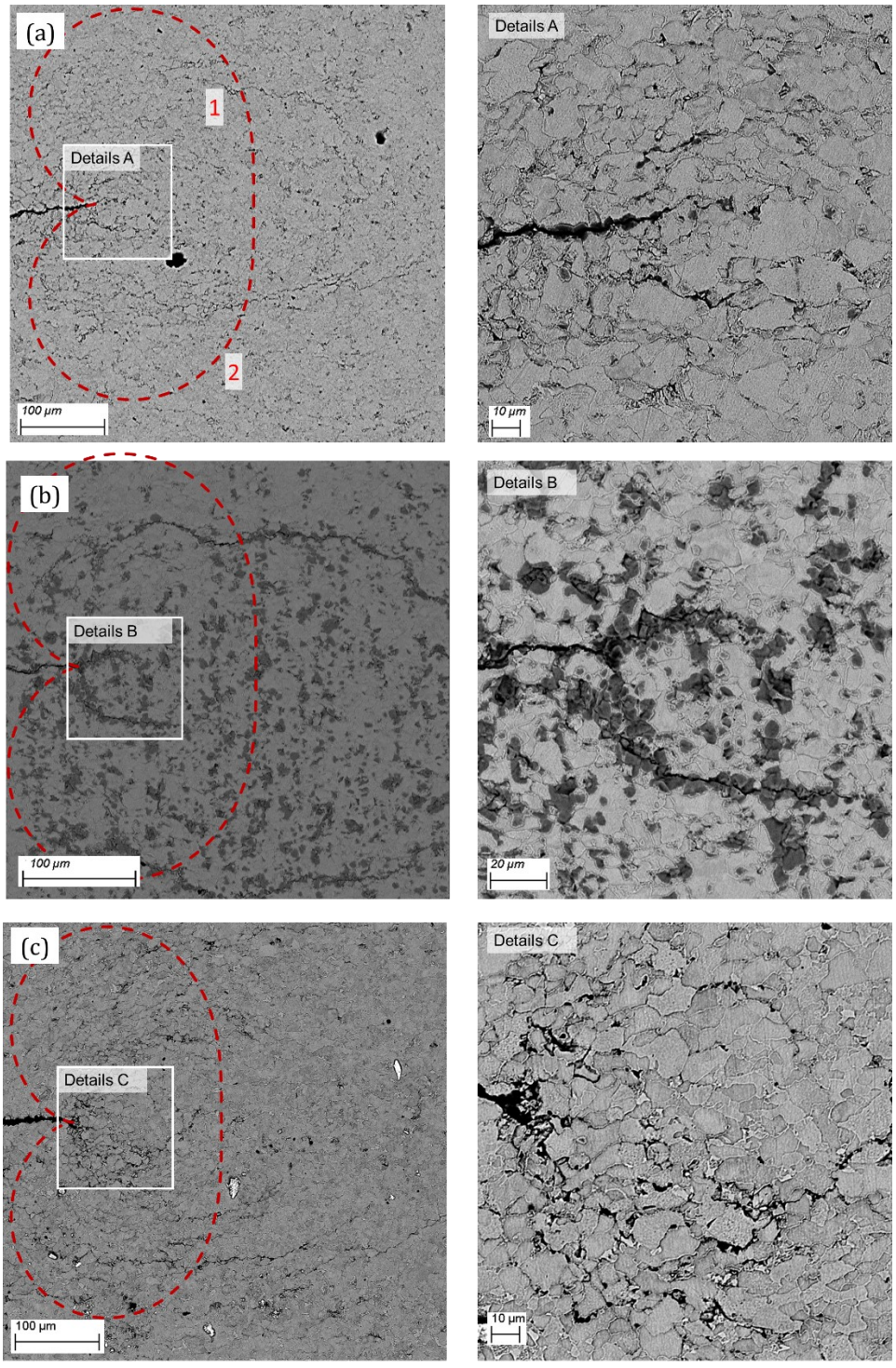

Figure 4.6. The intergranular crack morphologies on the free surfaces of the CT specimens were tested under constant amplitude waveforms with the *R*-ratio of 0.5 at frequencies of (a) 10^{-4}, (b) 10^{-3}, and (c) 10^{-2} Hz.

Equation 4.3 is based on the Von Mises criterion, where yielding occurs when the effective stress is equal to yielding. Additionally, the theoretical plastic zone in Equation 4.3 is based on an elastic crack-tip solution, in which redistribution of stress after yielding is neglected. Further discussion about the theoretical plastic zone is given in section 4.3.3 (stress condition at the crack tip).

There are a number of intergranular cracks on the side face of the CT specimens, and the intergranular crack density increases as the frequency increases. The intergranular cracks can be classified into four categories with regard to their relative position from the fatigue-pre-crack tip, as will be discussed later.

Regardless of the position of the secondary cracks, the reason for crack growth is selective dissolution at the grain boundaries. In general, when the HpHSCC environment is established, intergranular corrosion occurs on the surfaces exposed to the HpHSCC environment. However, the intergranular corrosion is gradually reduced, as passive films form at the penetrating tip of intergranular corrosion. Therefore, unstressed steel exposed to the HpHSCC environment shows intergranular etching. However, the brittle passive film can be ruptured at grain boundaries by an adequate amount of mechanical driving force, and then dissolution proceeds until the passive film reforms. Here, the critical mechanical driving force is the strain rate, *i.e.*, the amount of strain generated over time. It implies the amount of strain and the time frame that the strain is generated are equally important. The amount of strain must exceed the fracture ductility of the passive film, and the time for fracturing the passive film must be short enough to prevent re-passivation. Otherwise, any fracture of the passive film is healed by re-passivation. If the passive film's rupturing rate surpasses the re-passivation rate at some grain boundaries, selective corrosion at those grain boundaries proceeds, and those boundaries undergo intergranular cracking. The

physical meaning of threshold stress is the stress condition that provides a sufficient strain rate to crack the passive film at the grain boundaries. Crack initiation happens at multiple sites [3,20,24], although all the grain boundaries are prone to cracking theoretically [21]. These newly nucleated cracks can merge with each other and form longer cracks [23,24]. For the intact steel pipeline, it has been shown that there is a threshold stress that can provide the requirement for crack initiation[21,22]. The threshold value for the stress for crack initiation is about at the yield stress, and it decreases under cyclic loading conditions[21,22]. Metallurgical discontinuities assist the crack initiation by altering the stress state at the crack tip and locally providing the micro-scale threshold stress[3,39,45,46]. Accordingly, the preexisting cracks intensify the stress in the adjacent area and increase the chance for crack initiation[39]. Stage 1b in HpHSCC crack growth, where an intergranular crack exists on the free surface, represents the situation mentioned above. In the same manner, the fatigue pre-crack CT specimens used in this study represent the same situation. Hence, the stress condition at the crack tip is of paramount importance[39,46].

4. 3. 4 Stress Conditions at the Crack Tip

From a fracture mechanics point of view, when the cracked structure is loaded uniaxially, the stress state near the pre-crack tip will be biaxial or triaxial in the cases of plane stress and plane strain conditions, respectively. Additionally, the stress state near the crack tip will be intensified so that the stress at this region is higher than the nominal stress applied to the body. Figure 4.7 illustrates a cracked body under a Y-direction uniaxial loading condition. The intensified stress condition in Y-direction (σ_y) under plane strain condition, existing on the free surface, is shown in Figure 4.7. The complete elastic solution for σ_y on the crack plane (θ=0) is described by Equation 4. 4. In this equation, K is the stress intensity factor, and x is the distance from the crack tip. In this equation C, D, and E are constants [47].

$$\sigma_y = \frac{K}{\sqrt{2\pi x}} + Cx^0 + Dx^{1/2} + Ex^1 + \ldots$$ Eq'n. 4.4

According to Equation 4.4, the stress approaches the nominal stress for large *x*. In the case of load fluctuation, the *K* in Equation 4.4 is devoted to the maximum stress intensity factor. All the terms except the first one become negligible when *x* approaches zero. The first term increases towards infinity as *x* decreases. This behaviour is shown with the dashed blue line in Figure 4.7. However, plastic deformation happens in the real material so that stress will not increase much further than yielding and depends on the three-dimensional stress state and the appropriate yield surface for that state. Therefore, there is a plastic region at the crack tip, as discussed in the following paragraphs.

According to Equation 4. 4, the stress follows a decreasing trend by increasing *x*, and it becomes equal to the yield strength of the material at a point. For the plane stress condition, like the stress condition on the free surface, yielding occurs when σ_y equals the yield strength of the material. Assuming that the boundary between elastic and plastic occurs when the stress satisfies the yield criterion, the first-order estimate of the plastic zone can be calculated by Equation 4. 5. It is worth mentioning that this equation is identical to Equation 4. 3 on the crack plane (θ=0). The first approximation is also known as the theoretical plastic zone, and it is shown with a dark blue circle in Figure 4.7.

$$r_y = \frac{1}{2\pi}\left(\frac{K_I}{\sigma_{ys}}\right)^2$$ Eqn.4. 5

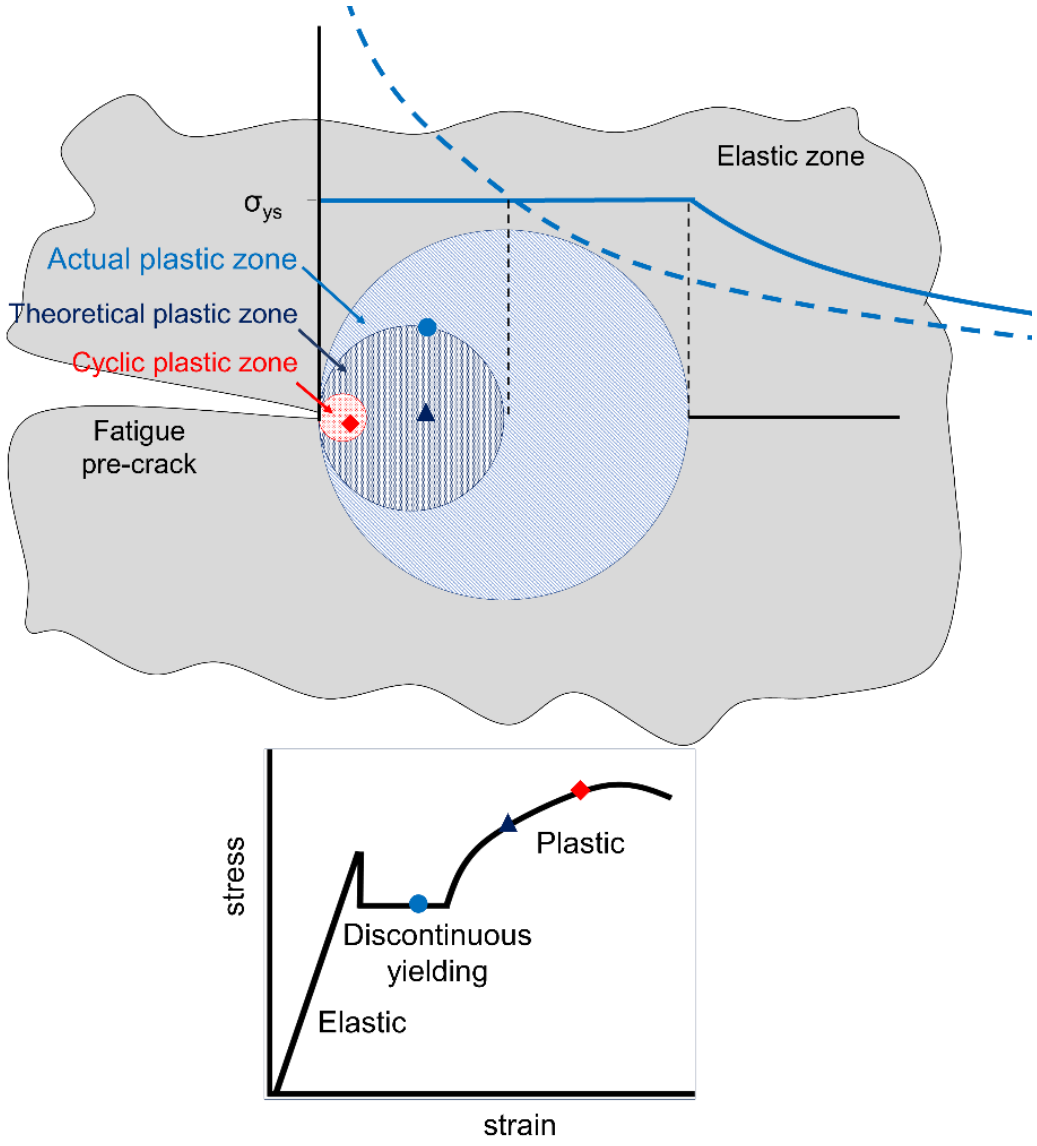

Figure 4.7. Schematic representation of cyclic plastic zone, theoretical plastic zone and actual plastic zone at the primary crack loaded under cyclic loading conditions and corresponding stresses from the stress-strain curve.

According to Figure 4.7, σ_y is greater than yield strength in the theoretical plastic zone. The second-order estimate of the plastic zone size is based on the redistribution of those stresses to satisfy equilibrium. The load capacity in the theoretical plastic zone is limited by yielding. Hence, the stresses higher than the yield point must be bypassed around the plastic zone. Redistribution of the

extra stresses causes more material to yield and expands the plastic zone. A simple force balance leads to Equation 4. 6, which provides a second-order estimate of plastic zone size under a plane stress condition. The second-order estimate is also known as the actual plastic zone and is shown with a light blue circle in Figure 4.7. According to Equation 4. 6, the actual plastic zone size is about twice the theoretical one [47]. Additionally, note that the plastic zone shape can be determined by Equation 4. 3; however, here, it is assumed $\theta = 0$ for the sake of simplicity.

$$r_y = \frac{1}{\pi}\left(\frac{K_I}{\sigma_{ys}}\right)^2 \qquad \text{Eqn.4. 6}$$

The above analysis of the theoretical and actual plastic zones formation considered the monotonic loading condition. However, it has been proposed that a cyclic plastic zone forms at the crack tip in the presence of cyclic loading [48]. The cyclic plastic zone can be defined by damage accumulation models, developed to explain fatigue crack growth behaviour. According to the damage accumulation model, the crack tip materials are divided into small blocks, as shown in Figure 4.8. Under cyclic loading conditions, different amounts of damage are accumulated in those material blocks depending on their position relative to the crack tip. There are three different zones at a crack tip subjected to a cyclic loading condition, *viz.* cyclic plastic zone, monotonic plastic zone, and elastic region. The elastic zone, which is far ahead of the crack tip, is the same as that defined in Figure 4.7. The materials located in the elastic zone deform in a purely elastic manner. The materials located in the monotonic plastic zone deform plastically during loading to the maximum stress. After that, elastic deformation takes place during the loading-unloading of each load cycle. The monotonic plastic zone size varies systematically with the maximum stress applied to the crack body or maximum stress intensity factor, as shown in Equation 4. 6. The third zone, known as the cyclic plastic zone, forms close to the crack tip. The load fluctuations in this region

form a complete hysteresis loop. Therefore, materials located in this region undergo plastic deformation in every load cycle [48–50]. The cyclic plastic zone shape and size depend on *R*-ratio and the ΔK value. Several empirical equations estimate the cyclic plastic zone size[51], and its size can be estimated as a quarter of the monotonic plastic zone [48]. Irwin proposed Equation 4. 7 to estimate the plastic zone size (r_{CPZ}) for plane stress condition [51].

$$r_{CPZ} = \frac{1}{8\pi}\left(\frac{K_I}{\sigma_{ys}}\right)^2 \qquad \text{Eqn. 4. 7}$$

The cyclic plastic zone is the region where cumulative strain is generated. According to damage accumulation, the fatigue crack propagates once the cumulative level of strain fully damages a material block. Given that the intergranular crack propagation happened during the test conditions, the cumulative strain in the cyclic plastic zone provides the mechanical driving force for passive film rupture, as will be discussed in the next section.

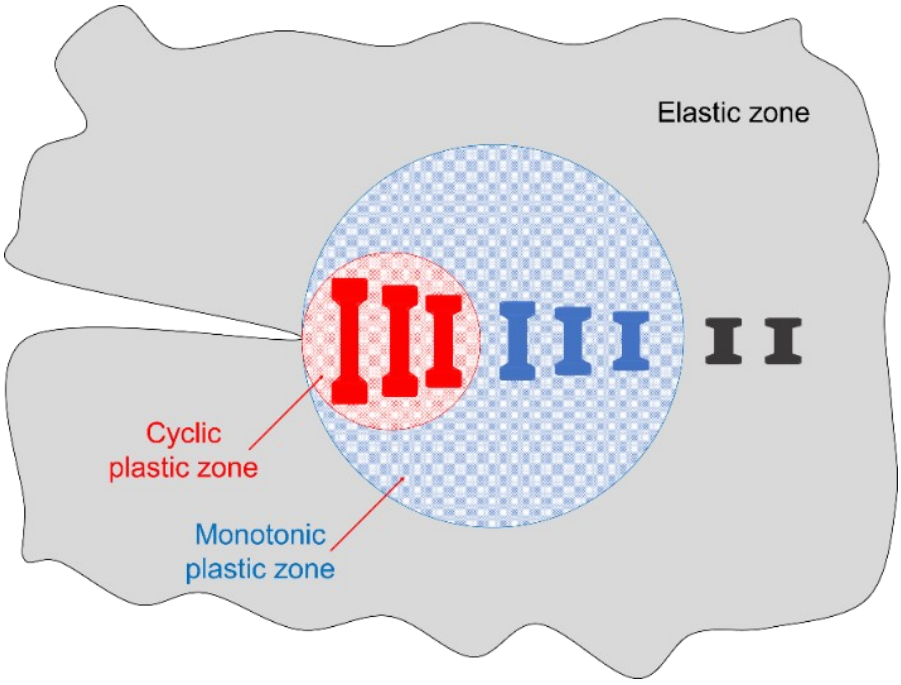

Figure 4.8. Schematic illustration of the damage accumulation model for fatigue crack propagation.

4. 3. 5 Classification of Secondary Cracks at the Crack Tip

Figure 4.9 shows typical crack morphologies on the side face of the CT specimens. This specimen is chosen because it has an intermediate density of secondary cracks at the crack tip region. In this figure, the area near the crack tip is divided into 15 squares so that each one has an area of 0.01 mm^2. The density of cracks at each square was determined with the use of Image J software. As is evident, the maximum crack density is right at the crack tip. The density of the secondary cracks decreases as the distance from the pre-crack tip increases so that the density becomes less than 1% beyond the theoretical plastic zone. However, the initiation of a relatively long crack was observed at the boundary between the actual theoretical plastic zones. The condition that leads to the formation of these cracks will be discussed in this section with regards to their relative distance from the fatigue pre-crack tip and the stress condition. The intergranular cracks on the side face of the pre-cracked CT specimens can be classified into four categories, as labeled in Figure 4.9 and discussed below.

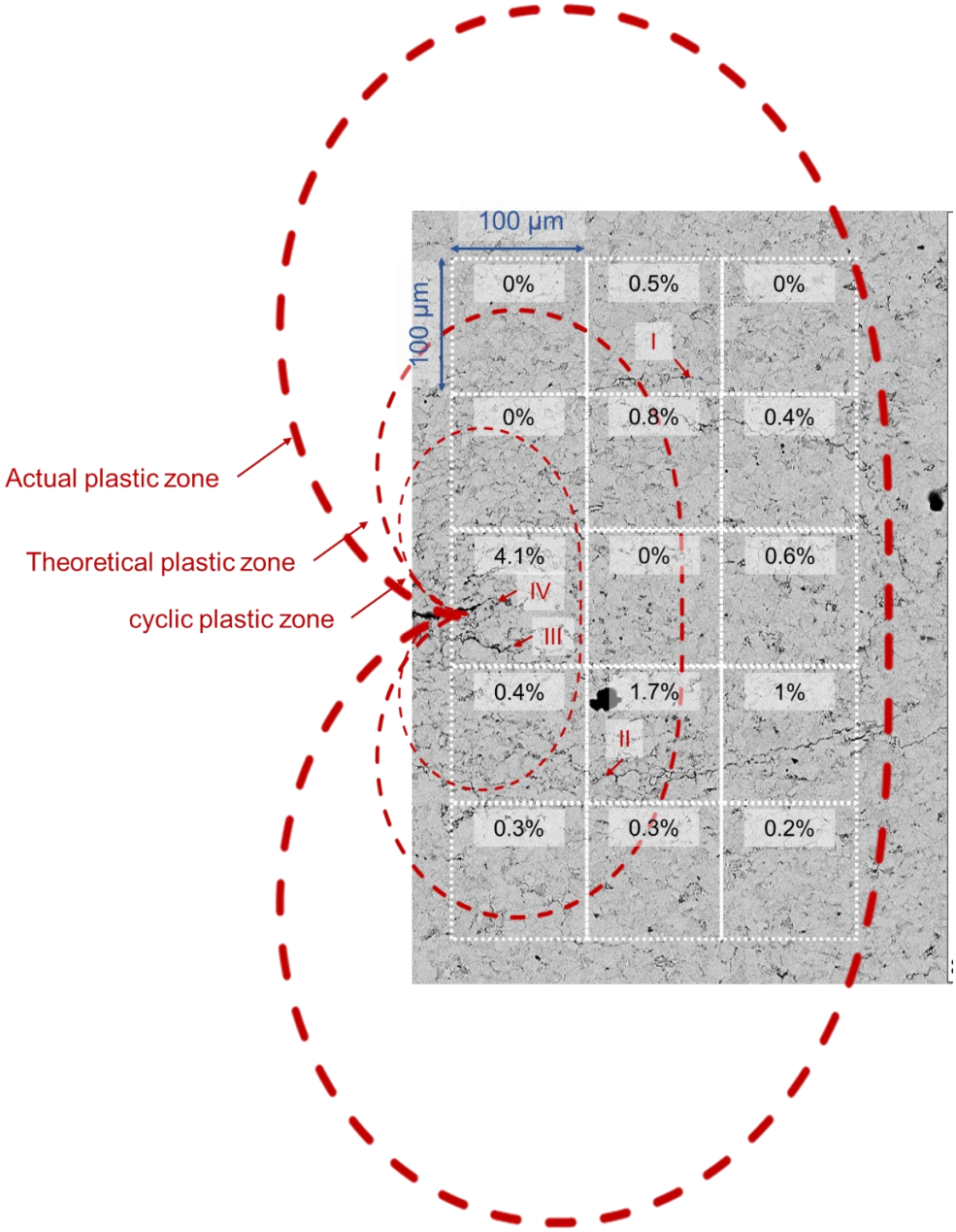

Figure 4.9. Analysis of the density of intergranular cracks at the area near the pre-crack tip. The numbers in each square show the density of the intergranular cracks. Example of the crack categories (I) crack initiated at the boundary of the theoretical plastic zone, (II) crack initiated within the theoretical plastic zone, (III) cracks initiated in the cyclic plastic zone, and (IV) crack initiated from the pre-crack tip.

- Group I: Crack initiated at the boundary of the theoretical plastic zone

Figure 4.10 shows the crack labelled as I in Figure 4.9 at higher magnification. Here a total of six small intergranular cracks with individual lengths below 100 μm have been initiated. These small intergranular cracks are labeled as "*AB*", "*CD*", "*EF*", "*GH*", "*IJ*", and "*KL*". As mentioned earlier, the crack propagation in the depth direction is initially rapid [3]. However, the crack propagation rate gradually decreases, and newly-initiated cracks reach the limiting size of 50 μm[19,20]. It has been shown that the cracks at this stage have a semi-elliptical shape, where the crack length on the surface ($2c$) is larger than the crack depth (a) [3,19,20,39]. Given that these cracks are in the early stage of growth and their short length on the surface, it can be estimated that these cracks are shallow. Hence, the stress intensification near these cracks' tips will be relatively small [20] and can be neglected in this study. Reviewing both experimental and field data, Parkins found empirically that neighboring cracks tend to merge and form larger cracks on the surface if the conditions for Equation 4. 8 are met. In this equation, y is the normal distance between two cracks, and $2c_m$ is the average length of two adjacent cracks [20,21,24]. The tendency for coalescence is conspicuous in Figure 4.10 as the nearest tips of two adjacent cracks are bending to link the cracks. Hence, from point A to point L can be considered as a single crack.

$$y \leq 0.14(2c_m) \qquad \text{Eqn. 4. 8}$$

From the previous explanations, the metal in that region transmits the high stresses in the plastic zone to the surrounding metal. Hence, the stress in this region can be about at the yield stress. According to Figure 4.2, this particular steel has an upper and lower yield point and yield point elongation. The yield point phenomenon represents the condition that the stress decreases when the dislocations start gliding. In the materials showing yield point phenomena, dislocations are locked because of either the high density of dislocations (dislocation locking) or atmosphere

pinning by segregated interstitial atoms in the dislocation core [52,53]. Hence, the stress increases to the upper yield point to release locked dislocation. After that the dislocation motions generate considerable amount of strain at extremely high strain rate, which is also known as strain shock [46].The strain rate, generated by strain shock, is sufficient in this region to fracture the passive film on a considerable number of grain boundaries and sustain intergranular corrosion. Further progress of the intergranular cracking through the grain boundaries at the film-free conditions will form intergranular cracks.

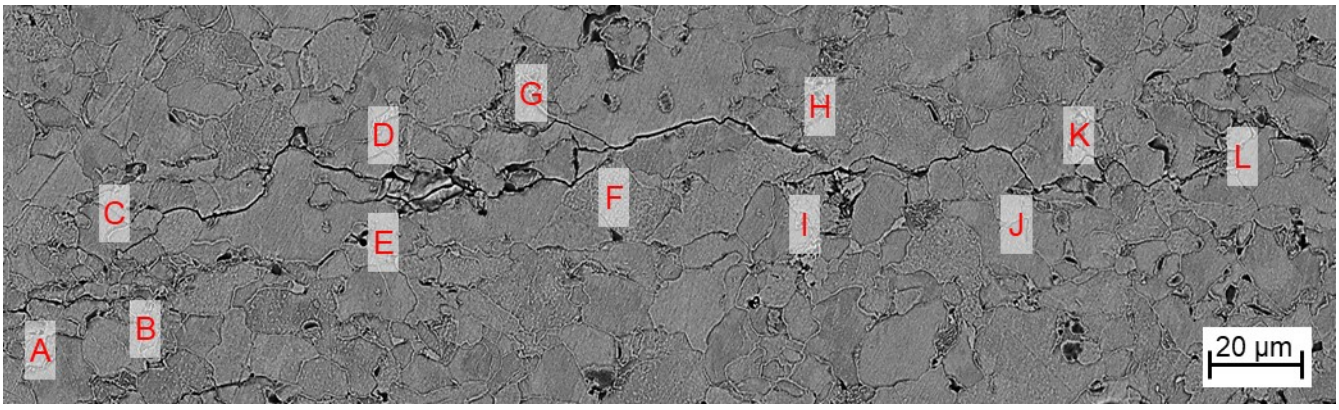

Figure 4.10. Evidence of crack initiation and crack initiation and crack coalescence along the boundary of the theoretical and the actual plastic zones. Higher magnification of crack labeled I in Figure 4.9, which is composed of the following six smaller cracks: *"AB," "CD," "EF," "GH," "IJ," and "KL."*.

The condition in Figure 4.10 is an ideal representative for Stages 1a and 1b in a small scale of intact steel pipeline. Accordingly, a few cracks were initiated at multiple sites and merge to form longer cracks. It has been shown that these cracks are not deep, and their crack growth decreases over time so that they reach a maximum limiting depth of 50 µm [19]. However, the crack coalescence increases the driving force for crack propagation in the depth direction. Considering

the small depth of such cracks, the adjacent stress field is relatively small compared to the pre-fatigue crack tip, and it is ignored here.

- Group II: Crack initiated within the theoretical plastic zone

The second group of the intergranular cracks are nucleated in the theoretical plastic zone. According to Figure 4.9, the intergranular crack density reduces in the theoretical plastic zone compared to the cyclic plastic zone. The condition that produces initiation of this group of cracks is identical to the situation at the narrow sections of the tapered specimens tested under cyclic loading conditions with maximum stress greater than the yield strength. As a side note, a tapered specimen is a tensile specimen in which the cross-sectional area decreases linearly from one end to another end in the gauge section. The tapered specimen's geometry allows applying a variety of stresses to a single specimen to determine the threshold stress for crack initiation [21]. Obviously, the stress increases from the wide end to the narrow end. Some important points have been established by using tapered specimens. First, the threshold value is about the yield point under monotonic loading conditions [21]. Secondly, cyclic loading reduces the threshold value for crack initiation so that Parkins proposed that every 0.1 decrease in R-ratio reduced the threshold value by about 81 MPa [21]. Thirdly, the propensity for crack initiation increases under cyclic loading conditions [22]. As for the narrow tip of the tapered specimen, the local stresses exceed the yield point at the theoretical crack tip plastic zone. Additionally, the load fluctuation assists the crack initiation. Therefore, the density of the cracks in this region increases as the magnitude of the load fluctuation increases. Additionally, the orientation of these cracks is not perpendicular to the applied load direction. These cracks are inclined towards the group I cracks (cracks at the boundary of the theoretical plastic zone) and this favors the coalescence between group I and group II cracks.

Parkins reports nucleation of small cracks between two adjacent cracks as a mechanism to bridge between the cracks in Stage 1b.

- Group III: Cracks initiated in the cyclic plastic zone

The group III intergranular cracks, the nucleated cracks close to the crack tip, were observed only in the presence of low *R*-ratio cycles. Therefore, the initiation of these cracks can be explained with the aid of the damage accumulation model with some modifications to fit the context of HpHSCC crack growth. According to Equation 4. 7, the cyclic plastic zone size increases as ΔK increases. Therefore, a larger cyclic plastic zone formed under low *R*-ratio cycles allows the secondary cracks to become easily visible. HpHSCC crack propagation mechanism relies on the dissolution of the grain boundaries, and the cracks are intergranular in nature. If the accumulated strain were potent enough to cause a fracture, the cracks would be transgranular. Hence, this mechanism cannot be responsible for crack propagation solely in the case of HpHSCC. However, the generated strain by such load fluctuation helps form film-free conditions at the grain boundaries located in the cyclic plastic zone. The materials in this region experience stress well above the yield stress, as schematically shown in Figure 4.7 and Figure 4.8. In this region, the accumulated strain leads to rupture of the passive film at the grain boundaries. The strain rate applied in this study was high enough to suppress the re-passivation on the grain boundaries. Therefore, grains at the crack tip are under film free conditions, and intergranular cracks initiate. These cracks were shown in Figure 4.5 (c) and Figure 4.6 (a) to (c). The observed increasing trend in crack density by increasing the load cycle frequency is because of the higher strain rate generated at higher frequencies. The higher strain rate is in favour of film-free conditions by preventing re-passivation.

- Group IV: A single crack initiated from pre-crack tip

The group IV crack, an extension of the preexisting crack, was observed in all the samples to different extents, and are considered the main crack in this study. This crack is formed through either extension of the preexisting crack tip on the surface or merging of the secondary cracks and the main crack. One mechanism for the propagation of the existing crack is a low-temperature creep. This mechanism can be applied to any of the nucleated cracks as well [34, 35]. Low-temperature creep is a phenomenon caused by high *R*-ratio loading cycles in the materials that develop strain hardening. When such material is loaded monotonically beyond the yield point, the interaction between the dislocations or dislocations and existing barriers like grain boundaries increases the internal stresses. Therefore, an increase in applied stress is required for further strain, *i.e.*, strain rate decreases. This behaviour is known as strain hardening or work hardening. Nevertheless, this behaviour might alter under cyclic loading conditions where the load is partially removed and then restored. During the unloading event, the glissile dislocations move backward because of back stresses from sessile dislocations. During the backward movement of these dislocations, cross slip or rearrangement of the dislocations can occur. Accordingly, the effects of work hardening are eliminated to some extent. At the onset of reloading, the mobile dislocations glide forward again and restore strain. The motion of dislocations and resultant plastic strain continue unless the strain rate decreases by strain hardening again. Considering the dislocation network's changes during the unloading, strain hardening is postponed to strains greater than the initial strain. Hence, each load cycle generates a strain increment. The strain caused by low-temperature creep is cumulative, yet the creep increment decreases progressively [18,54–56]. Low-temperature creep is the primary mechanism for the early stage of the HpHSCC crack growth [3]. The strain generated by low-temperature creep can provide film-free conditions at the grain

boundaries close to the pre-crack tip and cause the crack length on the free surface to increase. The concept of low-temperature creep can be applied to the other nucleated cracks as well. However, the strain caused by low-temperature creep will be exhausted within 24 hours.

The small secondary cracks near the main crack tip may merge to the predominant crack and elongate the crack on the surface form. Any factor that increases the density of secondary cracks near the existing crack tip increases the possibility of crack coalescence. For example, low *R*-ratio cycles contribute to the crack propagation of the fourth group of the cracks through assisting nucleation of intergranular cracks near the main crack tip.

4. 3. 6 Crack Growth Behaviour

Regardless of the crack's relative location to the pre-crack tip, some points must be clarified. First, both initiation of new cracks and propagation of the existing cracks are controlled by anodic dissolution at the grain boundaries. So, neither initiation of the crack nor propagation happens unless the mechanical driving force, *i.e.,* sufficient strain rate to rupture of the passive film on the grain boundaries, is provided. When this film is ruptured, the grain boundaries will be corroded, and intergranular cracks will initiate or propagate. However, the time frame over which the strain is provided is critical as well. When a given amount of strain is applied during a shorter time, *i.e.,* at higher frequencies, the chance for re-passivation on the grain boundaries decreases. Consequently, the dissolution of the grain boundary can proceed to either form or propagate the intergranular crack. As mentioned earlier, it can be hypothesized that there is a critical strain rate for crack initiation rather than a threshold stress. Secondly, large load fluctuation assists the nucleation of secondary cracks. Reduction in the *R*-ratio is accompanying by a decrease in threshold stress for crack initiation, based on the Parkins experiments on tapered specimens.

Hence, the chance for crack nucleation increases under cyclic loading conditions. Third, low-temperature creep is assisting the propagation of both nucleated cracks and preexisting cracks.

Figure 4.6 shows that the density of intergranular cracks increases as the frequency of the low *R*-ratio cycle increases. Assuming the same stress condition caused by cyclic loading with the *R*-ratio of 0.5, an increase in the frequency means an increase in the strain rate. Therefore, it can be postulated that there is a critical strain rate for cracking and a threshold for crack initiation. Further investigation that calculates the strain rate at the grain boundaries is needed to prove this hypothesis. It is suggested that future research should consider the characteristics of the grain boundaries since statistics showed that the high-angle grain boundaries are more prone to cracking [57,58]. This postulation should be a research topic for the future.

Among the above crack categories, group IV cracks are of most interest to this paper. As mentioned earlier, many of the nucleated cracks become dormant and do not grow. However, group IV represents growing cracks. If the geometrical evolution of such cracks continues, the threshold mechanical driving force for Stage 2 will be achieved at the crack tip. Additionally, the growth of group IV cracks increases the chance for coalescence, according to Equation 4. 8. All the crack growth rates are based on this group of cracks. The dimensions of Group IV can be measured on the fracture surface of the CT specimens. Figure 4.11 shows the fracture surfaces of the CT specimen tested under constant amplitude loading waveforms. For small load fluctuation, like R0.9_F5E-2, a tiny intergranular region forms between the fatigue pre-crack and lab fracture regions, as shown in Figure 4.11 (a). The length of this region on the free surface is 24 μm. This intergranular crack is probably the extension of the existing crack because of low-temperature

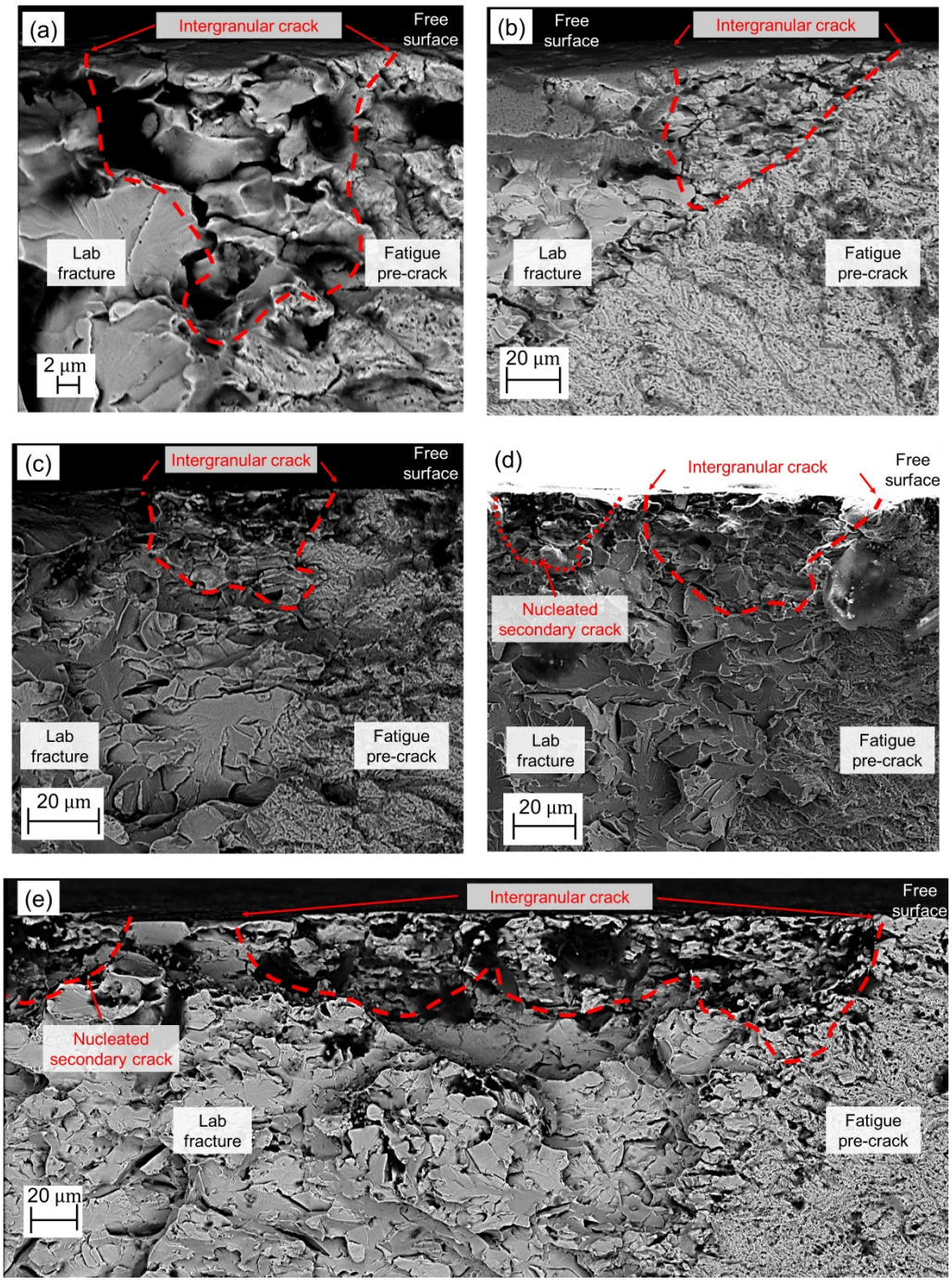

Figure 4.11. SEM images of the fracture surfaces of CT specimens tested under constant amplitude loading conditions (a) *R*-ratio of 0.9 and frequency of 5×10^{-2} Hz (b) *R*-ratio of 0.7 and frequency of 10^{-2} Hz (c) *R*-ratio of 0.5 and frequency of 10^{-4} Hz, (d) *R*-ratio of 0.5 and frequency of 10^{-3} Hz, and (e) *R*-ratio of 0.5 and frequency of 10^{-2} Hz.

creep. No secondary crack initiation is evident on the fracture surface which is aligned with the metallography observations (See Figure 4.5 (a)). Figure 4.11 (b) and (c) show the CT specimens' fracture surfaces under R0.7_FE-2 and R0.5_FE-4 test conditions, respectively. Under these test conditions, the crack length on the free surface is higher than in the thickness direction suggesting the occurrence of secondary crack coalescence and the extension of the preexisting crack. Figure 4.11 (d) and (e) shows the fracture surface of the CT specimens tested at *R*-ratio = 0.5 at frequencies of 10^{-3} Hz, and 10^{-2} Hz, respectively. Crack coalescence is evident in both conditions. This observation is in accordance with Figure 4.6, which shows an increasing trend in the density of intergranular crack density at the cyclic plastic zone with increasing load cycle frequency. It can be concluded that large load cycles assist the crack propagation through the initiation and coalescence of secondary cracks in the cyclic plastic zone.

Figure 4.12 depicts the HpHSCC crack growth rates on the side face of the CT specimens under different constant amplitude loading conditions. The minimum crack growth rate was 8×10^{-9} mm/s and was obtained under the R0.9_5E-3 test condition, where the *R*-ratio was 0.9, and the frequency was 5×10^{-3} Hz. On the other hand, the R0.5_E-2 test condition yields the highest crack growth rate. According to Figure 4.12, the HpHSCC crack growth at Stage 1b is sensitive to the load cycles' characteristics so that the maximum crack growth rate was found on CT specimens under the largest and most rapid load changes. Two significant trends are evident in the crack growth behaviours reported in Figure 4.12. First, the crack growth rate increases as the amplitude of load fluctuation increases, *i.e.*, decreases in *R*-ratio. Secondly, the crack propagates faster at a higher frequency of cycling under the same *R*-ratio. These trends are in accordance with metallographic observations and fractographic examinations. Accordingly, the secondary crack initiated in the cyclic plastic zone contributes to crack propagation of a single crack at this stage.

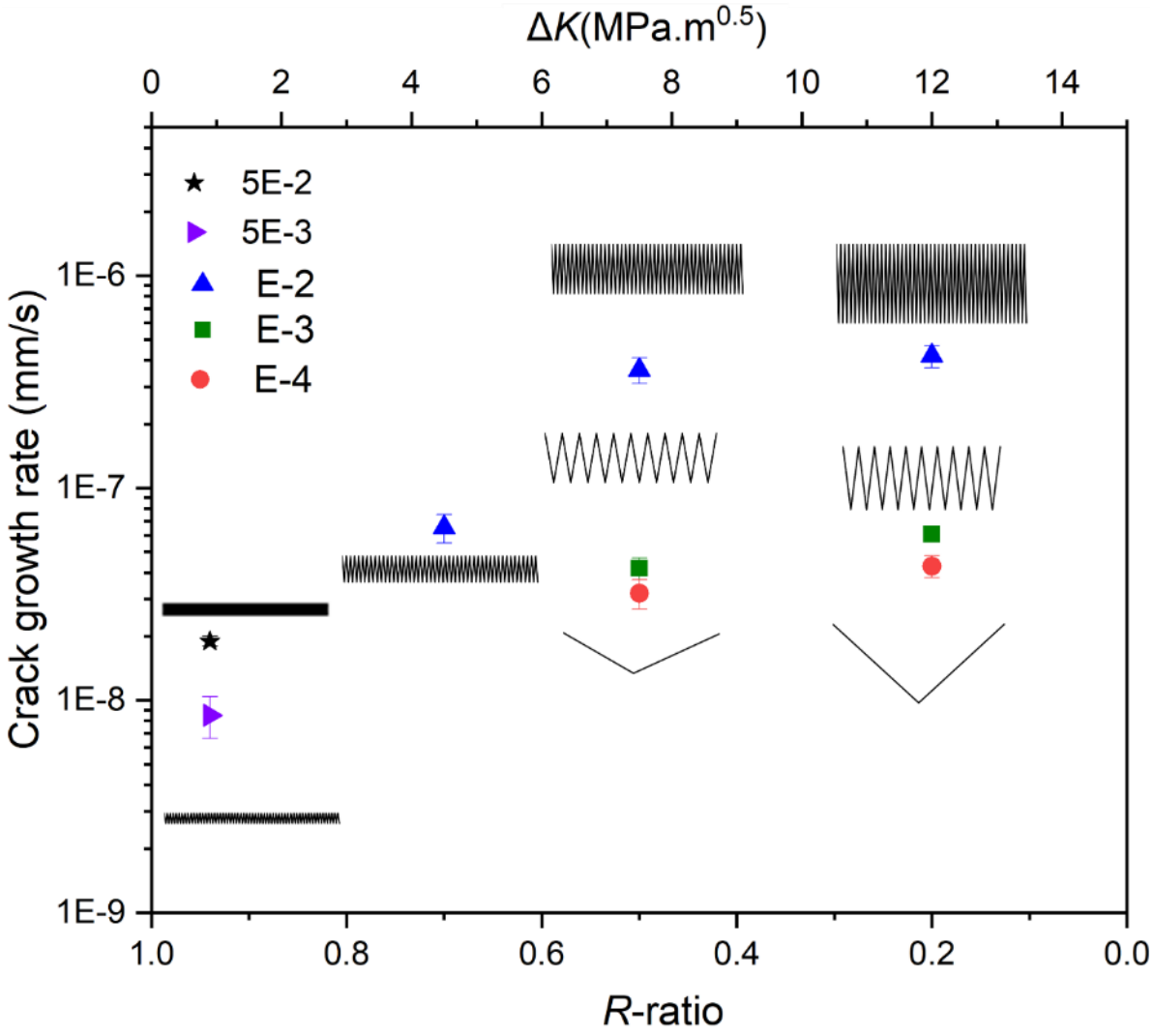

Figure 4.12. Variation of crack growth rates on the side face of the CT specimens under different constant amplitude loading scenarios.

4. 4 The Implication for Pipeline Operators

For pipelines vulnerable to HpHSCC, where environmental prerequisites for HpHSCC are established, intergranular cracks are most likely to initiate at metallurgical discontinuities. Although the maximum allowable hoop stress for the pipeline is less than 72% of the specified minimum yield strength, HpHSCC cracks can form at the metallurgical discontinuities where operating stress is intensified and can reach the yield stress. Other stress sources such as residual

stress can be added to the hoop stress and help provide the threshold stress for cracking. It has been shown that internal pressure fluctuations assist crack initiation. Cracks initiate at multiple sites. When the first intergranular cracks emerge on the surface of the pipe, they will act as stress risers. The neighboring area to the initiated crack, where the stress is intensified, is a breeding ground for secondary crack initiation. Similar to the initiation of the first crack, secondary crack initiation is facilitated by load fluctuations. In the presence of large load fluctuation, particularly high-frequency ones, a high density of tiny secondary cracks forms close to the main crack tip. Then crack coalescence in this region causes the existing crack to propagate. According to Equation 4. 8, the tendency for crack coalescence increases when the average length of two adjacent cracks increases. When two large cracks coalesce on the free surface, the mechanical driving force in the crack depth increases significantly. If K_{depth} exceeds K_{ISCC}, Stage 2 of crack propagation starts where crack propagates continuously through an anodic dissolution mechanism. It can be concluded that rapid and large load cycles have negative impacts on the pipeline lifetime. Therefore, controlling the pressure fluctuation to decrease either or both their amplitude and frequency will delay the onset of Stage 2, as shown in Figure 4.13. This illustration assumes that the crack nucleation and Stage 2 of HpHSCC crack growth are independent of load condition.

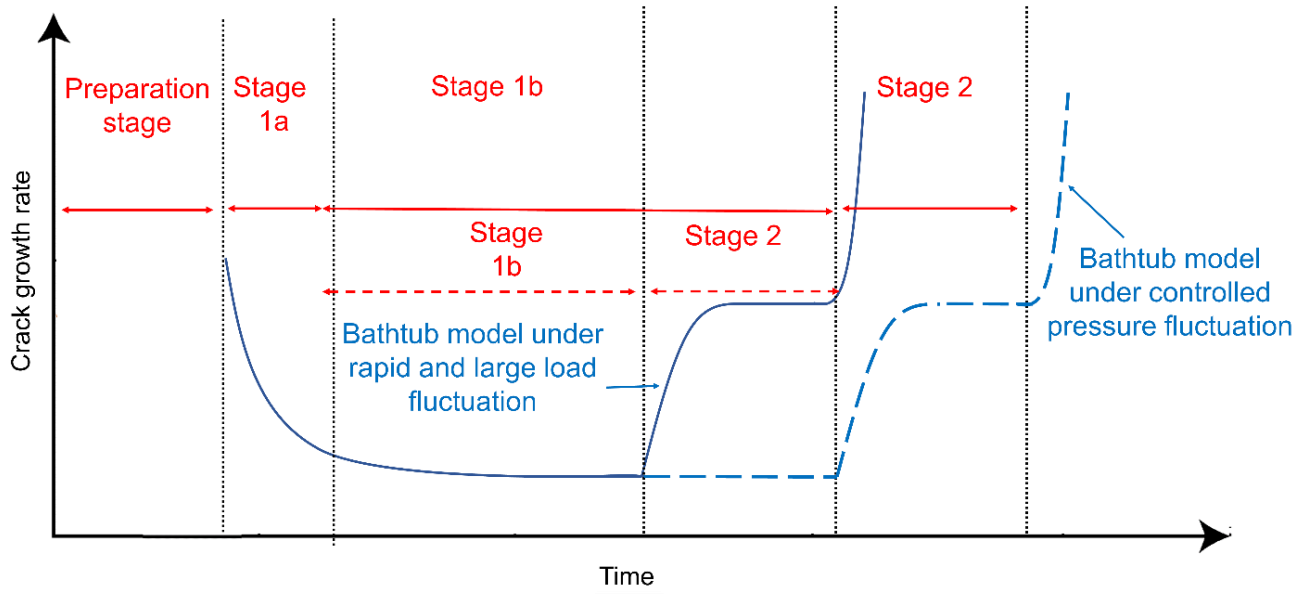

Figure 4.13. Schematic illustration of the bathtub model under uncontrolled load fluctuation and controlled load fluctuation.

4. 5 Conclusion

The effect of pressure fluctuations on HpHSCC crack growth behaviour at Stage 1b (where $K_{max}<K_{ISCC}$) were studied in an aqueous solution of 0.5 M Na_2CO_3 and 1 M $NaHCO_3$ at 40 °C and applied cathodic protection of -590 mV_{SCE}. It was observed that the crack growth during Stage 1b is sensitive to the size of the load fluctuations and the cycling frequency. The main findings of this research are as follows.

- This research was one of the first systematic studies on Stage 1b of HpHSCC crack growth. The current study provides insight into the fact that there are preferential regions for secondary crack initiation in Stage 1b. Accordingly, crack propagation in Stage 1b is not a random process and depends on loading characteristics.
- A number of intergranular cracks initiate in the plastic zone of the preexisting crack. Intensified stress in this zone ruptures the passive film at the grain boundaries, and some

of the grain boundaries persist in film-free conditions. Anodic dissolution at these bare grain boundaries causes the formation of intergranular cracks. The intergranular cracks can be classified into four groups based on their relative distance from the preexisting crack tip *viz.* cracks initiated at the boundary of the actual plastic zone, cracks nucleated in the theoretical plastic zone, cracks nucleated in the cyclic plastic zone, and cracks nucleated at or ahead of the preexisting crack.

- Large load fluctuations generate a cyclic plastic zone at the crack tip. The cumulative strain is developed in this region. Depending on the strain rate, film free conditions formed on the grain boundaries located in this region. Therefore, the intergranular crack density in the cyclic plastic zone is comparatively higher than in the other zones. These tiny cracks are close to the main crack tip; therefore, these cracks coalesce to the main crack easily and cause the preexisting crack to propagate.
- Increasing the length of individual cracks increases the chance for large crack coalescence accompanied by an acceleration of the onset of Stage 2.
- The crack initiation dependency on the frequency of the load cycles suggests there is a critical strain rate rather than threshold stress for crack initiation. Further investigations that consider grain boundaries characteristics, strain distribution, and localized strain rates at the grain boundaries within the plastic zone are suggested to prove this postulate.

References:

[1] C.I. Ossai, B. Boswell, I.J. Davies, "Pipeline failures in corrosive environments – A conceptual analysis of trends and effects American Society of Mechanical Engineers," Engineering Failure Analysis 53, (2015), p. 36–58.

[2] R. Pourazizi, M.A. Mohtadi-Bonab, J.A. Szpunar, “Investigation of different failure modes in oil and natural gas pipeline steels,” Engineering Failure Analysis 109, (2020), p. 104400.

[3] W. Chen, “Modeling and prediction of stress corrosion cracking of pipeline steels,” in A. M, El-Sherik (Eds), Trends in oil and gas corrosion research and technologies, Woodhead Publishing, Boston, 2017, pp. 707–748.

[4] A. W. Peabody, R. L. Bianchetti, “Control of pipeline corrosion,” Second ed., NACE, Houston, 2000, p. 5-47.

[5] I. Thompson, J.R. Saithala, “Review of pipeline coating systems from an operator’s perspective,” Corrosion Engineering, Science and Technology 51, 2, (2016), p. 118-135.

[6] G.M. Harris, A. Lorenz, “New coatings for the corrosion protection of steel pipelines and pilings in severely aggressive environments,” Corrosion Science 35, 5 (1993), p. 1417-1423.

[7] F. Mahdavi, M. Forsyth, M.Y.J. Tan, “Techniques for testing and monitoring the cathodic disbondment of organic coatings: An overview of major obstacles and innovations,” Progress in Organic Coatings 105, (2017), p. 163-175.

[8] D. Kuang, Y.F. Cheng, “Study of cathodic protection shielding under coating disbondment on pipelines,” Corrosion Science 99, (2015), p. 249-257.

[9] Z. Abbasi, H. Niazi, M. Abdolrazzaghi, W. Chen, M. Daneshmand, “Monitoring pH level using high-resolution microwave sensor for mitigation of stress corrosion cracking in Steel pipelines,” IEEE Sensors Journal 20, 13 (2020), p. 7033-7043.

[10] E.A. Charles, R.N. Parkins, “Generation of stress corrosion cracking environments at pipeline surfaces,” Corrosion 51, 07 (1995), p. 518-527.

[11] National Energy Board, “Stress corrosion cracking on Canadian oil and gas pipelines,” Natl. Energy Board, Calgary, Alberta. (1996).

[12] J.A. Beavers, B.A. Harle, “Mechanisms of high-pH and near-neutral-pH SCC of underground pipelines,” Journal of Offshore Mechanics and Arctic Engineering 123, 3 (2001), p. 147-151.

[13] J. Beavers, T.A. Bubenik, “Stress corrosion cracking,” in A. M, El-Sherik (Eds), Trends in oil and gas corrosion research and technologies, Woodhead Publishing, Boston, 2017, pp. 295–314.

[14] J.A. Beavers, “Integrity management of natural gas and petroleum pipelines subject to stress corrosion cracking,” Corrosion 70, 1 (2014), p. 3-18.

[15] A. D. Batte, R. R. Fessler, J. E. Marr, S. C. Rapp, “Managing the threat of SCC in gas transmission pipelines,” International Pipeline Conference, (2012), IPC2012-90231.

[16] S. A. Shipilov, I. L. May, “Structural integrity of aging buried pipelines having cathodic protection,” Engineering Failure Analysis 13, 7 (2006), p1159-1176.

[17] I. V. Ryakhovskikh, R. I. Bogdanov, V. E. Ignatenko, “Intergranular stress corrosion cracking of steel gas pipelines in weak alkaline soil electrolytes,” Engineering Failure Analysis 94, (2018), p. 87-95.

[18] R.N. Parkins, “1990 Plenary lecture: strain rate effects in stress corrosion cracking,” Corrosion 46, 3 (1990), p. 178-189.

[19] T. R. Baker, R. N. Parkins, G. G. Rochfort, “Investigations relating to stress corrosion Cracking on the pipeline authority’s Moomba-to-Sydney pipeline,” Proceedings 7th Symposium Line Pipe Research (1986), p. 21-27.

[20] H. Niazi, R. Eadie, W. Chen, H. Zhang, “High pH stress corrosion cracking initiation and crack evolution in buried steel pipelines: a review,” Engineering Failure Analysis 120, (2021), 105013.

[21] R.N. Parkins, E. Belhimer, W.K.Blanchard. “Stress corrosion cracking characteristics of a range of pipeline steels in carbonate-bicarbonate solution,” Corrosion 49, 12 (1993), p. 951-966.

[22] R. R. Fessler, T. J. Barlo, “Threshold-stress determination using tapered specimens and cyclic stresses environment-sensitive fracture: evaluation and comparison of test methods,” (West Conshohocken, PA: ASTM International, 1984), p. 368-382.

[23] Y.-Z. Wang, J.D. Atkinson, R. Akid, R.N. Parkins, “Crack interaction, coalescence and mixed mode fracture mechanics,” Fatigue & Fracture of Engineering Materials & Structures 19, 4 (1996), p. 427-439.

[24] R.N. Parkins, P.M. Singh, “Stress corrosion crack coalescence,” Corrosion 46, 6 (1990), p. 485-499.

[25] W. Chen, J. Zhao, K. Chevil, E. Gamboa, B. Alvarado, “Threshold Geometrical Dimensions of Stage II Cracks Versus Required Resolution of Crack-Detection Techniques,” International Pipeline Conference, (2018). IPC2018-78751.

[26] R.N. Parkins, B.S. Greenwell, “The interface between corrosion fatigue and stress-corrosion cracking,” Metal Science 11, (1977), p. 405–413.

[27] B. N. Leis, R. N. Parkins, “Mechanics and material aspects in predicting serviceability limited by stress-corrosion cracking,” Fatigue and Fracture of Engineering Materials and Structures 21, 5 (1998), p. 583-601.

[28] A.K. Pilkey, S.B. Lambert, A. Plumtree, “Stress corrosion cracking of x-60 line pipe steel in a carbonate-bicarbonate solution,” Corrosion 51, 2 (1995), p. 91-96.

[29] H. Niazi, H. Zhang, K. Korol, W. Chen, “High pH crack growth sensitivity to underload-type of pressure fluctuations,” International Pipeline Conference, (2018). IPC2018-78394.

[30] H. Niazi, K. Chevil, E. Gamboa, L. Lamborn, W. Chen, H. Zhang, “Effects of loading spectra on high pH crack growth behaviour of X65 pipeline steel”, Corrosion 76, 6 (2020), p. 601-615.

[31] J. Griggs, E. Gamboa, “A review of modelling high pH stress corrosion cracking of high pressure gas pipelines,” Materials and Corrosion 67, (2015), p. 251–263.

[32] B.T. Lu, “Further study on crack growth model of buried pipelines exposed to concentrated carbonate–bicarbonate solution,” Engineering Fracture Mechanics 131, (2014), p. 296-314.

[33] L. Yan, R. Worthingham, F. King, J. Been, “Factors Affecting the generation of high-pH environments required for stress corrosion cracking (SCC),” International Pipeline Conference, (2012) IPC2012-90515.

[34] R.N. Parkins, S. Zhou, “The stress corrosion cracking of C-Mn steel in CO_2-HCO_3^--CO_3^{2-} solutions. I: Stress corrosion data,” Corrosion Science 39, 1 (1997), p. 159-173.

[35] R.N. Parkins, S. Zhou, “The stress corrosion cracking of C-Mn steel in CO_2-HCO_3^--CO_3^{2-} solutions. II: Electrochemical and other data,” Corrosion Science 39, 1 (1997), p. 175-191.

[36] R.N. Parkins, “The application of stress corrosion crack growth kinetics to predicting lifetimes of structures,” Corrosion Science 29, 8 (1989), p. 1019-1038.

[37] M. Yu M, X. Xing, H. Zhang, J. Zhao, E. Eadie, W. Chen, J. Been, G. Van Boven, R. Kania, “Corrosion fatigue crack growth behaviour of pipeline steel under underload-type variable amplitude loading schemes,” Acta Materialia 96, (2015), p. 159-169.

[38] ASTM E647-15e1 Standard test method for measurement of fatigue crack growth rates, ASTM International, West Conshohocken, (2015), p. 1–49.

[39] H. Niazi, H. Zhang, L. Lamborn, W. Chen, “The impact of pressure fluctuations on the early onset of stage II growth of high pH stress corrosion crack,” International Pipeline Conference, IPC2020-14744.

[40] E. Sadeghi Meresht, T. Shahrabi Farahani, J. Neshati, “Failure analysis of stress corrosion cracking occurred in a gas transmission steel pipeline,” Engineering Failure Analysis 18, (2011), p. 963–970.

[41] R. N. Parkins, “Predictive approaches to stress corrosion cracking failure,” Corrosion Science 20, 2 (1980), p.147-166.

[42] N. J. H. Holroyd, R. N. Parkins, “The predictability of stress corrosion cracking susceptibility of steels in acetate solutions from potentiodynamic polarization curves,” Corrosion Science 20, 6 (1980), p. 707-721.

[43] J. Might, D. J. Duquette, “Stress corrosion cracking of high-purity carbon Steel in carbonate solutions,” Corrosion 52, 6 (1996), p. 428-434.

[44] R. N. Parkins, “Mechanistic aspects of intergranular stress corrosion cracking of ferritic steels,” Corrosion 52, 5 (1996), p. 363-374.

[45]. R. N. Parkins, “Localized corrosion and crack initiation,” Materials Science Engineering A 103, 1 (1988), p. 143-156.

[46]. S. Wang, H. Niazi, L. Lamborn, W. Chen, “Strain-shock-induced early stage high pH stress corrosion crack initiation and growth of pipeline steels,” Corrosion science 178, (2021), 109056.

[47] T.L. Anderson, “Fracture Mechanics: Fundamentals and Applications,” CRC Press, Boca Raton, Florida, USA (2017), p. 457-464.

[48] S.K. Paul, S. Tarafder, “Cyclic plastic deformation response at fatigue crack tips,” International Journal of Pressure Vessel and Piping 101, (2013), p. 81–90.

[49] R. Hosseini, R. Seifi, “Fatigue crack growth determination based on cyclic plastic zone and cyclic J-integral in kinematic–isotropic hardening materials with considering Chaboche model,” Fatigue & Fracture of Engineering Materials Structures 43, 11 (2020), p.2668-2682.

[50] C. Jingjie, H. Yi, D. Leilei, L. Yugang, “A new method for cyclic crack-tip plastic zone size determination under cyclic tensile load,” Engineering Fracture Mechanics 126, (2014), p. 141-154.

[51] A. T. Taddesse, S, -P. Zhu, D. Liao D, B. Keshtegar, “Cyclic plastic zone-based notch analysis and damage evolution model for fatigue life prediction of metals,” Materials & Design 191, (2020), 108639.

[52] W. Chen, H. Zhu, S. -H. Wang, “Low temperature creep behaviour of pipeline steels,” Canadian Metallurgical Quarterly 48, 3 (2009), p. 271-283.

[53] S, -H. Wang, Y. Zhang Y, W. Chen, “Room temperature creep and strain-rate-dependent stress-strain behaviour of pipeline steels,” Journal of Materials Science 36, (2001), p. 1931-1938.

[54] J. T. Evans, R. N. Parkins, “Creep induced by load cycling in a C-Mn steel,” Acta Metallurgica 24, 6 (1976), p. 511-515.

[55] B.N. Leis, “Some aspects of stress-corrosion-cracking analysis for gas transmission pipelines,” in Proceeding of Metallurgical Society of Canadian Institute of Mining and Metallurgy, Material Performance Maintenance, Pergamon, Oxford, (1991), pp. 107–121.

[56] W. Chen, S.-H. Wang, R. Chu, F. King, T.R. Jack, R.R. Fessler, “Effect of precyclic loading on stress-corrosion-cracking initiation in an X-65 pipeline steel exposed to near-neutral pH soil environment,” Metallurgical and Materials Transactions A. 34, (2003), p. 2601–2608.

[57] A. Roccisano, S. Nafisi, R. Ghomashchi, “Stress corrosion cracking observed in ex-service gas pipelines: a comprehensive study,” Metallurgical and Materials Transactions A 51, (2020), p. 167-188

[58] M. A. Arafin, J. A. Szpunar, “A new understanding of intergranular stress corrosion cracking resistance of pipeline steel through grain boundary character and crystallographic texture studies,” Corrosion Science 51, 1, (2009), p. 119-128.

Chapter 5 Effects of Load Interactions on the Onset of Stage Two of High pH Stress Corrosion Cracking[1]

5. 1 Introduction

High pH stress corrosion cracking (HpHSCC) is a type of environmentally assisted cracking (EAC) in buried pipeline steels that occurs when the following three requirements are met [1][2]:

1- Exposure to a potent environment for HpHCC. The required environmental characteristics for HpHSCC are the formation of a high concentration carbonate-bicarbonate solution beneath the coating defects and partial loss of cathodic protection [3–5].

2- The pipeline steel is susceptible to HpHSCC [6][7].

3- The pipe is subjected to sufficient tensile stress (applied stress plus residual stress) [1,8].

In the best-case scenario of protection, all the contributing parameters could be controlled to prevent the occurrence of HpHSCC unconditionally. A more realistic solution is preventing HpHSCC by removing one of the requirements mentioned above. This includes efforts undertaken before the installation of the pipe and during the pipe operation. The actions before installation include but are not limited to improving the coating system, enhancing the cathodic protection, and improving the steel's resistance to intergranular cracking. Improved coating systems decrease the chance for the generation of HpHSCC environment by preventing the formation of coating

[1] A version of this chapter is accepted for publication as H. Niazi, Sh. Wang, L. Lamborn, R. Eadie, W. Chen, H. Zhang, "Effects of Load Interactions on the Onset of Stage Two of High pH Stress Corrosion Cracking," Journal of Pipeline Science and Engineering.

defect, penetration of groundwater, and diffusion of the chemical species beneath the coating [4,9,10]. Enhancing the cathodic protection [11] also prevents the formation of the HpHSCC environment by providing sufficient protection in the disbonded area and maintaining the potential out the cracking potential window. Steel's resistance to intergranular cracking can be improved by several methods, such as avoiding tensile residual stress on the pipe's external surface or imposing compressive residual stress [1,12]. The residual tensile stress on the free surface of the pipe can be added to the hoop stress and provide the mechanical driving force for crack initiation [1,2]. Additionally, grain boundary modification, such as fabrication of steels containing low angle grain boundaries and coincidence site lattice (CSL) rather than random high angle grain boundaries, might improve the steel's resistance to cracking as cracks always propagate through high angle grain boundaries [13,14]. Controlling phase composition of the steel, in particular, using the more uniform microstructure such as bainitic microstructure increases the threshold stress for crack initiation [7].

Furthermore, the pipeline's design and operation are important to reduce field tensile stresses and ensure that the pipes are operated below the maximum allowable hoop stresses [15, 16]. During the pipeline operation, monitoring the coating condition and effectiveness of cathodic protection is mandatory to ensure that a HpHSCC environment is not formed [4,9,10]. Of particular note in this paper, the operating conditions, particularly the pressure fluctuations, can be controlled to not only meet the design goals but to minimize the early stages of crack propagation. Despite the designs and best practices mentioned above, the HpHSCC environment sometimes forms near coating defects in some pipes. Thereafter, an understanding of crack initiation and crack evolution is necessary to predict the pipes' reliable lifetime for safe operation. Parkins proposed the primary model for HpHSCC growth behaviour, which has been dubbed the "bathtub model" [1,17,18].

This model shows the time-dependent behaviour of HpHSCC and a slightly revised version of this model is shown in Figure 5.1. Based on this model, four sequential stages are leading to failure for HpHSCC [1,17,18]:

1. The emergence of small intergranular facets on the free surface of the pipe (stage 1a).
2. Continuous nucleation of intergranular cracks followed by cracks coalescence to form a crack capable of providing the mechanical driving force for sustainable crack propagation (stage 1b). The threshold for stage 2 can be defined as a critical stress intensity factor (K_{ISCC}) under static loading conditions or a critical range of the stress intensity factor (ΔK_{th}) under cyclic loading conditions [1, 2].
3. Sustainable crack growth caused by repeated formation and rupture of the passive film at the crack tip (stage 2).
4. Rapid crack growth to rupture or leakage of the pipe (stage 3).

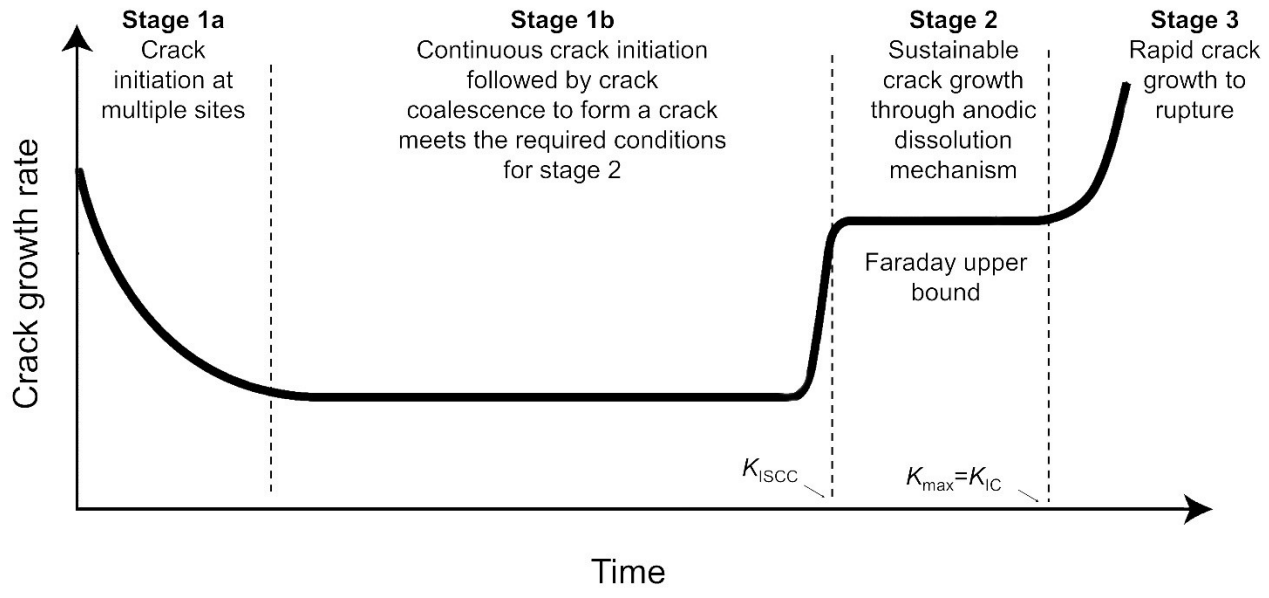

Figure 5.1. Schematic illustration of the bathtub model for HpHSCC after Parkins [1,2,18,19].

The current trends in the modelling of HpHSCC have narrowed down the bathtub model to get a more accurate fit with the field observations. There are two main drawbacks related to the bathtub model. First, stage 1b, which is lifetime-determining in HpHSCC modelling, rests on the assumption that cracks initiate randomly [19]. However, our previous studies have shown that the preexisting cracks' plastic zone is a preferential location for new crack initiation [20]. In this region, the stress magnification assists crack initiation and coalescence within the crack tip plastic zone. Accordingly, the crack growth is highly dependent on the characteristics of load fluctuation, including stress ratio (*R*-ratio) and frequency of load cycles. The crack growth rates under constant amplitude loading waveforms follow two major trends. First, the crack growth rate increases as the stress ratio (*R*-ratio) decreases, *i.e.,* the magnitude of load fluctuation increases. Second, the crack propagation rate increases by increasing load cycle frequency, *i.e.,* higher loading/unloading rates [20].

Secondly, constant amplitude (CA) loading waveforms were employed to develop this model. However, pipelines, like other engineering components, experience variable amplitude cyclic loading during their service. It has been shown that load interactions within these variable amplitude cycles can either accelerate or decelerate crack growth kinetics during fatigue in the presence of overload or underload cycles, respectively [21,22]. This consideration proved to be quite important for near-neutral-pH stress corrosion cracking [16,23–26]. Therefore, to ensure the integrity and safe operation of the cracked pipes, load interaction considerations should be considered. According to pipeline experience, more than 90 percent of HpHSCC failures happen in the first 30 km downstream from the pump or compressor station. This region's pressure fluctuation is known as type I or the underload type of pressure fluctuation [1,2,15,26,27]. A schematic illustration of this type of loading condition is shown in Figure 5.2. The maximum

applied hoop stress under this loading condition is controlled to be below 80% of specified minimum yield strength (SMYS). The loading waveform involves both small and large cycles, which are so-called minor cycles and underload cycles, respectively. Minor cycles are characterized by a high-stress ratio (*R*-ratio = minimum load/maximum load), and they are much more frequent than major underload cycles (low *R*-ratio cycles) [1,26], particularly in the case of mainline gas pipelines.

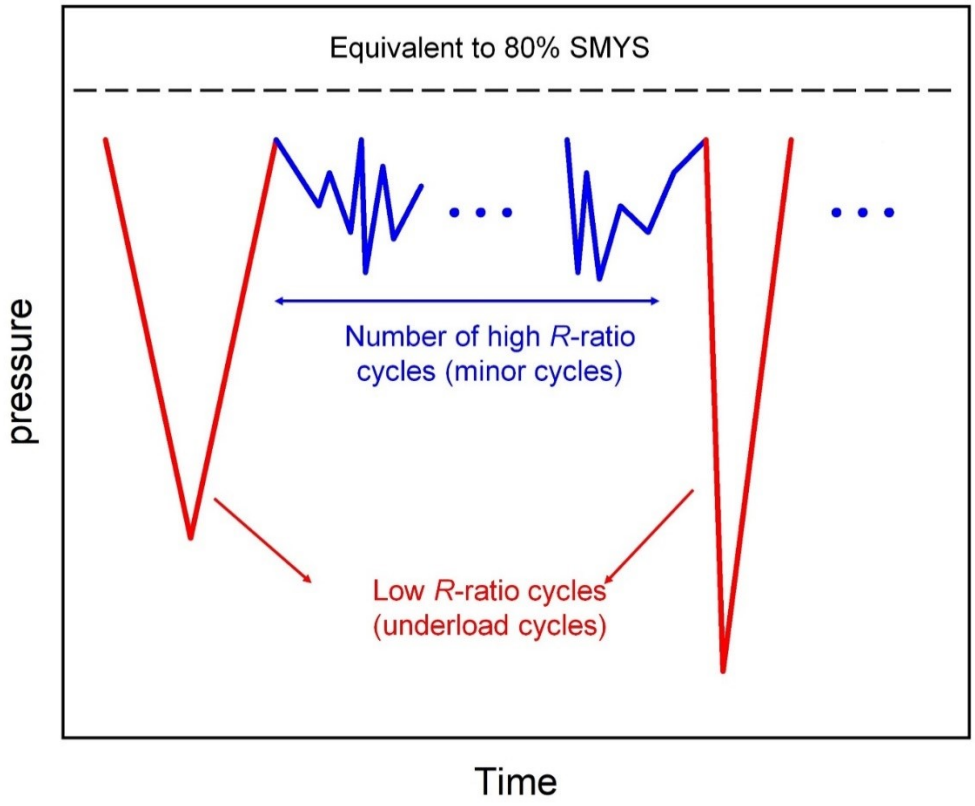

Figure 5.2. Schematic illustration of the load fluctuation in the pipeline up to 30 km downstream from a pump or compressor station, where more than 90 percent of HpHSCC failures occur.

This paper investigates stage 1b of HpHSCC crack growth behaviour by applying several variable amplitude loading conditions to pre-cracked compact tension specimens. The crack morphologies on the free surface of the CT specimens are analyzed. The length of the cracks on the fracture

surfaces of the specimens are measured, and the crack growth rates are calculated accordingly. A comparison between crack growth rates under constant and variable amplitude loading waveforms is made. The similarities between crack growth behaviour under variable amplitude loading waveform are elaborated to identify the predominant parameter for crack propagation at stage 1b. The load interactions between the high and low *R*-ratio cycles are discussed.

5. 2 Experimental Procedure

In this study, compact tension (CT) specimens with linear dimensions shown in Figure 5.3 were machined from API- 5L Grade X65 pipeline steel with a wall thickness of 12 mm and an outer diameter of 1067 mm. Table 5.1 displays the chemical composition of the steel. X65 pipeline steel is widely used in oil and gas buried pipelines, and it is reported as susceptible steel to HpHSCC [13,14]. The machined notch was oriented perpendicular to the hoop stress direction. Consequently, crack propagation was parallel to the pipe's longitudinal direction, the same orientation observed in the field. The sample preparation included mechanical polishing using abrasive papers up to 600 grit and ultrasonically cleaning in acetone for 15 min. After that, air fatigue pre-cracking was conducted in compliance with ASTM E647-08 to produce a sharp crack extending from the root of the notch [28]. The final length of the fatigue pre-crack was controlled to be 2.5±0.2 mm on each side of the CT specimen. Using pre-cracked specimens provides the opportunity to know precisely the crack tip's stress intensity factor [29]. Stress intensity factor was calculated through Equation 5. 1

$$K = \frac{P}{B\sqrt{W}} f\left(\frac{a}{W}\right) \qquad \text{Eq'n. 5. 1}$$

where *B* is specimen thickness, *P* is the applied load to CT specimen, a and W are shown in Figure 5.3. In this equation, the dimensionless factor of *f(a/W)* is known as a geometrical factor and can be expressed by Equation 5. 2 for pre-cracked CT specimen.

$$f(W)=\frac{a+\frac{a}{W}}{\left(1-\frac{a}{W}\right)^{\frac{3}{2}}}\left[0.886+4.64\left(\frac{a}{W}\right)-13.32\left(\frac{a}{W}\right)^{2}+14.72\left(\frac{a}{W}\right)^{3}-5.60\left(\frac{a}{W}\right)^{4}\right]$$

Eq'n. 5. 2

Table 5.1. Elemental composition of the X65 pipeline steel

Element	C	Mn	P	Si	Ni	Cr	Mo	Cu	V	Ni	Ti	Al	Fe
Wt %	0.06	1.43	0.01	0.31	0.06	0.06	0.02	0.21	0.03	0.07	0.01	0.02	Balance

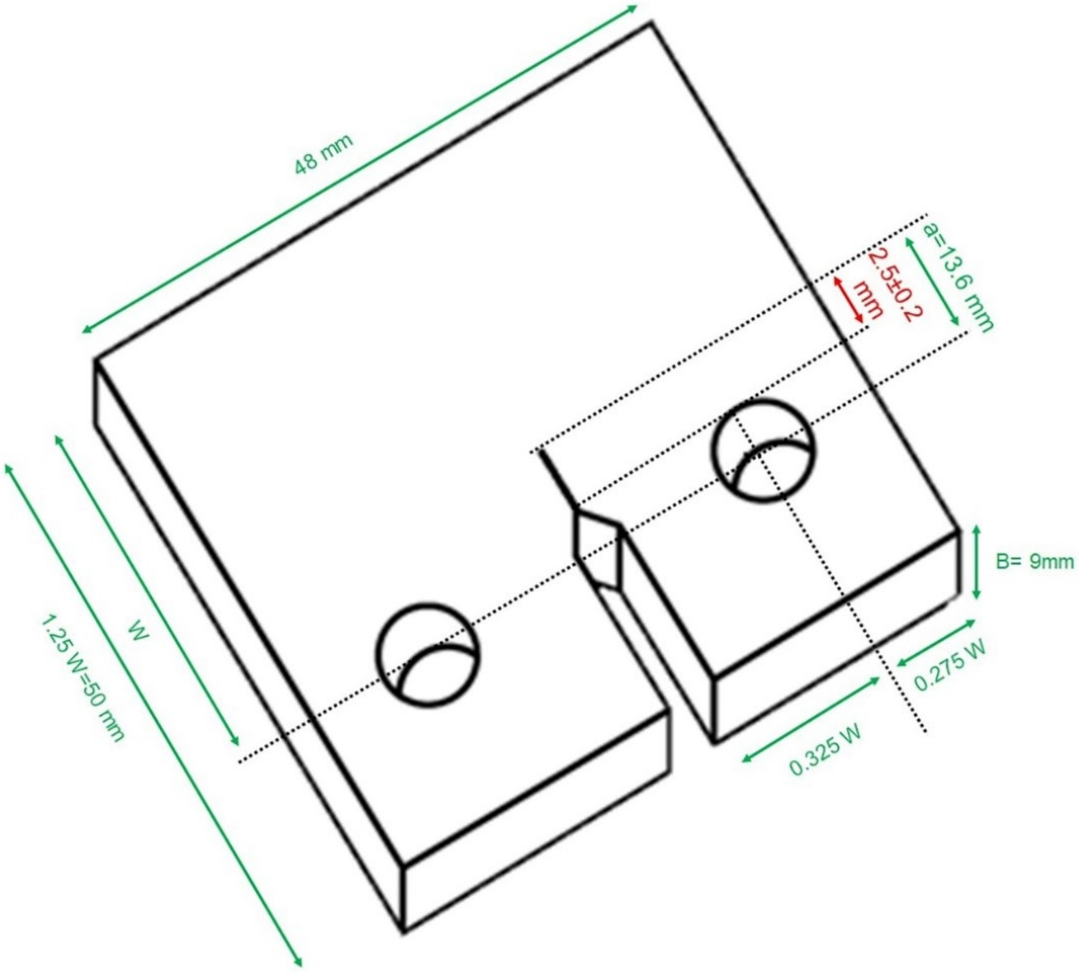

Figure 5.3. Drawing of the used CT specimens in this study

The experimental set-up for the current test included two separate cells. The HpHSCC tests were conducted in the two cells concurrently so that the cells replicate one another. In each cell, a pre-cracked CT specimen acted as a cathode, and a stainless-steel ribbon that surrounds the CT specimen acted as an auxiliary electrode. The HpHSCC tests' electrolyte was an aerated aqueous solution composed of 0.5 M Na_2CO_3 and 1 M $NaHCO_3$ at a temperature of 40 °C. Although the chemical composition of the electrolyte was identical to the standard solution for HpHSCC (known as 1N Na_2CO_3 and 1 N $NaHCO_3$), the temperature was adjusted to 40 °C rather than 75 °C to be consistent with the field observation in Canada as determined by the National Energy Board report [30]. The potential of the pre-cracked CT specimens was maintained at -590 mV versus Saturated Calomel Electrode (SCE) by employing a potentiostat. This potential was selected within the cracking range reported in the literature [31–33]. Our previous research showed that these environmental conditions produce HpHSCC in steel pipelines [32–34].

Load application was initiated only 24 hours after the test cells had been set up to allow equilibrium to be established in temperature and potential. The pre-cracked CT specimens were loaded in the test environment by employing a horizontal pneumatic loading frame. The prerequisite for studying the load interaction at stage 1a of HpHSCC crack growth is to determine the stress intensity factor that guarantees the crack is at stage 1b. Hence, blocks of variable amplitude loading waveforms composed of an underload cycle followed by 50 minor cycles were applied to the pre-cracked CT specimens at three different maximum stress intensity factors *viz.* 36, 20, and 15 $MPa.m^{0.5}$. The frequency of underload cycles was selected based on the Canadian SCADA (Supervisory Control and Data Acquisition) for these tests. The details of the loading waveform are reported in Table 5.2.

Table 5.2. Details of variable amplitude loading waveforms to determine the stress intensity factor associated with stage 1b

Sample ID	K_{max} (MPa.m$^{0.5}$)	**Minor cycles**			**Underload cycles**			Number of blocks
		R	Frequency (Hz)	Number of minor cycles	*R*	Frequency (Hz)	Number of underload cycle	
K36	36	0.9	4.6×10^{-3}	50	0.5	9.6×10^{-5}	1	100
K20	20	0.9	4.6×10^{-3}	50	0.5	9.6×10^{-5}	1	100
K15	15	0.9	4.6×10^{-3}	50	0.5	9.6×10^{-5}	1	120

Based on the test results, the tests at a K_{max} of 15 MPa.m$^{0.5}$ showed the crack growth characteristics of stage 1b, as will be discussed later in the results and discussion section. Therefore, this K_{max} was selected for further tests in this study. Eight variable amplitude loading conditions were designed and applied to pre-cracked CT specimens. The variable triangular waveforms were composed of high and low *R*-ratio cycles. Triangular waveform was selected to be consistent with previous research on HpHSCC [2,32,35] and NNpHSCC [25,27]. The advantage of the triangular waveform is to keep the loading/unloading rate the same for the whole cycle duration. The disadvantage of the triangular waveform is drastic changes in pressure at the peak or trough of the load cycle. In the real world, pressure changes are gradual and slower at the peak and trough of the load cycles. The high and low *R*-ratio cycles were identical to our previous work to draw an analogy between constant amplitude and variable amplitude loading waveforms. The minor cycles represent frequent small load fluctuations; whereas, the major underload cycles stand for the sporadic large load fluctuations typically found in gas mainlines. Four of these waveforms were designed to study the effect of underload cycles. Each block of those waveforms was composed of 50 minor cycles with an *R*-ratio of 0.9 at a frequency of 5×10^{-2} Hz followed by an underload cycle with the *R*-ratio of either 0.5 or 0.2 and a frequency of either 10^{-2} or 10^{-3} Hz. The frequencies for these underload cycles were higher compared to those obtained from SCADA. However, these

frequencies were chosen from the published literature to accelerate tests [32,35,36]. Table 5.3 summarizes the details of those loading waveforms.

Table 5.3. Details of the variable amplitude loading waveforms

Sample ID	K_{max} (MPa.m$^{0.5}$)	**Minor cycles**			**Underload cycles**			Number of blocks
		R	Frequency (Hz)	Number of minor cycles	*R*	Frequency (Hz)	Number of underload cycle	
MU_R0.2_FE-3	15	0.9	5×10^{-2}	50	0.2	10^{-3}	1	1800
MU-R0.2_FE-2	15	0.9	5×10^{-2}	50	0.2	10^{-2}	1	1800
MU-R0.5_FE-3	15	0.9	5×10^{-2}	50	0.5	10^{-3}	1	1200
MU-R0.5_FE-2	15	0.9	5×10^{-2}	50	0.5	10^{-2}	1	1200

Following the above experiments, three loading waveforms were designed composed of an underload cycle with the *R*-ratio of 0.5 at 10^{-2} Hz frequency followed by 100, 200, or 400 minor cycles at *R*-ratio 0.9 and frequency 5×10^{-2} Hz. The load cycles' characteristics were identical to the MU-R0.5_FE-2 condition except for the number of minor cycles between underload events. These tests were designed to study the possible load interactions between the major underload and the minor cycles. Table 5.4 reports the details of these loading waveforms.

Table 5.4. Details of variable amplitude triangular loading waveforms to study the effect of minor cycles

Sample ID	K_{max} (MPa.m$^{0.5}$)	**Minor cycles**			**Underload cycles**			Number of blocks
		R	Frequency (Hz)	Number of minor cycles	*R*	Frequency (Hz)	Number of underload cycle	
100M-R0.5_FE-2	15	0.9	5×10^{-2}	100	0.5	10^{-2}	1	700
200M-R0.5_FE-2	15	0.9	5×10^{-2}	200	0.5	10^{-2}	1	700
400M-R0.5_FE-2	15	0.9	5×10^{-2}	400	0.5	10^{-2}	1	700

To verify the observations related to the effect of underload as well as the load interactions between underload and minor cycles, 225 blocks of variable amplitude loading waveforms composed of 50

minor cycles with an *R*-ratio of 0.9 at a frequency of 5×10^{-3} Hz and an underload cycle with *R*-ratio of 0.5 and frequency of 10^{-3} Hz were applied to the pre-cracked CT specimens.

After each test, the pre-cracked CT specimens were removed from the cells. The CT specimens' free surfaces were mechanically polished using an oil-based suspension of diamond particles to remove the thin black film that covered the surfaces exposed to the test environment. After that, the free surfaces were etched with 5% Nital. A Scanning Electron Microscope (SEM) equipped with Energy Dispersive Spectroscopy (EDS) was used to study the specimens' free surface and the crack paths. Then, all the CT specimens were fractured along the notch in liquid Nitrogen. An aqueous solution composed of 3.5 g/L hexamethylenetetramine and 8 N HCl was used to remove the oxide from the crack walls. The total length of intergranular cracks on the fracture surface was measured and used to calculate the crack growth rates. In this study, the continuous intergranular cracks initiated from the pre-crack tip were considered as the main crack. The term continuous crack refers to the primary intergranular crack extension from the pre-crack tip and the secondary cracks that merged to the primary crack. Stage 1b of HpHSCC is highly dependent on the crack propagation on the free surface of the pipe, *i.e.,* an increase in the crack length on the free surface. Therefore, all the crack propagation rates are based on the measurement of the continuous crack length on the outside edge of the fracture surfaces of the CT specimens. These edges represented the crack propagation on the free surface of the specimens, where materials had been readily exposed to the corrosive environment. An example of the main intergranular crack is labelled in Figure 5.4 and Figure 5.5.

5. 3 Results

5. 3. 1 Visual Observations and Metallography

As stated earlier, the CT specimens were exposed to the test environment 24 hours before the load application. During this time, a black film formed and covered the CT specimens' free surfaces. This black film remained on the free surface of the CT specimens during the test and after removal of the specimens from the test solution. For unstressed steel, the passive film could form on both grains and grain boundaries yet at different rates so that intergranular etching becomes visible. Upon applying sufficient stress, microplastic deformation happens at some grain boundaries that fractures the passive film on grain boundaries [37]. Depending on the microplastic deformation rate, a passive film might or might not form on the penetrating tip of the intergranular corrosion. If the strain rate provides the condition that the film formation is suppressed by film rupturing, intergranular corrosion continues [2, 32]. Further dissolution of the grain boundaries causes the formation of intergranular cracks.

The area near the pre-crack tip, where the applied stress is intensified, could provide the necessary film-free condition on some grain boundaries if the strain rate is sufficient. Therefore, this region is a preferential place for intergranular crack initiation. Figure 5.4 shows high magnification micrographs of a typical crack morphology at the area near the fatigue pre-crack tip in this study. A number of intergranular cracks are conspicuous in this figure. Among these cracks, a single crack is initiated from the fatigue pre-crack tip, labelled as "main intergranular crack." This crack follows a zigzag path along the grain boundaries. However, the crack direction is perpendicular to the load direction on a macro scale.

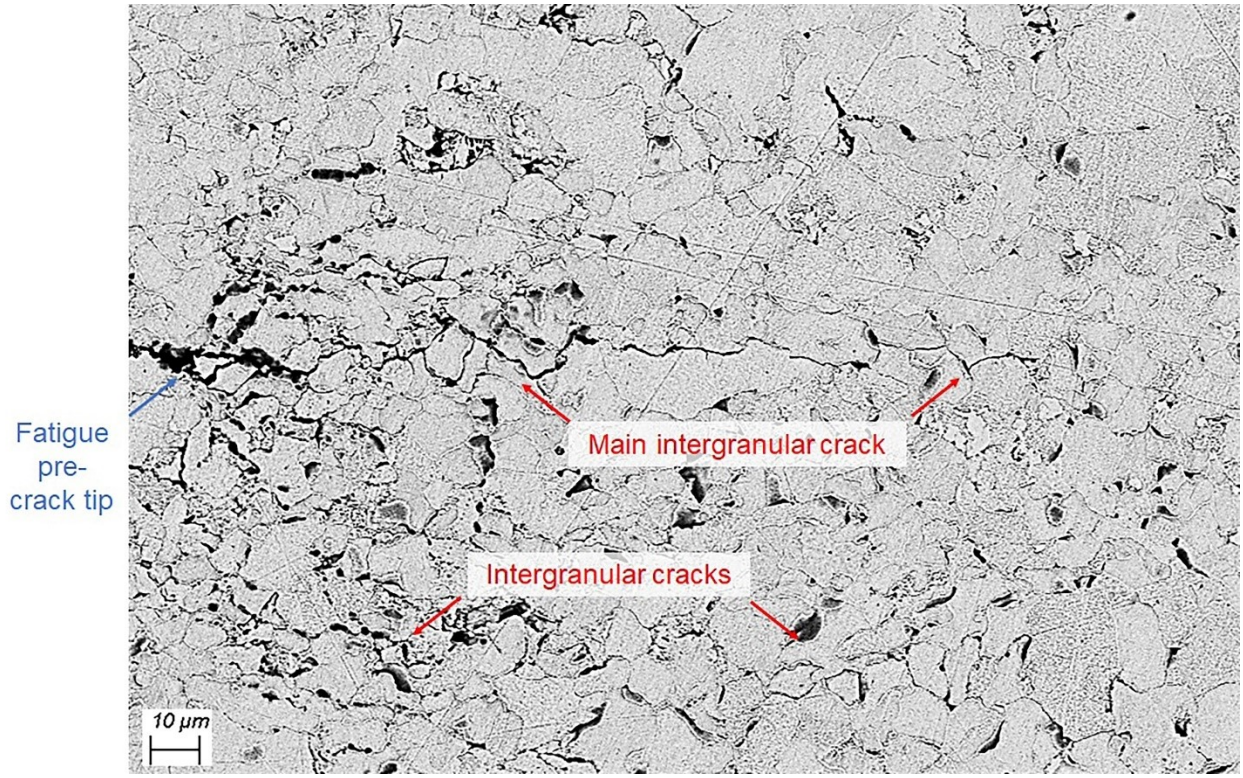

Figure 5.4. High magnification of a typical crack morphology near the fatigue pre-crack tip.

5. 3. 2 Fractography

Figure 5.5 shows a high magnification micrograph of a typical fracture surface of the CT specimens used in this study. In terms of microscopic features, there are three individual regions on the fracture surfaces. On top of the figure, there is a fatigue pre-crack region that possesses transgranular growth characteristics. This region is associated with the fatigue pre-cracking in the air during the sample preparation. A cleavage fracture region on the bottom side represents the rapid crack propagation resulting from laboratory brittle fracture at low temperatures. In the middle of each fracture surface, there is an area that possesses intergranular crack growth characteristics. This intergranular region is associated with crack propagation because of load application during exposure to the HpHSCC environment. The mechanism for intergranular crack propagation is anodic dissolution at the grain boundaries. This mechanism will be discussed in more detail in the

discussion section (Section 5.4.1 and 5.4.2). The line "*AB*" represents the so-called main intergranular crack in the previous section. The intergranular crack lengths on the free surface along the line AB were measured on the specimens' fracture surface to calculate the crack growth rates. The length and depth of the intergranular region vary with loading conditions..

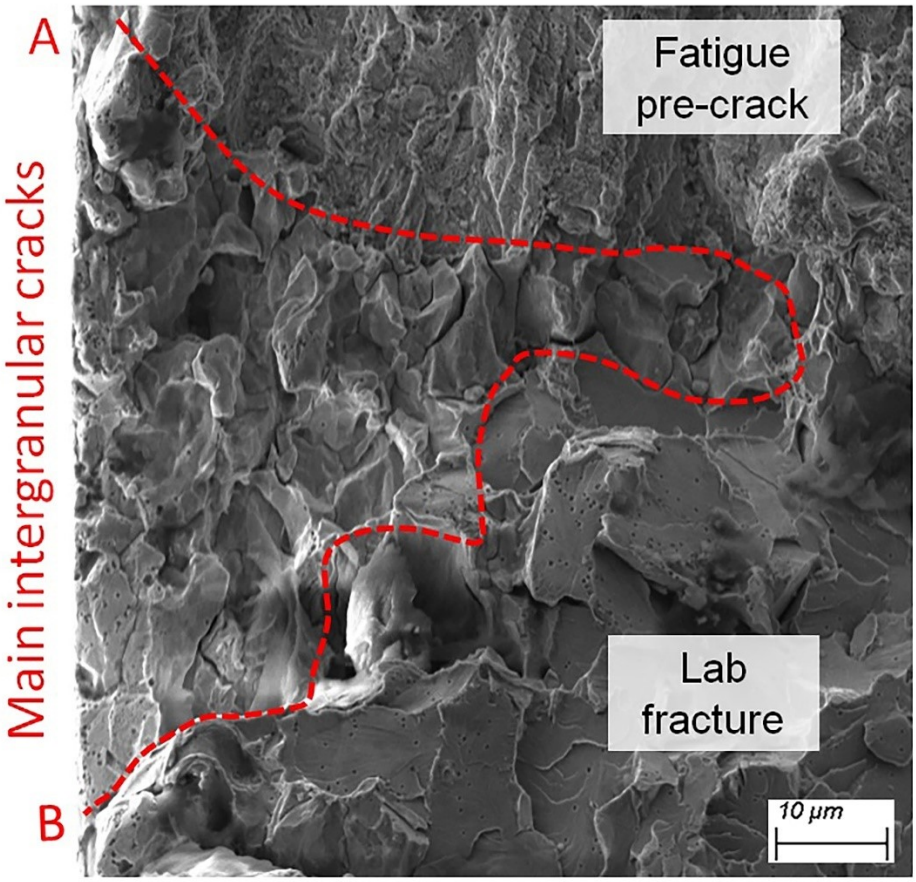

Figure 5.5. High magnification of a typical fracture surface of CT specimens tested at K_{max} of 15 MPa.m$^{0.5}$ showing the main intergranular crack

5. 3. 3 Determination of Stage 1b Conditions

Figure 5.6 (a) to (c) (a) to (c) show fracture surfaces of CT specimens tested under variable amplitude loading waveforms with maximum stress intensity factors of 36, 20, and 15 MPa.m$^{0.5}$, respectively. Each loading waveform block was composed of 50 minor cycles with an *R*-ratio of

0.9 and frequency of 4.6E-3 Hz plus an underload cycle with an *R*-ratio of 0.5 and frequency of 9.6E-5 Hz. There are three individual regions on the fracture surfaces in terms of microscopic features, similar to Figure 5.5. Three major points are conspicuous by drawing a comparison between fracture surfaces in Figure 5.6. First and foremost, the crack growth rate is highly dependent on the magnitude of the maximum stress intensity factor. Indeed, the higher the maximum stress intensity factor, the higher the possibility of forming film-free conditions at the grain boundaries, which leads to more crack advance. Secondly, on the CT specimens' free surface, where the steel was exposed to the test solution, crack growth is higher for all values of K_{max}. Our previous work showed that nucleation of secondary cracks followed by crack coalescence results in more crack advance on the free surface [32,33]. The average crack growth rates under variable amplitude loading waveforms with K_{max} of 36, 20, and 15 MPa.m$^{0.5}$ were 1.5×10^{-7}, 1.1×10^{-7}, and 2.5×10^{-8} mm/s, respectively. Thirdly, the crack propagation was limited to the surface in Figure 5.6 (c), where the K_{max} was 15 MPa.m$^{0.5}$.

The results under a K_{max} of 15 MP.m$^{0.5}$ had the two following characteristics that prove the crack was at stage 1b. First, the crack growth was limited to the free surface. Secondly, the crack growth rate was one order of magnitude smaller than for the other conditions. Hence, a maximum stress intensity factor of 15 MPa.m$^{0.5}$ was selected for further investigation in this study. However, the loading rate was increased to speed up the tests.

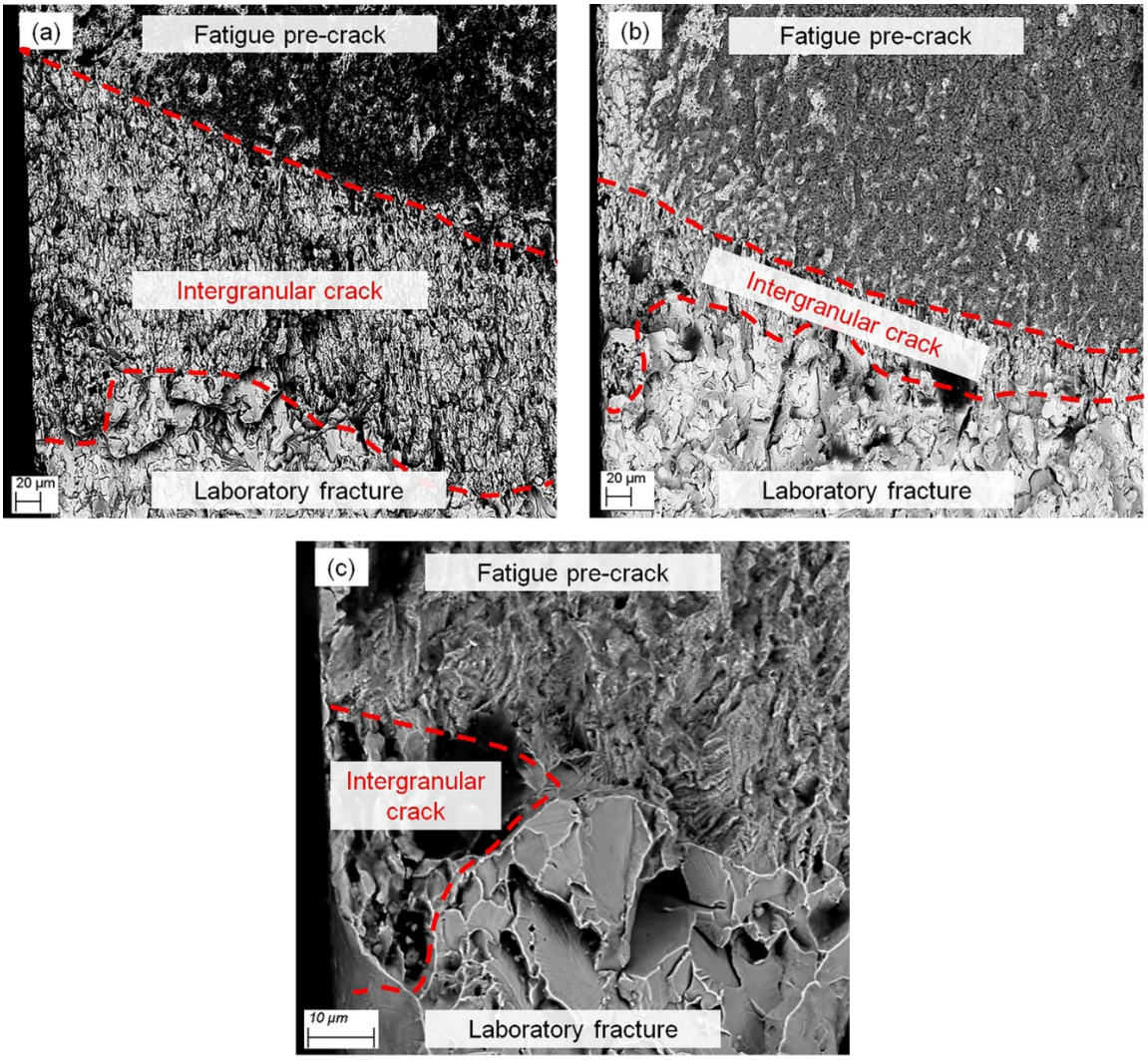

Figure 5.6. The fracture surface of CT specimens near the free surface tested under variable amplitude loading waveforms containing 50 minor cycles with the *R*-ratio of 0.9 at a frequency of 4.6E-3 and an underload with *R*-ratio of 0.5 and frequency of E-4 (a) K_{max}= 36 MPa.m$^{0.5}$ (b) K_{max}= 20 MPa.m$^{0.5}$ (c) K_{max}= 15 MPa.m$^{0.5}$.

5. 3. 4 Crack Growth Behaviour

- Effects of Underload Cycles in Variable Amplitude Loading Conditions

Four variable amplitude loading waveforms were designed that contained an underload followed by 50 minor cycles (with *R*-ratio = 0.9 and frequency = 5×10^{-2} Hz). The *R*-ratio of the underload

cycles was either 0.5 or 0.2, and the frequency of minor cycles was either 10^{-2} or 10^{-3} Hz. Two approaches can be taken to study the variable amplitude loading waveforms. The first approach calculates the crack growth rates versus time (See Figure 5.7 (a)). The second approach is to calculate crack growth rates with regards to crack propagation per loading block (See Figure 5.7 (b)). In the latter approach, the loading block is considered a single load cycle in constant amplitude loading conditions. For variable amplitude loading waveform, a combination of an underload plus several minor cycles (50 minor cycles) is defined as a loading block.

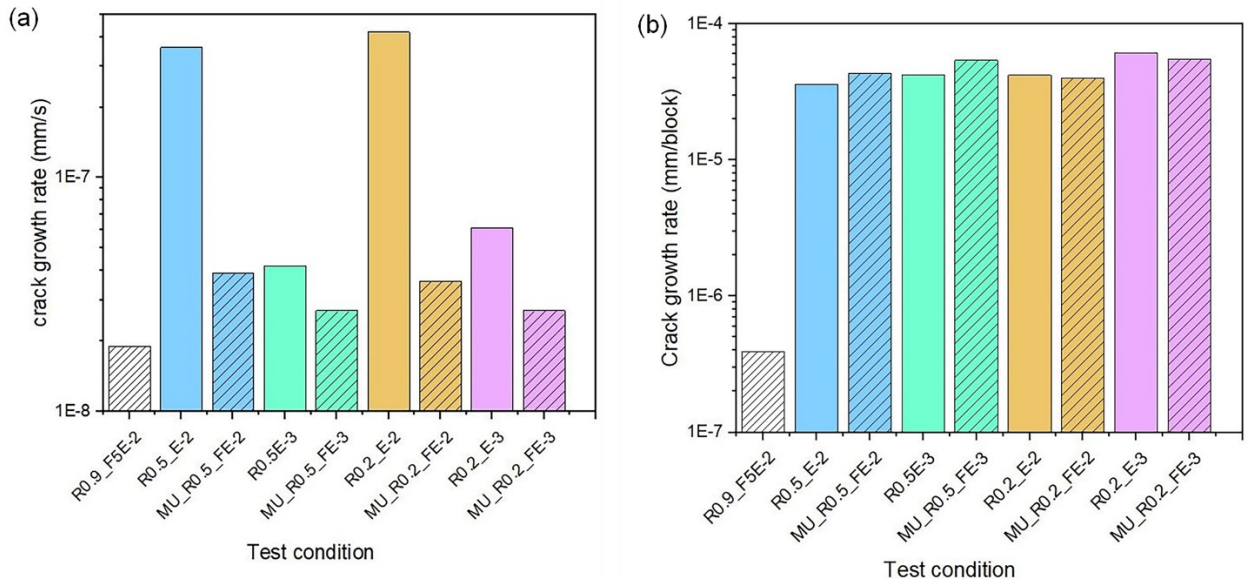

Figure 5.7. Comparison between the crack growth rates under constant amplitude and variable amplitude loading waveforms (a) in terms of mm/s (b) in terms of mm/block.

Figure 5.7 (a) displays the crack growth rates versus time for variable amplitude loading waveforms and corresponding constant amplitude loading conditions [20]. In this figure, the first column, which is cross-hatched, represents the crack growth obtained in the high *R*-ratio constant amplitude test. The solid coloured columns show the crack growth rates associated with low *R*-ratio constant amplitude tests. The coloured and cross-hatched columns represent the crack growth rates under variable amplitude loading waveforms. On the one hand, cracks advance was more

rapid per unit time under variable amplitude loading conditions compared to the R0.9_F5E-2 condition. On the other hand, the variable amplitude loading waveforms result in lower crack growth rates per unit time than the corresponding low *R*-ratio cycles. Accordingly, the crack growth rates obtained by variable amplitude loading waveforms are between those of high and low *R*-ratio constant amplitude loading cycles.

Figure 5.7 (b) shows the calculated crack growth rates by dividing the intergranular crack length by the number of loading blocks. As is seen, the crack growth rates under variable amplitude loading conditions approximate the corresponding growth rate obtained by constant amplitude loading waveforms. These results imply that the low *R*-ratio cycles are the dominant factor in HpHSCC crack growth during stage 1b.

- Effects of Minor Cycles

Although discussed results imply that stage I of HpHSCC crack growth is highly dependent on major underload cycles, those cycles are sporadic and less frequent than high *R*-ratio load cycles. Hence, it is important to study the crack growth behaviour in the interval between two major underload events. Consequently, four loading waveforms were designed, as detailed in Table 5.4. These waveforms were composed of an underload cycle with an *R*-ratio and frequency of 0.5 and 10^{-2} Hz accompanied by a different number of minor cycles (50, 100, 200, 400) with an *R*-ratio of 0.9 and frequency of 5×10^{-2} Hz. If the minor cycles had a negligible impact on Stage 1b of HpHSCC growth behaviour, the crack growth rates would remain close to the growth rates obtained during high *R*-ratio constant amplitude loading conditions (R0.9_F5E-2) regardless of the number of minor cycles. Interestingly, the calculated crack growth rates show different behaviours. The crack growth rates have an increasing trend when the number of minor cycles

between two adjacent underload cycles increases. The calculated crack growth rates in terms of propagated intergranular crack length versus time are shown in Figure 5.8 (a).

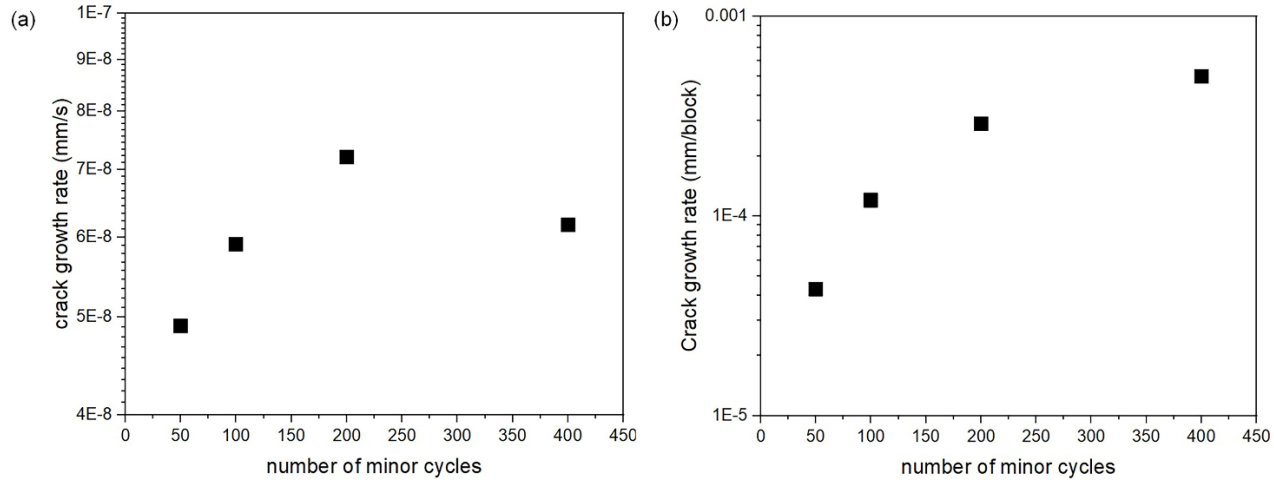

Figure 5.8. The effect of minor cycles on HpHSCC crack growth rate under variable amplitude loading condition in terms of (a) mm/s and (b) mm/block.

Figure 5.8 (b) shows the crack growth rates in terms of d*a*/dblock. In this figure, the crack growth rate increases with an increase in the number of minor cycles in the same fashion as Figure 5.8 (a). These results suggest the high *R*-ratio cycles are propagating cycles when they closely follow an underload cycle. A variable γ is often used to determine the load interaction under variable amplitude loading waveforms. This parameter is defined in Equation 5.1. If this parameter is greater than 1, it is the so-called acceleration factor and means the load interaction accelerates the crack growth and *vice versa*.

$$\gamma = \frac{\text{measured crack growth rate per block}}{\text{predicted crack growth rate by a linear summation}} \qquad \text{Eq'n. 5.1}$$

The parameter γ is plotted versus the time allocated to minor cycles between two adjacent major underloads in Figure 5.9. When the number of minor cycles is 50, this parameter is smaller than 1, implying that the crack growth is retarded. Then, there is an increasing trend in γ with increasing

minor cycles up to 200 minor cycles. The parameter γ does not increase further when the number of minor cycles increased to 400. These results imply that minor cycles play a role in stage 1b of HpHSCC, and their role will be considered in the discussion session.

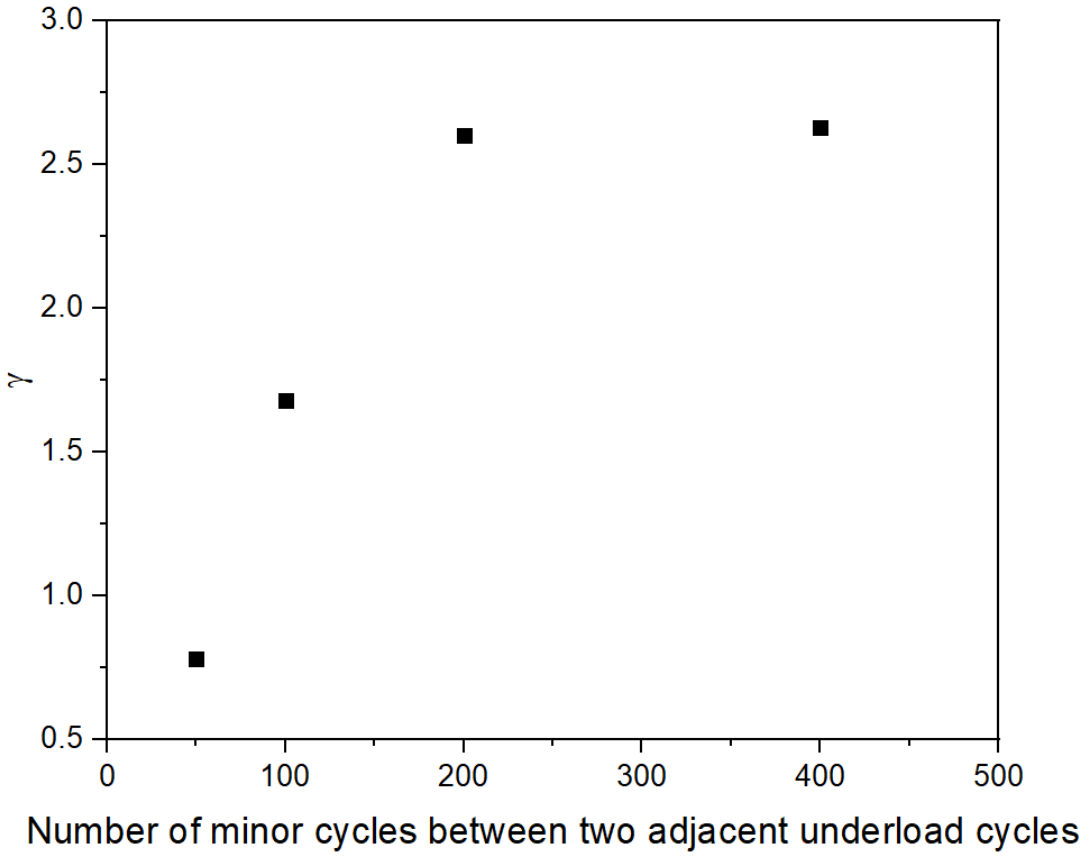

Figure 5.9. Variation of γ with the number of minor cycles in variable amplitude loading waveform.

5. 4 Discussion

5. 4. 1 Crack Evolution During Stage 1b

Stage 1b of HpHSCC crack growth is characterized by crack evolution to provide a mechanical driving force for sustainable crack growth later in stage 2. In this stage, there are already existing cracks that formed during stage 1a. These cracks are initiated randomly at multiple sites, like crack 1 and 2 shown schematically in Figure 5.10. Under this condition, three possible scenarios can be

considered for crack advance, *viz.* continued stochastic appearance of new cracks, the extension of existing crack, and initiation of secondary cracks followed by crack coalescence.

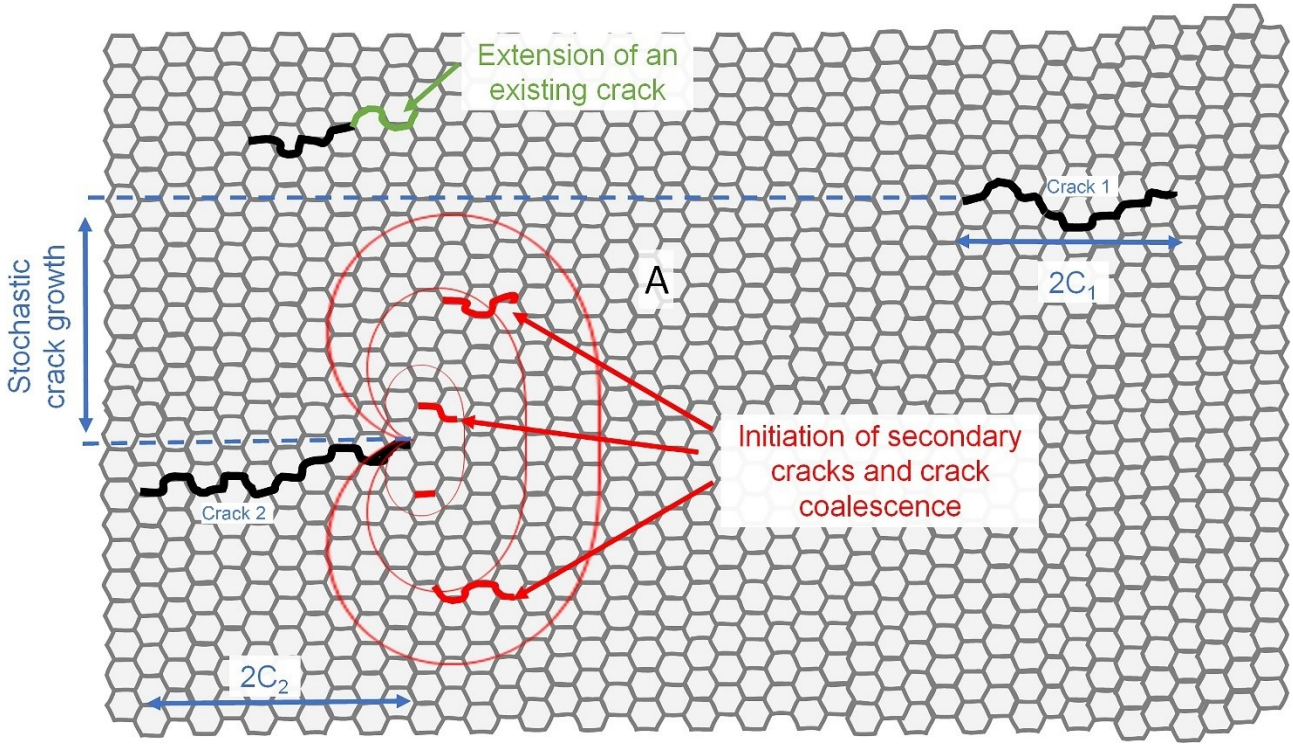

Figure 5.10. Schematic illustration of the three mechanisms for crack evolution: chaotic crack growth, an extension of an existing crack, and initiation of secondary cracks and crack coalescence.

- The Chaotic Appearance of New Cracks

This mechanism relies on multiple crack initiations followed by crack coalescence. Crack initiation and their growth at locations that are independent of an existing crack can occur. For instance, the coalescence of crack 1 and 2 in Figure 10 causes crack evolution. In this illustration, it is assumed crack 2 is nucleated randomly. Based on this mechanism, the randomly nucleated cracks at multiple sites can grow towards each other and merge to form the geometrical requirements for the onset of stage 2. An individual crack propagation under this mechanism is assumed random,

and cracks can coalesce when the conditions for Equation 5. 4 are met [2,19,38]. Equation 5.4 is an empirical equation obtained from both field and laboratory data [2,19,38].

$$y \leq 0.14 \times 2C_m \qquad \text{Eq'n. 5.4}$$

In this equation, y and $2c_m$ are normal distance and average crack length, respectively, as shown in Figure 5.10. Based on Equation 5. 4, the chance for crack coalescence increases when either y decreases or $2c_m$ increases. Furthermore, nucleation of a third crack at positions like point "*A*" in Figure 5.10 helps the interlinking of the cracks. Therefore, a high density of cracks assists crack coalescence based on Equation 5. 4. However, a high density of cracks will form either with stresses well above the yield point or with high tensile residual stress on the free surface of the pipe [37]. Both conditions tend to be avoided during pipeline manufacturing and operation.

Analysis of cracks in the field shows that HpHSCC failures happen when the initial crack spacing is greater than 20 percent of the wall thickness. Conversely, the areas with high densities of the cracks were almost remote from the failure or leakage. If the cracks' initial spacing is less than 15 to 20 percent of the pipe's wall thickness, the cracks shield one another from applied stress. Consequently, cracks become dormant [39]. The state of dormancy refers to the activity of the crack in-depth direction. It has been shown that the initiated cracks propagate relatively fast in the depth direction and reach to limiting size (about 50 μm depth). Simultaneously, the crack growth rate follows the decreasing trend for newly initiated cracks [2]. The aspect ratio (length/depth) of the active cracks is around two, whereas the aspect ratio of dormant cracks is larger. This implies active cracks propagate in depth along with an increase in crack length. The other important factor that must be considered is the applied stress. Cracks in the field keep growing at areas of high local stresses that occasionally cause failure [39].

- Extension of an Existing Crack

This mechanism causes an increase in an individual crack's length on the free surface because of the film-free condition at the grain boundary crossing the crack tip. However, this mechanism is not likely as a crack propagation causes work hardening at the neighbouring area, implying that more mechanical driving force is needed as the crack advances [2,37]. For small crack dimensions at this stage, the mechanical loading conditions, particularly the stress intensity factor, are not strong enough to provide sustainable crack growth. The green crack in Figure 5.10 shows the crack propagation caused by this mechanism. This mechanism is the primary mechanism in stage 2, where sustainable crack propagation occurs. In stage 2, a combination of crack geometry and loading conditions generates sustainable film-free conditions on the crack tips, and the crack propagates at higher rates [32]. This mechanism is discussed in more detail in subsequent sections.

- Initiation of Secondary Cracks and Crack Coalescence

This mechanism relies on secondary crack initiation in the plastic zone of an existing crack followed by crack coalescence. This mechanism relies on crack coalescence like the first discussed mechanism. However, preferential crack initiation at the existing crack tip distinguishes this mechanism from the stochastic new crack initiation mechanism. This mechanism is the focus of this study. The secondary cracks initiated by this mechanism are shown in red in Figure 5.10. Since the secondary cracks formed by this mechanism are pretty close to the main crack, they are more likely to merge to the main crack, according to Equation 5. 4 .

Crack propagation by the two latter mechanisms is the focus of the current study because of two reasons. First, increasing the length of the existing crack increases the chance for crack coalescence through Equation 5. 4. Secondly, if the existing crack propagation continues, it eventually will reach the required mechanical conditions for stage 2 since the relevant factors

increase with crack length. This research is designed to study the mechanisms of "extension of existing crack" and "initiation of secondary cracks and crack coalescence." To study these two mechanisms, the stress condition at the crack tip must be considered in the context of anodic dissolution at the grain boundary, as will be done in the next section.

5. 4. 2 The Relation Between Stress State and Crack Morphology at the Pre-crack Tip

The occurrence of either or both of the mechanisms mentioned above increases the length of an existing crack length on the free surface. Both scenarios rely on breaking the passive film and selective dissolution of the grain boundaries as already described. As stated earlier, intergranular corrosion can occur on the surface of the steel exposed to the HpHSCC environment. However, the formation of a passive film mainly composed of iron oxide and iron carbonate stops the intergranular corrosion [1, 2]. The passive film covers both grains and grain boundaries, and it manifests itself as a black film. Localized plastic deformation can fracture the passive film on the grain boundaries. The localized strain rate determines the rate of passive film rupture on the grain boundaries. If the strain rate surpasses the grain boundaries' re-passivation rate, bare grain boundaries are exposed to the corrosive environment, resulting in intergranular crack formation. The critical strain rate that causes the film-free condition on the grain boundaries has not been defined yet. As an alternative, Parkins proposed threshold stress for crack initiation. The threshold stress for crack initiation is close to the yield point for monotonic loading, and its value decreases under load fluctuations [2]. For stage 1b of HpHSCC crack growth, where there is already an existing crack, the stress condition near this existing-crack tip is intensified, and hence the strain rate is intensified. From the fracture mechanics perspective, the crack tip region experiences stress greater than the body's nominal applied stress. Upon applying a tensile load, a plastic zone forms at the crack tip. As the tensile stress increases, the plastic zone size increases. The theoretical and

actual plastic zones for any applied stress intensity factor can be approximated by Equations 5 and 6, respectively. In these equations, K and σ_{ys} represent the maximum stress intensity factor and yield strength, respectively. Figure 5.11 illustrates the theoretical and actual plastic zones schematically [40].

$$r_p = \frac{K^2}{2\pi\sigma_{ys}^2} \qquad \text{Eq'n. 5.3}$$

$$r_p = \frac{K^2}{\pi\sigma_{ys}^2} \qquad \text{Eq'n. 5.4}$$

Furthermore, damage accumulation models interpret fatigue crack growth by considering a cyclic plastic zone at the crack tip [41]. The cyclic plastic zone is a small region within the plastic zone where plastic strain is accumulated at the crack tip, and material located in this zone experiences accumulated strain and the most extreme loading conditions. The formation of the cyclic plastic zone and its size depends on the range of fluctuation in the stress intensity factor and *R*-ratio. The size of the cyclic plastic zone is approximately a quarter of the plastic zone. The smallest circle in Figure 5.11 shows the cyclic plastic zone schematically. The materials located in different zones have different strain-strain responses, as shown in Figure 5.11 (b). Of particular note is the large strain responses at the yield point, when discontinuous yielding is present. Our previous work has shown that the following four intergranular crack categories can initiate in these crack tip zones under constant amplitude cyclic loading conditions. These cracks are schematically shown and labelled in Figure 5.11 as well [20].

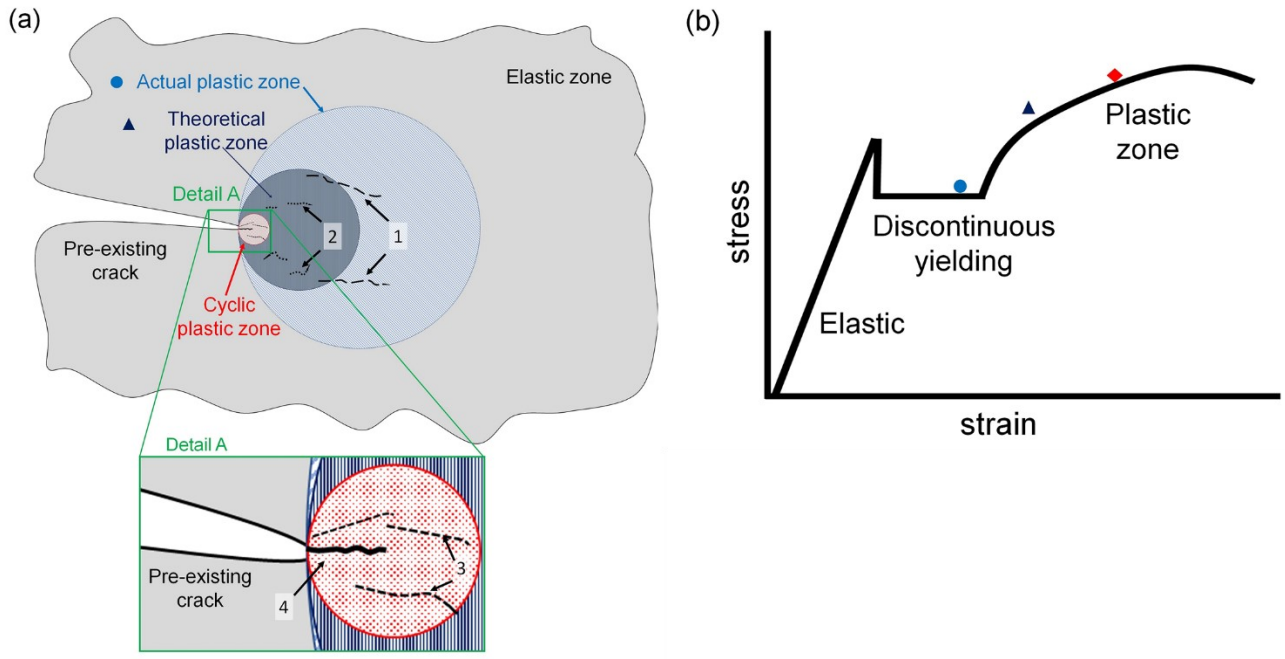

Figure 5.11. Schematic illustration of the cyclic plastic zone, theoretical plastic zone and actual plastic zone at the pre-crack tip along with four categories of nucleated intergranular cracks.

- Group 1: This group involves cracks initiated at the boundary between the theoretical plastic zone and the actual plastic zone. At this region, the stresses fall within the discontinuous yielding. The strain shock caused by discontinuous yielding plays an important role in intergranular crack initiation [34]. Discontinuous yielding is non-uniform plastic deformation that occurs in some metals that shows upper and lower yield points. In such metals, the dislocations are locked by interstitial solute atoms, and beyond the upper yield point, they become free and glide easily. The glide of dislocation continues until the work hardening starts. Therefore, a strain shock, *i.e.* a large amount of strain, happens quickly. The high strain rate in this region can fracture the grain boundaries' passive film and suppress re-passivation. Therefore, this strain shock assists in crack initiation.
- Group 2: This category involves cracks within the theoretical plastic zone, where the material experience stresses higher than the yield point.

- Group 3: This group of cracks was only observed under low *R*-ratio load cycles, so they can be attributed to the region of the cyclic plastic zone, where the plastic strain is accumulated.
- Group 4: A single crack extends from the pre-crack tip.

Figure 5.12 depicts the crack morphology on the free surface of the pre-cracked CT specimen tested under 200 MC_R0.5_FE-2 test conditions. This crack morphology is a typical crack morphology observed after applying variable amplitude loading waveforms to pre-cracked CT specimens. The cyclic plastic zone, the theoretical plastic zone, and the actual plastic zones are sketched in this figure. The crack morphology is identical to that observed under low *R*-ratio constant amplitude loading conditions, *i.e.* cracks can be categorized to the aforementioned crack categories, as shown in Figure 5.12. The similarities between the crack morphology under variable amplitude and low *R*-ratio constant amplitude conditions imply that even occasional large load fluctuations cause significant crack growth and have a negative impact on pipeline integrity.

The cyclic plastic zone formation influences both extensions of existing cracks and nucleation of secondary cracks followed by crack coalescence. First, the high-stress level and accumulated strain in this region can generate the required strain rate to fracture the passive film at the grain boundaries close to the fatigue pre-crack tip. Consequently, the extension of the preexisting crack might occur. Secondly, a high density of tiny intergranular cracks forms in the cyclic plastic zone. These cracks are close to the primary crack tip and are likely to merge with the main crack. It is worth mentioning that Figure 5.4 shows the cracks in the cyclic plastic zone of Figure 5.12 at a higher magnification.

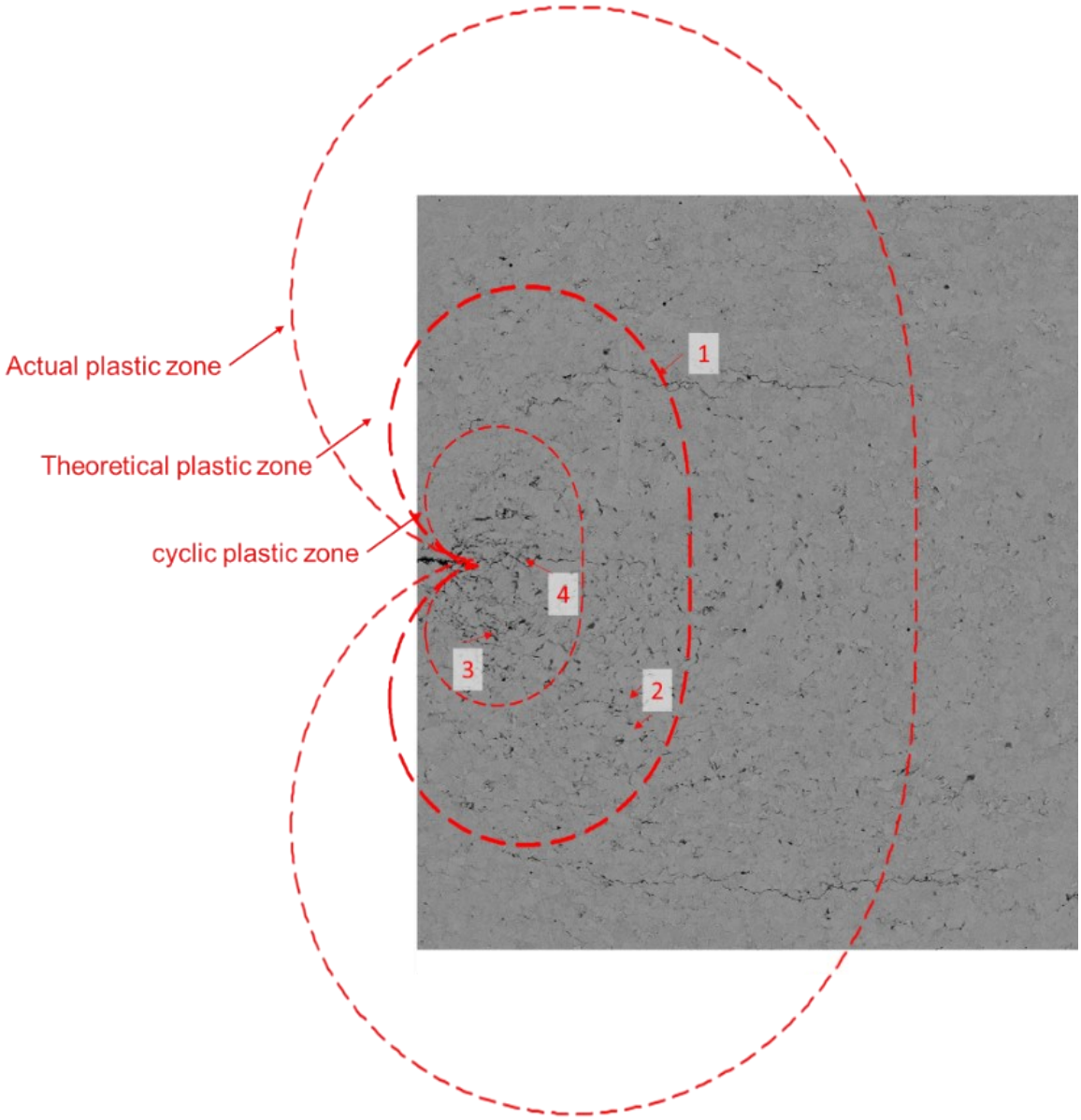

Figure 5.12. Typical morphology of the intergranular cracks at the crack tip.

5. 4. 3 Crack Growth Behaviour under Variable Amplitude Loading Waveforms

The similarities in crack growth rates per loading block (See Figure 5.7(b)) in addition to identical crack morphologies under VA conditions and low *R*-ratio loading waveforms suggest that nucleated tiny intergranular cracks in the cyclic plastic zone contribute significantly to stage 1b HpHSCC crack propagation. However, the crack growth rates in mm/s are different under VA and

low *R*-ratio constant amplitude (CA) conditions. A possible reason for the higher crack growth rate caused by low *R*-ratio CA conditions is higher contributions from the existing crack extension under low *R*-ratio cycles. The extension of the existing cracks can be applied to both primary cracks and those nucleated secondary cracks. Crack growth of the secondary cracks increases the chance for crack coalescence as well, according to Equation 5.4.

According to the reported results in Figure 5.8 (a) and (b), the HpHSCC crack growth rate increases when the number of minor cycles in a block of VA loading waveform increases. Figure 5.13 (a) to (c) show the surface morphology of the crack at the area near the pre-crack tip for 100M-R0.5_FE-2, 200M-R0.5_FE-2, 400M-R0.5_FE-2, respectively. The figures show that the length of the single crack initiated from the pre-crack tip increases as the number of minor cycles between two underload events increases. Figure 5.14 (a) to (c) show the fracture surface of CT specimens tested under 100M-R0.5_FE-2, 200M-R0.5_FE-2, 400M-R0.5_FE-2 conditions, respectively (see Table 5.4). This figure highlights the formation of a single deep crack as the number of minor cycles increases. According to Figure 5.9, there is an increasing trend in parameter γ with an increase in the number of minor cycles between two underload events. Both crack tip stress condition and crack propagation mechanisms must be considered to understand the role of minor cycles and parameter γ. Accordingly, four possible reasons might cause an increase in the crack growth rate with an increasing number of minor cycles following an underload, as detailed below.

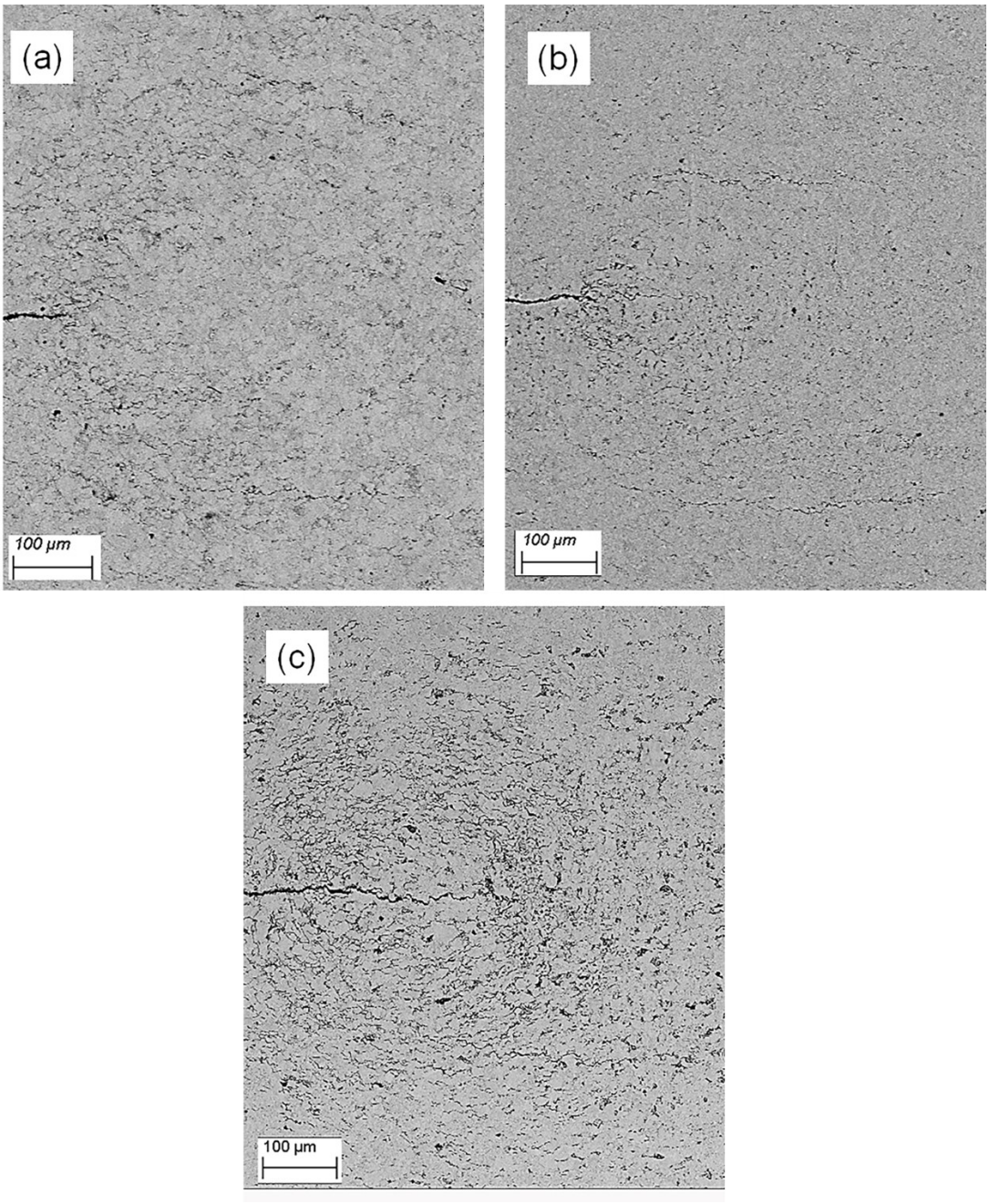

Figure 5.13. Crack morphology at the crack tip of pre-cracked CT specimens tested under variable amplitude loading waveform where K_{max}=15 MPa.$^{0.5}$ composed of an underload cycle (R-ratio=0.5 and Frequency= 10^{-2} Hz) followed by (a) 100, (b) 200 (c) 400 minor cycles with R-ratio of 0.9 and frequency of 5×10^{-2}HZ

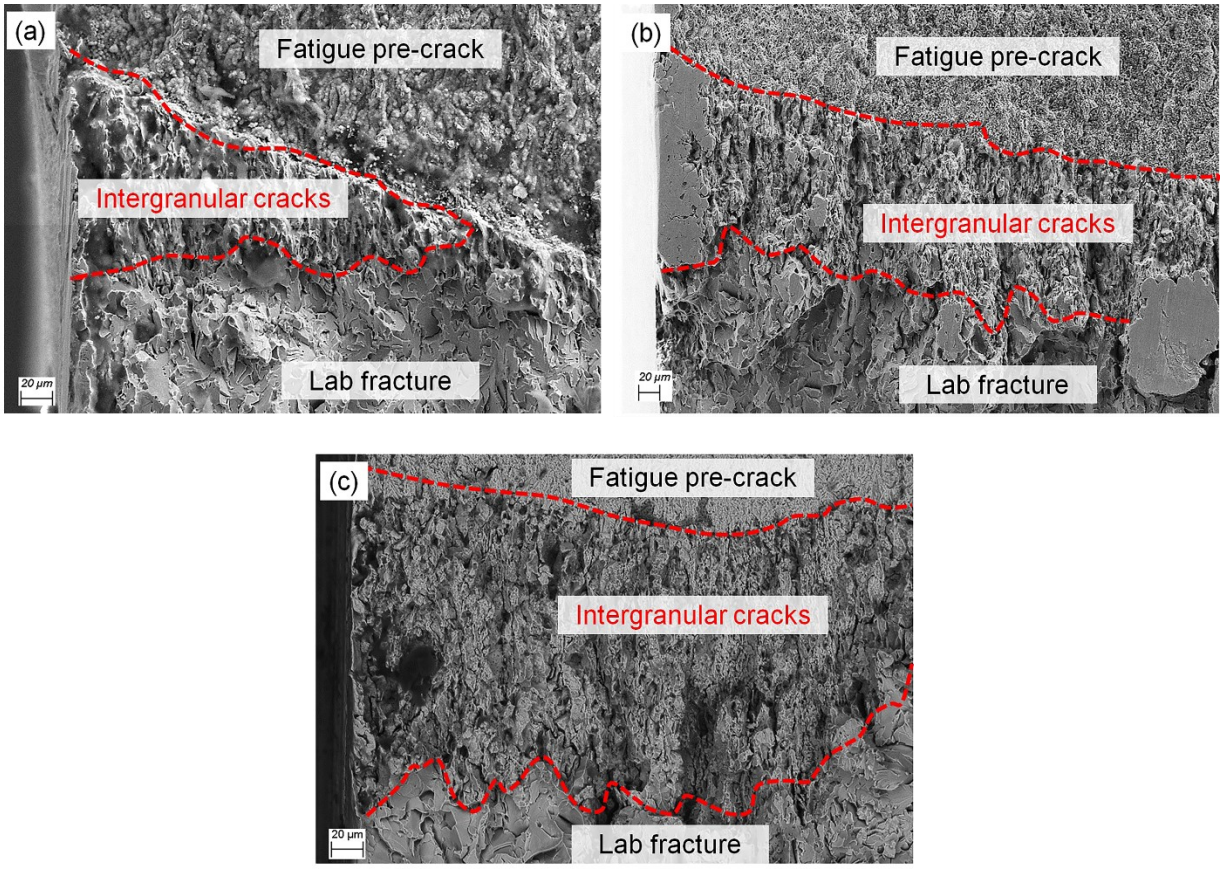

Figure 5.14. Fracture surfaces of pre-cracked CT specimens tested under variable amplitude loading waveform where K_{max}=15 MPa.m$^{0.5}$ composed of an underload cycle (R-ratio=0.5 and Frequency= 10^{-2} Hz) followed by (a) 100, (b) 200 (c) 400 minor cycles with R-ratio of 0.9 and frequency of 5×10^{-2} HZ.

First, the cyclic plastic region forms at the crack tip in the presence of underload cycles. In this region, the stress condition is intensified, and materials are strained. Potentiodynamic polarization tests show the anodic current density increases for either stressed materials [42] or strained materials [43]. Both conditions are applied to the materials at the crack tip under the test condition during the application of minor cycles. In other words, materials in the cyclic plastic zone are plastically deformed and bear higher stresses. Therefore, the electrochemical dissolution is accelerated in this region. Hence, if the film rupturing happens at some spots, selective dissolution

happens at higher rates in the cyclic plastic zone compared to the other zones. Consequently, corrosion at the grain boundaries is enhanced.

Secondly, minor cycles can be incorporated into the crack propagation process by extending the existing cracks. The driving force for the extension of the existing crack is the exhaustion of the low-temperature creep strain. Low-temperature creep is a phenomenon that occurs when metals that experience strain hardening, such as pipeline steels, are subjected to cyclic loading. Upon applying monotonic stresses greater than the yield strength of such materials, the strain rate decreases so that generating more strain requires larger stresses. The reason for strain hardening is the interactions between glissile and sessile dislocations. However, when the load is partially or wholly removed during the cycle, mobile dislocations glide in reverse, providing opportunities for either cross slip or rearrangement of obstacle dislocations. On the reloading event, the mobile dislocations move forward again and regenerate strain. However, more strain can be generated because of the dislocation rearrangement until the strain rate decreases again because of the reoccurrence of strain hardening. The condition at the crack tip during the minor cycles is ideal for low-temperature creep strain exhaustion. Materials in the cyclic plastic zone are experiencing stresses in the work-hardening region. Hence, load fluctuation generates the low-temperature creep strain. The strain rate caused by low-temperature creep is initially high until the strain hardening happens again. The low-temperature creep strain is cumulative, yet the strain increment decreases with time. Therefore, when the number of minor cycles increases, *i.e.* the time between two underload events increases, a greater portion of the low-temperature creep can be exhausted. The primary crack and the newly initiated secondary cracks can take advantage of low-temperature creep, and crack coalescence becomes more feasible according to Equation 5. 4. A significant portion of low-temperature creep strain will be exhausted within an hour. An increase in

dislocation density and subsequent dislocation locking sets the stages for the third possible reason, as discussed in the following paragraph.

The third possible reason for the effect of the minor cycle is associated with the occurrence of strain ageing. The physical reason for strain ageing caused by minor cycles differs from the strain shock discussed earlier in the boundary between the actual and theoretical plastic zones (Group 1 cracks). The presence of yield point and consequently the strain shock is normally attributed to either atmosphere pinning of dislocations (like the strain shock caused cracking at the boundary of the actual plastic zone and theoretical plastic zone) or dislocation locking [44]. The latter condition, *i.e.,* yield point caused by dislocation locking, could be considered as a phenomenon occurring during the application of minor cycles. As was stated earlier, low-temperature creep causes rearrangement of dislocations and further plastic strain. However, the low-temperature creep strain is gradually decreasing so that a significant portion of the strain is exhausted within an hour. Exhaustion of the low-temperature creep is followed by strain hardening that increases the dislocation densities. Therefore, mobile dislocations are locked, and the condition for the emergence of yield point elongation is provided. Reoccurrence of serrated yielding might provide strain shock in the plastic zone that helps propagate existing cracks and increases the chance for crack coalescence.

As stated earlier, the parameter γ is less than 1 for 50 minor cycles. This parameter follows an increasing trend by increasing the number of minor cycles up to 200. Further increase in the number of minor cycles to 400 does not change the parameter γ significantly. When the number of minor cycles is 50, *i.e.,* there is a short time between two underload events, the time is insufficient to generate the dislocation locking required for the occurrence of the yield point phenomenon. However, an increase in the number of minor cycles provides additional time to

generate a high density of dislocations. Therefore, dislocation locking happens when the number of minor cycles increases, followed by the occurrence of the yield point phenomenon at the crack tip. The strain shock caused by the yield point phenomenon sustains the grain boundary under a film-free condition and assists the intergranular crack propagation. The results suggest that the yield point phenomenon happens when the number of minor cycles is larger than 50. Additionally, it seems the effects caused by strain ageing is saturated when the number of minor cycles is 200, as the parameter γ decreased slightly when the number of minor cycles increased to 400.

Fourthly, minor cycles between major underload events might contribute to secondary crack initiation in the cyclic plastic zone. As stated earlier, the cyclic plastic zone undergoes the most severe loading condition. Parkins shows that the tendency for crack initiation increases at higher stresses [37]. Higher stresses are potent to provide the required strain rate to fracture the passive film on the grain boundaries and assist the intergranular crack formation. Additionally, the cyclic loading encourages the nucleation of intergranular cracks [37]. Therefore, small load fluctuation at high stress might facilitate small cracks initiation as well. If secondary crack initiation occurs during minor cycles, it can contribute to crack growth by the crack coalescence mechanism.

According to the above discussion, the small load fluctuations are not a threat to pipeline integrity unless they follow a major underload cycle. This behaviour is identical to crack propagation during stage 2 of NNpHSCC, where high *R*-ratio cycles are considered none-propagating cycles in the absence of underload cycles. However, the mechanism for NNpHSCC crack propagation is distinguished from the mechanisms discussed for HpHSCC in this paper. Subsequently, the role of minor cycles and underload cycles are different. For NNpHSCC, the environment is non-passivating in nature, and the crack growth mechanism is hydrogen-enhanced corrosion fatigue [1, 26]. Hydrogen could be generated as a byproduct of corrosion or by cathodic protection applied to

the pipe. Small load fluctuation or minor cycles are not potent enough to provide the mechanical driving force for crack propagation. However, these cycles assist segregation of the hydrogen in the crack tip plastic zone. During minor cycles, hydrogen atoms segregate in the plastic zone area because of high hydrostatic stresses and high density of dislocations in the plastic zone. This leads to the occurrence of hydrogen embrittlement. On the other hand, underload cycles provide sufficient mechanical driving force for fatigue crack propagation. Hence, an underload cycle that follows the minor cycles causes crack propagation in the embrittled material at the crack tip [23,25,27].

In the case of HpHSCC, hydrogen evolution is not likely to occur. The susceptible potential for HpHSCC is -526 to -676 mV_{SCE} [5]. This potential range is more positive than the equilibrium potential for the hydrogen evolution reaction in the HpHSCC solution (-794 mV_{SCE}) [45]. Hence the cathodic reaction will be oxygen reduction instead of hydrogen evolution. Therefore, the hydrogen embrittlement cannot influence the plasticity of the crack tip under HpHSCC environmental conditions.

5. 4. 4 Further Supporting Evidence for Discussion

To validate the above discussion, 225 blocks of variable amplitude loading waveform composed of 50 minor cycles with the *R*-ratio of 0.9 at a frequency of 5×10^{-3} Hz and one underload cycle with the *R*-ratio of 0.5 and frequency of 10^{-3} were designed and applied to pre-cracked CT specimens. Figure 5.15 (a) and (b) compare the crack growth rate obtained under this variable loading condition and the corresponding constant amplitude tests. From Figure 5.15 (a), the crack growth rates in terms of mm/s ranked in the order: low *R*-ratio cycles< variable amplitude< high *R*-ratio cycles, which is identical to Figure 5.7 (a). Converting the crack growth rates to mm/block shows that the crack growth rates ranked in the order of variable amplitude> low *R*-ratio cycles>

high *R*-ratio cycles, as shown in Figure 5.15 (b). This observation is analogous to Figure 5.7 (b). However, the difference between variable amplitude loading waveform and low *R*-ratio constant amplitude test is larger than those in Figure 5.7 (b). The allocated time for the variable amplitude waveform in Figure 5.15 is 10,000 seconds. This time is larger than other tests reported in previous sections. Therefore, more time is available during the minor cycles for crack propagation through the mechanisms discussed earlier. Accordingly, the parameter γ is equal to 2, implying the interaction between the minor cycles and underload cycles accelerates crack propagation.

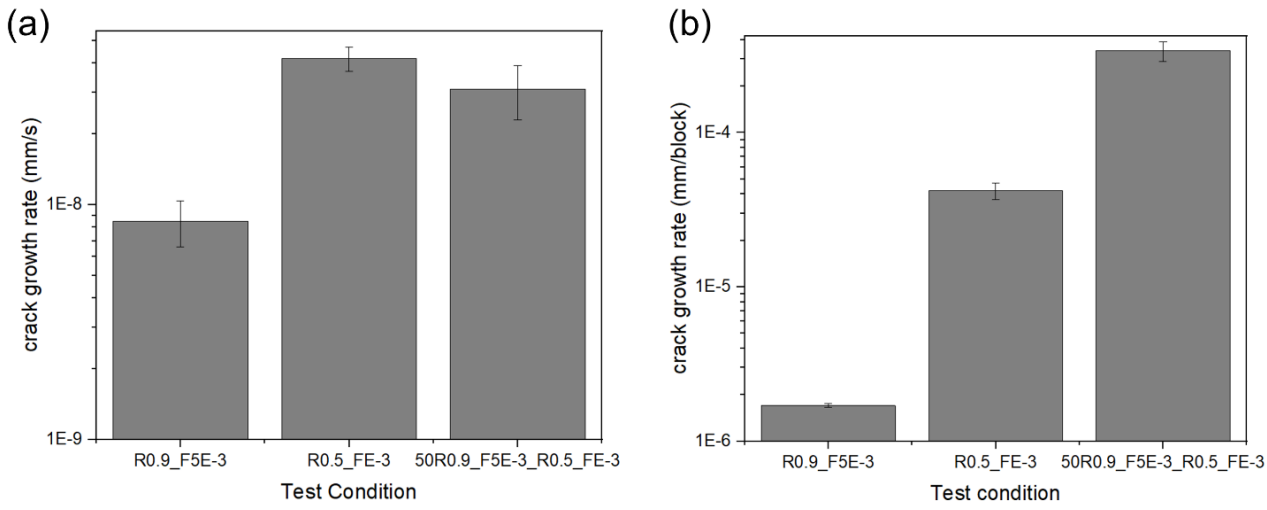

Figure 5.15. Comparison between the crack growth rate under high and low *R*-ratio constant amplitude loading cycle with variable amplitude loading in terms of (a) mm/s and (b) mm/block.

5. 5 The Implication for Pipeline Operators

In the presence of the HpHSCC environmental conditions, intergranular cracks initiate on the external surface of the pipe. Crack initiation happens at multiple sites, where the localized strain rate sustains the grain boundaries under film-free conditions. These cracks are semi-elliptical in shape where the crack length (2c) is higher than crack depth (a). The initiated cracks propagate at a high rate at first. However, their propagation in the depth direction is always limited to 50 μm

[46]. The nucleated cracks intensify the stress near their tips. The degree of intensification depends on the crack geometry as well as the loading conditions. Large load fluctuations form a cyclic plastic zone at the crack tip, wherein the metal experiences high plasticity [20]. In the cyclic plastic zone, the required strain rate for film-free conditions is provided on some grain boundaries. Hence, this region is a preferential region for the initiation of secondary cracks. The nucleated cracks merge to the main crack and increase its length on the free surface. Small load fluctuation can be considered non-propagating cycles by themselves. However, the minor cycles (small load fluctuations) that follow an underload cycle contribute to crack propagation by different mechanisms, such as increasing the dissolution rate, exhausting low-temperature creep, strain shock caused by dislocation interlocking, and secondary crack nucleation. As a result, the crack length on the free surface increases either by extension of existing crack and/or coalescence of small cracks in the cyclic plastic zone, as shown in Figure 5.16.

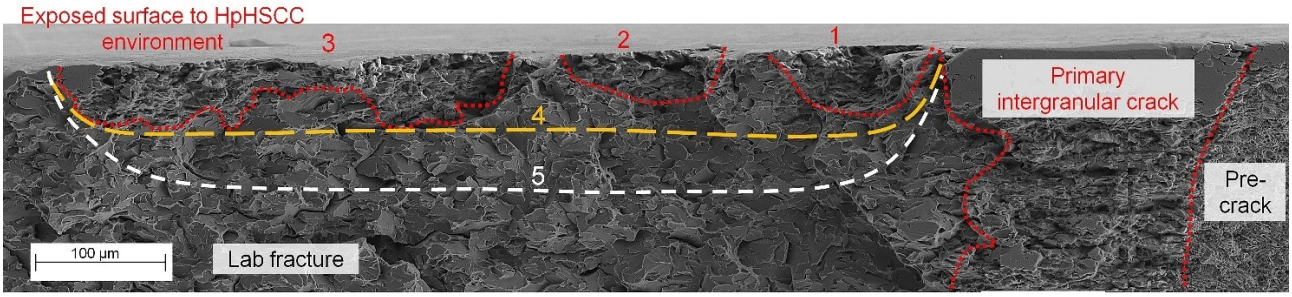

Figure 5.16. Evidence of crack initiation and crack coalescence on the free surface of X65 pipeline steel.

Cracks labelled 1 to 3 are secondary cracks formed at the crack tip. These secondary cracks have semi-elliptical shapes. Crack 3 in this figure appears to have been formed by the coalescence of two cracks. In the same manner, cracks 1 to 3 can merge and form an even longer crack. Two possible outcomes can be considered. First, crack coalescence on the surface with no significant

growth in-depth direction, this condition is shown with the large dashed yellow curve in Figure 5.16, and it is labelled crack 4. Secondly, crack coalescence on the free surface followed by crack growth in the depth direction, illustrated by the white short dashed shows in Figure 5.16 and labelled crack 5. It must be noted that the depth of crack 5 is selected arbitrarily.

If cracks 1 to 3 were nucleated randomly independent of the primary crack tip, *i.e.* far from the primary crack tip, the stress applied to those cracks is about the pipe's hoop stress. Assuming these cracks are on 9 mm wall-thickness X65 pipeline steel loaded to 65% of SMYS, the stress intensity factor in the depth tip (K_{depth}) and the surface tips ($K_{surface}$) of the crack 1 to 5 are shown in the second and third column in Table 5.5. However, these cracks are formed in the plastic zone at the primary crack tip, where the stress is above the yield strength. The fourth and fifth columns show the stress intensity factor assuming the stress at this region is equal to the yield strength (525 MPa). The stress intensity factors increase as the applied stress increases. As stated earlier, the stress at the crack tip is greater than the yield point. Assuming the stress is equal to 1.5 times the yield strength, the stress intensity factors are calculated in the sixth and seventh columns of Table 5.5. These calculations show that the mechanical driving force for propagating the secondary cracks nucleated at the primary crack's plastic zone is higher than for crack with the same geometry remote from the existing crack. Therefore, the propagation of these cracks is more feasible. These cracks can merge to the preexisting crack and increase the crack length on the free surface.

From Table 5.5, K_{depth} increases as the crack length on the free surface increases through crack coalescence. If the merged crack propagates in the depth direction simultaneously (like crack 5 in Figure 5.16), an increase in K_{depth} is more rapid than no growth in the depth direction (crack 4 in Figure 5.16). An increase in K_{depth} provides more mechanical driving force for crack propagation

in the pipe's thickness direction. The literature reports that a K_{depth} of 21 MPa.m$^{0.5}$ is necessary for crack propagation in the depth direction under monotonic loading conditions.

Table 5.5. Calculated crack growth for the cracks shown in Figure 5.16 with the assumption of a 9 mm wall-thickness X65 steel pipeline is subjected to the maximum load of 65% SMYS

Crack number	*65% SMYS*		*Yield strength*		*1.5 yield strength*	
	$K_{surface}$ (MPa.m$^{0.5}$)	K_{depth} (MPa.m$^{0.5}$)	$K_{surface}$ (MPa.m$^{0.5}$)	K_{depth} (MPa.m$^{0.5}$)	$K_{surface}$ (MPa.m$^{0.5}$)	K_{depth} (MPa.m$^{0.5}$)
1	2.9	3.1	4.4	4.1	6.7	6.1
2	2.7	3.0	4.2	4.8	6.3	6.9
3	2.8	4.4	4.3	6.8	6.5	10.2
4	2.2	4.8	3.4	7.4	5.1	11.0
5	3.3	5.7	5.0	8.8	7.6	13.2

The above-discussed mechanism, *i.e.* initiation of secondary crack followed by crack coalescence, continues before the onset of stage 2. This study shows that an existing crack influences crack propagation during stage 1b depending on the loading condition. The major underload cycles, which are sporadic and less frequent than the minor cycles, form a cyclic plastic zone at the crack tip. The strain accumulates in this region, and the region becomes a breeding ground for secondary crack initiation.

During the minor cycles, the primary intergranular crack and secondary cracks can propagate through different mechanisms. The primary crack and secondary cracks can propagate through exhaustion of low-temperature creep [1]. The exhaustion of low-temperature creep is followed by yield point elongation that generates strain shock. The strain shock sustains the film-free condition on grain boundaries in the cyclic plastic zone and causes intergranular crack propagation. Moreover, the small load fluctuation during the minor cycles helps secondary cracks to initiate at the crack tip. The intensified stress accelerates the selective dissolution rate in the plastically strained materials in the cyclic plastic zone.

Therefore, the major underload cycle is the dominant load cycle in crack propagation in stage 1b. Additionally, high *R*-ratio cycles can be considered as a non-propagating cycle by themselves, *i.e.* small load fluctuation cannot be considered a threat to pipeline integrity in the absence of underload cycles. However, their behaviour changes when they are proceeded by an underload cycle. Therefore, avoiding large load fluctuations, *i.e.* underload cycles, during pipeline operation increases the duration of stage 1b and delays the onset of stage 2. Therefore, each significant underload cycle has negative impacts on the HpHSCC crack growth in stage 1.

5. 6 Conclusion

The effects of minor cycles and underload cycles on HpHSCC crack growth behaviour at stage 1b (where $K_{max}<K_{ISCC}$) were studied in a potent environment for intergranular cracking in steel pipelines. It was observed that both minor cycles and underload cycles contributed to crack propagation. The main findings of the research were as follows:

- The similarity between crack growth rates under variable amplitude (a major underload followed by minor cycles) and low *R*-ratio constant amplitude loading waveforms implies that the formation of a cyclic plastic zone by large load fluctuation plays an important role in stage 1b of HpHSCC crack growth. Secondary cracks form in this region that can easily merge to the main crack and increase the crack length.
- High *R*-ratio cycles (minor cycles) are non-propagating unless preceded by underload cycles. The minor cycles that follow an underload cycle contribute to crack propagation by different mechanisms, including exhaustion of low-temperature creep, secondary cracks initiation and crack coalescence, providing the condition for yield point elongation. The minor cycle contribution increases as the number of the minor cycle between two underload events increases.

- Stage 1b is the lifetime determining stage in HpHSCC. The key parameter to increase the duration of stage 1b is avoiding underload cycles. Underload cycles not only seed secondary crack initiation but also change the behaviour of minor cycles from non-propagating to propagating cycles.

References

[1] W. Chen, Modeling and prediction of stress corrosion cracking of pipeline steels, in: A. M. -El-Sherik (Eds), Trends in Oil and Gas Corrosion Research and Technologies, Woodhead Publishing, Boston, 2016, pp. 707–748. https://doi.org/10.1016/B978-0-08-101105-8.00030-9.

[2] H. Niazi, R. Eadie, W. Chen, H. Zhang, High pH stress corrosion cracking initiation and crack evolution in buried steel pipelines: A review, Eng. Fail. Anal. 120 (2021) 105013. https://doi.org/10.1016/j.engfailanal.2020.105013.

[3] E.A. Charles, R.N. Parkins, Generation of Stress Corrosion Cracking Environments at Pipeline Surfaces, Corrosion 51 (1995), 518-527, https://doi.org/10.5006/1.3294372.

[4] J. Beavers, T.A. Bubenik, Stress corrosion cracking, in: A. M. -El-Sherik (Eds), Trends in Oil and Gas Corrosion Research and Technologies, Woodhead Publishing, Boston, 2016, pp. 295–314. https://doi.org/10.1016/B978-0-08-101105-8.00012-7.

[5] Y.F. Cheng, Stress Corrosion Cracking of Pipelines, John Wiley & Sons, Inc., New York, 2013. https://doi.org/10.1002/9781118537022.

[6] A. Atrens, J.Q. Wang, K. Stiller, H.O. Andren, Atom probe field ion microscope measurements of carbon segregation at an α:α grain boundary and service failures by intergranular stress corrosion cracking, Corros. Sci. 48 (2006) 79–92. https://doi.org/10.1016/j.corsci.2004.11.014.

[7] H. Asahi, T. Kushida, M. Kimura, H. Fukai, S. Okano, Role of Microstructures on Stress Corrosion Cracking of Pipeline Steels in Carbonate-Bicarbonate Solution, Corrosion 55 (1999) 644–652. https://doi:10.5006/1.3284018.

[8] R.N. Parkins, Mechanistic aspects of intergranular stress corrosion cracking of ferritic steels, Corrosion 52 (1996) 363–374. https://doi.org/10.5006/1.3292124.

[9] Y.F. Cheng, R. Norsworthy, Pipeline Coatings, NACE International, Huston, 2016.

[10] L. Yan, R. Worthingham, F. King, J. Been, Factors affecting the generation of high-pH environments required for stress corrosion cracking (SCC), International Pipeline Conference, IPC2012 (2012) 511–524. https://doi.org/10.1115/IPC2012-90515.

[11] R.R. Fessler, A.J. Markworth, R.N. Parkins, Cathodic protection levels under disbonded coatings, Corrosion. 39 (1983) 20–25. https://doi.org/10.5006/1.3580809.

[12] E. Gamboa, Inclined stress corrosion cracks in steel pipelines, Corros. Eng. Sci. Technol. 50 (2015) 191–195. https://doi.org/10.1179/1743278215Y.0000000006.

[13] M.A. Arafin, J.A. Szpunar, A new understanding of intergranular stress corrosion cracking resistance of pipeline steel through grain boundary character and crystallographic texture studies, Corros. Sci. 51 (2009) 119–128. https://doi.org/10.1016/j.corsci.2008.10.006.

[14] A. Roccisano, S. Nafisi, R. Ghomashchi, Stress corrosion cracking observed in ex-service gas pipelines: a comprehensive study, Metall. Mater. Trans. A. 51 (2020) 167–188. https://doi.org/10.1007/s11661-019-05496-3.

[15] Zhao, J., Chevil, K., Yu, M., Been, J., Keane, S., Van Boven, G., Kania, R., Chen, W, Statistical analysis on underload-type pipeline spectra, J. Pipeline Syst. Eng. Pract. 7 (2016) 4016007. https://doi.org/10.1061/(ASCE)PS.1949-1204.0000241.

[16] M. Yu, W. Chen, R. Kania, G. Van Boven, J. Been, Depressurization-induced crack growth enhancement for pipeline steels exposed to near-neutral pH environments, International Pipeline Conference, IPC 2014 (2014) V002T06A076. https://doi.org/10.1115/IPC2014-33282.

[17] J.A. Beavers, 2013 Frank Newman Speller Award Lecture: Integrity management of natural gas and petroleum pipelines subject to stress corrosion cracking, Corrosion. 70 (2014) 3–18. https://doi.org/10.5006/0998.

[18] R.N. Parkins, 1990 Plenary Lecture: Strain rate effects in stress corrosion cracking, Corrosion. 46 (1990) 178–189. https://doi.org/10.5006/1.3585089.

[19] R.N. Parkins, P.M. Singh, Stress corrosion crack coalescence, Corrosion. 46 (1990) 485–499. https://doi.org/10.5006/1.3585136.

[20] H. Niazi, G. Nelson, L. Lamborn, R. Eadie, W. Chen, H. Zhang, Crack growth sensitivity to the magnitude and frequency of load fluctuation in stage one of High pH Stress Corrosion Cracking, (2020).

[21] M. Skorupa, Load interaction effects during fatigue crack growth under variable amplitude loading—a literature review. Part II: qualitative interpretation, Fatigue Fract. Eng. Mater. Struct. 22 (1999) 905–926. https://doi.org/10.1046/j.1460-2695.1999.00158.x

[22] M. Skorupa, Load interaction effects during fatigue crack growth under variable amplitude loading—a literature review. Part I: empirical trends, Fatigue Fract. Eng. Mater. Struct. 21 (1998) 987–1006. https://doi.org/10.1046/j.1460-2695.1998.00083.x.

[23] M. Yu, W. Chen, R. Kania, G. Van Boven, J. Been, Crack propagation of pipeline steel exposed to a near-neutral pH environment under variable pressure fluctuations, Int. J. Fatigue. 82 (2016) 658–666. http://dx.doi.org/10.1016/j.ijfatigue.2015.09.024.

[24] M. Yu, W. Chen, K. Chevil, G. Van Boven, J. Been, Retarding crack growth by static pressure hold for pipeline steel exposed to a near-neutral pH environment, International Pipeline Conference, IPC 2016 (2016) V001T03A091. http://dx.doi.org/10.1115/IPC2016-64627.

[25] M. Yu, X. Xing, H. Zhang, J. Zhao, R. Eadie, W. Chen, J. Been, G. Van Boven, R. Kania, Corrosion fatigue crack growth behaviour of pipeline steel under underload-type variable amplitude loading schemes, Acta Mater. 96 (2015) 159–169. http://dx.doi.org/10.1016/j.actamat.2015.05.049.

[26] W. Chen, An overview of near-neutral pH stress corrosion cracking in pipelines and mitigations for its initiation and growth, Corrosion. 72 (2016) 962–977. https://doi.org/10.5006/1967.

[27] M. Yu, W. Chen, R. Kania, G. Van Boven, J. Been, Underload-induced crack growth behaviour of minor cycles of pipeline steel in near-neutral pH environment, Fatigue Fract. Eng. Mater. Struct. 38 (6) (2014) 681–692. https://doi.org/10.1111/ffe.12274.

[28] ASTM, Standard Test Method for Measurement of Fatigue Crack Growth Rates E647-15e1, ASTM B. Stand. (2016) 1–49. 10.1520/E0647-15E01.2.

[29] B.F. Brown, C.D. Beachem, A study of the stress factor in corrosion cracking by use of the pre-cracked cantilever beam specimen, Corros. Sci. 5 (1965) 745–750. http://dx.doi.org/10.1016/S0010-938X(65)80002-6.

[30] N.E. Board, Stress corrosion cracking on Canadian oil and gas pipelines, Natl. Energy Board, Calgary, Alberta. (1996).

[31] J.A. Beavers, R.G. Worthingham, The influence of soil chemistry on SCC of underground pipelines, International Pipeline Conference, IPC 2002 (2002) 1671–1678. https://doi.org/10.1115/IPC2002-27146.

[32] H. Niazi, K. Chevil, E. Gamboa, L. Lamborn, W. Chen, H. Zhang, Effects of Loading Spectra on High pH Crack Growth Behaviour of X65 Pipeline Steel, Corrosion. 76 (6) 601-615 (2020). https://doi.org/10.5006/3472.

[33] H. Niazi, H. Zhang, L. Lamborn, W. Chen, The impact of pressure fluctuations on the early onset of stage II growth of high pH stress corrosion crack, Proceedings of the 2020 13th International Pipeline Conference IPC 2020 (2020) IPC2020-9511.

[34] S. Wang, H. Niazi, L. Lamborn, W. Chen, Strain-shock-induced early-stage high pH stress corrosion crack initiation and growth of pipeline steels, Corros. Sci. 178 (2020) 109056. https://doi.org/10.1016/j.corsci.2020.109056.

[35] A.K. Pilkey, S.B. Lambert, A. Plumtree, Stress corrosion cracking of X-60 line pipe steel in a carbonate-bicarbonate Solution, Corrosion. 51 (2) (1995) 91–96. https://doi.org/10.5006/1.3293588.

[36] R.N. Parkins, B.S. Greenwell, The interface between corrosion fatigue and stress-corrosion cracking, Met. Sci. 11 (1977) 405–413. https://doi.org/10.1179/msc.1977.11.8-9.405.

[37] R.N. Parkins, E. Belhimer, W.K. Blanchard, Stress corrosion cracking characteristics of a range of pipeline steels in carbonate-bicarbonate solution, Corrosion. 49 (12) (1993) 951–966. https://doi.org/10.5006/1.3316023.

[38] Y.-Z. Wang, J.D. Atkinson, R. Akid, R.N. Parkins, Crack interaction, coalescence and mixed mode fracture mechanics, Fatigue Fract. Eng. Mater. Struct. 19 (1) (1996) 51–63. https://doi.org/10.1111/j.1460-2695.1996.tb00931.x.

[39] B.N. Leis, Initiation of SCC on gas transmission pipelines in related cracking environments, Corrosion 96. (1996), NACE96268, NACE International, Houston, Texas.

[40] T.L. Anderson, Fracture mechanics: fundamentals and applications, CRC press, Boca Raton, 2017.

[41] S.K. Paul, S. Tarafder, Cyclic plastic deformation response at fatigue crack tips, Int. J. Press. Vessel. Pip. 101 (2013) 81–90. https://doi.org/10.1016/j.ijpvp.2012.10.007.

[42] A.Q. Fu, Y.F. Cheng, Electrochemical polarization behaviour of X70 steel in thin carbonate/bicarbonate solution layers trapped under a disbonded coating and its implication on pipeline SCC, Corros. Sci. 52 (7) (2010) 2511–2518. http://dx.doi.org/10.1016/j.corsci.2010.03.019.

[43] J. Griggs, O. Lavigne, E. Gamboa, Influence of strain on current densities and stress corrosion cracking growth rates in X65 pipeline steel, Corrosion. 73 (2) (2016) 192–198. https://doi.org/10.5006/2186.

[44] S.-H. Wang, Y. Zhang, W. Chen, Room temperature creep and strain-rate-dependent stress-strain behaviour of pipeline steels, J. Mater. Sci. 36 (2001) 1931–1938. https://doi.org/10.1023/A:1017545907676.

[45] S. Wang, L. Lamborn, K. Chevil, E. Gamboa, W. Chen, Near-neutral pH corrosion of mill-scaled X-65 pipeline steel with paint primer, J. Mater. Sci. Technol. 49 (2020) 166–178. https://doi.org/10.1016/j.jmst.2020.01.016.

[46] T.R. Baker, R.N. Parkins, G.G. Rochfort, Investigations relating to stress corrosion cracking on the pipeline authority's Moomba-to-Sydney pipeline, in: Proc. 7th Symp. Line Pipe Res. Cat., 1986: pp. 21–27.

Chapter 6 Effects of Loading Spectra on High pH Crack Growth Behaviour of X65 Pipeline Steel [1]

6. 1 Introduction

Buried pipelines play a vital role in the safe and economical transportation of oil and natural gas over long distances [1]. Buried pipelines typically employ cathodic protection (CP) and external coatings to protect against external threats such as corrosion. The external coating isolates the pipeline from the corrosive soil environment, while the CP controls the corrosion at coating defects by changing the potential of pipe [2]–[6]. Regardless of the type of coating, coating defects such as coating disbondments and holidays commonly occur during pipeline installation and may develop during operation. At coating defects, groundwater comes in direct contact with the pipe surface, leading to the formation of an occluded environment. Additionally, the shielding effect of the disbonded coatings reduces the efficacy of the CP. Consequently, the integrity of the pipeline is endangered by not only corrosion but also the potential formation of colonies of cracks, known as Stress Corrosion Cracks (SCC) [7]–[11]. Such SCC colonies are formed from the synergistic interaction between the pipeline steel, the surrounding corrosive soil environment, and the pipeline operating conditions [7], [8]. Two types of SCC have been reported in steel pipelines, where each occurs under different environmental pHs and soil chemistries. These types of SCC are High pH SCC (HpHSCC) and Near-neutral pH SCC (NNpHSCC) [9]-[14]. The focus of this paper is HpHSCC, and the role of mechanical loading factors on crack growth rate will be discussed in

[1] A version of this chapter has been published. H. Niazi, K. Chevil, E. Gamboa, L. Lamborn, W. Chen, H. Zhang, "Effects of loading spectra on high pH crack growth behaviour of X65 pipeline steel", Corrosion 76 (6), 601-615

more detail. Further information related to NNpHSCC can be found elsewhere [9], [15]–[18]. It must be clarified that in some literature, SCC is referred to as environmental crack growth under monotonic loads. However, SCC represents both crack growth under cyclic loadings and monotonic loadings in some other publications [15]–[20]. In the present paper, HpHSCC refers to intergranular crack propagation under either static load or cyclic loading conditions.

HpHSCC was first discovered in the mid-1960s following a series of failures [9], [18]. Since these first occurrences of failures caused by HpHSCC, many research studies have been conducted to understand the mechanism and to identify remedies to prevent future failures. The "Bathtub" model, which is shown in Figure 6.1, was proposed by Parkins to explain the time-dependent behaviour of a HpHSCC failure [16], [17], [21]. In order to be consistent with fracture mechanic conventions, this model has been revised, and the crack initiation is marked as stage 1 rather than the preparation stage[17]. In the preparation stage, an occluded environment required for HpHSCC, concentrated carbonate-bicarbonate aqueous solution beneath the defected coating and localized loss of appropriate level of CP [22], [23], are developed. The length of the preparation stage depends on several factors such as coating properties [22], [24], cathodic protection, groundwater pH[25], [26], soil chemistry [26], [27], temperature [24], transportation rate of electrochemical species, and seasonal changes[27]. According to the bathtub model, pipelines experience three following stages before failure [28], [29]. Stage 1 is initiation of intergranular cracks at the stresses below yield stress (stage 1a) followed by secondary cracks nucleation and crack coalescence (stage 1b) [16], [17], [19]–[21], [30], [31]. When the length of the HpHSCC crack reaches a critical value, *i.e.,* around 6 mm under field conditions [19], stage 2 of crack propagation starts. From the fracture mechanics' point of view, Stage 2 begins when the stress intensity factor (K) ahead of the crack tip exceeds the critical stress intensity factor (K_{ISCC}),

allowing a change in propagation mechanism[32]–[37]. The crack growth mechanism at this stage is anodic dissolution or repeated formation and rupture of the passive film ahead of the crack tip. The maximum crack growth rate for a single crack at this stage could be obtained by Faraday's second law [33]. This stage is followed by stage 3, where rapid crack growth may result in a slow leak or sudden rupture of the pipe, posing a risk to the environment, assets, and people. Hence, crack propagation at stage 2 is of paramount importance, and crack at this stage must be monitored and repaired to maintain safe operation[17].

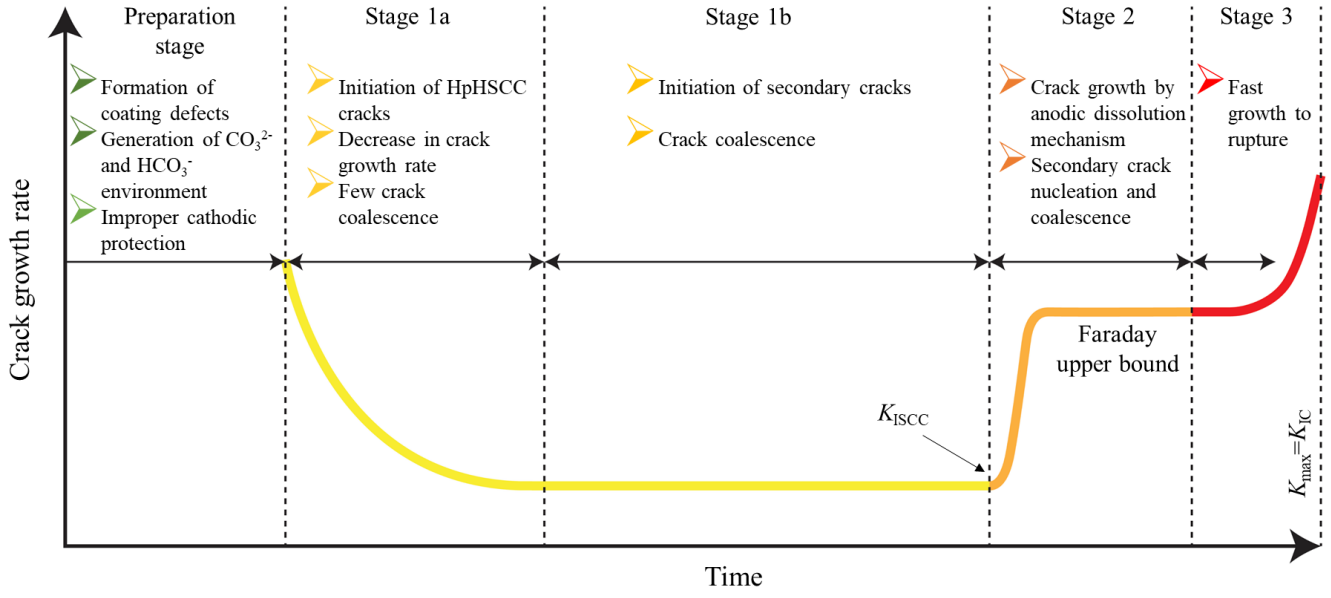

Figure 6.1. Schematic illustration of the bathtub model for HpHSCC.

To date, most research has studied crack growth behaviour under constant amplitude loading conditions at different stress ration (R) and frequencies [19], [38]. For stage 1 of HpHSCC, cyclic loading has detrimental impacts on pipeline integrity through assisting crack initiation[16], [19], [20], [28], [30]. It has been shown that threshold stress could vary between 88% and 75% of the yield strength for monotonic loading and some cyclic loading conditions, respectively[20]. It has been found that the threshold stress for crack initiation decreases as the magnitude of load

fluctuation increases [30], and the number of initiated cracks increases as the number of load cycles increases [29]. For stage 2 of HpHSCC (where $K>K_{ISCC}$), it has been shown that the crack growth increases as the maximum stress intensity factor or frequency of the loading cycle increases [38]. The critical stress intensity factor (K_{ISCC}) is reported to be between 20-25 MPa.m$^{0.5}$, depending on the type of steel and loading condition [17], [38]. It has been proposed that the corrosion fatigue caused by cyclic loading could decrease K_{ISCC} [38].

However, constant loading waveforms could not mimic the actual loading condition, as pipelines undergo variable amplitude loading waveforms during their operation. Neither time-dependent nor load history-dependent interactions are considered by constant amplitude loading tests. Hence, studying the crack growth behaviour under variable amplitude pressure fluctuation is needed to understand the mutual interactions between different concurrent crack growth mechanisms that a given crack undergoes in real situations. In the pipeline, the type of pressure fluctuation is highly dependent on the location of the pipe section, *i.e.,* the relative distance from compressor stations. According to the statistics, more than 90% of HpHSCC failures occurred within the first 30 km downstream from the compressor. It has been shown that pipes experience the most severe loading condition in this area, which is known as underload-minor-cycle type or type I pressure fluctuations [39]–[42]. The realistic pressure fluctuation spectra of oil and gas pipelines, and their analysis could be found elsewhere [40]. Figure 6.2 shows such fluctuations schematically. As is seen, type I of pressure fluctuation contains some high *R*-ratio cycles known as minor cycles followed by low *R*-ratio cycles known as underload cycles. Consequently, this type of pressure fluctuation attracts this paper's interest.

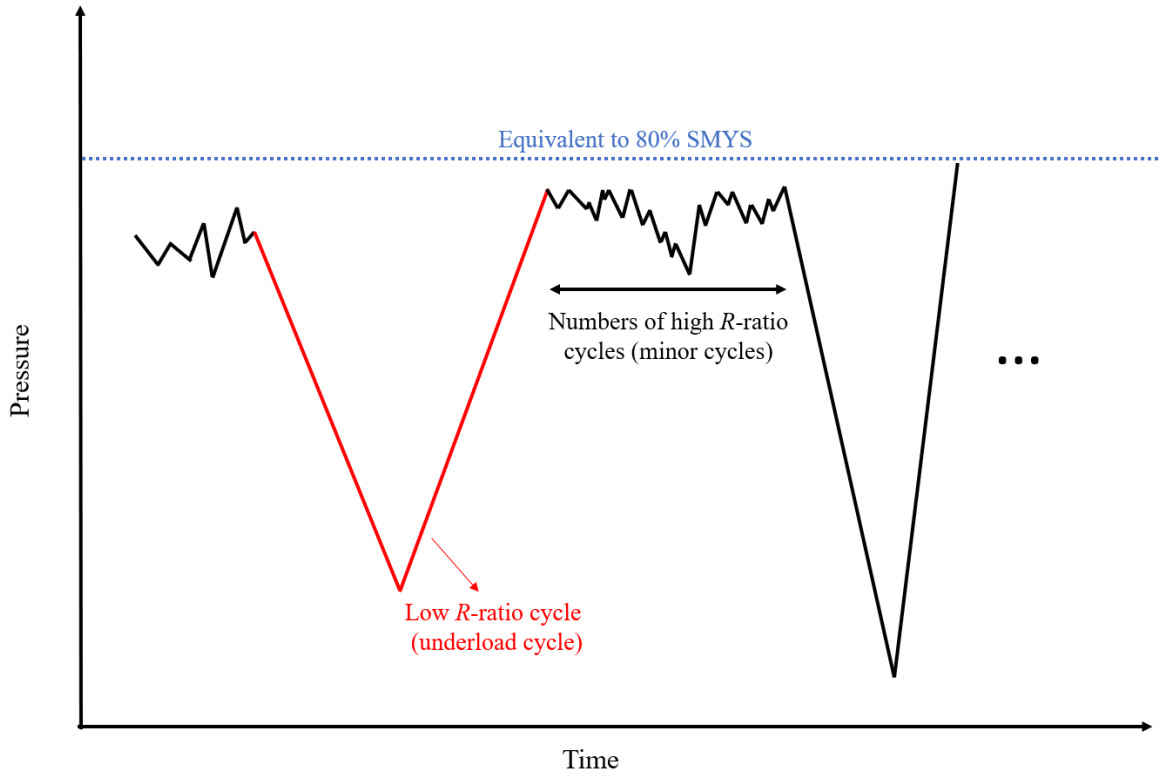

Figure 6.2. Schematic illustration of Type I pressure fluctuation in operation.

In the current study, stage 2 of HpHSCC crack growth behaviour is investigated under different loading conditions, including both high and low *R*-ratio constant amplitude waveforms and variable amplitude waveforms. These waveforms are designed to simulate type I pressure fluctuations either based on the statistical analysis of pressure fluctuations in gas pipelines [40] or more aggressive loading conditions. Evaluating the HpHSCC crack growth behaviour under variable amplitude loading conditions through studying both time-dependent phenomena and load interactions is the unique contribution of the current study. Results obtained in the current study generalized the current understanding about stage 2 of HpHSCC crack growth under simplified constant amplitude loading conditions to crack propagation behaviour under a more realistic variable amplitude loading condition. The results shown how loading parameters alter the balance between formation and rupture of the passive film through influencing time-dependent phenomena

such as crack tip strain rate, available time for re-passivation, and corrosion rate. Furthermore, particular attention is paid to the load interactions, *i.e.,* the effect of load interactions on secondary crack nucleation. The implications of the research findings for the pipeline operator is discussed, and the strategy for keeping the pipeline safe before repair or replacement is explored.

6. 2 Experimental Procedure

6. 2. 1 Materials and Environments

CT specimens with linear dimensions of 50 × 48 × 9 mm were machined from API 5L Grade X65 pipeline steel. A total of 28 CT samples were tested in this study. The chemical composition of X65 steel is shown in Table 6.1. The machined notch was perpendicular to the hoop direction so that the crack growth direction was parallel to the observed cracks in the field [41]. The CT specimens were mechanically polished using abrasive papers up to No. 600, followed by ultrasonically cleaning in acetone for 15 min. Afterwards, fatigue pre-cracking was carried out in the air according to ASTM E647-08 to initiate a sharp crack from the root of the notch [43]. The crack initiation could be in any direction near the notch tip, such as the direction with maximum shear stress or maximum tensile stress. The initiated crack propagates zigzag at higher magnification. However, the pre-crack propagation is perpendicular to the maximum tensile load/stress direction in a global scale. The length of the pre-crack on each side of the CT specimen was measured at certain intervals according to ASTM E647-08[43], and the final length of the crack on each side was controlled to be 2.5±0.2 mm. One of the advantages of using pre-cracked CT specimens was the simplicity of controlling the stress intensity factor at the crack tip [44].

Table 6.1. Chemical composition of the X65 pipeline steel

Element	C	Mn	P	Si	Ni	Cr	Mo	Cu	V	Ni	Ti	Al	Fe
Wt %	0.06	1.43	0.01	0.31	0.06	0.06	0.02	0.21	0.03	0.07	0.01	0.02	Balance

For each test, two separate cells were used so that two specimens could be running simultaneously under the same condition. In each cell, a pre-cracked CT specimen was exposed to an aerated aqueous solution with a pH value of 9.3 composed of 0.5 M Na_2CO_3 and 1 M $NaHCO_3$ (standard electrolyte for HpHSCC test known as 1N Na_2CO_3 and 1 N $NaHCO_3$) at a temperature of 40 ± 0.2˚C. A temperature of 40˚C was selected rather than the usual 75˚C to fit the context of the Canadian Pipeline Industry. According to National Energy Board report [9], the temperature of natural gas transmission pipe section and gas is about 40˚C on leaving the compressor station in North America. A potentiostat was used to maintain a cathodic potential of -590 mV versus Saturated Calomel Electrode (SCE) on the pre-cracked specimens. The magnitude of the CP potential is selected within the cracking range based on values reported in the literature [26]. The environmental conditions were chosen to simulate actual field conditions for HpHSCC [25]. A stainless-steel ribbon that surrounded the CT specimens was employed as an auxiliary electrode.

6. 2. 2 Potentiodynamic Polarization Tests

Potentiodynamic polarization tests at two scan rates were carried out in a solution of 0.5 M Na_2CO_3 and 1 M $NaHCO_3$ at a temperature of 40˚C to evaluate the electrochemical behaviour of the X65 pipeline steel under the environmental condition in this study. Rectangular coupons with dimensions of 10 mm × 10 mm × 9 mm were cut from the aforementioned X65 pipeline steel. Specimens were mounted with epoxy except one surface to ensure the exposed area was 1 cm^2. The mounted coupons were mechanically polished by abrasive papers up to No. 600, followed by cleaning in ethanol. Electrochemical measurements were conducted with Gamry Reference 600 workstation using a three-electrode cell system, where the specimen was used as a working electrode, a Pt plate as a counter electrode, and a saturated calomel electrode (SCE) was used as a

reference electrode. Slow and fast scan rate polarization tests were carried out from -1000 mV_{SCE} to 1000 mV_{SCE} with scan rates of 0.33 mV/s and 50 mV/s, respectively.

6. 2. 3 Loading Parameters

The pre-cracked CT specimens were pinhole loaded using a horizontal pneumatic loading machine in the test environment. Both constant and variable amplitude testing were performed (see Tables 7.2 to 7.4). The applied loading waveforms were somehow more aggressive than the pressure fluctuation in pipeline operation. For each test, two separate pre-cracked CT specimens were used. Some of the tests were repeated to confirm the results. However, the results in this study were extracted from two CT specimens to be consistent for all conditions. The maximum initial stress intensity factor was 36 $MPa.m^{0.5}$ for every test. It is worth mentioning the magnitude of K_{max} increases due to crack length expansion during the test; however, the increase in K_{max} is below 0.3% of the initial value. This magnitude of K_{max} simulates the condition in the field where a pressure equal to 75% of specified minimum yield stress (SMYS) is applied to the pipe containing a long and shallow semi-elliptical crack (a crack with crack length to crack depth ratio of 10 where the crack depth is 20-30% of wall thickness) [41], [42]. As a result, an intergranular crack initiates from the pre-crack tip and propagates. Constant amplitude loading waveforms were designed to understand the effect of either frequency or amplitude of loading fluctuation on the crack advance. Constant amplitude tests with low *R*-ratios were used to study the frequency effect (see Table 6.2). These conditions mimic the underload cycles under field conditions when the *K* value falls below the K_{ISCC}. In addition, constant amplitude tests with a variety of *R*-ratios under constant frequency were applied to study the effect of the stress ratio (see Table 6.3). Variable amplitude loading waveforms, composed of both high and low *R*-ratio cycles, were applied to pre-cracked CT specimens to simulate realistic pipeline loading conditions (see Table 6.4). High *R*-ratio and low

R-ratio cycles represent frequent minor load fluctuations and infrequent primary loading cycles during pipeline operation, respectively [40]. Furthermore, variable amplitude tests (see Table 6.4), composed of static hold, *i.e.,* a period of static loading or minor cycles and underload cycles, were employed to investigate the load interaction behaviour. Each loading block of variable amplitude loading waveforms was composed of one underload cycle plus either 50 minor cycles or a period of a static hold.

Table 6.2. Details of constant amplitude loading waveforms

Loading condition	Sample ID	*R*	Frequency (Hz)	Number of cycles	K_{max} (MPa.m$^{0.5}$)
Effect of loading frequency	F-4.6E-3	0.5	4.6×10^{-3}	3900	36
	F-9.6E-3	0.5	9.6×10^{-3}	5800	36
	F-9.6E-4	0.5	9.6×10^{-4}	500	36
	F-9.6E-5	0.5	9.6×10^{-5}	100	36

Table 6.3. Details of constant amplitude loading waveforms

Loading condition	Sample ID	*R*	Frequency (Hz)	Number of cycles	K_{max} (MPa.m$^{0.5}$)
Effect of stress ratio (R)	SH	1	4.6×10^{-3}	1	36
	R-0.9	0.9	4.6×10^{-3}	5050	36
	R-0.75	0.75	4.6×10^{-3}	3900	36
	R-0.5	0.5	4.6×10^{-3}	3900	36

Table 6.4. Details of variable amplitude loading waveforms

Sample ID	**Minor cycles**			**Underload cycles**			Number of blocks
	R	Frequency (Hz)	Number of minor cycles	*R*	Frequency (Hz)	Number of underload cycle	
SHLFU*	1	-	1	0.5	9.6×10^{-5}	1	100
MCLFU†	0.9	4.6×10^{-3}	50	0.5	9.6×10^{-5}	1	100
SHHFU‡	1	-	1	0.5	9.6×10^{-3}	1	120
MCHFU§	0.9	4.6×10^{-3}	50	0.5	9.6×10^{-3}	1	120

*Static hold plus low-frequency underload cycle

†Minor cycles plus low-frequency underload cycle

‡ Static hold plus high-frequency underload cycle

§ Minor cycles plus high-frequency underload cycle

6. 2. 4 Determination of Crack Growth Rate

Before and after each test, the free surfaces of the CT specimens were studied using a Scanning Electron Microscope (SEM) equipped with Energy Dispersive Spectroscopy (EDS). Afterwards, the CT specimens were sectioned at the mid-point in their thickness. In order to find the crack path on both the free surface and the thickness direction, those surfaces were polished using an oil-based suspension of alumina and etched with 5% Nital. Then, all the CT specimens were fractured open along the notch direction in liquid nitrogen, and the oxides on the crack walls were removed using an aqueous solution composed of 3.5 g/L hexamethylenetetramine and 8 N HCl. The fracture surfaces were studied using SEM imaging, and the length of intergranular crack growth was measured using 100 points across the fracture surface on each CT specimens. These measurements were used to calculate the average intergranular crack propagation rate.

6. 3 Results and Discussion

6. 3. 1 Electrochemical Behaviour Under Stress-Free Condition

Figure 6.3 depicts the potentiodynamic polarization curves for X65 pipeline steel in a solution of 0.5 M Na_2CO_3 and 1 M $NaHCO_3$ at a temperature of 40˚C at two sweeping rates. Regardless of the scanning rate, X65 pipeline steel shows active-passive behaviour in a high concentration carbonate-bicarbonate environment [38], [45]–[47]. For a slow scan rate curve, the corrosion potential is -855 mV_{SCE}, the primary passive potential is -650 mV_{SCE}, the critical current density is 1 $mA.cm^{-2}$, and the passive current density is 0.004 $mA.cm^{-2}$. A cathodic loop occurs at the potential near -350 mV_{SCE}. The cathodic loop is a region with the net cathodic current, which is surrounded by the regions of net anodic current. At this region, the net current is cathodic, although both anodic and cathodic processes are occurring at the same time. A possible reason for the cathodic loop is the reduction of the small amount of the dissolved oxygen in the test solution [48].

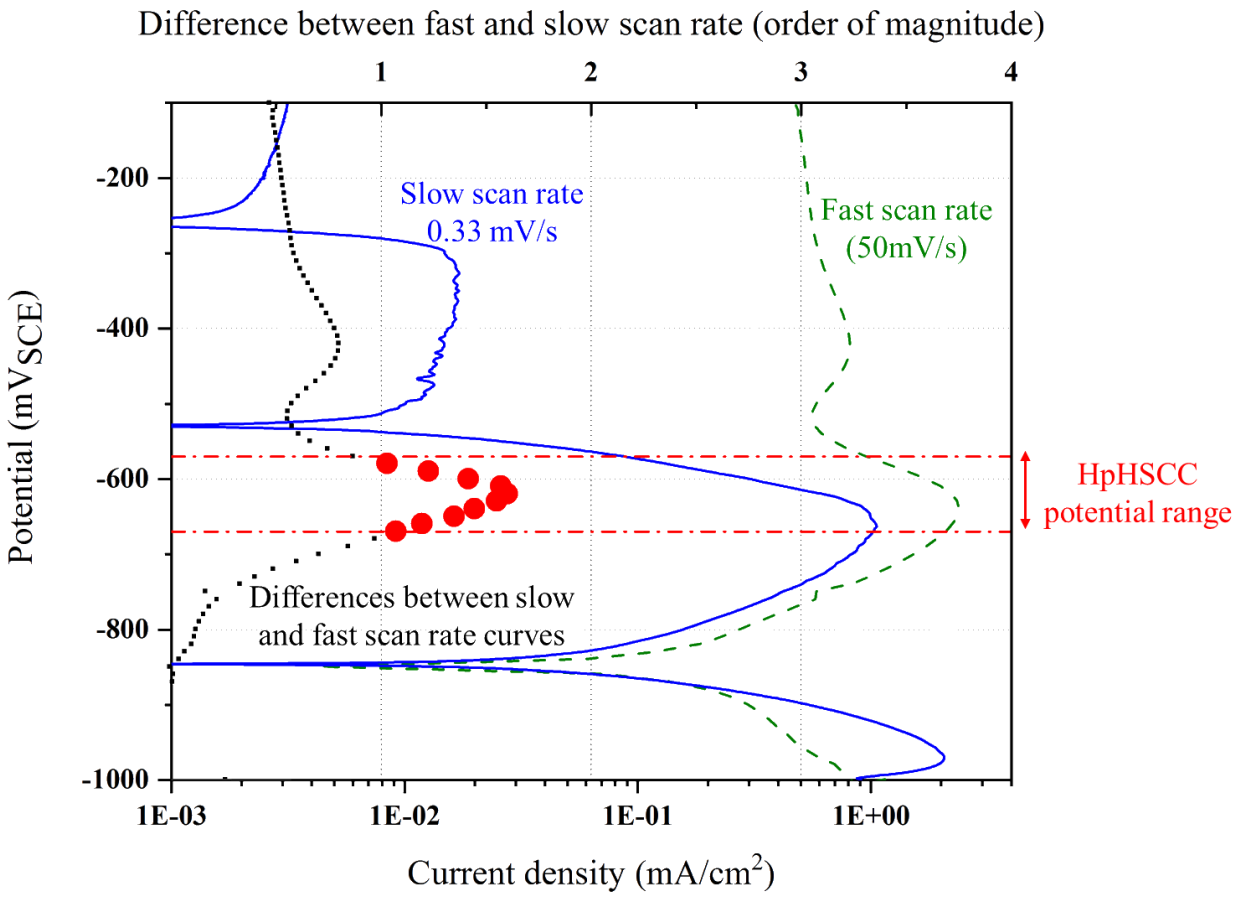

Figure 6.3. Slow (0.33 mV/s) and fast (50 mV/s) scan rates potentiodynamic polarization curves of X65 pipeline steel in a solution of 0.5 M Na_2CO_3 and 1 M $NaHCO_3$ at a temperature of 40˚C along with the differences between two curves to determine the susceptible potentials for HpHSCC.

On the other hand, there are two anodic peaks in the fast scan rate potentiodynamic curve which are at the potentials approximating -660 and -425 mV_{SCE}, respectively. The fast scan rate is employed to minimize film formation, representing a significant anodic activity as a result of a film rupture event. Conversely, the slow scan rate test will detect film formation, and here represents the gradual formation of passive film. Drawing a comparison between slow and fast scan rate tests indicates a specific potential range where high anodic dissolution in film free

condition is superseded by insignificant activity when the required time condition is met. This potential range in known as the active-to-passive transition range as has been depicted in Figure 6.3. Two conditions were applied to determine this potential window in Figure 6.3. First, the current density in fast scan rate must be greater than 1 mA/cm^2. Second, the differences between fast and slow current density must exceed one order of magnitude [33], [38], [47], [49]. In Figure 6.3, the differences between slow and fast scan rates are shown with red scatters at this potential window and black scatter at other potentials.

It is well established that when the potential of unstressed pipeline steel exposed to test solution falls within the active-to-passive potential range, intergranular corrosion occurs. Under these conditions, a passive film composed of $FeCO_3$, Fe_3O_4, and Fe_2O_3 forms on the grains, and the selective corrosion happens at the grain boundaries unless a passive film forms on the penetrating tip[47], [50]. As will be discussed in the next section, the intergranular corrosion transforms to intergranular cracking in the presence of an adequate stress level. As is evident from Figure 6.3, the passivation rate is intermediate when the potential of the pipeline steel falls within the active-to-passive transition zone. This implies that if the passive film is ruptured for any reason, dissolution at grain boundaries proceeds. Such intermediate re-passivation rate supports the anodic dissolution mechanism, the main mechanism for stage 2 crack growth. According to this mechanism, the plastic strain caused by applied load ruptures the passive film ahead of the crack tip, which is followed by crack advancement through grain boundary dissolution. It is worth mentioning that the fast scan rate shows the condition where the passive film is ruptured at the crack tip, and the slow scan rate shows the crack wall condition where the passive film can form gradually. This mechanism will be elaborated more in the next sections.

6. 3. 2 Visual Observations and Metallography

After each test, it was observed that the free surfaces of the CT specimens were covered with black films with no evidence of general corrosion. According to the discussion in Section 6.3.1, passive film forms gradually on the steel surface exposed to the test environment. This film prevents general corrosion; however, intergranular corrosion occurred on the specimen under a test environment. As intergranular corrosion starts, it initially penetrates at a high rate, yet it gradually ceases to grow because of the formation of a passive film at the penetrating tip [51], [52]. However, the penetration tip remains film-free in the presence of an adequate stress level [53], [54]. Sustaining the grain boundaries dissolution transforms intergranular corrosion to intergranular cracking. This condition could be met at the pre-crack tip, where the stress is intensified[19]. At this region, the plastic strain rate is high enough to prevent the formation of a continuous passive film at the penetration tip, keeping the grain boundaries exposed to corrosive environment. Consequently, the grain boundaries corrosion proceeds and intergranular cracks form. Figure 6.4 (a) shows the pre-crack region after polishing and etching in Nital 5%. Apparently, many parallel crack branches initiate from the pre-crack tip rather than the continuous propagation of a single crack. These cracks have an intergranular nature and are localized in the plastic zone ahead of the crack tip. These intergranular cracks take preferential paths and propagate either along the ferritic grain boundaries or across the pearlite grains [55]. For an individual crack, crack propagation relies on the extent of the critical plastic strain rate ahead of the crack tip. Therefore, the bare metal is exposed to the corrosive environment, and the crack propagates through grain boundary dissolution. At the same time, the crack walls are covered by a protective film which prevents lateral corrosion of the crack [52].

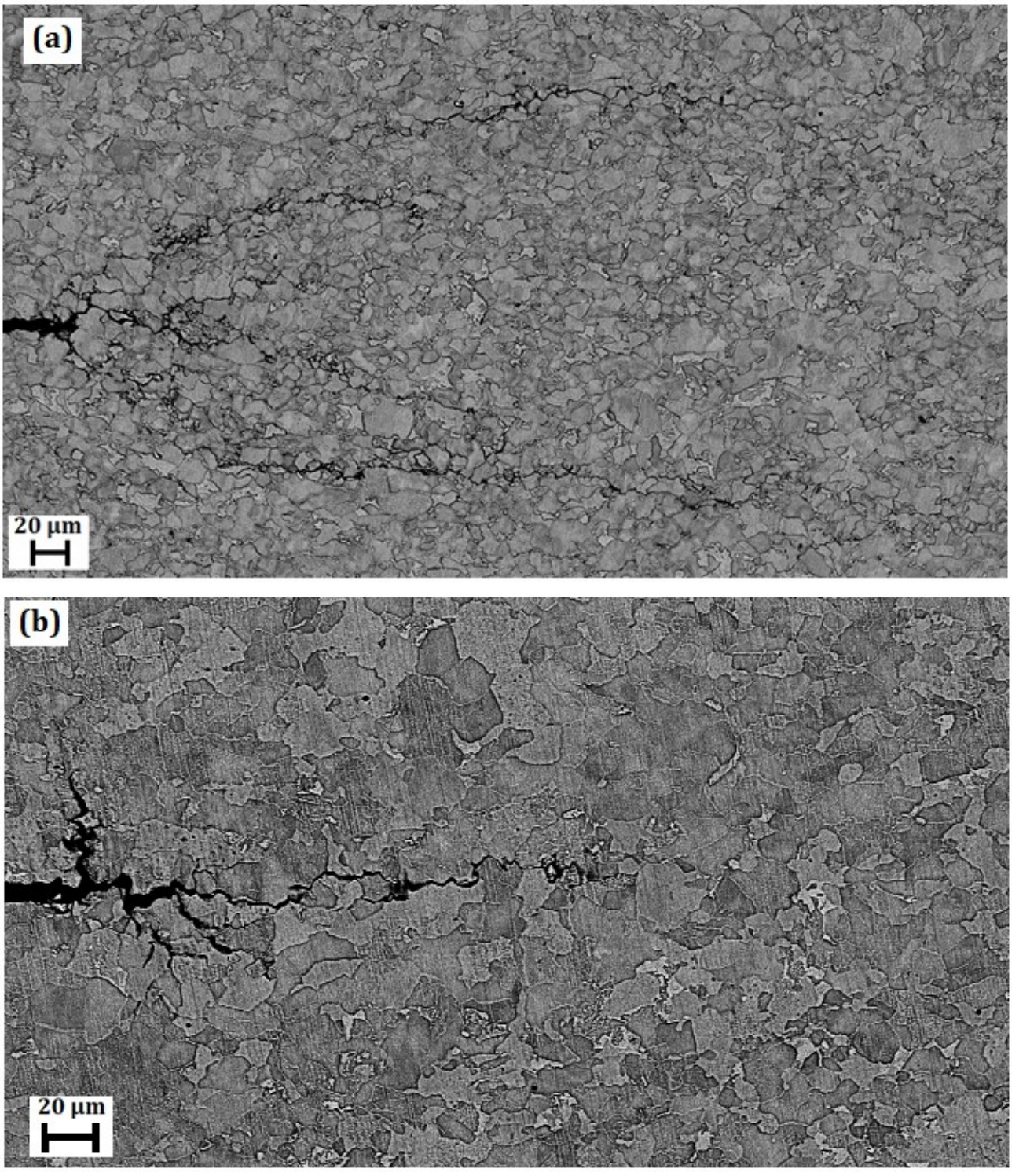

Figure 6.4. Crack tip morphology (a) free surface exposed to high pH environment, (b) middle section in thickness direction after polishing and etching in Nital 5%.

Figure 6.4 (b) illustrates the crack tip morphology in the middle plane in the thickness direction of the CT specimen. Unlike the exposed surface, a single intergranular crack is initiated from the pre-crack tip and propagated along the grain boundaries. As is seen, this crack is branched to some extent. In the case of the middle plane of the CT specimen in the thickness direction, the fatigue pre-crack tip is the sole path for corrosive media to reach the crack tip. Hence, initiation of secondary cracks ahead of the crack tip is not possible in the middle section of the CT specimen.

6. 3. 3 Fractography

Figure 6.5 shows a typical fracture surface from the current study. Three distinct regions in terms of microscopic features are evident on the fracture surface. In the middle of the fracture surface, there is a narrow ribbon that possesses the characteristics of intergranular growth. This ribbon is surrounded by a transgranular region at the top side (labelled "*fatigue pre-crack*") and cleavage fracture at the bottom. The transgranular region represents the crack growth during the fatigue pre-cracking in air, and the cleavage fracture region stands for rapid crack propagation as a result of laboratory fracture. The narrow ribbon is associated with HpHSCC crack growth where crack propagated through repeated formation and rupture of the passive film at the grain boundaries [38], [55]. When a pre-cracked CT specimen is exposed to the test environment, a passive film forms on both crack walls and crack tip. However, the passive film is able to be fracture at the crack tip where the plastic strain rate as a consequence of load application reaches or exceeds the threshold rate. Rupture of the passive film is followed by localized anodic dissolution at the grain boundaries and subsequent crack advancement along the grain boundaries[18], [53]. Grain boundaries dissolution, *i.e.* crack propagation, continues unless a passive film covers the grain boundaries again. Therefore, the crack propagates as a consequence of repeated formation and rupture of the passive film ahead of the crack tip. The relation between these two competing phenomena is

discussed in more detail later. Considering the anodic dissolution mechanism, *i.e.* repeated formation and rupture of the passive film at the crack tip, as a primary growth mechanism, cracks followed the intergranular path across the entire thickness of CT specimens regardless of the nature of the waveform. Hence, crack propagation correlated to different loading waveforms could not be differentiated in terms of the microscopic appearance of the crack.

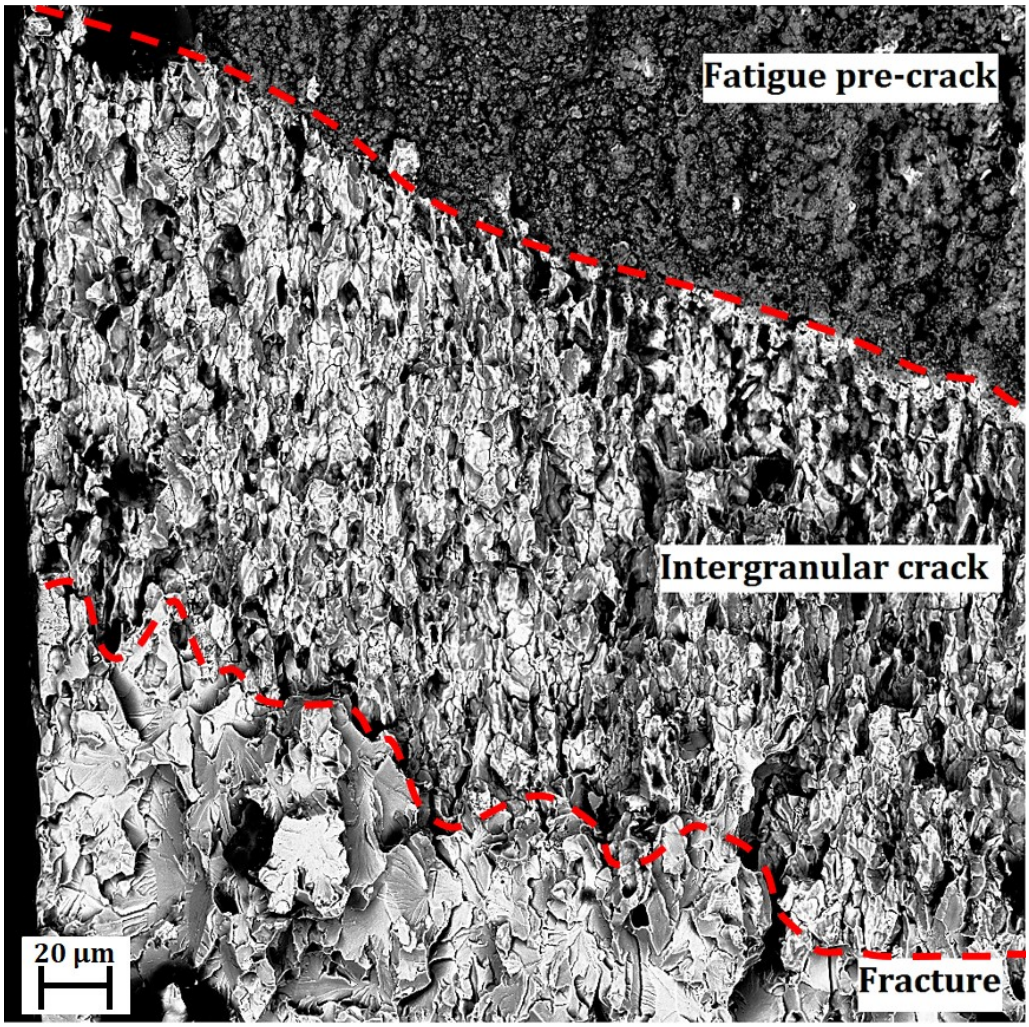

Figure 6.5. The typical fracture surface of the CT specimen after liquid nitrogen fracture.

As was discussed earlier, nucleation of secondary cracks ahead of the crack tip followed by crack coalescence is a secondary mechanism for HpHSCC crack growth [20], [31]. A numerical simulation estimated that under field conditions, approximately seven cracks need to join together

before failure [19]. Secondary cracks initiate on the external surface of the pipe where the material is exposed to the corrosive environment, and the required mechanical condition for crack initiation is met. However, areas near present intergranular cracks are breeding grounds for secondary-cracks nucleation [20], [28]. The secondary cracks develop from intergranular corrosion at the free surface, where the pipe is in direct contact with the corrosive environment [19]. As was discussed in section 6.3.2, the plastic strain rate plays a crucial role in the transformation of intergranular corrosion to intergranular cracking. Since the area ahead of the crack tip is plastically deformed, and under higher applied stress, some grain boundaries within the plastic zone may have reached a strain rate equal to or higher than the critical strain rate for film rupture. This would lead to the initiation of intergranular cracks ahead of the main intergranular cracks. Once a secondary crack nucleates on the free surface, the adjacent cracks merge, and form longer cracks on the free surface. Figure 6.6 (a) shows the evidence of secondary crack initiation and crack coalescence under SHLFU test condition (static hold plus low-frequency underload cycle). Regions I1 and I2 in Figure 6.6 (a) illustrate the nucleation of the secondary intergranular cracks ahead of the main crack tip, and Figure 6.6 (b) shows the region I2 at higher magnification. These secondary cracks are shallow and have a semi-elliptical shape. When the secondary cracks' tip on the free surface coincides with the main intergranular crack tip, the secondary cracks merge with the main crack and the surface crack length increases.

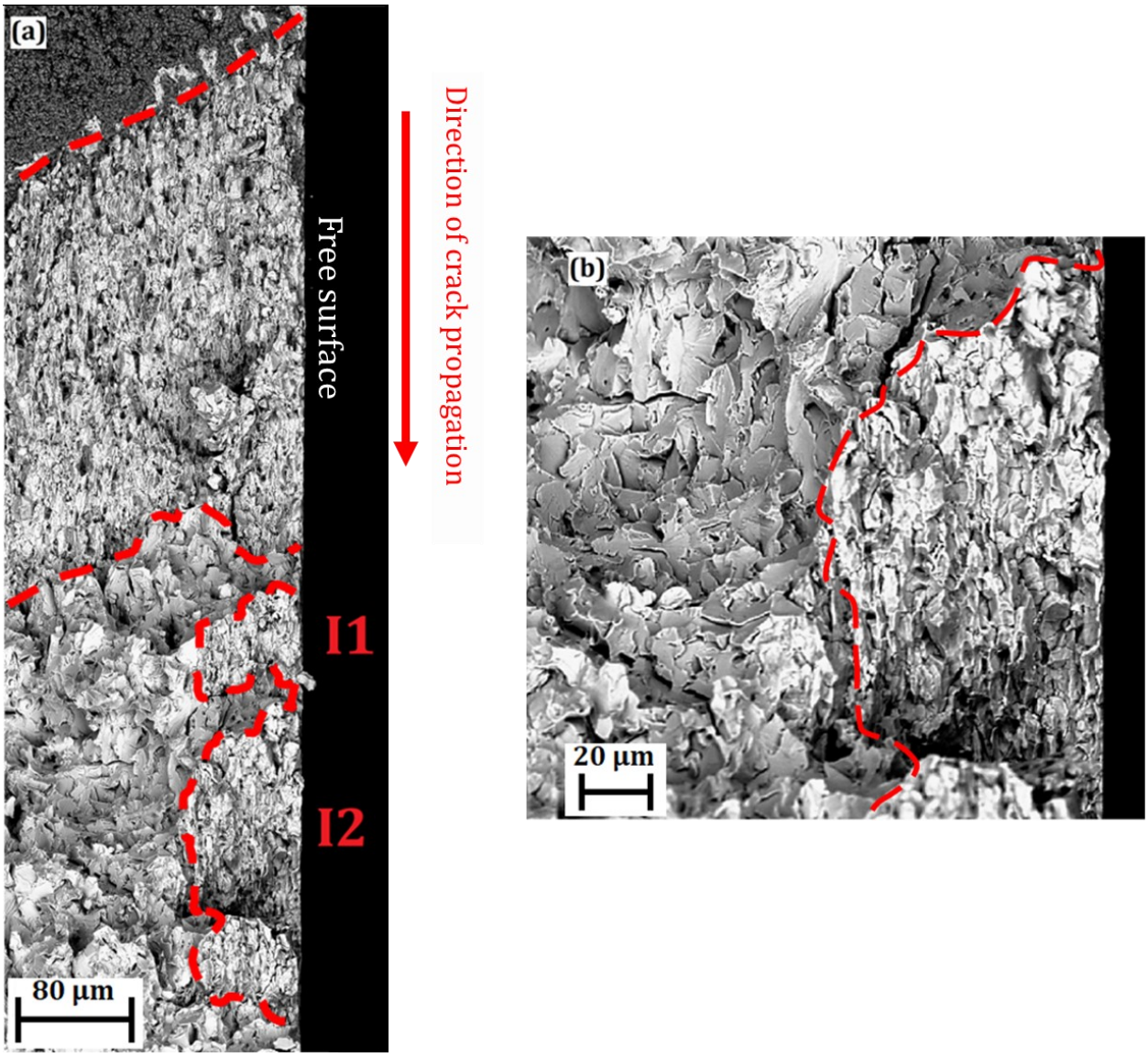

Figure 6.6. (a) Nucleation and coalescence of secondary cracks ahead of the main intergranular crack, (b) region I2 at higher magnification.

In the current study, this mechanism is more noticeable under the variable amplitude loading waveforms, as is shown in Figure 6.7. In this figure, the fracture surface of CT specimens near the free surface under R_0.9, MCLFU (minor cycles plus low-frequency underload cycle), and MCHFU (minor cycles plus high-frequency underload cycle) conditions are illustrated. It is evident from Figure 6.7 that the contribution of this mechanism to crack growth is highly

dependent on the presence of low *R*-ratio cycles, especially at high frequency and low *R*-ratio cycles. It is believed that the initiation of secondary intergranular cracks found in the plastic zone is governed by the same mechanism of cracking as the main crack. In both situations, reaching a critical strain rate at the grain boundaries is a prerequisite to cracking. For the secondary cracks formed in the plastic zone, cyclic loading generates cumulative strain ahead of the crack tip [16], [19]. At a given temperature, there is a direct relation between the magnitude of the load fluctuation and cumulative strain [16]. Therefore, low *R*-ratio cycles cause more cumulative strain compared to high *R*-ratio cycles. The cumulative strain provides the required plastic strain rate for the transformation of intergranular corrosion to intergranular cracking. Consequently, low *R*-ratio cycles have a great contribution in secondary crack nucleation [16], [19], [30]. At higher frequency, the required strain for transforming the intergranular corrosion to intergranular cracking could be accomplished within a shorter period. Hence, the likelihood of secondary crack nucleation increases, which assists crack growth on the free surface. This result is in accordance with the literature where the number of nucleated cracks on plain specimens increases as the frequency increases [29]. More details related to this mechanism, and its impact on pipeline lifespan will be discussed later.

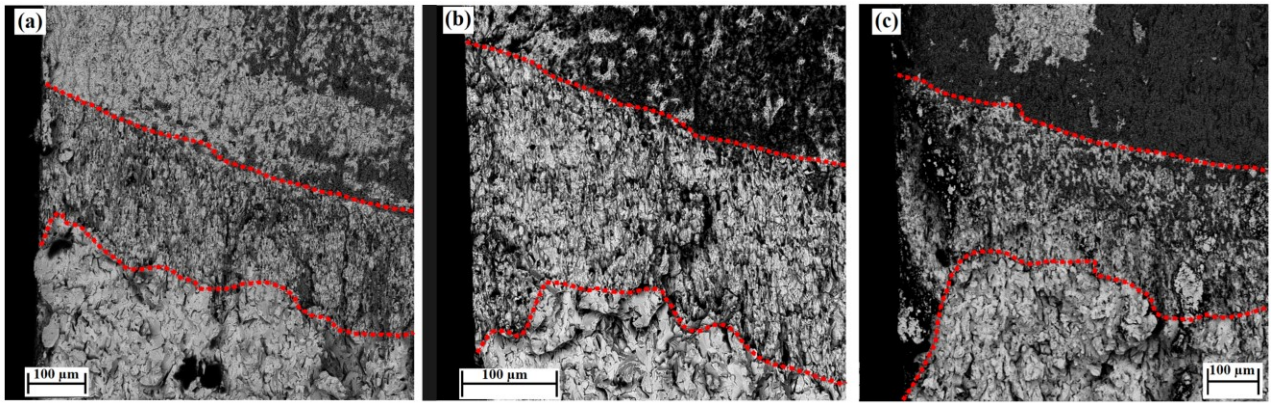

Figure 6.7. The fracture surface near the free surface (a) R-0.9, (b) MCLFU, (c) MCHFU.

6. 3. 4 Crack Growth Behaviour

- **Constant Amplitude Loading Waveforms**

Constant amplitude loading waveforms were applied to the pre-cracked CT specimens to investigate the effect of loading frequency and stress ratio on HpHSCC growth behaviour when K_{max}=36 MPa.m$^{0.5}$. Figure 6.8 (a) illustrates how the amplitude of loading fluctuation influences the HpHSCC growth rate under a constant frequency, whereas Figure 6.8 (b) shows the frequency effect on the HpHSSC propagation rate under a low *R*-ratio. Figure 6.8 (a) and (b) show that all the recorded crack growth rates are on the order of 10^{-7} mm/s, which is the same order as those reported in the literature [32], [38]. According to Figure 6.8 (a), samples tested under R-0.75, R-0.9, and SH show very similar crack growth rates that mean small load fluctuation at the frequency of 4.6×10-3 cannot alter the crack growth rate significantly. On the contrary, large fluctuation under the R-0.5 condition leads to a significant increase in the crack propagation rate. Figure 6.8 (b) shows the frequency effect when the K_{max} and *R*-ratio are 36 MPa.m$^{0.5}$ and 0.5, respectively. The results follow an increasing trend with increasing load frequency. When the *R*-ratio is 0.5, the *K* value falls below K_{ISCC} for a part of the cycle. Therefore, as the frequency decreases, the period below K_{ISCC} increases, which leads to lower crack growth. This issue will be discussed in more detail later.

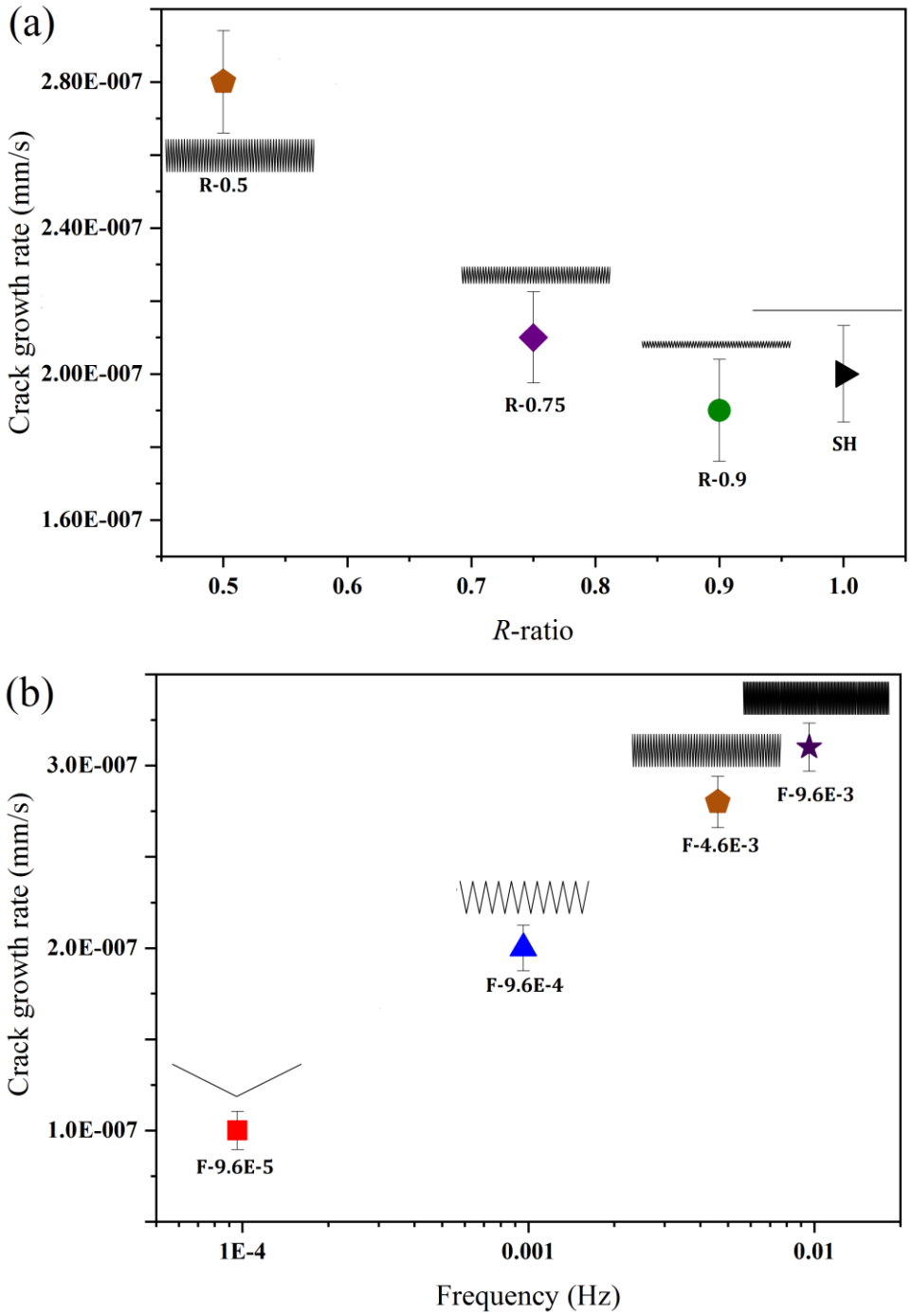

Figure 6.8. HpHSCC growth rate under constant amplitude condition with K_{max} of 36 MPa.m$^{0.5}$ (a) the effect of *R*-ratio at a frequency of 4.6 ×10^{-3} Hz and SH (static hold) (b) the effect of frequency where the *R*-ratio was 0.5 in an aqueous solution of 0.5 M Na_2CO_3 + 1M $NaHCO_3$ at 40°C and -590 mV_{SCE}.

Figure 6.8 (a) and (b) show that the HpHSCC growth rate differs slightly with the loading condition. These differences could be explained with regards to the HpHSCC mechanism, which is a competition between film formation and film rupture ahead of the crack tip. Whatever stabilizes the passive film ahead of the crack tip decreases the HpHSCC growth rate and *vice versa*. In the best-case scenario, uniform passive film forms to block the intergranular crack path, and grain boundaries are completely insulated against a corrosive environment. If such a film forms, the HpHSCC growth rate will be zero. On the other hand, bare metal could be continuously exposed

to the corrosive environment in the absence of the passive film ahead of the crack tip. This circumstance causes the maximum crack growth rate, which could be calculated by Faraday's second law, as it is expressed in Equation 6.1 [32]–[37]:

$$\text{Maximum crack growth rate} = i_a \frac{M}{zF\rho} \qquad \text{Eq'n. 6.1}$$

where M, Z, and ρ are atomic weight, valence and density of iron, respectively. The i_a stands for anodic current density obtained by a fast scan rate potentiodynamic polarization test[16][17]. Generally, the HpHSCC growth rate could be obtained through the balance between film formation and film rupture events and falls between zero and the calculated value from Equation 6.1. This balance is affected by time-dependent phenomena interactions. Time-dependent phenomena are the synergistic interactions between mechanical driving forces, environmental conditions, and the pipeline steel [17]. There are various time-dependent interactions associated with HpHSCC in steel pipelines, which are briefly discussed below. 1) The strain rate that determines the frequency of film rupturing [16], [32], [56]. Strain rate is a function of loading parameters such as amplitude and frequency of the loading waveform. 2) Electrochemical response of materials, including both the re-passivation kinetics ahead of the crack tip and the corrosion rate at the interval between film

rupture and film formation[17]. The re-passivation kinetic refers to the tendency for film formation, *i.e.,* how a passive film covers the crack tip again after a film rupture event. The corrosion rate indicates the rate of losing materials, *i.e.*, how fast crack propagates, between film rupture event and re-passivation. Both of the re-passivation kinetics and the corrosion rate rely on the material-environment system [46], [47] and the applied loading conditions[57], [58]. 3) The strain caused by time-dependent plastic deformation, such as low-temperature creep ahead of the crack tip [17], [59]. Among these time-dependent interactions, the strain rate is of paramount importance. Equation 6.2 has been derived from Equation 6.1 to express the relation between HpHSCC growth rate ($\dot{a}$) as a function of strain rate at the crack tip ($\dot{\varepsilon}_{tip}$) [37], [60].

$$\dot{a} \approx A_{\circ} i_a^* \dot{\varepsilon}_{tip}^n \qquad \text{Eq'n. 6.2}$$

where i_a^*, and n are the peak current density immediately after the film rupture event and exponent of transient current decay, respectively, and $A_{\circ}$ is a constant for a given material-environment system, as Equation 6.3 shows

$$A_{\circ} = \frac{1}{1-n}\frac{M}{zF\rho}\left(\frac{t_{\circ}}{\varepsilon_F}\right)^n \qquad \text{Eq'n. 6.3}$$

where $t_{\circ}$ is a critical time for the anodic current density to start decaying from its peak value and ε_F is fracture ductility of the passive film [37]. According to Equation 6.2, the crack tip strain rate plays a crucial role in determining HpHSCC growth in stage 2. To date, considerable efforts have been made to express the crack tip strain rate. Equation 6.4 is one of the simplest equations that shows the relation between the strain rate and loading parameters [38].

$$\dot{\varepsilon}_{tip} = \frac{1}{2t}\frac{(\Delta K)^2}{WG\sigma_y} = \frac{K_{\max}}{WG\sigma_y}(1-R)f \qquad \text{Eq'n. 6.4}$$

where $2t$ is the cycle duration, f is the frequency of loading/unloading, ΔK is the amplitude of the fluctuation in stress intensity factor ahead of the crack tip, G is shear modulus (80.7 GPa), σ_y is the yield strength (448 MPa), and W is the specimen thickness (=9 mm). According to Equations 6.4 and 6.2, both the crack tip strain rate and crack growth velocity increase as either loading/unloading frequency or amplitude of the loading fluctuation increases. This is in accordance with the results obtained in this study (see Figure 6.8). From Figure 6.8 (a), as the R-ratio decreases, a higher strain is generated within the same time period (*i.e.*, higher strain rate), which provides a higher mechanical driving force to rupture the passive film. This favours the anodic dissolution mechanism and increases the chance for the crack tip to remain under the film-free condition. Figure 6.8 (b) shows as the frequency increases under a constant R-ratio (*i.e.,* an increase in strain rate), the formation of the passive film ahead of the crack tip is less feasible. Figure 6.9 illustrates a power-law relationship between HpHSCC growth rates and strain rates calculated by Equation 6.4.

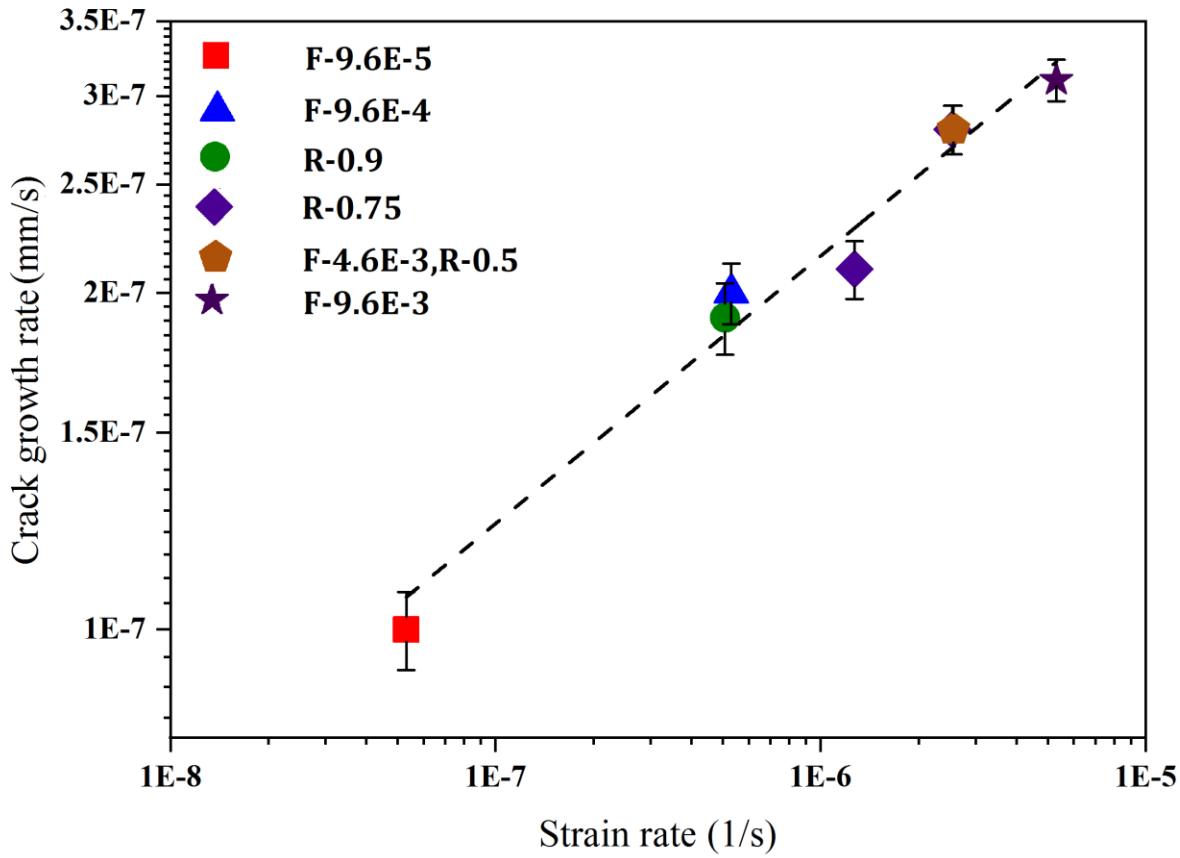

Figure 6.9. The relation between HpHSCC growth rate and strain rate was obtained by Equation 6.4 under different constant amplitude loading waveforms.

Although Figure 6.9 shows a reasonably good agreement between the crack growth rates and strain rates calculated by Equation 6.4, there are two drawbacks with this equation. First, Equation 6.4 cannot be applied when the static loading ($R = 1$) is applied to the specimens. Second, the emphasis of this equation is the amplitude of the fluctuation and frequency that neglects the magnitude of the maximum stress intensity factor or mean stress intensity factor (K_m) ahead of the crack tip. In 2014, Lu proposed Equation 6.5, which addresses the problems associated with Equation 6.4 to express the strain rate ahead of the crack tip in a more detailed formulation [37]. This equation contains K_m, and it can predict the crack tip strain rate for both cyclic and static loading conditions.

Based on this model, strain rate ahead of the crack tip has two main components, which are strain rate generated by crack tip advance ($\dot{\varepsilon}_a$) and crack tip strain caused by cyclic loading ($\dot{\varepsilon}_K$) [37]

$$\dot{\varepsilon}_{tip} = \dot{\varepsilon}_a + \dot{\varepsilon}_K = \frac{\dot{a}}{r_\circ}\frac{2N}{N-1}\frac{\beta\sigma_Y}{E}\left[\ln\left(\frac{K_m^2 - K_{ISCC}^2}{\pi r_\circ \sigma_Y^2}\right)\right]^{\frac{N+1}{N-1}} + \varepsilon_\circ f\left(\frac{1-R^*}{1+R^*}\right)^2\left(K_m^2 - K_{ISCC}^2\right) \quad \text{Eq'n. 6.5}$$

where f represents the frequency of the loading waveform and R^* is

$$R^* = \begin{cases} \dfrac{K_{\min}}{K_{\max}}; & K_{\min} \geq K_{ISCC} \\ \dfrac{K_{ISCC}}{K_{\max}}; & K_{\min} < K_{ISCC} < K_{\max} \end{cases} \quad \text{Eq'n. 6.6}$$

Other parameters of Equation 6.5 and their corresponding values in this research are summarized in Table 6.5 [37]. According to Equation 6.5, the contribution of $\dot{\varepsilon}_K$ increases as either f increases, or R-ratio decreases, which is in accordance with the results in Figure 6.8 (a) and (b). Figure 6.10 shows the power-law relation between HpHSCC growth rate and strain rate ahead of the crack tip as predicted by Equation 6.5. Similar to Figure 6.9, the crack growth rates under constant amplitude conditions follow an increasing trend with an increase in strain rate. The agreement between the experimental data and the proposed model denotes that stage 2 of HpHSCC crack growth is highly dependent on strain rate ahead of the crack tip caused by the mechanical loading conditions.

As Figure 6.10 shows, Equation 6.5 yields pretty similar strain rates for R-0.75, R-0.9, and SH conditions. These results imply that small fluctuations with the frequency of 4.6×10^{-3} Hz are unable to alter strain rate. Although the strain rates are comparable under these conditions, the causes that generate these strain rates are different. These differences could be elaborated by considering Equation 6.5, which express the strain rate by $\dot{\varepsilon}_a$ and $\dot{\varepsilon}_K$. Under SH condition, the second term in

Equation 6.5 is zero, *i.e.*, the strain rate generated by crack advancement is the sole component of the strain rate. On the other hand, both $\dot{\varepsilon_a}$ and $\dot{\varepsilon_K}$ contribute in generating strain rate under the R-0.75 condition. Under this condition, $\dot{\varepsilon_a}$ decreases due to the decrease in K_m and $\dot{a}$, yet $\dot{\varepsilon_K}$ contribution increases as a result of an increase in the amplitude of fluctuation.

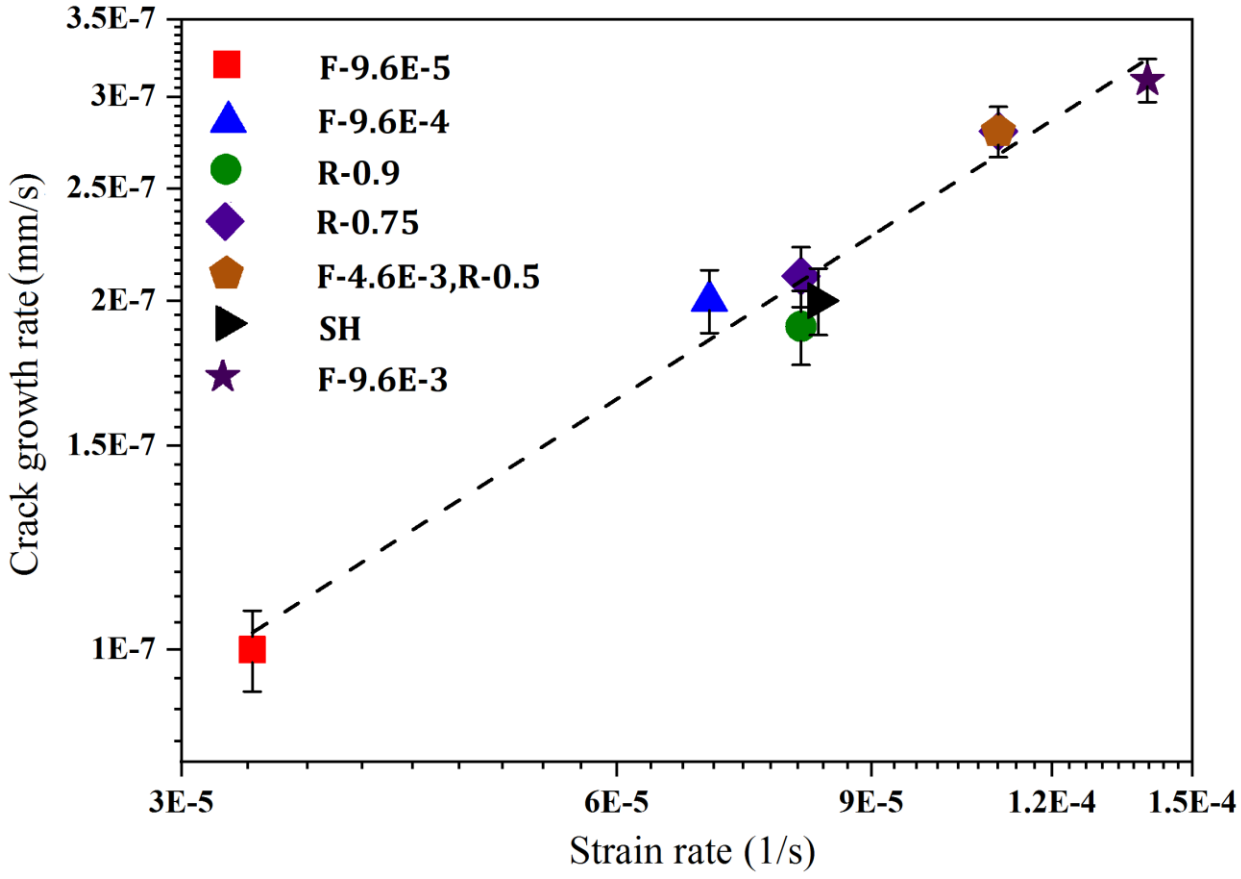

Figure 6.10. The relation between HpHSCC growth rate and strain rate was obtained by Equation 6.5 under different constant amplitude loading waveforms.

Table 6.5. Parameters in Equation 6.5 and their corresponding assumed values in the current study, which are chosen from the literature [37]

Parameter	Definition	value
r_c	Specific length for crack tip strain rate calculation	1×10^{-6} m
N	Strain-hardening exponent	6
β	Rice's coefficient	5.08
σ_Y	Yield strength	448.15 MPa
E	Young's modulus of pipeline steel	210 GPa
ε_c	Cyclic crack tip strain rate coefficient	1.56×10^{-4} MPa^{-2} m^{-1}
K_{ISCC}	Threshold stress intensity factor	25 MPa.m$^{0.5}$

- **Variable Amplitude Loading Waveforms**

Crack growth rate under variable amplitude loading conditions is more complicated in comparison with constant amplitude loading waveforms. Under variable amplitude conditions, not only time-dependent phenomena but also load-history dependent interactions affect HpHSCC growth behaviour. The load-history dependent interaction could accelerate or retard crack growth rate through influencing concurrently occurring mechanisms. A good example of load-history interaction is the nucleation of the secondary cracks in front of the main crack under variable amplitude loading waveforms. This section provides a more detailed analysis of the effect of load-history interactions on both primary and secondary HpHSCC crack growth mechanisms.

Based on the results in the previous section, variable amplitude loading waveforms were designed and applied to pre-cracked CT specimens. These waveforms were composed of a single underload cycle and either a period of static hold or many minor cycles. The *R*-ratio for the underload cycles in these tests was 0.5, but at two frequencies. The characteristics of these waveforms are reported in Table 6.4. Figure 6.11 shows HpHSCC growth rates for several constant amplitudes and variable amplitude waveforms. According to Figure 6.11, the highest and lowest crack growth rates are measured under high frequency and low frequency low *R*-ratio cycles, respectively. SH and R-0.9

conditions yield to moderate crack propagation rates. As was discussed in the previous section, the time-dependent phenomena determine the crack propagation rate under the constant amplitude loading condition. Among the time-dependent phenomena, the strain rate was of importance, and there is a power-law between crack growth rates and strain rate ahead of the crack tip (See Figure 6.10). Consequently, F-9.6E-5, which causes the lowest strain rate ahead of the crack tip, shows the lowest crack growth rate among constant amplitude conditions. Comparison of the results of variable amplitude loading waveforms and constant amplitude loading waveforms shows that the HpHSCC growth rates are highly dependent on the frequency of the underload cycles. On the one hand, MCLFU and SHLFU conditions yield to lower crack growth rates compared to R-0.9 and SH conditions. On the other hand, the crack growth rates of loading waveforms containing high-frequency underload cycles (SHHFU and MCHFU) are not significantly different from constant amplitude loading waveforms (SH and R-0.9).

Figure 6.11 implies that adding low *R*-ratio cycles, especially low-frequency ones, to high *R*-ratio cycles could alter the balance between formation and rupture of the passive film through influencing time-dependent phenomena interactions. For low *R*-ratio cycles, the stress intensity factor falls below the K_{ISCC} for a certain period during each cycle. Dropping the *K* value below the K_{ISCC} favours film formation because of the decrease in stress level at the crack tip. When $K < K_{ISCC}$, re-passivation at the crack tip controls anodic dissolution rate. Figure 6.12 (a) and (b) show variable amplitude waveforms that containing low and high-frequency underload cycles, respectively. The period when the stress intensity factor is below the K_{ISCC} increases as the loading frequency decreases. According to the slow scan rate potentiaodynamic polarization test in Figure 6.3, the passive film gradually forms when the potential is within the active-to-passive region. As the tests were conducted at a potential within that region (-590 mV_{SCE}), the chance for re-

passivation at the crack tip increases at lower frequencies. Consequently, low-frequency underload cycles lead to a lower crack growth rate. In addition, at low stress intensity factors, the passive film wedges between crack faces and insulates the crack tip from a corrosive environment. Accordingly, there is a stress intensity factor at which the crack opens (K_{op}), and a corrosive environment can reach the crack tip. This phenomenon is known as oxide-induced closure[61].

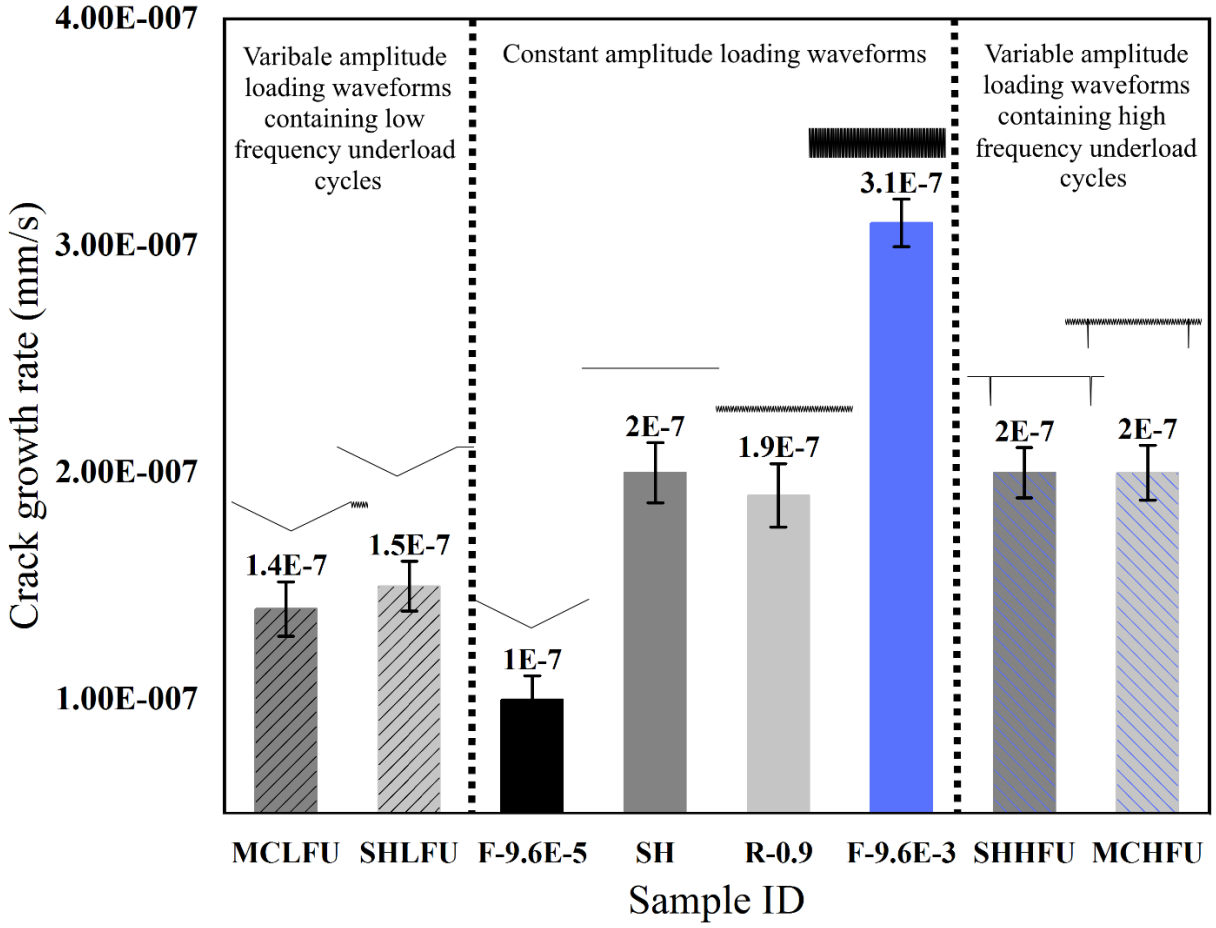

Figure 6.11. HpHSCC under variable amplitude loading waveforms and some constant amplitude loading conditions.

Similar to the above discussion about K_{ISCC}, the period when the K value is below, K_{op} is higher at a lower frequency. Hence both oxide-induced closure effect and restriction in anodic dissolution mechanism at the crack tip become more pronounced in the presence of low-frequency underload

cycles for two reasons. First, low-frequency cycles provide more time for the formation of the passive film. Second, the period when the mechanisms discussed above are in effect increases as the loading frequency decreases.

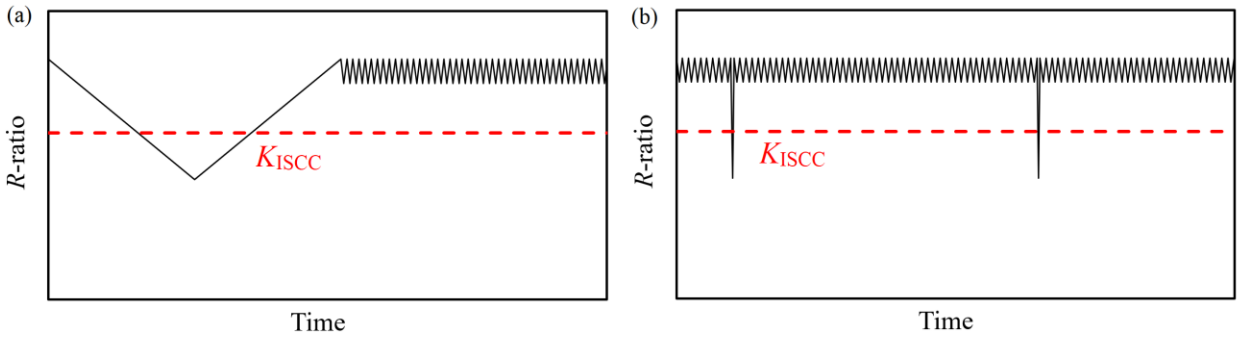

Figure 6.12. Variable amplitude waveforms with (a) low-frequency (b) high-frequency underload cycle.

In addition to the above discussion, the mechanical driving force to rupture the passive film is highly dependent on the frequency of low *R*-ratio cycles. As was stated earlier, the strain rate ahead of the crack tip is of importance for Stage 2 HpHSCC growth, *i.e.*, the higher the strain rate, the higher the crack growth rate. Figure 6.13 shows the datapoints associated with variable amplitude loading conditions (hollow icons), which are added to constant amplitude data points from Figure 6.10. It is worth mentioning that the time-average strain rate is calculated for variable amplitude loading waveforms. According to Figure 6.13, the strain rate of MCHFU and SHHFU is very close to the strain rate of R-0.9 and SH. For these conditions, high frequency low *R*-ratio cycles were too short (100 s) compared to the loading block duration (12,120 s). Hence, the presence of high frequency low *R*-ratio cycles in the loading waveform does not alter the time average strain rate significantly. Conversely, the duration of low-frequency underload cycles is considerable compared to the loading block duration. Consequently, SHLFU and MCLFU cause a lower strain

rate compared to SH and R-0.9. Apparently, the results fit the power-law relation observed previously, *i.e.,* an increase in strain rate is accompanied by increased HpHSCC growth rate.

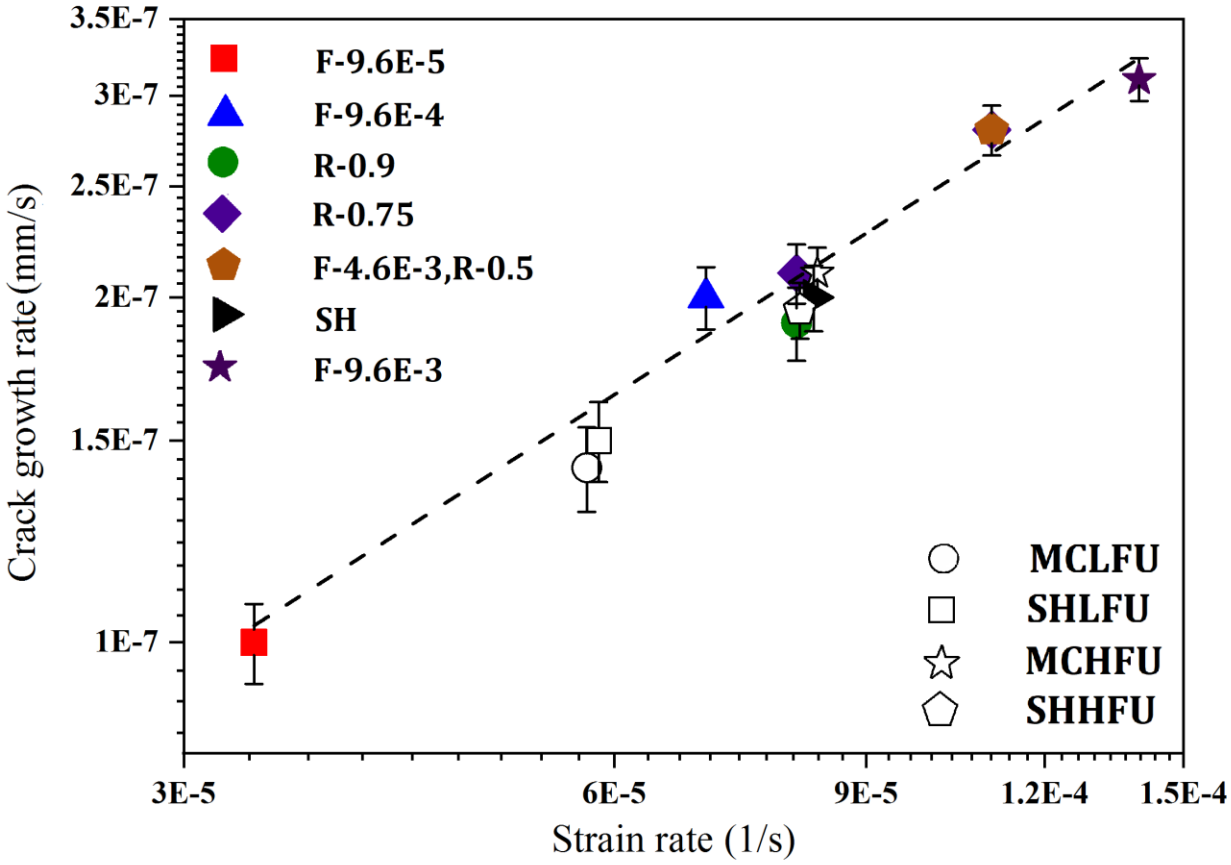

Figure 6.13. The relation between HpHSCC growth rate and strain rate was obtained by Equation 6.5 under constant and variable amplitude loading waveforms.

Figure 6.14 compares the crack growth rates on the free surfaces and middle sections of the CT specimens under selected constant amplitude and variable amplitude loading conditions. The variable amplitude loading waveforms show higher crack growth rates on the free surfaces of the CT specimens compared to the middle section growth rates, as was visually shown in Figure 6.7. Additionally, MCHFU and SHHFU conditions lead to higher surface crack growth rates compared to R-0.9 and SH condition, respectively. Conversely, MCLFU and SHLFU surface crack growth

rates are lower than constant amplitude conditions. Hence, it is evident that high frequency low *R*-ratio cycles play a vital role in crack propagation on the free surface.

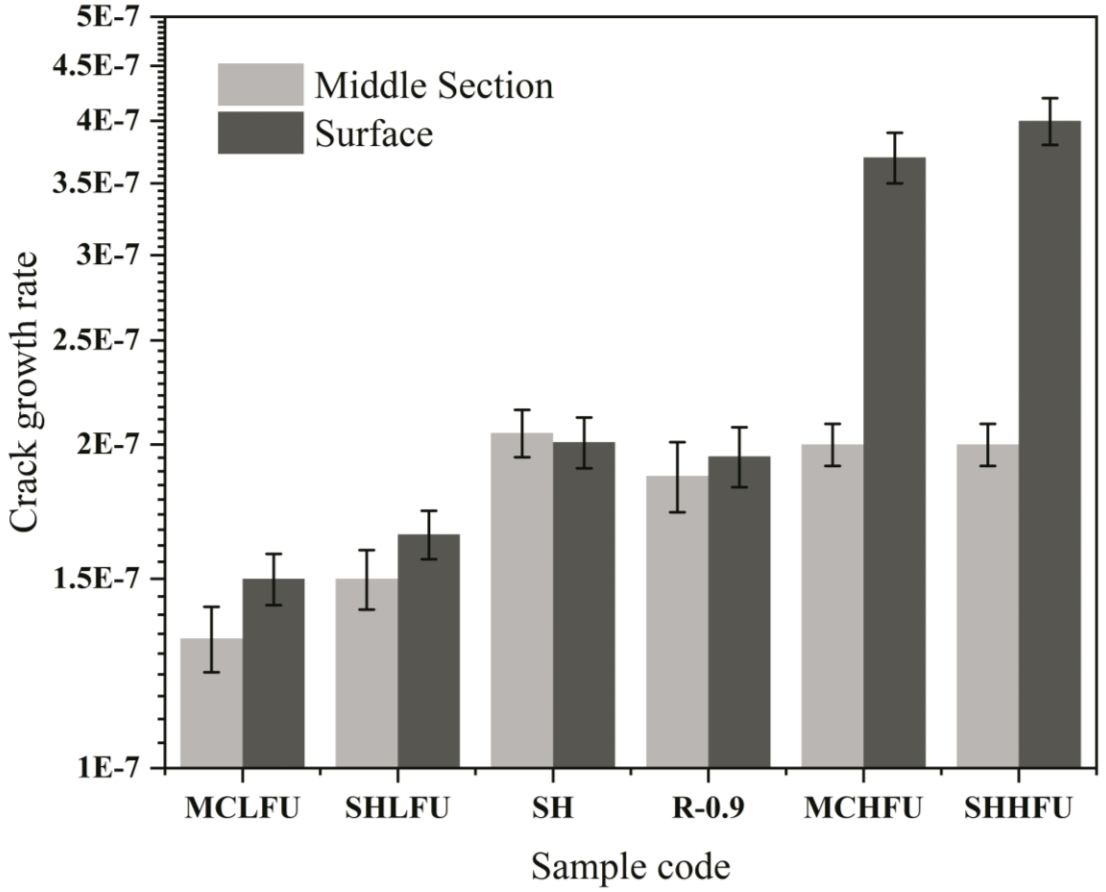

Figure 6.14. Comparison of HpHSCC growth rate on the free surface and in the middle plane in the thickness direction of CT specimens.

As discussed earlier, the higher surface growth rate is caused by the mechanism of nucleation and coalescence of secondary cracks ahead of the main crack tip. According to Figure 6.7 and Figure 6.14, this mechanism depends on underload cycles' frequency, and it is more evident when the loading waveform is composed of high frequency low *R*-ratio cycles. However, initiation and coalescence of secondary cracks caused by low frequency low *R*-ratio cycles should not be ignored. Any circumstances that increase the crack length on the free surface is detrimental to

pipeline integrity and must be avoided. The serious consequences of the increase of crack length on the free surface are discussed in more detail in the next section. It is worth mentioning that nucleation of the secondary cracks and crack coalescence is the main growth mechanism for stage 1 of HpHSCC.

6. 4 The Implication of Results for Pipeline Operation

As was stated earlier, stage 2 of HpHSCC growth behaviour must be monitored, and pipes must be repaired before the onset of stage 3. Figure 6.15 (a) illustrates the free surface of the pipeline schematically where crack propagates through both anodic dissolution and secondary cracks coalescence. The main mechanism for stage 2 of HpHSCC growth is repeated formation and rupture of the passive film ahead of the crack tip. The time average strain rate caused by the loading condition is the main factor that alters the balance between film rupture and re-passivation at the crack tip. Therefore, for pipelines confirmed to be at stage 2 of HpHSCC, pipeline operators could minimize the crack growth rate by a factor of 3 and delay the onset of stage 3 by modifying the pipeline operating conditions. Some of the operating conditions could be extracted from Equation 6.5, which expresses the strain rate ahead of the crack tip as a function of several loading parameters [37]. Accordingly, high internal pressure and high frequency load fluctuation must be avoided. Particular attention must be paid to the high frequency low *R*-ratio cycles which caused the highest strain rate in this study. Additionally, Figure 6.15 (a) shows that secondary cracks nucleate in the vicinity of the main crack as a result of plastic strain in this region and exposure to corrosive environment. This crack could merge to the main crack and increase crack length on the free surface. As was discussed in the fractography section, secondary cracks are likely to nucleate in the area near the present crack.

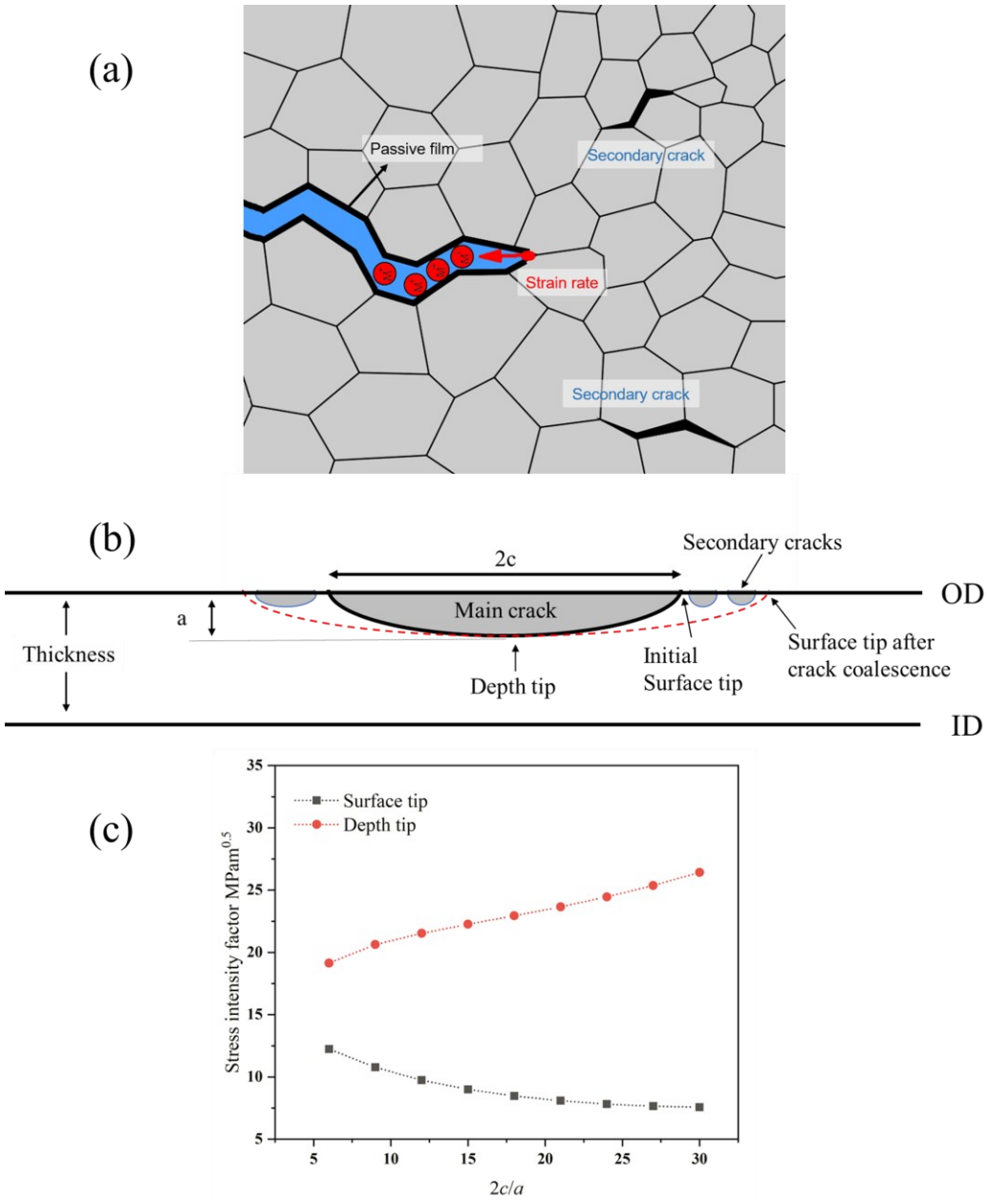

Figure 6.15 (a) schematic illustration of crack propagation mechanisms on the free surface of the pipe exposed to carbonate bicarbonate solution, *i.e.*, anodic dissolution and secondary crack initiation followed by crack coalescence (b) side-view of the pipe that showing secondary crack nucleation near the main crack tip is followed by crack coalescence (c) variation of stress intensity factor on free surface tip and depth tip of the semi-elliptical crack with the depth of 1 mm in X65 pipeline steel as a function of aspect ratio (*2c*/*a*).

Although the pipeline operator could make a rough estimate on the duration of stage 2 of HpHSCC by considering the strain rates, the mechanism of secondary cracks initiation and coalescence might shorten the estimated time. Figures 7.6 and 7.7 display the increase in crack length on the free surface by this mechanism. Implication of this result under the field condition is illustrated in Figure 6.15 (b) schematically. This figure shows a side view of the pipe containing a main semi-elliptical crack and nucleated secondary cracks. The red dashed line in this figure shows the crack geometry when the main semi-elliptical crack merge to the secondary cracks. As it can be seen, the crack is elongated on the free surface due to crack coalescence mechanism. Increase in crack length on the surface is followed by an increase in the mechanical driving force for crack propagation in the depth direction, as determined by fracture mechanics calculations and depicted in Figure 6.15 (c). This figure shows how the increase in the crack length of the semi-elliptical crack (with 1 mm depth in X65 steel loaded to 75% SMYS) alters both the surface tip's and depth tip's stress intensity factor. According to this figure, the stress intensity factor on the crack depth shows an increasing trend as the crack length increases. Once the stress intensity factor on the depth tip exceeds K_{ISCC}, crack growth in the depth direction increases rapidly. According to Figure 6.11, low R-ratio cycles, especially high ones, activate the secondary mechanism for HpHSCC growth. Hence, avoiding such loading cycles will extend the lifespan of an operating pipeline.

6. 5 Conclusion

HpHSCC growth rates in API 5L Grade X65 pipeline steel were measured under both constant and variable amplitude loading waveforms in an aqueous solution of 0.5 M Na_2CO_3 and 1 M $NaHCO_3$ at 40°C and applied cathodic protection of -590 mV_{SCE}. The magnitude of the K_{max} was 36 $MPa.m^{0.5}$ for all tests, which was higher than K_{ISCC}. The main mechanism for HpHSCC growth under the test condition was anodic dissolution ahead of the crack tip. According to this

mechanism, both time-dependent phenomena and load interactions influence the competition between film rupture and re-passivation ahead of the crack tip. Consequently, competition determines the HpHSCC growth rate. All of the crack growth rates were on the order of 10^{-7} mm/s, where the highest and lowest crack growth rates were 3.1×10^{-7} and 1.0×10^{-7}, respectively. The main findings of the research are:

- Among the time-dependent phenomena, the time average crack tip strain rate is the main factor that governs stage 2 of the HpHSCC growth rate. The strain rate ahead of the crack tip is a function of loading parameters such as mean stress, the loading frequency, and stress amplitude. Any factor that increases the crack-tip strain rate destabilizes the passive film ahead of the crack tip and enhances anodic dissolution. The increasing trend in HpHSCC growth rate with the increase in strain rate follows a power-law relationship.
- If the stress intensity factor falls below the K_{ISCC} during a part of the loading cycle, the re-passivation possibility at the crack tip is raised. The passive film formed at low K values restricts anodic dissolution. Additionally, oxide-induced closure might block the corrosive environment path to the crack tip. Both stabilizing of the passive film and oxide-induced closure effect are fortified with a decrease in loading frequency. As a result, the addition of the low-frequency underload cycles to high R-ratio cycles or static loading retards stage 2 of HpHSCC growth rate.
- The addition of low R-ratio cycles, particularly high-frequency ones, to either static loading or high R-ratio cycles results in a higher crack growth rate on the free surface compared to the middle section of the CT specimens. These cycles assist the crack propagation on the free surface through nucleation of secondary cracks and their coalescence with the main crack, which is identified as a secondary mechanism for stage 2 of HpHSCC. Crack

coalescence on the free surface plays a crucial role in the onset of stage 3 through shortening the duration of stage 2. An increase in surface crack length is followed by an increase in K value at the depth crack tip. As a result, the crack propagation rate along with the thickness direction increases. Hence, avoiding high frequency low R-ratio cycles increases the lifespan of pipes in stage 2 of HpHSCC.

References

[1] P. Venturino, J.N. Booman, M.O. Gonzalez, J.L. Otegui, "Pipeline failures due to lightning," Engineering Failure Analysis 64, (2016), p.1-12.

[2] A. W. Peabody, R. L. Bianchetti, "Control of Pipeline Corrosion," Second ed., NACE, Houston, 2000, p. 5-47.

[3] I. Thompson, J.R. Saithala, "Review of pipeline coating systems from an operator's perspective," Corrosion Engineering, Science and Technology 51, 2 (2016), p. 118-135.

[4] G.M. Harris, A. Lorenz, "New coatings for the corrosion protection of steel pipelines and pilings in severely aggressive environments," Corrosion Science 35, 5 (1993), p. 1417-1423.

[5] F. Mahdavi, M. Forsyth, M.Y.J. Tan, "Techniques for testing and monitoring the cathodic disbondment of organic coatings: An overview of major obstacles and innovations," Progress in Organic Coatings 105, (2017), p. 163-175.

[6] D. Kuang, Y.F. Cheng, "Study of cathodic protection shielding under coating disbondment on pipelines," Corrosion Science 99, (2015), p. 249-257.

[7] C.J. Maier, J.A. Beavers, T.M. Shie, P.H. Vieth, "Interpretation of External Cracking on Underground Pipelines," 2006 International Pipeline Conference (2006), p. 289-296.

[8] H. R. Hajibagheri, A. Heidari, R. Amini, “An experimental investigation of the nature of longitudinal cracks in oil and gas transmission pipelines,” Journal of Alloys and Compounds 741, (2018), p. 1121-1129.

[9] National Energy Board, “Stress Corrosion Cracking on Canadian Oil and Gas Pipelines,” Natl. Energy Board, Calgary, Alberta. (1996).

[10] I.V. Ryakhovskikh, R.I. Bogdanov, V.E. Ignatenko, “Intergranular stress corrosion cracking of steel gas pipelines in weak alkaline soil electrolytes,” Engineering Failure Analysis 94, (2018), p. 87-95.

[11] C. Manfredi, J.L. Otegui, “Failures by SCC in buried pipelines,” Engineering Failure Analysis 9, 5 (2002), p. 495-509.

[12] O. Lavigne, E. Gamboa, W. Costin, M. Law, V. Luzin, V. Linton, “Microstructural and mechanical factors influencing high pH stress corrosion cracking susceptibility of low carbon line pipe steel,” Engineering Failure Analysis 45, (2014), p. 283-291.

[13] S.A. Shipilov, I. Le May, “Structural integrity of aging buried pipelines having cathodic protection,” Engineering Failure Analysis 13, 7 (2006), p. 1159-1176.

[14] Z. Abbasi, H. Niazi, M. Abdolrazzaghi, W. Chen, M. Daneshmand, “Monitoring pH level using high-resolution microwave sensors for mitigation of stress corrosion in steel pipeline,” just accepted in IEEE Sensors Journal 2020.

[15] W. Chen, “An Overview of Near-Neutral pH stress corrosion cracking in pipelines and mitigation strategies for its initiation and growth,” Corrosion 72, 7 (2016): p. 962-977.

[16] R.N. Parkins, “1990 Plenary lecture: strain rate effects in stress corrosion cracking,” Corrosion 46, 3 (1990): p. 178-189.

[17] W. Chen, “Modeling and prediction of stress corrosion cracking of pipeline steels,” in A. M, El-Sherik (Eds), Trends in oil and gas corrosion research and technologies, Woodhead Publishing, Boston, 2017, pp. 707–748.

[18] J.A. Beavers, B.A. Harle, “Mechanisms of high-pH and near-neutral-pH SCC of underground pipelines,” Journal of Offshore Mechanics and Arctic Engineering 123, 3 (2001), p. 147-151.

[19] T. R. Baker, R. N. Parkins, G. G. Rochfort, “Investigations Relating to Stress Corrosion Cracking on the Pipeline Authority’s Moomba-to-Sydney Pipeline,” Procedding 7th Symposium Line Pipe research (1986), p. 21-27.

[20] R.N. Parkins, “The application of stress corrosion crack growth kinetics to predicting lifetimes of structures,” Corrosion Science 29, 8 (1989), p. 1019-1038.

[21] J.A. Beavers, “Integrity management of natural gas and petroleum pipelines subject to stress corrosion cracking,” Corrosion 70, 1 (2014), p. 3-18.

[22] Y. F. Cheng, R. Norsworthy, “Pipeline Coating,” NACE, Houston 2016, p. 121-147.

[23] F. King, “Development of guidelines for identification of SCC sites and estimation of re-inspection intervals for SCC direct assessment, US Department of Transportation Pipeline and Hazardous Materials Safety Administration and Pipeline Research Council International, Inc. 2010.

[24] J.A. Beavers, C.L. Durr, B.S. Delanty, “High-Ph Scc: Temperature and Potential Dependence for Cracking in Field Environments,” 2nd International Pipeline Conference 1998, p. 423-437.

[25] R.N. Parkins, C.S. O'Dell, R.R. Fessler, “Factors affecting the potential of galvanostatically polarised pipeline steel in relation to scc in CO32--HCO3- solutions,” Corrosion Science 24, 4 (1984), p. 343-374.

[26] J.A. Beavers, R.G. Worthingham, “The Influence of Soil Chemistry on Scc of Underground Pipelines,” in 4th International Pipeline Conference (2002), p. 1671-1678.

[27] F. Song, “Predicting the Effect of Soil Seasonal Change on Stress Corrosion Cracking Susceptibility of Buried Pipelines at High pH,” Corrosion 2010 (2010), p. 1-14.

[28] R.N. Parkins, P.M. Singh, “Stress corrosion crack coalescence,” Corrosion 46, 6 (1990), p. 485-499.

[29] R.N. Parkins, E. Belhimer, W.K.Blanchard. “Stress corrosion cracking characteristics of a range of pipeline steels in carbonate-bicarbonate solution,” Corrosion 49, 12 (1993), p. 951-966.

[30] R. R. Fessler, T. J. Barlo, “Threshold-Stress Determination Using Tapered Specimens and Cyclic Stresses Environment-Sensitive Fracture: Evaluation and Comparison of Test Methods,” ASTM International, 1984.

[31] Y.-Z. Wang, J.D. Atkinson, R. Akid, R.N. Parkins, “Crack interaction, coalescence and mixed mode fracture mechanics,” Fatigue & Fracture of Engineering Materials & Structures 19, 4 (1996), p. 427-439.

[32] J. Griggs, E. Gamboa, O. Lavigne, “A review of modelling high pH stress corrosion cracking of high-pressure gas pipelines,” Materials and Corrosion 67, 3 (2016), p. 251-263.

[33] R.N. Parkins, “Predictive approaches to stress corrosion cracking failure,” Corrosion Science 20, 2 (1980), p. 147-166.

[34] R.N. Parkins, “Current topics in corrosion: factors influencing stress corrosion crack growth kinetics,” Corrosion 43, 3 (1987), p. 130-139.

[35] B.T. Lu, F. Song, M. Gao, M. Elboujdaini, “Crack growth prediction for underground high-pressure gas lines exposed to concentrated carbonate–bicarbonate solution with high pH,” Engineering Fracture Mechanics 78, 7 (2011), p. 1452-1465.

[36] B.T. Lu, F. Song, M. Gao, M. Elboujdaini, “Crack growth prediction for underground high-pressure gas lines exposed to concentrated carbonate–bicarbonate solution with high pH,” Engineering Fracture Mechanics 78, 7 (2011), p. 1452-1465.

[37] B.T. Lu, “Further study on crack growth model of buried pipelines exposed to concentrated carbonate–bicarbonate solution,” Engineering Fracture Mechanics 131, (2014), p. 296-314.

[38] A.K. Pilkey, S.B. Lambert, A. Plumtree, “Stress corrosion cracking of x-60 line pipe steel in a carbonate-bicarbonate solution,” Corrosion 51, 2 (1995): p. 91-96.

[39] R.R. Fessler, “Applications of Stress Corrosion Cracking Research to the Pipeline Problem,” Fifth Symposium Line Pipe Research1974.

[40] J. Zhao, K. Chevil, M. Yu, J. Been, S. Keane, G.V. Boven, R. Kania, W. Chen, “Statistical analysis on underload-type pipeline spectra,” Journal of Pipeline Systems Engineering and Practice 7, 4 (2016), p. 04016007-1-14.

[41] M. Yu, X. Xing, H. Zhang, J. Zhao, R. Eadie, W. Chen, J. Been, G.V. Boven, R. Kania, “Corrosion fatigue crack growth behavior of pipeline steel under underload-type variable amplitude loading schemes,” Acta Materialia 96, (2015), p. 159-169.

[42] M. Yu, W. Chen, R. Kania, G. Van Boven, J. Been, “Underload-induced crack growth behavior of minor cycles of pipeline steel in near-neutral pH environment,” Fatigue & Fracture of Engineering Materials & Structures 38, 6 (2015), p. 681-692.

[43] ASTM E647-15e1 Standard test method for measurement of fatigue crack growth rates, ASTM International, West Conshohocken, (2015), p. 1–49.

[44] B.F. Brown, C.D. Beachem, “A study of the stress factor in corrosion cracking by use of the pre-cracked cantilever beam specimen,” Corrosion Science 5, 11 (1965): p. 745-750.

[45] F. F. Eliyan, A. Alfantazi A, “Mechanisms of corrosion and electrochemical significance of metallurgy and environment with corrosion of iron and steel in bicarbonate and carbonate solutions—a review”. Corrosion 70, 9 (2014): p. 880-898.

[46] R.N. Parkins, S. Zhou, “The stress corrosion cracking of C-Mn steel in CO2-HCO3--CO32- solutions. I: Stress corrosion data,” Corrosion Science 39, 1 (1997), p. 159-173.

[47] R.N. Parkins, S. Zhou, “The stress corrosion cracking of C-Mn steel in CO2-HCO3¬--CO32- solutions. II: Electrochemical and other data,” Corrosion Science 39, 1 (1997), p. 175-191.

[48] J. Stiksma, S. A. Bradford, “Stress corrosion cracking of dual-phase steel in carbonate/bicarbonate solutions. Corrosion 41, 8 (1985), p.446-450.

[49] N. J. Holroyd, R. N. Parkins, “The predictability of stress corrosion cracking susceptibility of steels in acetate solutions from potentiodynamic polarization curves,” Corrosion Science 20, 6 (1980), p. 707-721.

[50] J. Might, D. J. Duquette, “Stress corrosion cracking of high-purity carbon steel in carbonate solutions. Corrosion 52, 6(1996), p. 428-434.

[51] D. Yavas, P. Mishra, A. Alshehri, P. Shrotriya, K.R. Hebert, A.F. Bastawros, “Nanoindentation study of corrosion-induced grain boundary degradation in a pipeline steel,” Electrochemistry Communications 88, (2018), p. 88-92.

[52] D. Yavas, A. Alshehri, P. Mishra, P. Shrotriya, A.F. Bastawros, K.R. Hebert, “Morphology and stress evolution during the initial stages of intergranular corrosion of X70 steel,” Electrochimica Acta 285, (2018), p. 336-343.

[53] R.N. Parkins, “Mechanistic aspects of intergranular stress corrosion cracking of ferritic steels,” Corrosion 52, 5 (1996), p. 363-374.

[54] B. N. Leis, R. N. Parkins, “Mechanics and material aspects in predicting serviceability limited by stress-corrosion cracking,”Fatigue and Fracture of Engineering Materials and Structures 21, 5 (1998), p. 583-601.

[55] J. Li, M. Elboujdaini, B. Fang, R.W. Revie, M.W. Phaneuf, “Microscopy study of intergranular stress corrosion cracking of X-52 line pipe steel,” Corrosion 62, 04 (2006), p. 316-322.

[56] M. Henthorne, The slow strain rate stress corrosion cracking test ─ A 50 year retrospective, Corrosion 72, 12 (2016), p.1488-1518.

[57] A. Q. Fu, Y. F. Cheng, “Electrochemical polarization behavior of X70 steel in thin carbonate/bicarbonate solution layers trapped under a disbonded coating and its implication on pipeline SCC,” Corrosion Science 52, 7(2010), P.2511-2518.

[58] X. Tang, Y.F. Cheng, “Micro-electrochemical characterization of the effect of applied stress on local anodic dissolution behavior of pipeline steel under near-neutral pH condition,” Electrochimica Acta 54, 5 (2009), p. 1499-1505.

[59] W. Chen, H. Zhu, S.H. Wang, “Low temperature creep behavior of pipeline steels,” Canadian Metallurgical Quarterly 48, 3 (2009), p. 271-283.

[60] F. Song, B. Lu, M. Gao, M. Elboujdaini, “Development of a Commercial Model to Predict Stress Corrosion Cracking Growth Rates in Operating Pipelines,” U. S. Department of Transportation Pipeline Hazardous Materials Safety Administration, No. 20.14080, Washington (2011), P. 2(1-2).

[61] T.L. Anderson, “Fracture Mechanics: Fundamentals and Applications,” CRC press, Boca Raton, Florida, USA (2017), p. 457-464.

Chapter 7 Conclusion and Recommendations

7. 1 Concluding Remarks

The conducted literature review showed that stage 1b, which is a lifetime determining stage for HpHSCC modelling, had been less studied. For this stage, it is assumed stochastic crack growth is caused by random crack initiation and crack coalescence mechanism. Additionally, it was understood that less attention had been paid to HpHSCC crack growth behaviour under variable amplitude loading waveforms. This study was designed to address the gaps described above in knowledge. The intergranular crack propagation behaviour of X65 pipeline steel in an aqueous solution of 0.5 M Na_2CO_3 and 1 M $NaHCO_3$ at a temperature of 40 °C and applied cathodic protection of -590 mV_{SCE} was investigated in this research. The experimental conditions simulate HpHSCC crack propagation at either stage 1b or stage 2 of the bathtub model. The main findings are summarized as follows:

1. This research made two novel contributions to our understanding of HpHSCC crack growth behaviour. First, this research shed light on crack growth during stage 1b and proved that crack initiation and coalescence are influenced by loading conditions. This research showed crack initiation happens at preferential locations, near the pre-existing crack tip, depending on loading condition. Secondly, this study showed that load interaction caused by variable amplitude loading conditions changes the crack propagation behaviour during stages 1b and 2. According to the results, both preferential crack growth locations and load interactions during stage 1b and 2 of HpHSCC influence the crack growth Behaviour and the remaining life of the cracked pipes. Therefore, the findings of

this research contribute to estimating the reliable lifetime of the HpHSCC cracked pipes section and protect human safety, environment, assets, and economy.

2. For stage 1b, where there is a preexisting crack, four distinctive regions can be considered at the crack tip, *viz.* the cyclic plastic zone, theoretical plastic zone, actual plastic zone, and elastic zone. Formation of the cyclic plastic zone depends on cyclic loading parameters (*R*-ratio) so that this region is observed in the presence of large load fluctuation only. The stress-strain responses, particularly strain rate, of the materials located in these regions are different. If the localized strain rate exceeds the critical value, film-free condition forms on some of the grain boundaries and crack initiation or growth happens. In the presence of a localized strain rate, the film formation rate on the grain boundary is suppressed by film rupturing. Both propagations of existing crack and initiation of secondary cracks depend on the film-free condition on the grain boundaries provided by strain rate.
3. Secondary cracks initiated at the preexisting crack tip can be classified into four categories. The first category of the secondary cracks are cracks formed at the boundary between theoretical and actual plastic zones, where there is a strain shock caused by the yield point phenomenon. The second group is the cracks formed within the theoretical plastic zone, where the localized stress is larger than the yield point. The generated strain rate on some grain boundaries provides film free condition and causes crack initiation. The third category of the cracks are within the cyclic plastic zone, where the plastic strain is accumulated, and materials experience the most severe loading condition. Depending on the *R*-ratio and frequency of load cycles, several intergranular cracks form in this region. These cracks play a crucial role in crack propagation during stage 1b, as they can easily

coalesce to the primary crack. The fourth group of cracks is a single crack extended from the preexisting crack.

4. Results showed that stage 1b of crack propagation depends on the presence of large load fluctuation so that constant amplitude high *R*-ratio load cycles can be considered non-propagating. The large load cycles form the cyclic plastic zone and assist secondary crack initiation near the crack tip. The secondary cracks in the cyclic plastic zone merge to the main crack and cause crack advancement. For variable amplitude loading conditions, the minor cycles that follow an underload cycle contribute to crack propagation. The main mechanism for the contribution of these minor cycles is the exhaustion of low temperature creep strain. Low-temperature creep causes existing cracks (both primary crack and secondary cracks) to propagate. Exhaustion of low-temperature creep strain causes an increase in dislocation density and interlocking of dislocations. The interlocking of dislocations is accompanied by strain shock. This strain shock is associate with the occurrence of yield point elongation at the preexisting crack tip. The strain shock accelerates the crack propagation under variable amplitude loading conditions. Therefore, the HpHSCC crack growth rate increases as the number of minor cycles between two underload events increases.
5. For stage 2 of HpHSCC, there are two mechanisms for crack propagation. The primary mechanism for crack propagation is repeated formation and rupture of the passive film at the crack tip. According to this mechanism, there is a power-law relationship between HpHSCC crack growth rate and strain rate. Strain rate depends on mechanical loading conditions such as mean stress intensity factor, amplitude and frequency of load fluctuation. The other mechanism for crack propagation in this stage is secondary crack

initiation and crack coalescence. This mechanism is identical to the crack coalescence mechanism in stage 2, and it is more pronounced in the presence of large and rapid load fluctuation.

6. The implication of the results for pipeline operators is controlled internal pressure fluctuation (*i.e.* minimizing or avoiding large and rapid load fluctuation) increases the lifetime of the cracked pipelines. Under controlled pressure fluctuation, the crack evolution at the early stage of crack propagation is retarded. The presence of large and rapid load fluctuation accelerate the crack development at early stages and reduce the lifetime of the pipe significantly in stage 1b. Postponing the onset of stage 2 is of utmost importance as sustainable crack propagation happens during stage 2. For the pipe confirmed in stage 2 of HpHSCC, the operating condition must be monitored carefully. Under this circumstance, any action that reduces the strain rate, such as a decrease in mean internal pressure or minimizing the amplitude and frequency of load fluctuation, is recommended.

7. 2 Recommendations for Future Studies

After conducting a comprehensive literature review and studying the effects of the underload type of loading on HpHSCC crack growth rates, suggestions for future work are as follows:

1. There are few available studies that link the crack propagation path to the grain boundaries' characteristics. Those studies show high angle grain boundaries are more susceptible to HpHSCC. There is a lack of a systematic investigation that correlates the crack initiation and crack growth path to the grain boundary characteristics. Employing Electron Backscatter Diffraction (EBSD) is recommended to characterize the grain

boundaries properties and crack growth pattern. The results of such a study play a vital role in developing steels more resistance to HpHSCC.

2. Considering the grain boundaries characteristics and loading conditions are needed to determine the critical strain rate for crack initiation. Such investigation is essential for the early stages of crack propagation (Stage 1a and 1b). For these stages, crack evolution is highly dependent on new crack nucleation. The critical strain rate that considers the crystallography of the grains, grain boundaries' characteristics and loading parameters will be a promising alternative for the crack initiation threshold.
3. Hydrostatic testing is a method to test the reliability of the pipes. The hydrostatic test is an overloading condition for pipes, *i.e.,* the pipe's internal pressure exceeds the design limit. The load interaction caused by overload cycles might influence HpHSCC crack growth. Studying the effects of the hydrostatic test for crack propagation during stage 1b and stage 2 is recommended.

Bibliography

- Abbasi Z., Niazi H., Abdolrazzaghi M., Chen W., Daneshmand M., "Monitoring pH Level Using High-Resolution Microwave Sensor for Mitigation of Stress Corrosion in Steel Pipelines," IEEE Sensors Journal 20 (13), 2020, pp. 7033–7043. https://doi.org/10.1109/JSEN.2020.2978086
- Abedi S.S., Abdolmaleki A., Adibi N., "Failure analysis of SCC and SRB induced cracking of a transmission oil products pipeline," Engineering Failure Analysis 14 (1), 2007, p. 250–261. https://doi.org/10.1016/j.engfailanal.2005.07.024 .
- Alamilla J. L., Sosa E., Sánchez-Magaña C. A., Andrade-Valencia R., Contreras A., "Failure Analysis and Mechanical Performance of an Oil Pipeline," Materials & Design, 50, 2013, pp. 766–73, https://doi.org/10.1016/j.matdes.2013.03.055.
- Anderson T.L., Fracture mechanics: fundamentals and applications, CRC press, Boca Raton, 2017.
- Arafin M. A., Szpunar J. A., "A New Understanding of Intergranular Stress Corrosion Cracking Resistance of Pipeline Steel through Grain Boundary Character and Crystallographic Texture Studies," Corrosion Science 51 (1), 2009, p. 119–28, https://doi.org/10.1016/j.corsci.2008.10.006.
- Arola D., Williams C. L., "Estimating the Fatigue Stress Concentration Factor of Machined Surfaces," International Journal of Fatigue 24 (9), 2002, p. 923–30, https://doi.org/10.1016/S0142-1123(02)00012-9.
- Asahi H., Kushida T., Kimura M., Fukai H., Okano S., "Role of Microstructures on Stress Corrosion Cracking of Pipeline Steels in Carbonate-Bicarbonate Solution," Corrosion 55 (7), 1999, p. 644–652, https://doi.org/10.5006/1.3284018.

- ASTM, Standard Test Method for Measurement of Fatigue Crack Growth Rates E647-15e1, ASTM B. Stand. 2016, p. 1–49, 10.1520/E0647-15E01.2.
- Atrens A., Wang J.Q., Stiller K., Andren H.O., "Atom Probe Field Ion Microscope Measurements of Carbon Segregation at an α:α Grain Boundary and Service Failures by Intergranular Stress Corrosion Cracking," Corrosion Science 45 (1), 2006, p. 79–92. https://doi.org/10.1016/j.corsci.2004.11.014.
- Atrens A., Wang J.Q., Mitchell D.R.G., "Grain Boundary Characterization of X42 Pipeline Steel in Relation to IGSCC," Corrosion 2001, NACE International Corrosion Conference, 2001.
- Baker T. N., "Microalloyed steels," Ironmaking & Steelmaking 43 (4), 2016, 264–307. https://doi.org/10.1179/1743281215Y.0000000063.
- Baker T.R., Parkins R.N., Rochfort G.G., "Investigations Relating to Stress Corrosion Cracking on the Pipeline Authority's Moomba-to-Sydney Pipeline," in: Proceedings 7th Symposium Line Pipe Research. 1986, p. 21–27.
- Barlo T.J., "Field Investigation of Stress Corrosion Cracking," in: 5th Symposium Line Pipe Research, 1974: p. T1.
- Batte A.D., Fessler R.R., Marr J.E., Rapp S.C., "Managing the Threat of SCC in Gas Transmission Pipelines," International Pipeline Conference, 2012, IPC2012-90231, p. 379–388, https://doi.org/10.1115/IPC2012-90231.
- Beavers J. A., Worthingham R. G., "The Influence of Soil Chemistry on SCC of Underground Pipelines" International Pipeline Conference, 2002, IPC2002-27146, p. 1671–78, https://doi.org/10.1115/IPC2002-27146.

- Beavers J.A., Durr C.L., Delanty B.S., “High-pH SCC: Temperature and Potential Dependence for Cracking in Field Environments”, International Pipeline Conference, 1998, IPC1998-2050, p. 423-437, https://doi.org/10.1115/IPC1998-2050.
- Beavers J. A., “Integrity Management of Natural Gas and Petroleum Pipelines Subject to Stress Corrosion Cracking,” Corrosion 70(1), 2014, p. 3–18. https://doi.org/10.5006/0998.
- Beavers J. A., Johnson J. T., Sutherby R. L, “Materials Factors Influencing the Initiation of Near-Neutral PH SCC on Underground Pipelines” International Pipeline Conference, 2000, IPC2000-221, V002T06A041, https://doi.org/10.1115/IPC2000-221.
- Beavers J. A., Harle B. A, “Mechanisms of High-PH and Near-Neutral-PH SCC of Underground Pipelines,” Journal of Offshore Mechanics and Arctic Engineering 123 (3), 2001, p. 147, https://doi.org/10.1115/1.1376716.
- Beavers J. A. Harle B. A., “Mechanisms of High-PH and Near-Neutral-PH SCC of Underground Pipelines,”. International Pipeline Conference, 1996, IPC1996-1860, p. 555-564, https://doi.org/10.1115/IPC1996-1860.
- Beavers, J. A., Thompson N. G., “External Corrosion of Oil and Natural Gas Pipelines,” ASM Handbook, vol. 13C, 2006, p. 1015–26.
- Beavers J. A, Bubenik T. A, “Stress Corrosion Cracking,” in: A. M. -El-Sherik (Eds), Trends in Oil and Gas Corrosion Research and Technologies, Woodhead Publishing, Boston, 2016, p. 295–314. https://doi.org/10.1016/B978-0-08-101105-8.00012-7.
- Beavers J. A., Christman T. K., Parkins, R. N., “Some Effects of Surface Condition on the Stress Corrosion Cracking of Line Pipe Steel,” Corrosion 87- Paper number 178, 1987.

- Been J., King F., Fenyvesi L., Sutherby R., "A Modeling Approach to High pH Environmentally Assisted Cracking," International Pipeline Conference, 2004, IPC2004-0361, p. 83–100, https://doi.org/10.1115/IPC2004-0361.
- National Energy Board, "Stress Corrosion Cracking on Canadian Oil and Gas Pipelines," National Energy Board, Calgary, Alberta, 1996.
- Brousseau R., Qian. S., "Distribution of Steady-State Cathodic Currents Underneath a Disbonded Coating," Corrosion 50 (12), 1994, p. 907–11, https://doi.org/10.5006/1.3293481.
- Brown B. F., Beachem C. D., "A Study of the Stress Factor in Corrosion Cracking by Use of the Pre-Cracked Cantilever Beam Specimen". Corrosion Science 5 (11), 1965, p. 745–50, http://dx.doi.org/10.1016/S0010-938X(65)80002-6.
- Carretero Olalla V., Bliznuk V., Sanchez N., Thibaux P., Kestens L.A.I., Petrov R.H., "Analysis of the strengthening mechanisms in pipeline steels as a function of the hot rolling parameters," Materials Science and Engineering A 604, 2014, p. 46–56. https://doi.org/10.1016/j.msea.2014.02.066.
- Castaneda H., Rosas O., "External Corrosion of Pipelines in Soil," in Oil and Gas Pipelines, R. W. Revie (Ed.), 2015, p. 265–74, https://doi.org/10.1002/9781119019213.ch20.
- Černý I., Linhart V., "An Evaluation of the Resistance of Pipeline Steels to Initiation and Early Growth of Stress Corrosion Cracks,". Engineering Fracture Mechanics71 (4), 2004, p. 913–21, https://doi.org/10.1016/S0013-7944(03)00011-0 .
- Cerny I., Mikulova D., Novak P., "Conditions of Stress Corrosion Crack Growth and Retardation in X70 Steel in Carbonate Environments," Communications- Scientific Letters of the University of Zilina 12(4), 2010, p. 68-67.

- Charles, E. A., Parkins R. N., "Generation of Stress Corrosion Cracking Environments at Pipeline Surfaces," Corrosion 51 (7), 1995, p. 518-527, https://doi.org/10.5006/1.3294372.
- Chen W., Wang S. H., Chu, R., King, F., Jack T. R., Fessler R. R., "Effect of Precyclic Loading on Stress-Corrosion-Cracking Initiation in an X-65 Pipeline Steel Exposed to near-Neutral PH Soil Environment," Metallurgical and Materials Transactions A 34 (11), 2003, p. 2601–2608, https://doi.org/10.1007/s11661-003-0019-y.
- Chen W., Zhu H., Wang S. -H., "Low Temperature Creep Behaviour of Pipeline Steels," Canadian Metallurgical Quarterly 48 (3), 2009, p. 271–283, https://doi.org/10.1179/cmq.2009.48.3.271.
- Chen W., "Modeling and Prediction of Stress Corrosion Cracking of Pipeline Steels" in: A. M. -El-Sherik (Eds), Trends in Oil and Gas Corrosion Research and Technologies, Woodhead Publishing, Boston, 2016, p. 707–748, https://doi.org/10.1016/B978-0-08-101105-8.00030-9.
- Chen W., "An Overview of Near-Neutral PH Stress Corrosion Cracking in Pipelines and Mitigation Strategies for Its Initiation and Growth'. Corrosion 72 (7), 2016, p. 962–77, https://doi.org/10.5006/1967.
- Chen W., Zhao J., Chevil K., Gamboa E., Alvarado B., "Threshold Geometrical Dimensions of Stage II Cracks Versus Required Resolution of Crack-Detection Techniques," International Pipeline Conference, 2018, IPC2018-78751, V001T03A057, https://doi.org/10.1115/IPC2018-78751.
- Cheng Y.F., "Stress Corrosion Cracking of Pipelines," John Wiley & Sons, Inc., New York, 2013. https://doi.org/10.1002/9781118537022.
- Cheng, Y. F, Norsworthy R., "Pipeline Coatings". NACE International, 2016.

- Christman T. K., “Relationships Between Pitting, Stress, and Stress Corrosion Cracking of Line Pipe Steels,”. Corrosion 46 (6), 1990, p. 450–53, https://doi.org/10.5006/1.3585131.
- Crawford, D. C., Was G. S., “The Role of Grain Boundary Misorientation in Intergranular Cracking of Ni-16Cr-9Fe in 360 °C Argon and High-Purity Water”. Metallurgical Transactions A 23 (4), 1992, p. 1195–1206, https://doi.org/10.1007/BF02665051 .
- Dai L., Wang D., Wang T., Feng Q., Yang X., “Analysis and Comparison of Long-Distance Pipeline Failures,” Journal of Petroleum Engineering 2017, 2017, p. 3174636, https://doi.org/10.1155/2017/3174636.
- Danielson M. J., Jones R. H., Krist K., “Effect of Microstructure and Microchemistry on the SCC Behavior of Archival and Modern Pipeline Steels in a High PH Environment,” Corrosion 2000, NACE-00359, 2000.
- Danielson M. J., Jones R. H., Dusek P. J., “Effect of Microstructure and Microchemistry on the SCC Behavior of Archival and Modern Pipeline Steels in a High PH Environment,” Corrosion 2001, NACE-01211, 2001.
- Zhao W., Zou Y., Xia D. X., Zou Z. D., “Effects Of Anodic Protection On SCC Behavior Of X80 Pipeline Steel In High-PH Carbonate-Bicarbonate Solution,” Archives of Metallurgy and Materials 60 (2A), 2015, p. 1009-1013, http://dx.doi.org/10.1515/amm-2015-0251.
- Elboujdaini M., Revie. R. W., “Metallurgical Factors in Stress Corrosion Cracking (SCC) and Hydrogen-Induced Cracking (HIC),” Journal of Solid State Electrochemistry 13 (7), 2009, p. 1091–99, https://doi.org/10.1007/s10008-009-0799-0.

- Elboujdaini M., Li J., Gao M., Gu, G. P., “Stress Corrosion Cracking - Microstructural and Material Property Preference for Crack Initiation of Linepipe Steel”. Corrosion 2004, 2004, NACE-04553.
- Eliyan F. F., Alfantazi A., “Mechanisms of Corrosion and Electrochemical Significance of Metallurgy and Environment with Corrosion of Iron and Steel in Bicarbonate and Carbonate Solutions—A Review”. Corrosion 70 (9), vol. 70, 2014, p. 880–98, https://doi.org/10.5006/1213.
- Evans, J. T., Parkins R. N., “Creep Induced by Load Cycling in a C-Mn Steel”. Acta Metallurgica 24 (6), 1976, p. 511–515, http://dx.doi.org/10.1016/0001-6160(76)90094-8.
- Fang B. Y., Atrens A., Wang A. Q, Han E. H., Zhu Z. Y., Ke W., “Review of Stress Corrosion Cracking of Pipeline Steels in “Low” and “High” PH Solutions”. Journal of Materials Science 38 (1), 2003, p. 127–32, https://doi.org/10.1023/A:1021126202539.
- Federal Power Commission. Final Staff Report on Investigation of Tennessee Gas Transmission Company Pipeline No. 100-1 Failure near Natchitoches, 1965.
- Fessler R. R. “Applications of Stress Corrosion Cracking Research to the Pipeline Problem,” Fifth Symposium on Line Pipe Research, 1974.
- Fessler R. R., Markworth A. J., Parkins, R. N., “Cathodic Protection Levels under Disbonded Coatings,”. Corrosion 39 (1), 1983, p. 20–25, https://doi.org/10.5006/1.3580809.
- Fessler R. R., Barlo T. J., “Threshold-stress determination using tapered specimens and cyclic stresses environment-sensitive fracture: evaluation and comparison of test methods,” (West Conshohocken, PA: ASTM International, 1984), p. 368-382.

- Fu A. Q., Cheng Y. F., “Electrochemical Polarization Behavior of X70 Steel in Thin Carbonate/Bicarbonate Solution Layers Trapped under a Disbonded Coating and Its Implication on Pipeline SCC,” Corrosion Science 52 (7), 2010, p. 2511–18, https://doi.org/10.1016/j.corsci.2010.03.019.
- Gamboa E., “Inclined Stress Corrosion Cracks in Steel Pipelines,” Corrosion Engineering, Science and Technology 50 (3), 2015, p. 191–95, https://doi.org/10.1179/1743278215Y.0000000006.
- Gamboa E. Giuliani M., Lavigne O., “X-Ray Microtomography Observation of Subsurface Stress Corrosion Crack Interactions in a Pipeline Low Carbon Steel”. Scripta Materialia, 81, 2014, pp. 1–3, https://doi.org/10.1016/j.scriptamat.2014.01.038.
- Griggs J., Lavigne O., Ga,mboa E., “Influence of Strain on Current Densities and Stress Corrosion Cracking Growth Rates in X65 Pipeline Steel”. Corrosion 73 (2), 2016, p. 192–98, https://doi.org/10.5006/2186.
- Hajibagheri H. R., Heidari A., Amini R., “An Experimental Investigation of the Nature of Longitudinal Cracks in Oil and Gas Transmission Pipelines,” Journal of Alloys and Compounds 741, 2018, p. 1121–29, https://doi.org/10.1016/j.jallcom.2017.12.311.
- George M. H., Lorenz a., “New Coatings for the Corrosion Protection of Steel Pipelines and Pilings in Severely Aggressive Environments,” Corrosion Science 35 (5), 1993, p. 1417–23, https://doi.org/10.1016/0010-938X(93)90366-O.
- Hasan F., Iqbal J., Ahmed F., “Stress Corrosion Failure of High-Pressure Gas Pipeline,” Engineering Failure Analysis 14 (5), 2007, p. 801–09, https://doi.org/10.1016/j.engfailanal.2006.11.002.

- Henthorne M., “The Slow Strain Rate Stress Corrosion Cracking Test—A 50 Year Retrospective,” Corrosion 72 (12), 2016, p. 1488–518, https://doi.org/10.5006/2137.
- Hikita H., Asai S., Takatsuka T., “Absorption of Carbon Dioxide into Aqueous Sodium Hydroxide and Sodium Carbonate-Bicarbonate Solutions,” The Chemical Engineering Journal 11 (02), 1976, p. 131–41, https://doi.org/10.1016/S0300-9467(76)80035-4.
- Holroyd N. J. H., Parkins R. N., “The Predictability of Stress Corrosion Cracking Susceptibility of Steels in Acetate Solutions from Potentiodynamic Polarization Curves,” Corrosion Science 20 (6), 1980, p. 707–21, http://dx.doi.org/10.1016/0010-938X(80)90052-9.
- Hosseini R., Seifi R., “Fatigue Crack Growth Determination Based on Cyclic Plastic Zone and Cyclic J-Integral in Kinematic–Isotropic Hardening Materials with Considering Chaboche Model,” Fatigue & Fracture of Engineering Materials & Structures 43 (11), 2020, p. 2668–82, https://doi.org/10.1111/ffe.13330.
- Hunt, C. P., “The Effect of Impurities on the Intergranular Stress Corrosion Cracking of a C/Mn Steel,” Corrosion Science 28 (9), 1988, p. 901–22, http://dx.doi.org/10.1016/0010-938X(88)90038-8.
- Griggs J., Gamboa E., Lavigne O., “A Review of Modelling High PH Stress Corrosion Cracking of High Pressure Gas Pipelines,” Materials and Corrosion 67 (3) 2015, p. 251–63, https://doi.org/10.1002/maco.201508454.
- Jingjie C., Yi H., Leilei D., Yugang L., “A New Method for Cyclic Crack-Tip Plastic Zone Size Determination under Cyclic Tensile Load,” Engineering Fracture Mechanics 126, 2014, p. 141–54, https://doi.org/10.1016/j.engfracmech.2014.05.001.

- Kentish P., “Stress Corrosion Cracking of Gas Pipelines – Effect of Surface Roughness, Orientations and Flattening,”. Corrosion Science 49 (6), 2007, p. 2521–33, https://doi.org/10.1016/j.corsci.2006.12.014.
- Kentish P. J., Influence of Surface Characteristics on the Stress Corrosion Cracking Resistance of Steel Gas Pipelines, University of South Australia, 2007.
- King F., Thomas R., Kolar M., Worthingham R. G., “A Permeable Coating Model for Predicting the Environment at the Pipe Surface Under CP-Compatible Coatings,” Corrosion 2004, NACE-04158.
- F. King, Development of Guidelines for Identification of SCC Sites and Estimation of Re-inspection Intervals for SCC Direct Assessment, 2010.
- Kuang D, Cheng Y. F., “Study of Cathodic Protection Shielding under Coating Disbondment on Pipelines,” Corrosion Science 99, 2015, p. 249–57, https://doi.org/10.1016/j.corsci.2015.07.012.
- Kuniya J., Anzari H., Masaoka I., “Effect of MnS Inclusions on Stress Corrosion Cracking in Low-Alloy Steels”. Corrosion 48 (5), 1992, p. 419–25, https://doi.org/10.5006/1.3315955.
- Lavigne O., Gamboa E., Griggs J., Luzin V., Law M., Roccisano A., “High-PH Inclined Stress Corrosion Cracking in Australian and Canadian Gas Pipeline X65 Steels,” Materials Science and Technology 32 (7), p. 684–90, https://doi.org/10.1080/02670836.2015.1132030.
- Lavigne O., Gamboa E., Costin W., Law M., Luzin V., Linton V., “Microstructural and Mechanical Factors Influencing High PH Stress Corrosion Cracking Susceptibility of Low

Carbon Line Pipe Steel," Engineering Failure Analysis 45, 2014, p. 283–91, https://doi.org/10.1016/j.engfailanal.2014.07.011.

- Lavigne O., Gamboa E., Luzin V., Law M., Giuliani M., Costin W., "The Effect of the Crystallographic Texture on Intergranular Stress Corrosion Crack Paths," Materials Science and Engineering: A 618, 2014, p. 305–09, https://doi.org/10.1016/j.msea.2014.09.038.
- Leis B. N., "Initiation of SCC on Gas Transmission Pipelines in Related Cracking Environments," Corrosion 96, 1996, NACE-96268.
- Leis B. N., "Some Aspects of Stress-Corrosion-Cracking Analysis for Gas Transmission Pipelines," Proceedings of Metallurgical Society of Canadian Institute of Mining and Metallurgy, edited by R W Revie et al., Pergamon, 1991, pp. 107–21, https://doi.org/10.1016/B978-0-08-041441-6.50014-X.
- Leis B. N., Parkins R. N., "Mechanics and Material Aspects in Predicting Serviceability Limited by Stress-Corrosion Cracking," Fatigue & Fracture of Engineering Materials & Structures 21 (5), 1998, p. 583–601, https://doi.org/10.1046/j.1460-2695.1998.00049.x.
- Li J., Elboujdaini M., Fang B., Revie R. W., Phaneuf M.W., "Microscopy Study of Intergranular Stress Corrosion Cracking of X-52 Line Pipe Steel," Corrosion 62 (4), 2006, p. 316–322. https://doi.org/10.5006/1.3280664.
- Longfei S., Zhiyong L., Xiaogana L., Cuiwei D., "Stress Corrosion Cracking of Simulated Weld Heat-Affected Zone on X100 Pipeline Steel in Carbonate/Bicarbonate Solution," Journal of Materials Engineering and Performance 29 (4), 2020, p. 2574–85, DOI: 10.1007/s11665-020-04750-9.

- Lu B. T., Song F., Gao M., Elboujdaini M., “Crack Growth Model for Pipelines Exposed to Concentrated Carbonate–Bicarbonate Solution with High PH,” Corrosion Science 52 (12), 2010, p. 4064–72, https://doi.org/10.1016/j.corsci.2010.08.023.
- Lu B. T., Song F., Gao M., Elboujdaini M., C”rack Growth Prediction for Underground High Pressure Gas Lines Exposed to Concentrated Carbonate–Bicarbonate Solution with High PH,” Engineering Fracture Mechanics 78 (7), 2011, p. 1452–65, https://doi.org/10.1016/j.engfracmech.2011.01.004.
- Lu B. T., “Further Study on Crack Growth Model of Buried Pipelines Exposed to Concentrated Carbonate–Bicarbonate Solution,” Engineering Fracture Mechanics 131, 2014, p. 296–314, http://dx.doi.org/10.1016/j.engfracmech.2014.08.006.
- Mahdavi F., Forsyth M., Tan M. Y. J., “Techniques for Testing and Monitoring the Cathodic Disbondment of Organic Coatings: An Overview of Major Obstacles and Innovations,” Progress in Organic Coatings105, 2017, p. 163–75, https://doi.org/10.1016/j.porgcoat.2016.11.034.
- Maier C., Beavers J. A., Shie T. M., Vieth P. H. “Interpretation of External Cracking on Underground Pipelines,” International Pipeline Conference, 2006, IPC 2006, IPC2006-10176, p. 289–296, https://doi.org/10.1115/IPC2006-10176.
- Manfredi C., Otegui J. L. “Failures by SCC in Buried Pipelines” Engineering Failure Analysis 9 (5), 2002, p. 495–509, https://doi.org/10.1016/S1350-6307(01)00032-2.
- Meletis E. I., Hochman R. F., “A Review of the Crystallography of Stress Corrosion Cracking,” Corrosion Science 26 (1)1986, p. 63–90, http://dx.doi.org/10.1016/0010-938X(86)90124-1.

- Might J., Duquette D. J., “Stress Corrosion Cracking of High-Purity Carbon Steel in Carbonate Solutions,” Corrosion 52 (6), 1996, p. 428–34, https://doi.org/10.5006/1.3292130.
- Mohtadi-Bonab M., Eskandari M., Ghaedini H., Das S., “Effect of Microstructural Parameters on Fatigue Crack Propagation in an API X65 Pipeline Steel,” Journal of Materials Engineering and Performance 25 (11), 2016, p. 4933–4490, https://doi.org/10.1007/s11665-016-2335-6.
- Niazi H., Nelson G., Lamborn L, Eadie R., Chen W., Zhang H., “Crack Growth Sensitivity to the Magnitude and Frequency of Load Fluctuation in Stage One of High PH Stress Corrosion Cracking,” 2021.
- Niazi H., Chevil K., Gamboa E., Lamborn L., Chen W., Zhang H., “Effects of Loading Spectra on High PH Crack Growth Behavior of X65 Pipeline Steel,” Corrosion 76 (6), 2020, p. 601-615, https://doi.org/10.5006/3472.
- Niazi H., Zhang H., Korol K., Chen W., “High pH Crack Growth Sensitivity to Underload-Type of Pressure Fluctuations,” International Pipeline Conference, 2018, IPC2018-V001T03A064, http://dx.doi.org/10.1115/IPC2018-78394.
- Niazi H., Eadie R., Chen W., Zhang H., “High pH Stress Corrosion Cracking Initiation and Crack Evolution in Buried Steel Pipelines: A Review,” Engineering Failure Analysis 120, 2021, p. 105013, https://doi.org/10.1016/j.engfailanal.2020.105013.
- Niazi H., Zhang H., Lamborn L., Chen W., “The Impact of Pressure Fluctuations on the Early Onset of Stage II Growth of High pH Stress Corrosion Crack,” International Pipeline Conference, 2020, IPC2020-9511, V001T03A022, https://doi.org/10.1115/IPC2020-9511.

- Norsworthy, R., "Coatings Used In Conjuction With Cathodic Protection Shielding Vs Non-Shielding Pipeline Coatings, Corrosion 2009, 2009, NACE-09043.
- Ogundele G. I., White W. E., "Observations on the Influences of Dissolved Hydrocarbon Gases and Variable Water Chemistries on Corrosion of an API-L80 Steel," Corrosion 43 (11) 1987, p. 665–73, https://doi.org/10.5006/1.3583847.
- Ogundele G. I., White W. E., "Some Observations on Corrosion of Carbon Steel in Aqueous Environments Containing Carbon Dioxide," Corrosion 42 (2), 1986, p. 71–78, https://doi.org/10.5006/1.3584888.
- Ossai, C. I., Boswell B., Davis I. J., "Pipeline Failures in Corrosive Environments – A Conceptual Analysis of Trends and Effects American Society of Mechanical Engineers," Engineering Failure Analysis 53, 2015, p. 36–58, https://doi.org/10.1016/j.engfailanal.2015.03.004.
- Parkins R N., "1990 Plenary Lecture: Strain Rate Effects in Stress Corrosion Cracking," Corrosion 46 (3), 1990, pp. 178–89, https://doi.org/10.5006/1.3585089.
- Parkins R. N., "Current Topics in Corrosion: Factors Influencing Stress Corrosion Crack Growth Kinetics," Corrosion 43 (3), 1987, p. 130–39, https://doi.org/10.5006/1.3583125.
- Parkins R. N., "Development of Strain-Rate Testing and Its Implications," in Stress Corrosion Cracking—the Slow Strain-Rate Technique, ed. G. Ugiansky abd J. Payer (West Conshohocken, PA: ASTM, 1979, https://doi.org/10.1520/STP38106S.
- Parkins R. N., O'dell C. S., Fessler R. R., "Factors Affecting the Potential of Galvanostatically Polarised Pipeline Steel in Relation to SCC in Co_3^{2-}—HCO_3^- Solutions," Corrosion Science 24 (4), 1984, p. 343–74, http://dx.doi.org/10.1016/0010-938X(84)90018-0.

- Parkins, R N., “Localized Corrosion and Crack Initiation,” Materials Science and Engineering: A 103 (1), 1988, p. 143–56, https://doi.org/10.1016/0025-5416(88)90562-9.
- Parkins, R N., “Mechanistic Aspects of Intergranular Stress Corrosion Cracking of Ferritic Steels,” Corrosion 52 (5), 1996, p. 363–74, https://doi.org/10.5006/1.3292124.
- Parkins, R. N., “Predictive Approaches to Stress Corrosion Cracking Failure,” Corrosion Science 20(2), 1980, p. 147–66, http://dx.doi.org/10.1016/0010-938X(80)90128-6.
- Parkins, R. N., Belhimer E., Blanchard W. K., “Stress Corrosion Cracking Characteristics of a Range of Pipeline Steels in Carbonate-Bicarbonate Solution,” Corrosion 49 (12), 1993, p. 951–66, https://doi.org/10.5006/1.3316023.
- Parkins, R N. “The Application of Stress Corrosion Crack Growth Kinetics to Predicting Lifetimes of Structures,” Corrosion Science 29 (8), 1989, p. 1019–38, https://doi.org/10.1016/0010-938X(89)90091-7.
- Parkins R. N., “The Controlling Parameters In Stress Corrosion Cracking’. 5th Symposium on Line Pipe Research, 1974, pp. U1–40.
- Parkins R. N., P. W. Slattery, Poulson B. S., “The Effects of Alloying Additions to Ferritic Steels upon Stress Corrosion Cracking Resistance,” Corrosion 37 (11), 1981, p. 650–64. https://doi.org/10.5006/1.3577554.
- Parkins R. N., Greenwel B. S., “The Interface between Corrosion Fatigue and Stress-Corrosion Cracking,” Metal Science 11 (8-9), 1977, p. 405–13, https://doi.org/10.1179/msc.1977.11.8-9.405.
- Parkins R. N., Singh P. M., “Stress Corrosion Crack Coalescence,” Corrosion 46 (6), 1990, p. 485–99, https://doi.org/10.5006/1.3585136.

- Parkins R. N., Zhou S., "The Stress Corrosion Cracking of C-Mn Steel in CO_2-HCO_3^--CO_3^{2-} Solutions. II: Electrochemical and Other Data," Corrosion Science39 (1), 1997, pp. 175–91, http://dx.doi.org/10.1016/S0010-938X(97)89248-7.
- Parkins R. N., Zhou S., "The Stress Corrosion Cracking of C-Mn Steel in CO_2-HCO_3^--CO_3^{2-} Solutions. I: Electrochemical and Other Data,". Corrosion Science 39 (1), 1997, p. 159–73, http://dx.doi.org/10.1016/S0010-938X(96)00116-3.
- Parkins, R. N., "A Review of Stress Corrosion Cracking of High Pressure Gas Pipelines," Corrosion 2000, 2000, NACE-00363.
- Parkins R. N., "Stress Corrosion Cracking of Pipelines - Its Control or Prevention," Corrosion 96, 1996, NACE-96249.
- Paul S. K., Tarafder S., "Cyclic Plastic Deformation Response at Fatigue Crack Tips," International Journal of Pressure Vessels and Piping 101, 2013, p. 81–90, https://doi.org/10.1016/j.ijpvp.2012.10.007.
- Peabody A. W., Bianchetti R. L., "Control of pipeline corrosion," Second ed., NACE, Houston, 2000, p. 5-47.
- Pharris T. C., Kolpa, R. L., "Overview of the Design, Construction, and Operation of Interstate Liquid Petroleum Pipelines," Technical Report, 2008, https://doi.org/10.2172/925387.
- Pilke, A. K., Lambert S. B., Plumtree A., "Stress Corrosion Cracking of X-60 Line Pipe Steel in a Carbonate-Bicarbonate Solution," Corrosion 51 (2), 1995, p. 91–96, https://doi.org/10.5006/1.3293588.
- Pipeline Across Canada. 2016, https://www.nrcan.gc.ca/energy/infrastructure/18856.

- Pourazizi R., Mohtadi-Bonab M. A., Szpunar J. A., “Investigation of Different Failure Modes in Oil and Natural Gas Pipeline Steels,” Engineering Failure Analysis 109, 2020, p. 104400, https://doi.org/10.1016/j.engfailanal.2020.104400.
- Psyrras N. K., Sextos A. G., “Safety of Buried Steel Natural Gas Pipelines under Earthquake-Induced Ground Shaking: A Review,” Soil Dynamics and Earthquake Engineering 106, 2018, p. 254–77, https://doi.org/10.1016/j.soildyn.2017.12.020.
- Fessler R. R., Batte A. D., Hereth M., “Integrity Management of Stress Corrosion Cracking in Gas Pipeline,”. ASME Standards Technology, LLC, 2008.
- Roccisano, A. Nafisi S., Ghomashchi R., “Stress Corrosion Cracking Observed in Ex-Service Gas Pipelines: A Comprehensive Study,”. Metallurgical and Materials Transactions A, vol. 51 (1), 2020, p. 167–88, doi:10.1007/s11661-019-05496-3.
- Ryakhovskikh I. V, Bogdanov R. I., Ignatenko V. E., “Intergranular Stress Corrosion Cracking of Steel Gas Pipelines in Weak Alkaline Soil Electrolytes,” Engineering Failure Analysis 94, 2018, p. 87–95, https://doi.org/10.1016/j.engfailanal.2018.07.036 .
- Sadeghi Meresht, E., Shahrabi Farahani T., Neshati J., “Failure Analysis of Stress Corrosion Cracking Occurred in a Gas Transmission Steel Pipeline,” Engineering Failure Analysis 18 (3), 2011, p. 963–70, https://doi.org/10.1016/j.engfailanal.2010.11.014.
- Saleem B., Ahmed F., Rafiq M. A., Aj,al M., Ali L., “Stress Corrosion Failure of an X52 Grade Gas Pipeline,” Engineering Failure Analysis 46, 2014, p. 157–65, https://doi.org/10.1016/j.engfailanal.2014.08.011.
- Seok M. -Y., Choi I/ -C., Moon J., Kim S., Ramamurty U., Jang J. -i., “Estimation of the Hall–Petch Strengthening Coefficient of Steels through Nanoindentation,” Scripta Materialia 87, 2014, p. 49–52, https://doi.org/10.1016/j.scriptamat.2014.05.004.

- Shipilov, S. A., May I., L., “Structural Integrity of Aging Buried Pipelines Having Cathodic Protection,” Engineering Failure Analysis 13 (7), 2006, p. 1159–76, https://doi.org/10.1016/j.engfailanal.2005.07.008.
- Shoji, Tetsuo, and V. S. Raja. Stress Corrosion Cracking : Theory and Practice. Woodhead Publishing, Woodhead Publishing Series in Metals and Surface Engineering, 2011,
- Skorupa, M., “Load Interaction Effects during Fatigue Crack Growth under Variable Amplitude Loading—a Literature Review. Part I: Empirical Trends,” Fatigue & Fracture of Engineering Materials & Structures 21 (8), 1998, p. 987–1006, https://doi.org/10.1046/j.1460-2695.1998.00083.x.
- Skorupa M., “Load Interaction Effects during Fatigue Crack Growth under Variable Amplitude Loading—a Literature Review. Part II: Qualitative Interpretation,” Fatigue & Fracture of Engineering Materials & Structures 22 (10), 1999, p. 905–26. https://doi.org/10.1046/j.1460-2695.1999.00158.x.
- Song F., “Predicting the Effect of Soil Seasonal Change on Stress Corrosion Cracking Susceptibility of Buried Pipelines at High pH,” Corrosion 66 (9), 2010, p. 095004-095014, https://doi.org/10.5006/1.3490309.
- Song F., Lu, B. T., Gao M., Elboujdaini M., “Development of a Commercial Model to Predict Stress Corrosion Cracking Growth Rates in Operating Pipelines: Southwest Research Institute, 2011.
- Stiksma J., Bradford S. A., “Stress Corrosion Cracking of Dual-Phase Steel in Carbonate/Bicarbonate Solutions,” Corrosion 41 (8), 1985, p. 446–50, https://doi.org/10.5006/1.3583825.

- Sutherby R., Chen W., "Deflected Stress Corrosion Cracks in the Pipeline Steel," International Pipeline Conference, 2004, IPC2004-0600, pp. 113–121, https://doi.org/10.1115/IPC2004-0600.
- Taddesse A. T., Zhu S, -P., Liao D., Keshtegar B., "Cyclic Plastic Zone-Based Notch Analysis and Damage Evolution Model for Fatigue Life Prediction of Metals," Materials & Design, 191, 2020, p. 108639, https://doi.org/10.1016/j.matdes.2020.108639.
- Tang X., Cheng Y. F., "Micro-Electrochemical Characterization of the Effect of Applied Stress on Local Anodic Dissolution Behavior of Pipeline Steel under near-Neutral pH Condition," Electrochimica Acta 54 (5), 2009, p. 1499–505, https://doi.org/10.1016/j.electacta.2008.09.037.
- Tanupabrungsun T., Young D., Brown B., Nesic S., "Construction and Verification of Pourbaix Diagrams For CO_2 Corrosion of Mild Steel Valid Up to 250°C," Corrosion 2012, 2012, NACE-2012-1418.
- Thomas R. J., K. Kirist, Erno B., Fessler R. R., "Generation of Near Neutral PH and High PH SCC Environments on Buried Pipelines," Corrosion 2000, NACE-00362.
- Thompson I., Saithala J. R., "Review of Pipeline Coating Systems from an Operator's Perspective," Corrosion Engineering, Science and Technology 51 (2), 2016, p. 118–35, https://doi.org/10.1179/1743278215Y.0000000038.
- Tong X. Zhang H., Li D., "Effects of Misorientation and Inclination on Mechanical Response Of< 1 1 0> Tilt Grain Boundaries in α-Fe to External Stresses," Modelling and Simulation in Materials Science and Engineering 22 (6), 2014, p. 65016, https://ui.adsabs.harvard.edu/link_gateway/2014MSMSE..22f5016T/doi:10.1088/0965-0393/22/6/065016.

- Toribio J. “Local Strain Rate at Crack Tip: Implications in Stress Corrosion Cracking,” British Corrosion Journal32 (1), 1997, p. 41–48, doi:10.1179/000705997798115165.
- Van Boven G., Chen W., Rogge, R., “The Role of Residual Stress in Neutral pH Stress Corrosion Cracking of Pipeline Steels. Part I: Pitting and Cracking Occurrence,” Acta Materialia 55 (1), 2007, p. 29–42, https://doi.org/10.1016/j.actamat.2006.08.037.
- Vanaei H. R., Eslami A., Egbewande A., “A Review on Pipeline Corrosion, in-Line Inspection (ILI), and Corrosion Growth Rate Models,” International Journal of Pressure Vessels and Piping 149, 2017, p. 43–54, https://doi.org/10.1016/j.ijpvp.2016.11.007.
- Venturino, P., Booman J. N., Gonzalez M. O., Otegui J. L., “Pipeline Failures Due to Lightning,” Engineering Failure Analysis 64, 2016, p. 1–12, https://doi.org/10.1016/j.engfailanal.2016.02.021.
- Villalobos J. C., Del-Pozo A., Campillo B., Mayan J., Serna S., “Microalloyed Steels through History until 2018: Review of Chemical Composition, Processing and Hydrogen Service,” Metals 8 (5), 2018, https://doi.org/10.3390/met8050351.
- Wang J., Atrens A., “Microstructure and Grain Boundary Microanalysis of X70 Pipeline Steel,” Journal of Materials Science 38 (2), 2003, p. 323–30, https://doi.org/10.1023/A:1021169700779.
- Wang J., Atrens A., Cousens D. R., Nockolds C., Bulcock S., “Boundary Characterisation of X65 Pipeline Steel Using Analytical Electron Microscopy,” Journal of Materials Science 34 (8), 1999, p. 1711–19, https://doi.org/10.1023/A:1004530420338.
- Wang, J., Atrens A., Cousens D. R., Kelly P. M., Nockolos C., Bulcock S., “Measurement of Grain Boundary Composition for X52 Pipeline Steel,” Acta Materialia 46 (16), 1998, p. 5677–87, http://dx.doi.org/10.1016/S1359-6454(98)00246-8.

- Wang J., Atrens A., Cousens D. R., Kinaev N., "Microstructure of X52 and X65 Pipeline Steels," Journal of Materials Science 34 (8), 1999, p. 1721–28, https://doi.org/10.1023/A:1004538604409.
- Wang S-H., Chen W., King F., Jack T. R., Fessler R. R., "Precyclic-Loading-Induced Stress Corrosion Cracking of Pipeline Steels in a Near-Neutral-pH Soil Environment," Corrosion 58 (6), 2002, p. 526–34, https://doi.org/10.5006/1.3277644.
- Wang, S., -H., Zhang Y., Chen W., "Room Temperature Creep and Strain-Rate-Dependent Stress-Strain Behavior of Pipeline Steels," Journal of Materials Science 36 (8), 2001, pp. 1931–38, https://doi.org/10.1023/A:1017545907676.
- Wang Sh., Lamborn L., Chevil K., Gamboa E., Chen W., "Near-Neutral PH Corrosion of Mill-Scaled X-65 Pipeline Steel with Paint Primer," Journal of Materials Science & Technology 49, 2020, pp. 166–78, https://doi.org/10.1016/j.jmst.2020.01.016.
- Wang Sh., Niazi H., Lamborn L., Chen W., "Strain-Shock-Induced Early Stage High pH Stress Corrosion Crack Initiation and Growth of Pipeline Steels," Corrosion Science 178, 2021, 109056, https://doi.org/10.1016/j.corsci.2020.109056.
- Wang Y.-Z., Atkinson J. D., Akid R., Parkins R. N., "Crack Interaction, Coalescence and Mixed Mode Fracture Mechanics," Fatigue & Fracture of Engineering Materials & Structures 19 (1), 1996, p. 51–63, https://doi.org/10.1111/j.1460-2695.1996.tb00931.x.
- Wang Z. F., Atrens A., "Initiation of Stress Corrosion Cracking for Pipeline Steels in a Carbonate-Bicarbonate Solution," Metallurgical and Materials Transactions A 27 (9), 1996, p. 2686–91, https://doi.org/10.1007/BF02652362.
- Wilmott M. Erno B., Jack T., Worthingham R., "The Role of Coatings in the Development of Corrosion and Stress Corrosion Cracking on Gas Transmission Pipelines," International

Pipeline Conference, 1998, IPC1998-2048, p. 399–408, https://doi.org/10.1115/IPC1998-2048.

- Wilmott M. Jack T. R., Van Boven G., Sutherby R., "Pipeline Stress Corrosion Cracking: Crack Growth Sensitivity Studies Under Simulated Field Conditions," Corrosion 96. 1996, NACE-96242.
- Xie F. Wang D., Yu C., Zong Y., Wu W., "Effect of HCO_3^- Concentration on the Corrosion Behaviour of X80 Pipeline Steel in Simulated Soil Solution," Journal of Electrochemical Society 12, 2017, p. 9565–74, doi:10.20964/2017.10.42.
- Xie M., Tian Zh. "A Review on Pipeline Integrity Management Utilizing In-Line Inspection Data," Engineering Failure Analysis 92, 2018, p. 222–39, https://doi.org/10.1016/j.engfailanal.2018.05.010.
- Wang Y.-Z., Atkinson J. D., Akid R., Parkins R. N., "Crack Interaction, Coalescence and Mixed Mode Fracture Mechanics," Fatigue & Fracture of Engineering Materials & Structures 19 (1), 1996, pp. 51–63, https://doi.org/10.1111/j.1460-2695.1996.tb00931.x.
- Yan L., Worthingham, King F., Been J., "Factors Affecting the Generation of High-pH Environments Required for Stress Corrosion Cracking (SCC)," International Pipeline Conference, 2012, IPC2012-90515, p. 511–524, https://doi.org/10.1115/IPC2012-90515.
- Yavas D., Alshehri A., Mishra P., Shrotriya P., Bastawos A., F., Hebert K. R., "Morphology and Stress Evolution during the Initial Stages of Intergranular Corrosion of X70 Steel," Electrochimica Acta 285, 2018, p. 336–43, https://doi.org/10.1016/j.electacta.2018.07.207.
- Yavas D., Mishra P., Alshehri A., Shrotriya P., Hebert K. R., Bastawos A., F., "Nanoindentation Study of Corrosion-Induced Grain Boundary Degradation in a Pipeline

Steel," Electrochemistry Communications 88, 2018, p. 88–92, https://doi.org/10.1016/j.elecom.2018.02.001 .

- Young L. M., Andresen P. L., Angeliu T. M., "Crack Tip Strain Rate: Estimates Based on Continuum Theory and Experimental Measurement," Corrosion 2001, 2001, NACE-01131.
- Yu M., Xing X., Zhang H., Zhao J., Eadie R., Chen W., Been J., Van Boven G., Kania R., "Corrosion Fatigue Crack Growth Behavior of Pipeline Steel under Underload-Type Variable Amplitude Loading Schemes,". Acta Materialia 96, 2015, p. 159–69, http://dx.doi.org/10.1016/j.actamat.2015.05.049.
- Yu M., Chen W., Kania R., Van Boven G., Been J., "Crack Propagation of Pipeline Steel Exposed to a Near-Neutral PH Environment under Variable Pressure Fluctuations," International Journal of Fatigue 82 (3), 2016, p. 658–666, http://dx.doi.org/10.1016/j.ijfatigue.2015.09.024.
- Yu M., Chen W., Kania R., Van Boven G., Been J., "Depressurization-Induced Crack Growth Enhancement for Pipeline Steels Exposed to Near-Neutral PH Environments," International Pipeline Conference, 2014, IPC2014-33282, 2014, p. V002T06A076, http://dx.doi.org/10.1115/IPC2014-33282.
- Yu M., Chen W., Kania R., Van Boven G., Been J., "Underload-induced Crack Growth Behaviour of Minor Cycles of Pipeline Steel in Near-neutral PH Environment," Fatigue & Fracture of Engineering Materials & Structures 38 (6), 2014, p. 681–92, https://doi.org/10.1111/ffe.12274.
- Zadow L., "Characterisation of the Morphology of Inclined SCC Cracks in Australian Gas Pipelines" Master Thesis, The University of Adelaide 2014.

- Zhao J., Chen W., Keane S., Been J., Van Boven G., "Development and Validation of Load-Interaction Based Models for Crack Growth Prediction," International Pipeline Conference, 2014, IPC2014-33325, p.V002T06A077, https://doi.org/10.1115/IPC2014-33325.
- Zhao J., Chevil K., Yu M., Been J., Van Boven G., Kania R., Chen W., "Statistical Analysis on Underload-Type Pipeline Spectra," Journal of Pipeline Systems Engineering and Practice 7 (4), 2016, p. 4016007, https://doi.org/10.1061/(ASCE)PS.1949-1204.0000241.
- Zhu M., Ou G., Jin H., Du C., Li X., Liu Z., "Influence of AC Waveforms on Stress Corrosion Cracking Behaviour of Pipeline Steel in High PH Solution," Corrosion Engineering, Science and Technology 51 (1), 2016, p. 18–24, https://doi.org/10.1179/1743278215Y.0000000028.
- Zhu M., Du C., Li X., Liu Zh., Wang Sh., Li J., Zhang D., "Effect of AC Current Density on Stress Corrosion Cracking Behavior of X80 Pipeline Steel in High PH Carbonate/Bicarbonate Solution," Electrochimica Acta 117, 2014, p. 351–59, https://doi.org/10.1016/j.electacta.2013.11.149.
- Zhu M., Du C., Li X., Liu Zh., Wang Sh., Zhao T., Jia J., "Effect of Strength and Microstructure on Stress Corrosion Cracking Behavior and Mechanism of X80 Pipeline Steel in High PH Carbonate/Bicarbonate Solution," Journal of Materials Engineering and Performance23 (4), 2014, p. 1358–65, doi:10.1007/s11665-014-0880-4.
- Zhu M., Du C., Li X., Li J., Li Q., Jia J., Liu. Zh. "Stress Corrosion Cracking Behavior and Mechanism of X65 and X80 pipeline steels in high pH solution," Acta Metallurgica Sinica 49 (12), p. 1590–96, 10.3724/SP.J.1037.2013.00315.